

AD-A147 486

HYDRODYNAMICS CALCULATIONS FOR MINI JADE GAGES(U)
SCIENCE APPLICATIONS INC LA JOLLA CA R N SCHLAUG
29 JUL 83 SAI-001-83-506-LJ DNA-TR-81-300

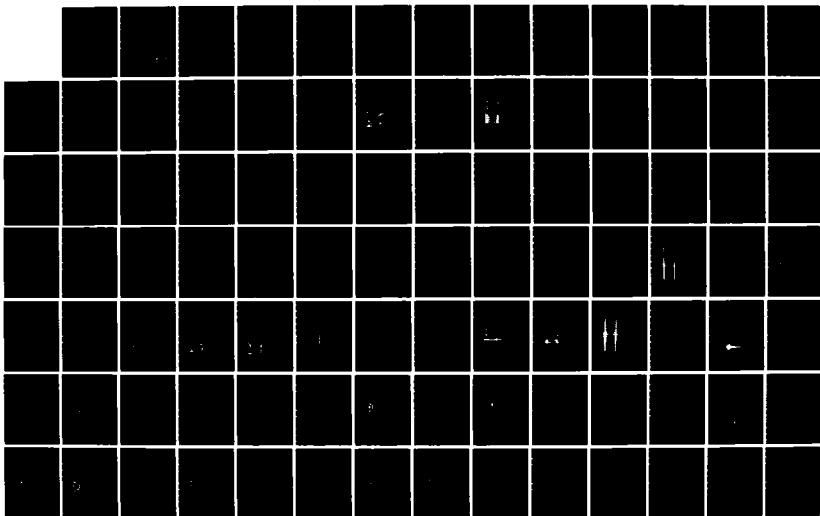
1/2

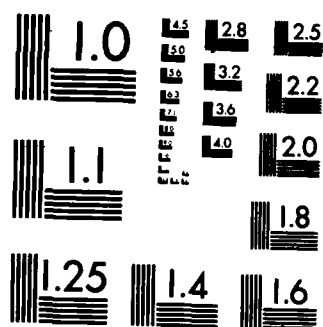
UNCLASSIFIED

DNA001-81-C-0167

F/G 18/3

NL





AD-E301510

12

DNA-TR-81-300

AD-A147 486

HYDRODYNAMICS CALCULATIONS FOR MINI JADE GAGES

Robert N. Schlaug
Science Applications, Inc.
P.O. Box 2351
La Jolla, California 92038

29 July 1983

Technical Report

CONTRACT No. DNA 001-81-C-0167

APPROVED FOR PUBLIC RELEASE;
DISTRIBUTION UNLIMITED.

THIS WORK WAS SPONSORED BY THE DEFENSE NUCLEAR AGENCY
UNDER RDT&E RMSS CODE B345081466 J11AAXA00009 H2590D.

DTIC FILE COPY

Prepared for
Director
DEFENSE NUCLEAR AGENCY
Washington, DC 20305

DTIC
ELECTE
NOV 14 1984
B

88

072

Destroy this report when it is no longer needed. Do not return to sender.

PLEASE NOTIFY THE DEFENSE NUCLEAR AGENCY,
ATTN: STTI, WASHINGTON, D.C. 20305, IF
YOUR ADDRESS IS INCORRECT, IF YOU WISH TO
BE DELETED FROM THE DISTRIBUTION LIST, OR
IF THE ADDRESSEE IS NO LONGER EMPLOYED BY
YOUR ORGANIZATION.



UNCLASSIFIED

SECURITY CLASSIFICATION OF THIS PAGE (When Data Entered)

| REPORT DOCUMENTATION PAGE | | READ INSTRUCTIONS BEFORE COMPLETING FORM |
|---|------------------------------------|---|
| 1. REPORT NUMBER DNA-TR-81-300 | 2. GOVT ACCESSION NO. ADA147426 | 3. RECIPIENT'S CATALOG NUMBER |
| 4. TITLE (and Subtitle) HYDRODYNAMICS CALCULATIONS FOR MINI JADE GAGES | | 5. TYPE OF REPORT & PERIOD COVERED Technical Report |
| | | 6. PERFORMING ORG. REPORT NUMBER SAI-011-83-506-LJ |
| 7. AUTHOR(s) Robert N. Schlaug | | 8. CONTRACT OR GRANT NUMBER(s) DNA 001-81-C-0167 |
| 9. PERFORMING ORGANIZATION NAME AND ADDRESS Science Applications, Inc. Post Office Box 2351 La Jolla, California 92038 | | 10. PROGRAM ELEMENT, PROJECT, TASK AREA & WORK UNIT NUMBERS Task J11AAXAX-00009 |
| 11. CONTROLLING OFFICE NAME AND ADDRESS Director Defense Nuclear Agency Washington, DC 20305 | | 12. REPORT DATE 29 July 1983 |
| | | 13. NUMBER OF PAGES 180 |
| 14. MONITORING AGENCY NAME & ADDRESS (if different from Controlling Office) | | 15. SECURITY CLASS (of this report) UNCLASSIFIED |
| | | 15a. DECLASSIFICATION/DOWNGRADING SCHEDULE N/A since UNCLASSIFIED |
| 16. DISTRIBUTION STATEMENT (of this Report) Approved for public release; distribution unlimited. | | |
| 17. DISTRIBUTION STATEMENT (of the abstract entered in Block 20, if different from Report) | | |
| 18. SUPPLEMENTARY NOTES This work was sponsored by the Defense Nuclear Agency under RDT&E RMSS Code B345081466 J11AAXAX00009 H2590D. | | |
| 19. KEY WORDS (Continue on reverse side if necessary and identify by block number) | | |
| 20. ABSTRACT (Continue on reverse side if necessary and identify by block number) Two-dimensional hydrodynamics calculations were made with the STEALTH code to determine the response under 10 GPa loading of three designs of the SAI particle velocity gage. The calculations showed which design best measured the free field particle velocity. Two-dimensional calculations were also made for four designs of the SRI cylindrical stress gage. The calculations determined that the internal gage dynamics, particularly shock reflections, were primarily responsible for | | |

UNCLASSIFIED

SECURITY CLASSIFICATION OF THIS PAGE (When Data Entered)

UNCLASSIFIED

SECURITY CLASSIFICATION OF THIS PAGE(When Data Entered)

20. ABSTRACT (Continued)

differences between the gage response and the free field stress. A material parameter study using a one-dimensional model was made to see if the use of other material combinations would improve the gage response.

The internal dynamics of the flat pack stress gage were investigated using a one-dimensional model. The calculations indicated the severe early-time "ringing" seen in the gage response is caused by oscillatory motion of the iron plates.

UNCLASSIFIED

SECURITY CLASSIFICATION OF THIS PAGE(When Data Entered)

LIST OF ILLUSTRATIONS

| <u>Figure</u> | | <u>Page</u> |
|---------------|---|-------------|
| 1.1 | Schematic of TDR gage design and operation. | 3 |
| 1.2 | Evolution of the TDR gage design--half actual size. | 5 |
| 1.3 | Comparison of flyer plate and free field velocities for the Al/silica and Mg/Teflon TDR gages with Al tube conductors | 6 |
| 1.4 | Pressure contour plot at 23.84 μ sec--Al/silica TDR gage with Al tube conductors. | 7 |
| 1.5 | Pressure contour plot at 24.66 μ sec--Mg/Teflon TDR gage with Al tube conductors. | 9 |
| 1.6 | Pressure contour plot at 152.9 μ sec--Mg/Teflon TDR gage with Al foil conductors. | 10 |
| 1.7 | Shock front and flyer plate displacement--Mg/Teflon TDR gage with Al foil conductors. | 11 |
| 1.8 | Schematic of cylindrical stress gage. | 13 |
| 1.9 | Cylindrical gage designs--actual size | 15 |
| 1.10 | Experimental and computed response of the brass/ epoxy cylindrical gage. | 16 |
| 1.11 | Grid plot at 5.92 μ sec--brass/epoxy cylindrical gage. | 17 |
| 1.12 | Average pressure around piezoresistive wire for the Mg/Teflon and Al/Teflon cylindrical gages | 19 |
| 1.13 | Deformation of the Mg/Teflon cylindrical gage | 21 |
| 1.14 | Average wire pressure to 19 μ sec--Al/silastic cylindrical gage. | 23 |
| 1.15 | Deformation of the Al/Teflon and Al/silastic cylindrical gages | 25 |
| 1.16 | Center pressure from 1-D calculations of the Al/ Teflon and Al/silastic cylindrical gages. | 29 |

TABLE OF CONTENTS

| <u>Section</u> | <u>Page</u> |
|---|-------------|
| LIST OF ILLUSTRATIONS | ii |
| LIST OF TABLES. | viii |
| 1. INTRODUCTION AND SUMMARY. | 1 |
| 1-1 TDR Particle Velocity Gage. | 2 |
| 1-2 Cylindrical Stress Gage | 12 |
| 1-3 Flat Pack Stress Gage | 31 |
| 2. TDR PARTICLE VELOCITY GAGE. | 36 |
| 2-1 Al/Silica Gage with Al Tubing | 36 |
| 2-2 Mg/Teflon Gage with Al Tubing | 49 |
| 2-3 Mg/Teflon Gage with Al Foil | 54 |
| 3. CYLINDRICAL STRESS GAGE | 62 |
| 3-1 Brass/Epoxy Gage. | 62 |
| 3-2 Mg/Teflon Gage. | 86 |
| 3-3 Al/Teflon Gage. | 101 |
| 3-4 Al/Silastic Gage. | 116 |
| 3-5 Gage Materials Study. | 136 |
| 4. FLAT PACK STRESS GAGE | 143 |
| REFERENCES. | 151 |
| APPENDIX Determination of the Velocity of the Piezoresistive Wire. | A-1 |

14

ORIGINAL
COPY
MAINTAINED

| | |
|---------------------|-------------------------------------|
| Accession For | |
| NTIS GRA&I | <input checked="" type="checkbox"/> |
| DTIC TAB | <input type="checkbox"/> |
| Unannounced | <input type="checkbox"/> |
| Justification | |
| By _____ | |
| Distribution/ _____ | |
| Availability Codes | |
| Dist | Avail and/or Special |
| A-1 | |

LIST OF ILLUSTRATIONS (Continued)

| <u>Figure</u> | | <u>Page</u> |
|---------------|--|-------------|
| 1.17 | Effect of Mg thickness on center pressure of Mg/Teflon gage (from 1-D calculations). | 30 |
| 1.18 | Center pressure from 1-D calculations of the Al foil/Teflon and Al foil/silastic cylindrical gages | 32 |
| 1.19 | Schematic of flat pack stress gage. | 33 |
| 1.20 | Effect of material variation on flat pack gage response | 35 |
| 2.1 | Dimensions and problem setup for the Al/silica TDR gage. | 37 |
| 2.2 | Initial grid for the Al/silica TDR gage | 40 |
| 2.3 | Pressure contour plot at 12.29 μ sec--Al/silica TDR gage. | 42 |
| 2.4 | Pressure contour plot at 14.80 μ sec--Al/silica TDR gage. | 44 |
| 2.5 | Pressure contour plot at 16.98 μ sec--Al/silica TDR gage. | 45 |
| 2.6 | Pressure contour plot at 19.21 μ sec--Al/silica TDR gage. | 46 |
| 2.7 | Pressure contour plot at 21.50 μ sec--Al/silica TDR gage. | 47 |
| 2.8 | Grid plot at 23.84 μ sec--Al/silica TDR gage | 48 |
| 2.9 | Pressure contour plot at 15.07 μ sec--Mg/Teflon TDR gage with Al tubing | 51 |
| 2.10 | Pressure contour plot at 17.49 μ sec--Mg/Teflon TDR gage with Al tubing | 52 |
| 2.11 | Grid plot at 24.66 μ sec--Mg/Teflon TDR gage with Al tubing. | 53 |
| 2.12 | Initial grid for the Mg/Teflon TDR gage with Al foil | 55 |

LIST OF ILLUSTRATIONS (Continued)

| <u>Figure</u> | | <u>Page</u> |
|---------------|---|-------------|
| 2.13 | Pressure contour plot at 97.40 μ sec--Mg/Teflon TDR gage with Al foil | 58 |
| 2.14 | Pressure contour plot at 129.3 μ sec--Mg/Teflon TDR gage with Al foil | 59 |
| 2.15 | Grid plot of flyer plate region at 152.9 μ sec-- Mg/Teflon TDR gage with Al foil | 60 |
| 3.1 | Initial grid for the brass/epoxy cylindrical gage | 63 |
| 3.2 | Initial zoning of gage region--brass/epoxy cylindrical gage. | 65 |
| 3.3 | Grid-velocity plot at 2.51 μ sec--brass/epoxy cylindrical gage. | 67 |
| 3.4 | Pressure contour plot at 2.51 μ sec--brass/epoxy cylindrical gage. | 68 |
| 3.5 | Grid distortion in Lagrange calculation of brass/ epoxy cylindrical gage. | 69 |
| 3.6 | Pressure contour plot at 3.47 μ sec--brass/epoxy cylindrical gage. | 71 |
| 3.7 | Pressure contour plot at 4.43 μ sec--brass/epoxy cylindrical gage. | 72 |
| 3.8 | Pressure contour plot at 4.74 μ sec--brass/epoxy cylindrical gage. | 74 |
| 3.9 | Pressure contour plot at 5.00 μ sec--brass/epoxy cylindrical gage. | 75 |
| 3.10 | Pressure contour plot at 5.60 μ sec--brass/epoxy cylindrical gage. | 76 |
| 3.11 | Pressure contour plot at 5.92 μ sec--brass/epoxy cylindrical gage. | 77 |
| 3.12 | Dezoned grid at 5.0 μ sec--brass/epoxy cylindrical gage. | 78 |
| 3.13 | Wire pressure and velocity--brass/epoxy cylindrical gage. | 80 |

LIST OF ILLUSTRATIONS (Continued)

| <u>Figure</u> | | <u>Page</u> |
|---------------|---|-------------|
| 3.14 | Models for cylindrical gage deformation | 82 |
| 3.15 | Displacement versus time for rigid body and ideal cylindrical gages | 83 |
| 3.16 | Deformation of brass/epoxy cylindrical gage | 85 |
| 3.17 | Change in gage major and minor axes versus time | 87 |
| 3.18 | Initial grid for the Mg/Teflon cylindrical gage | 89 |
| 3.19 | Initial zoning of gage region--Mg/Teflon cylindrical gage. | 90 |
| 3.20 | Pressure contour plot at 7.15 μ sec--Mg/Teflon cylindrical gage. | 91 |
| 3.21 | Pressure contour plot at 9.41 μ sec--Mg/Teflon cylindrical gage. | 92 |
| 3.22 | Pressure contour plot at 10.96 μ sec--Mg/Teflon cylindrical gage. | 93 |
| 3.23 | Pressure contour plot at 11.19 μ sec--Mg/Teflon cylindrical gage. | 95 |
| 3.24 | Grid plot of gage region at 13.73 μ sec--Mg/Teflon cylindrical gage. | 96 |
| 3.25 | Wire pressure and velocity--Mg/Teflon cylindrical gage. | 97 |
| 3.26 | Deformation of Mg/Teflon cylindrical gage | 99 |
| 3.27 | Initial grid for the Al/Teflon cylindrical gage | 102 |
| 3.28 | Initial zoning of gage region--Al/Teflon cylindrical gage. | 103 |
| 3.29 | Pressure contour plot at 5.41 μ sec--Al/Teflon cylindrical gage. | 104 |
| 3.30 | Pressure contour plot at 7.21 μ sec--Al/Teflon cylindrical gage. | 105 |
| 3.31 | Pressure contour plot at 8.66 μ sec--Al/Teflon cylindrical gage. | 106 |

LIST OF ILLUSTRATIONS (Continued)

| <u>Figure</u> | | <u>Page</u> |
|---------------|--|-------------|
| 3.32 | Pressure contour plot at 9.55 μ sec--Al/Teflon cylindrical gage. | 108 |
| 3.33 | Pressure contour plot at 12.25 μ sec--Al/Teflon cylindrical gage. | 109 |
| 3.34 | Grid plot of gage region at 12.25 μ sec--Al/Teflon cylindrical gage. | 110 |
| 3.35 | Wire pressure and velocity--Al/Teflon cylindrical gage. | 111 |
| 3.36 | Deformation of Al/Teflon cylindrical gage | 113 |
| 3.37 | Comparison of wire pressure and velocity for the two Al/Teflon gage calculations | 115 |
| 3.38 | Initial grid for the Al/silastic cylindrical gage | 117 |
| 3.39 | Initial zoning of gage region--Al/silastic cylindrical gage. | 118 |
| 3.40 | Pressure contour plot at 5.41 μ sec--Al/silastic cylindrical gage. | 120 |
| 3.41 | Pressure contour plot at 6.93 μ sec--Al/silastic cylindrical gage. | 121 |
| 3.42 | Pressure contour plot at 8.48 μ sec--Al/silastic cylindrical gage. | 122 |
| 3.43 | Pressure contour plot at 9.36 μ sec--Al/silastic cylindrical gage. | 123 |
| 3.44 | Pressure contour plot at 14.27 μ sec--Al/silastic cylindrical gage. | 124 |
| 3.45 | Wire velocity to 19 μ sec--Al/silastic cylindrical gage. | 126 |
| 3.46 | Grid plot at 19.16 μ sec--Al/silastic cylindrical gage. | 128 |
| 3.47 | Change in major and minor axes of Al/silastic gage versus time | 129 |

LIST OF ILLUSTRATIONS (Continued)

| <u>Figure</u> | | <u>Page</u> |
|---------------|---|-------------|
| 3.48 | Deformation of Al/silastic cylindrical gage | 130 |
| 3.49 | Effect of slide lines at the soil/gage interface-- Al/silastic cylindrical gage. | 134 |
| 3.50 | Al/silastic gage response with and without slide lines | 135 |
| 3.51 | Models for 1-D calculations of the cylindrical stress gage | 137 |
| 3.52 | Center pressure from 1-D calculations of the Al/epoxy and Al/polyethylene cylindrical gages. | 140 |
| 3.53 | Effect of insulator density on response of cylindrical stress gage | 141 |
| 4.1 | Initial configuration for flat pack gage calculations. | 144 |
| 4.2 | Pressure plots at several times for flat pack stress gage with 0.16 mm iron plates. | 146 |
| 4.3 | Center pressure from 1-D calculations of flat pack gages with 0.32-cm-thick plates. | 149 |
| A.1 | Web grid for test problem | A-3 |
| A.2 | Rectangular grid for test problem | A-7 |
| A.3 | Comparison of average pressure at gage center for rectangular and centroid grids. | A-8 |
| A.4 | Comparison of velocity at gage center for rectangular and centroid grids. | A-9 |
| A.5 | Zones used in the centroid wire motion algorithm. | A-11 |
| A.6 | Wire pressure as a function of wire velocity to the first pressure peak | A-15 |

LIST OF TABLES

| <u>Table</u> | | <u>Page</u> |
|--------------|--|-------------|
| 2.1 | Equations of state for gage calculations. | 39 |
| 2.2 | Initial zoning for the TDR gage problems with Al tubing | 41 |
| 2.3 | Initial zoning for the Mg/Teflon TDR gage with Al foil | 57 |
| 3.1 | Zoning for cylindrical gage calculations. | 64 |
| 4.1 | Zoning for the flat pack gage calculations. | 144 |

SECTION 1

INTRODUCTION AND SUMMARY

The ability to accurately predict ground shock and cratering phenomena is important to the survival of buried military systems that may be subjected to nuclear attack. The prediction techniques in current use are based to a large extent on data obtained from the atmospheric nuclear weapons tests of the 1950s and 1960s. Unfortunately, there is little data available, much of which is for weapons, geologies and burst heights that are not relevant to present day threats. Numerical calculations, if their accuracy were confirmed, could provide the information needed for systems design. However, our current computer codes are suspect because of the discrepancy between calculated and measured crater volumes for near-surface bursts.

The Defense Nuclear Agency has embarked on a combined computational and experimental program to understand cratering-related phenomena and improve the accuracy of the numerical predictions. This effort includes a test instrumentation development (TID) program for underground nuclear cratering simulation tests. The objective of the TID program is to upgrade existing stress and particle velocity gages and/or develop new instrumentation capable of making measurements in the 10 to 30 GPa stress regime.

We have participated in this effort by providing computational support for the TID program from June 1981 to April 1983. The major effort during this contract was a number of two-dimensional (2-D) numerical simulations made to predict gage response under 10 GPa loadings. Calculations were made for three designs of the time domain reflectometry (TDR) particle velocity gage being developed by Ken Sites (SAI-Las Vegas) and for four designs of the cylindrical stress gage under development by Doug Keough and Paul DeCarli (SRI International). Some one-dimensional (1-D) calculations were also made for the SRI flat pack stress gage and as part of a material variation study for the cylindrical stress gage.

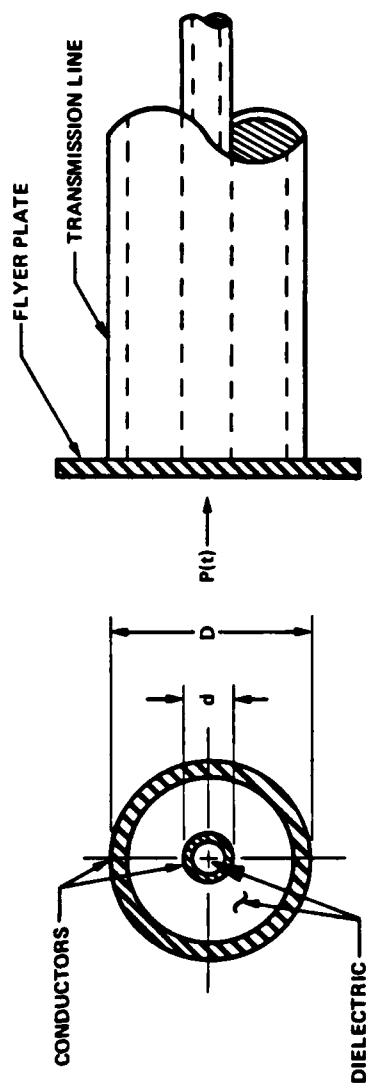
The results of our calculations are summarized in this section. The computational techniques and descriptions of the time evolution of each gage calculation are given in Section 2 for the TDR particle velocity gage, in Section 3 for the cylindrical stress gage, and in Section 4 for the flat pack stress gage.

All of the calculations described in this report were made using the STEALTH code (Reference 1), a Lagrange geometry, time explicit, finite difference transient continuum mechanics computer code. The initial calculations used Version 3.2I of STEALTH. In June 1982, Version 4.1A of this code was released by the Electric Power Research Institute and calculations made after that date used the updated code. The calculations were run on the DNA Cyber 176 computer located in Albuquerque, New Mexico, until December 1982 and thereafter in Los Alamos, New Mexico.

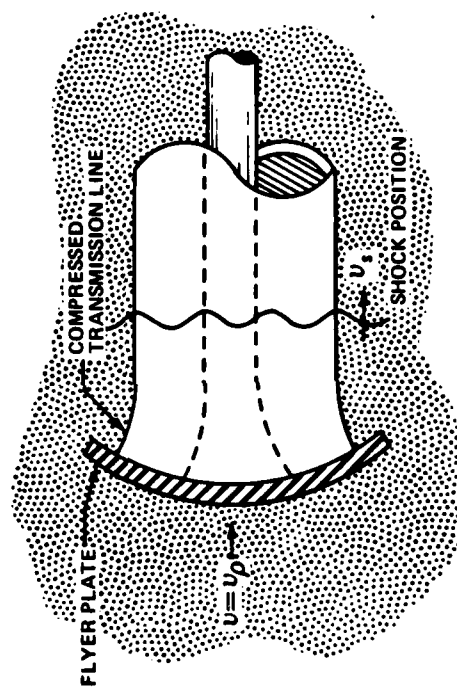
1-1 TDR PARTICLE VELOCITY GAGE

The basic design and operation of the time domain reflectometry particle velocity gage is shown in Figure 1.1. The gage consists of a circular conducting metal flyer plate attached to the end of a cylindrical coaxial transmission line (see Figure 1.1a). The two coaxial conductors are connected through the plate to form a complete electrical circuit. An insulating dielectric material separates the conductors leading to the flyer plate. In normal operation, the plate would be oriented perpendicular to the incident shock wave. The passage of the shock wave over the gage would cause the plate to move, thus shortening the electrical circuit path, and possibly also causing gage deformation similar to that shown in Figure 1.1b.

While there are several versions of this gage (varying in dimensions, materials of construction, etc.), they all measure the soil particle velocity in the same way. A high frequency electromagnetic signal is fed down the transmission line and reflected from the moving conductor (the flyer plate) imbedded in the soil. The reflected signal is compared with the incident signal and from this comparison the plate velocity is obtained. (The details of this process are described in Reference 2.) It is assumed that the flyer plate moves with the soil and therefore the plate velocity is equal to the soil particle velocity.



(a) Basic design of TDR gage



(b) Anticipated behavior of TDR gage under shock loading

Figure 1.1. Schematic of TDR gage design and operation.

Our task was to simulate through numerical calculations the various TDR gage designs to determine if the flyer plate did indeed move with the soil. A further objective was to compute the gage deformation and its effect on gage response and gage failure. It was hoped that by providing this information to the gage designers, more accurate and reliable gages could be designed. Only the most promising designs based on the computed results would actually be constructed and tested in a high explosive (HE) environment and subsequently used in an underground nuclear test.

Numerical simulation calculations were made for the three TDR gage designs shown in Figure 1.2. Each gage is cylindrically symmetric and was assumed to be surrounded by a uniform tuff-like soil in the calculations. Boundary conditions were used to generate a 10 GPa shock wave that was normally incident on the flyer plate. The 2-D STEALTH code was then used to calculate the gage response. All three of the designs shown in Figure 1.2 were considered for the prototype TDR gage but only one was built. Our numerical calculations indicated problems with two of the designs and contributed to the decision not to invest the time and expense required to build prototypes of those designs.

Our first calculation was of the gage shown in Figure 1.2a. This gage had an aluminum flyer plate, a fused-silica dielectric, and aluminum tube conductors to carry the signal current to and from the flyer plate. The STEALTH calculation showed this design was inadequate in two respects. First, the aluminum plate did not move at the same particle velocity as the soil (see Figure 1.3). Second, the shock passing over the gage traveled faster in the fused silica than in the surrounding soil. This led to a steep pressure gradient across the outer aluminum conductor tube tending to displace it outward. This can be seen in the pressure contour plot at the end of the calculation shown in Figure 1.4. (The darkened lines denote the flyer plate and the Al tube conductors. The pressure wave was incident from the top of the grid.)

In view of the computational results and the difficulty of fabricating fused silica, this gage was not built and tested. Instead, the use of other materials in the gage was investigated. A second calculation was made in which

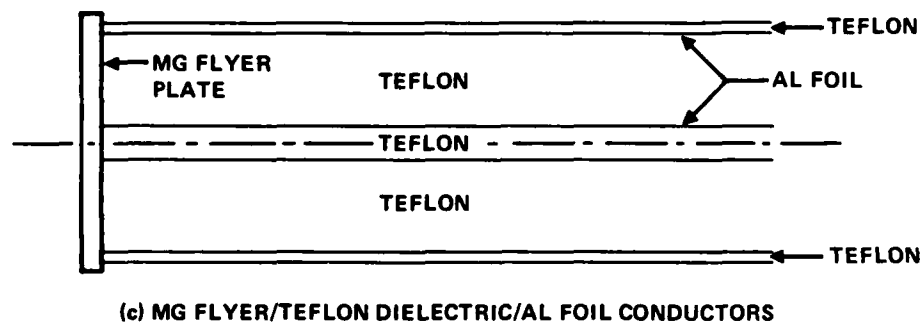
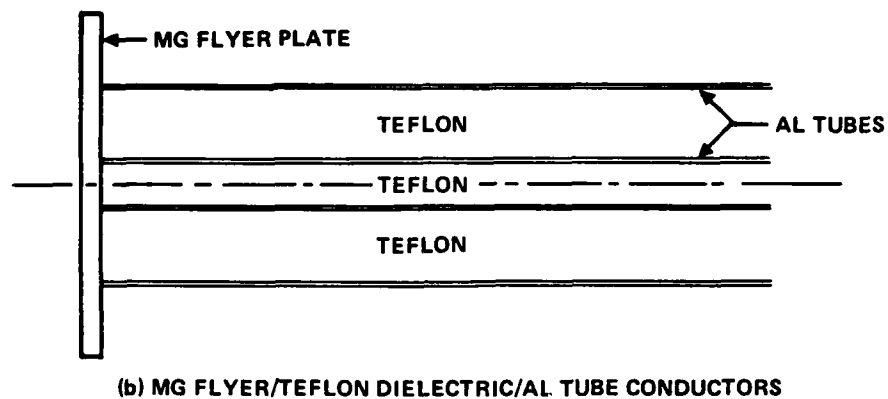
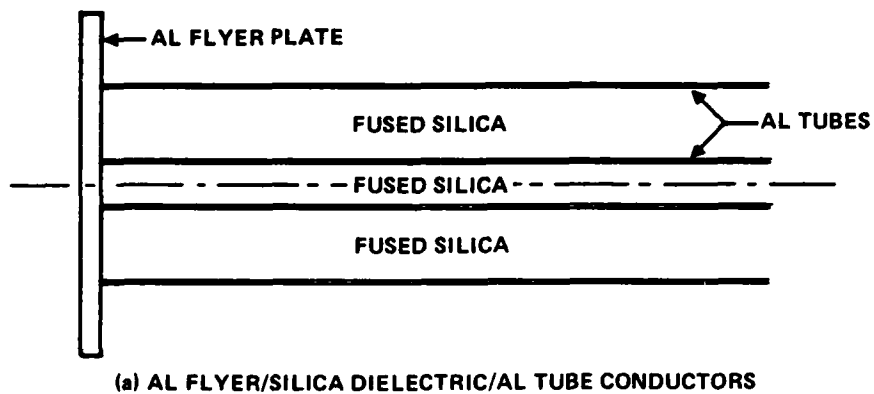


Figure 1.2. Evolution of the TDR gage design--
half actual size.

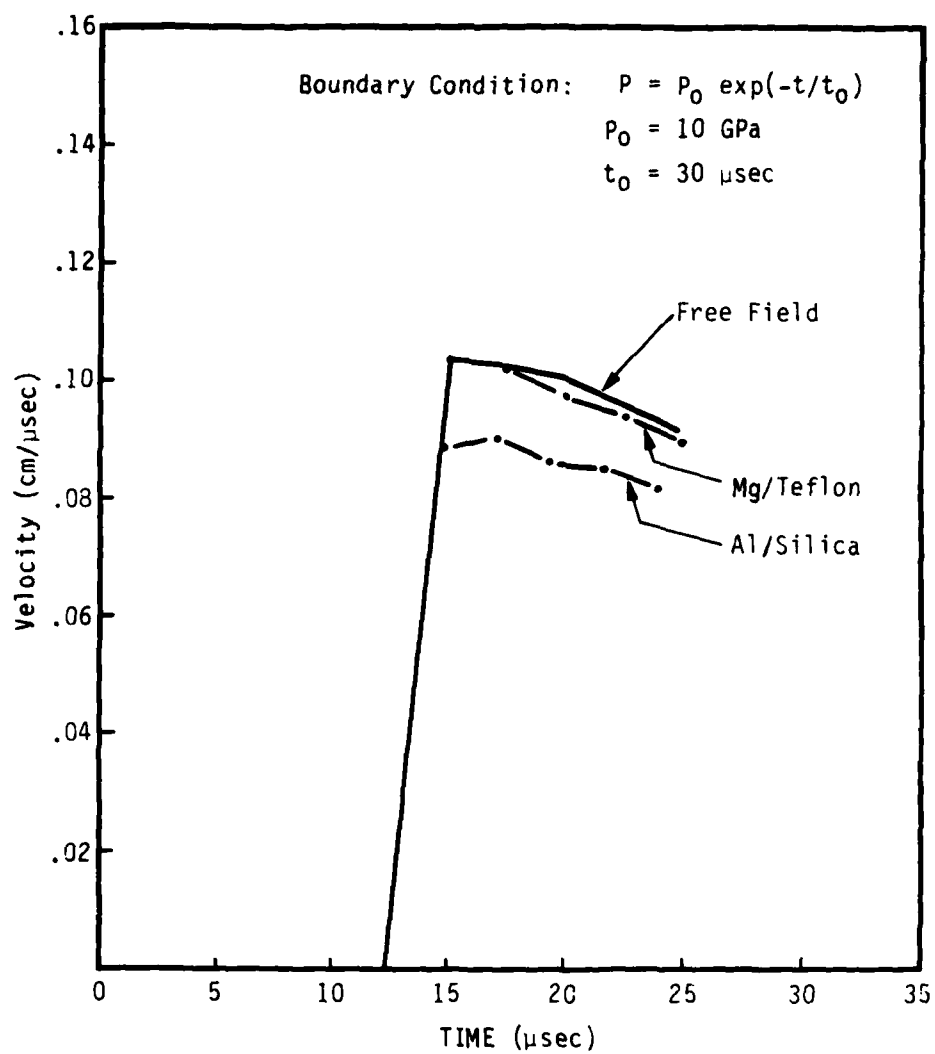


Figure 1.3. Comparison of flyer plate and free field velocities for the Al/silica and Mg/Teflon TDR gages with Al tube conductors.

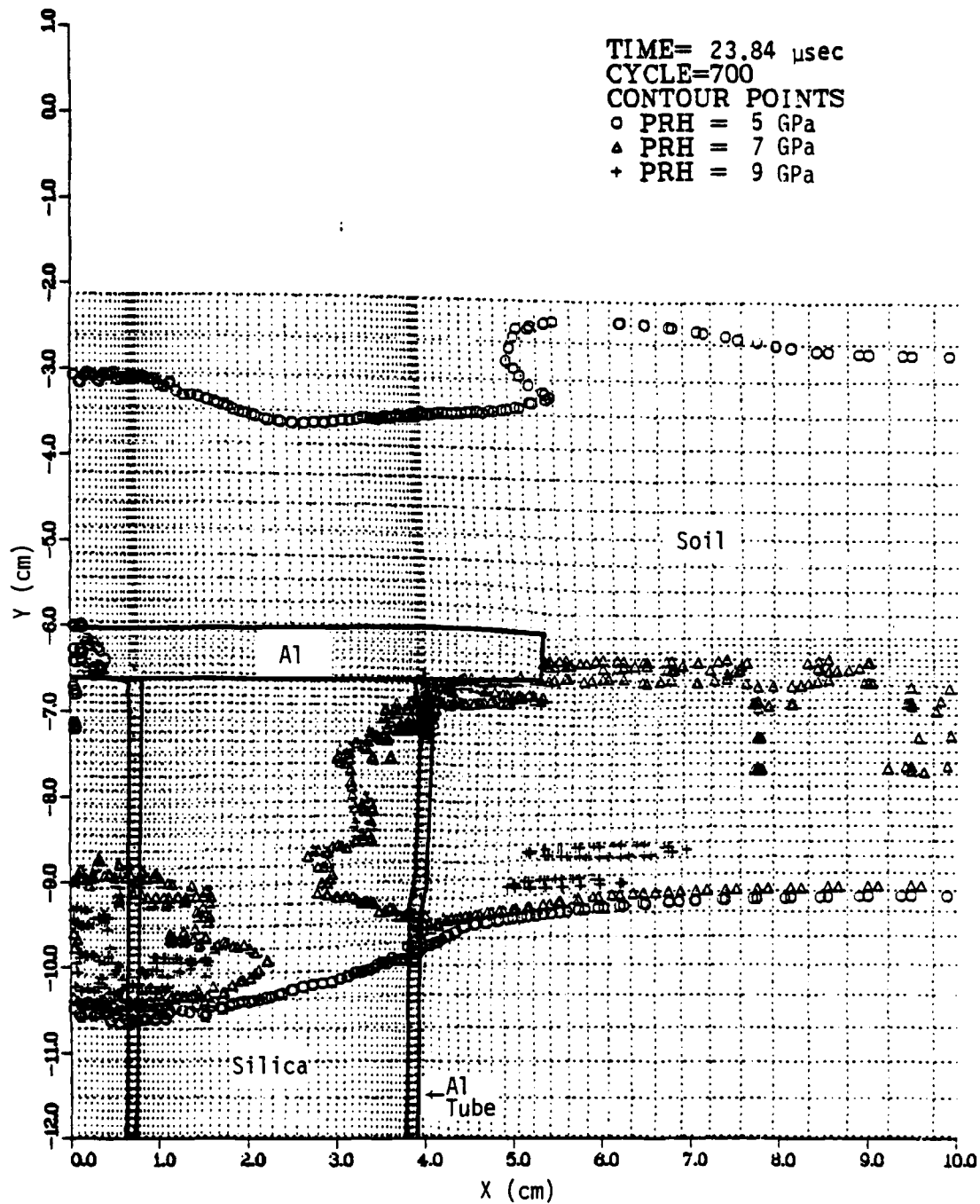


Figure 1.4. Pressure contour plot at 23.84 μ sec--
 Al/silica TDR gage with Al tube conductors.

magnesium was used for the flyer plate and Teflon for the dielectric material. The overall gage dimensions were unchanged (see Figure 1.2b). The STEALTH calculation of this gage showed a great improvement in the gage behavior. The magnesium flyer plate moved at nearly the same velocity as the soil (see Figure 1.3) and the shock front position in the gage was very close to shock position in the soil (see Figure 1.5). One can also see in Figure 1.5 some bending distortion occurring near the outer edge of the flyer plate and that the shock wave is traveling somewhat faster in the aluminum tubes than in the Teflon.

The TDR gages actually built had the design shown in Figure 1.2c. The Mg flyer plate has a smaller diameter and the aluminum tubes were replaced by aluminum foil which was wrapped around the Teflon dielectric. Prototypes of this gage were tested in HE experiments at SRI International in December 1981 and performed well (Reference 2). Other HE tests were conducted in 1982 and this gage was fielded in the HURON LANDING and MINI JADE underground nuclear tests.

The change from Al tubes to Al foil conductors enabled us to use larger zones in the STEALTH computational grid and, as a result, we were able to run the simulation calculation to a much longer problem time. The pressure contours at the end of the calculation are shown in Figure 1.6. The shock front is nearly identical in the gage and in the soil. Figure 1.6 also shows that significant distortion occurs in the Teflon dielectric just behind the flyer plate. This distortion may lead to errors in the gage response because of changes in the coaxial conductor impedance or to gage failure because the electrical connection to the flyer plate is broken.

The shock front displacement in the Teflon is shown in Figure 1.7a. This problem was run with a constant 10 GPa shock (no decay in time) so the displacement is linear in time. The shock velocity is nearly the same in both the Teflon and the soil as indicated by the nearly flat 5- and 10-GPa contours shown in Figure 1.6. The displacement of the bottom of the flyer plate versus time is shown in Figure 1.7b. The plate has a nearly constant velocity of

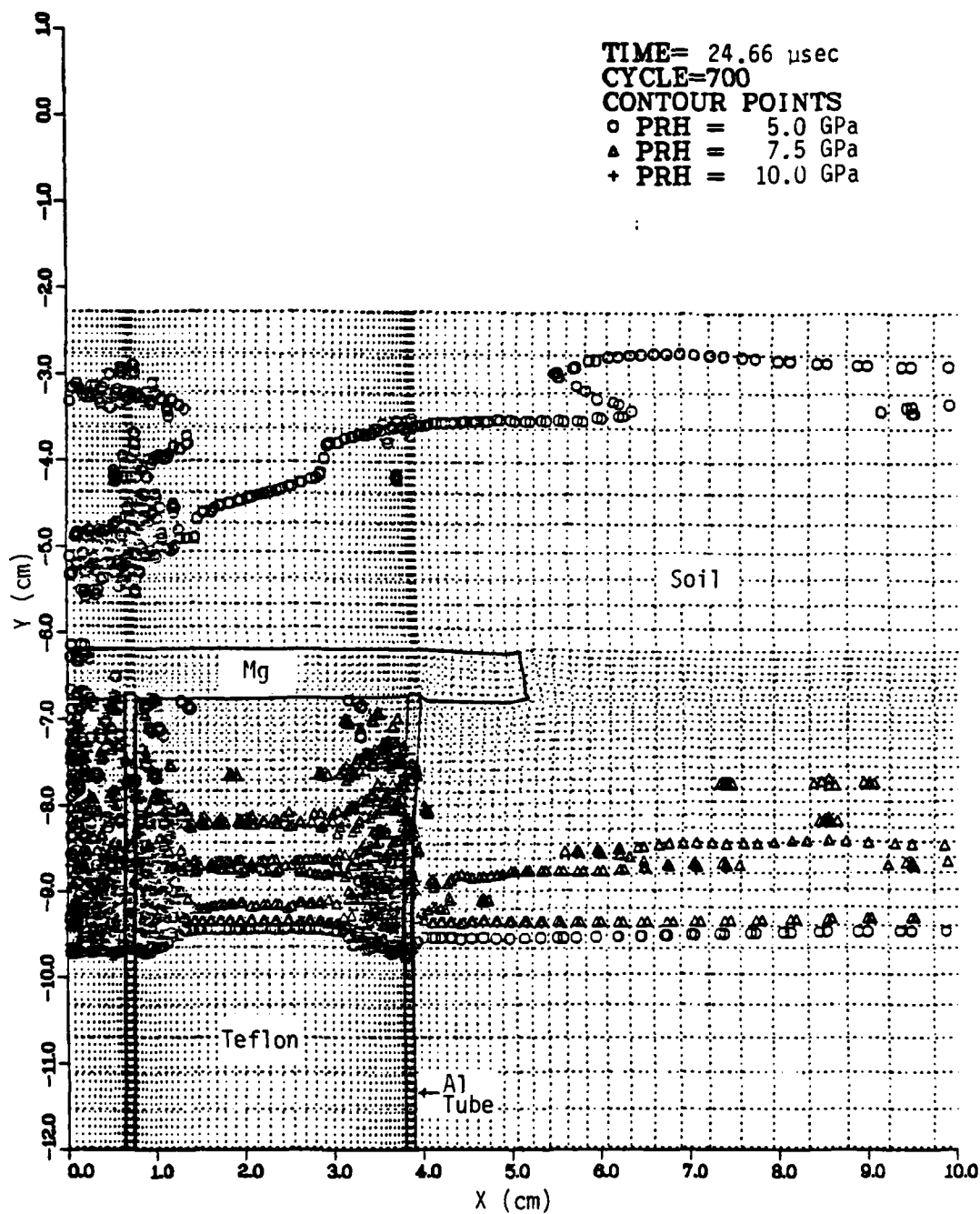


Figure 1.5. Pressure contour plot at 24.66 μ sec--
 Mg/Teflon TDR gage with Al tube conductors.

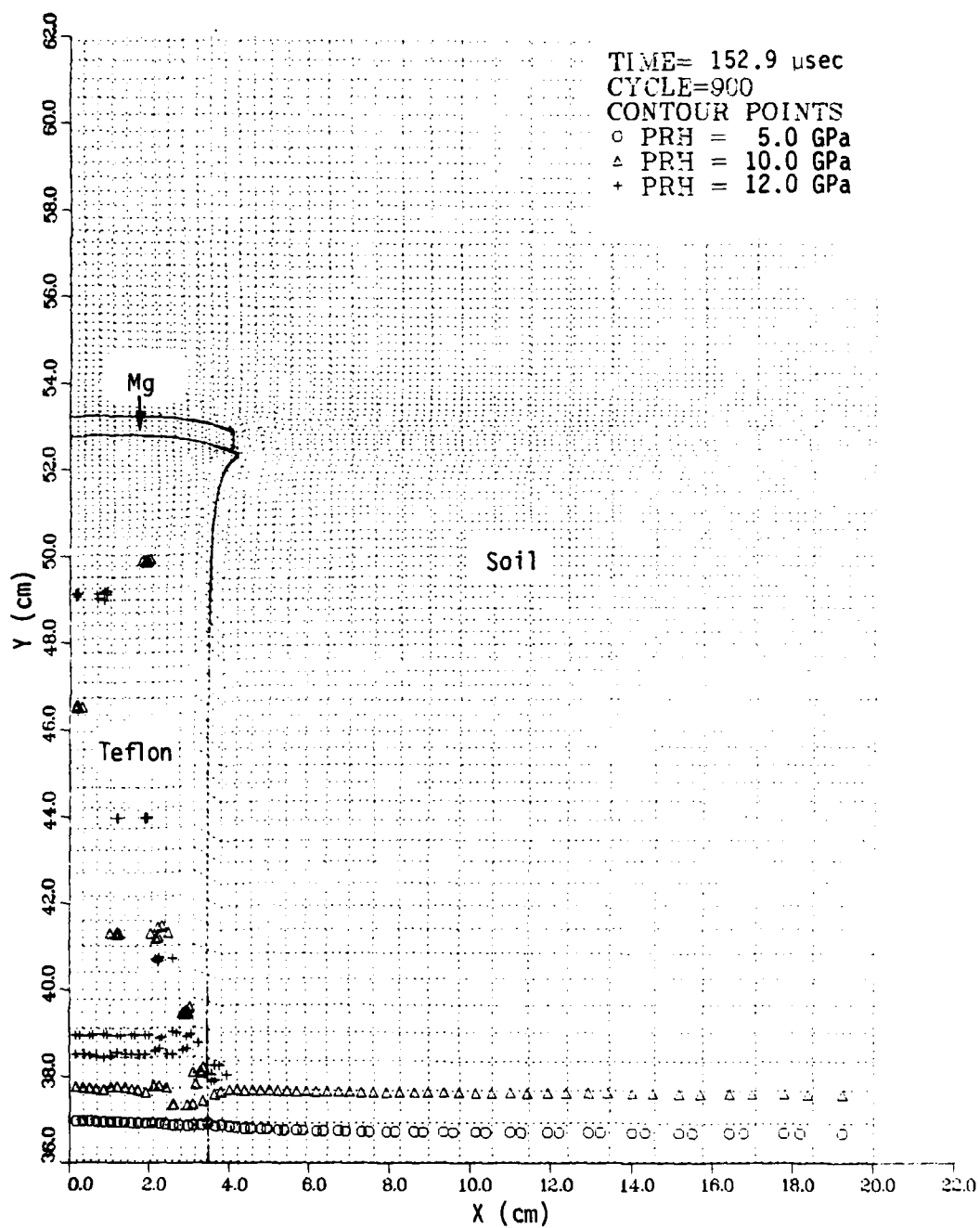
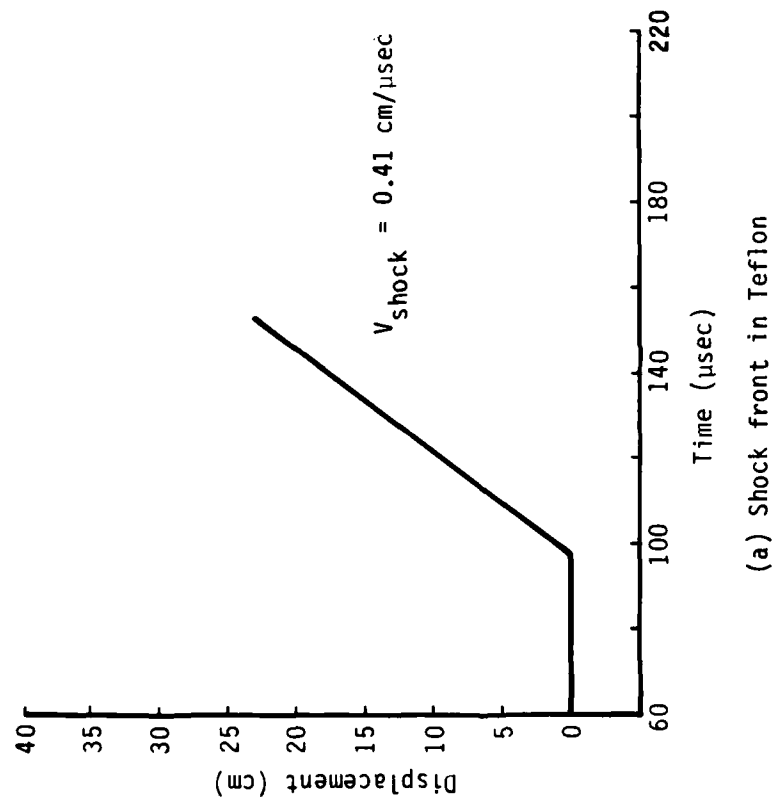
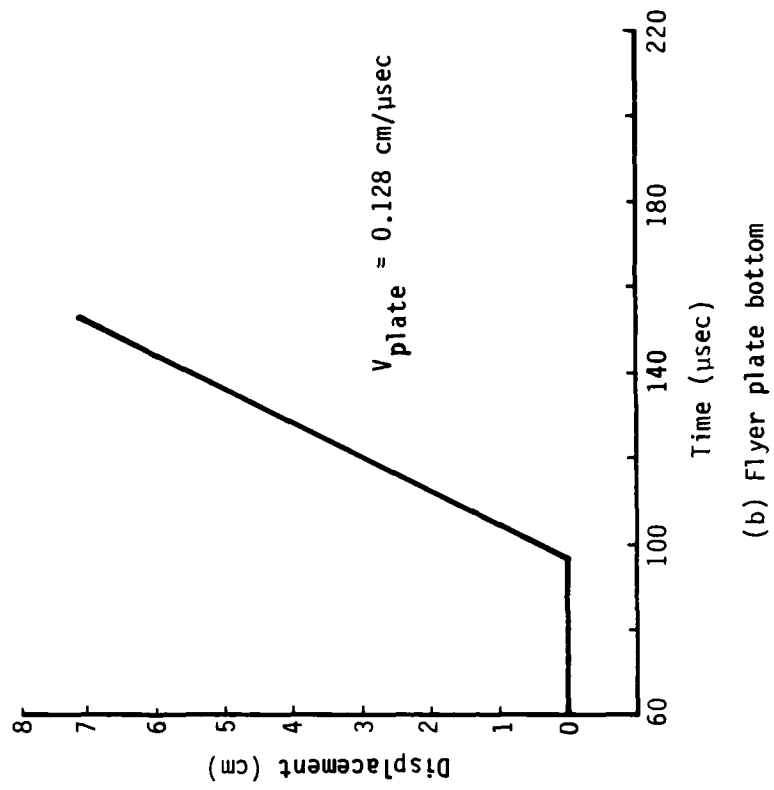


Figure 1.6. Pressure contour plot at 152.9 μ sec--
Mg/Teflon TDR gage with Al foil conductors.



(a) Shock front in Teflon



(b) Flyer plate bottom

Figure 1.7. Shock front and flyer plate displacement--Mg/Teflon TDR gage with Al foil conductors.

0.128 cm/ μ sec. This is about four percent slower than the soil particle velocity of 0.133 cm/ μ sec.

Flyer plate displacements measured in HE testing of the prototype TDR gage were of the same magnitude as shown in Figure 1.7b. Exact comparison is not possible because the HE pressure wave had a rapid decay. This gives a displacement velocity that decreases with time (Reference 2).

While exact correspondence between the field tests of the TDR gage and the STEALTH calculations was not demonstrated, several conclusions can be drawn from this study. The prototype TDR gage appears to work well in the field for measurement times up to about 80 μ sec. The calculations show that the flyer plate moves at nearly the soil particle velocity and thus the gage should be accurate under 10 GPa loading. The calculations further suggest that deformation of the dielectric behind the flyer plate is a probable cause of gage failure. Finally, the computational results were useful in choosing between several gage designs thus saving the time and expense of constructing prototypes of the less-attractive designs.

1-2 CYLINDRICAL STRESS GAGE

Many gages used to make high stress measurements in soil have a preferred direction but often there is uncertainty in the direction of the incident shock wave on the gage. In an attempt to solve this problem, SRI International has constructed and tested several models of a cylindrical stress gage. The basic design and operation of these gages is shown in Figure 1.8. Each gage consists of a long cylindrical metallic tube that is filled with an insulating material. There is a piezoresistive wire (typically manganin or ytterbium) at the center of the gage that is connected by wires to a power supply and to a voltage-measuring circuit.

This gage measures stress as a function of time in the following way. The power supply keeps a constant current flowing through the piezoresistive wire which in the absence of any external stress corresponds to a constant voltage drop across the wire. A change in the stress field surrounding the

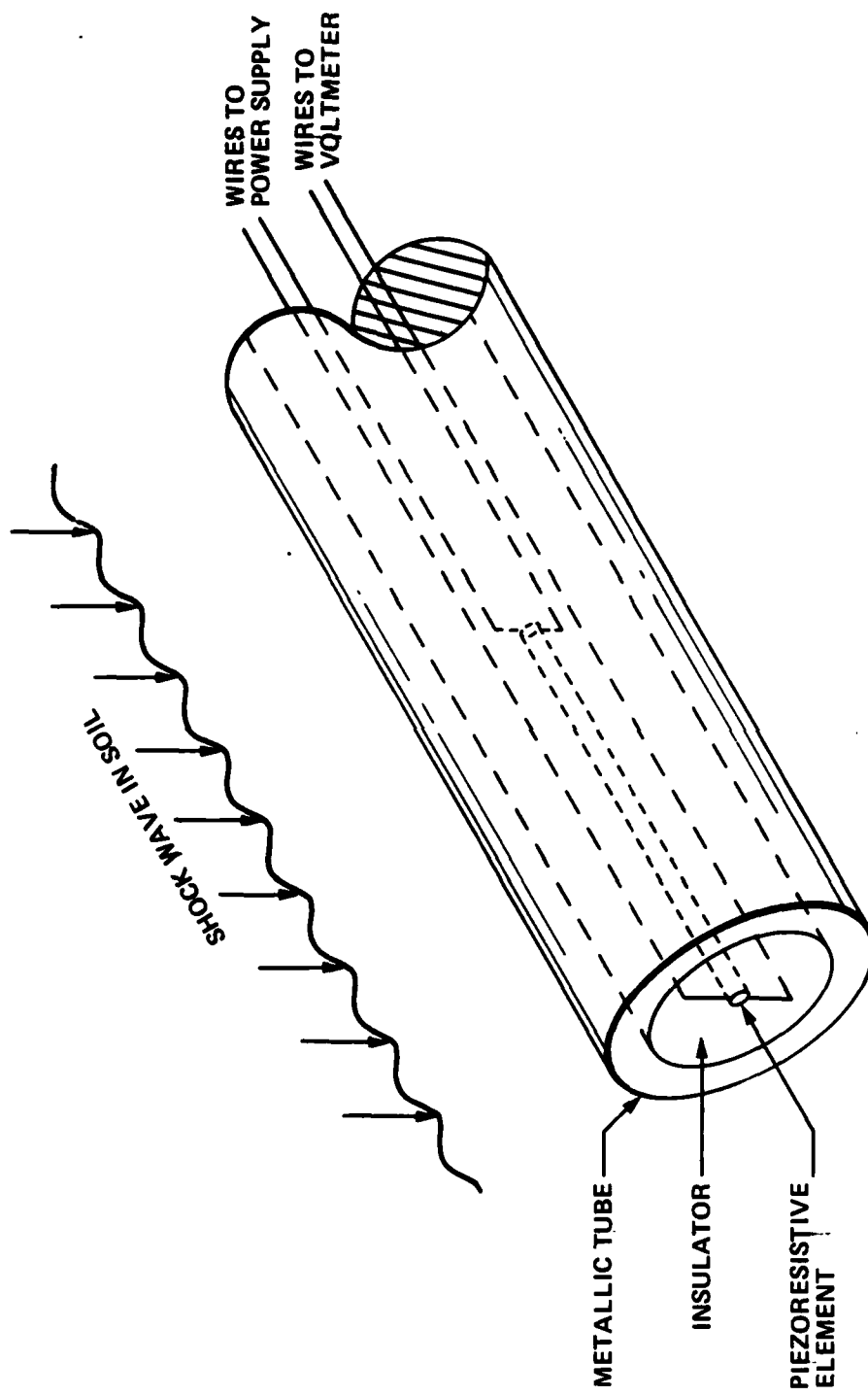


Figure 1.8. Schematic of cylindrical stress gage.

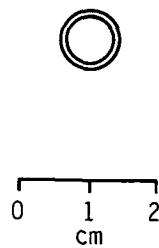
piezoresistive wire causes a measurable change in the voltage drop which can be related to the magnitude of the applied stress. The resistivity change is very rapid so the time dependence of the applied stress can also be determined. It is then assumed that the measured stress is the same as that in the soil surrounding the gage.

Four versions of the cylindrical stress gage have been considered. The dimensions and materials of construction for these designs are shown in Figure 1.9. We have run STEALTH calculations for each of these designs to simulate the gage response and deformation, compare the response to the soil stress field, and identify possible failure mechanisms.

The first cylindrical gage constructed by SRI International was the thin-wall brass tube and epoxy insulator design shown in Figure 1.9a. Experimental tests of this gage using HE charges were made in February 1982 (Reference 3). The experimental gage response for a 10 GPa peak loading stress is shown in Figure 1.10a. We performed a 2-D STEALTH calculation of this gage subjected to a nondecaying 10 GPa incident pressure wave. The computed pressure around the ytterbium center wire (treated in the calculation as a rigid body) is shown in Figure 1.10b.

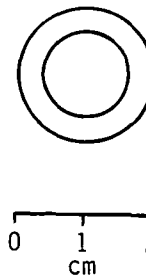
The experimental and computed gage response for the brass/epoxy gage are very similar. Both are characterized by a sharp initial rise, then a flat relatively constant plateau followed by a sharp spike and then an oscillatory behavior that lasts until the gage breaks. The magnitude in the plateau region is about the peak value of the incident pressure wave while the sharp pressure spike is caused by a reflected wave from the bottom of the brass tube (i.e., the opposite side from which the pressure wave is incident). The calculation also indicated that some of the later oscillations were the result of successively weaker shock reflections from the inside wall of the brass tube.

The numerical simulation of this gage was also able to reveal several aspects of the gage behavior that are difficult to determine experimentally. For example, Figure 1.11 shows the STEALTH grid at a time of 5.9 μsec . The significant zone distortion at the tuff-brass interface indicates the top of the gage is moving more slowly than the particle velocity in the surrounding soil. We also see that the gage has nearly flattened on the top (the direction



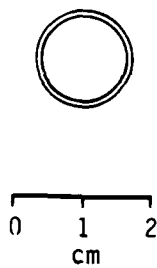
Brass Tube
8.0 mm OD
7.2 mm ID
Epoxy Insulator

(a)



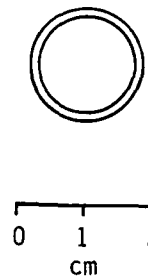
Magnesium Tube
19.0 mm OD
12.5 mm ID
Teflon Insulator

(b)



Aluminum Tube
14.2 mm OD
12.7 mm ID
Teflon Insulator

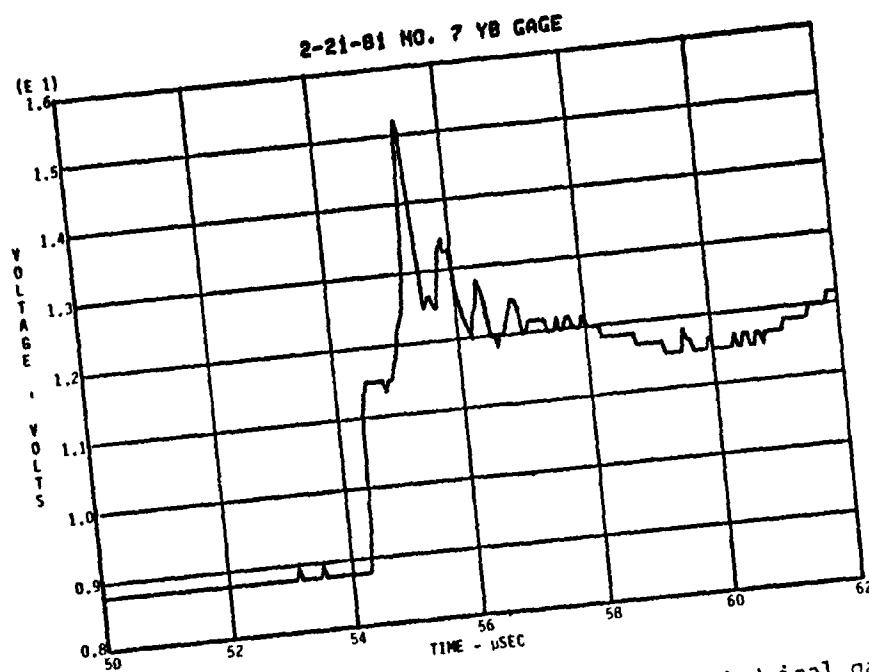
(c)



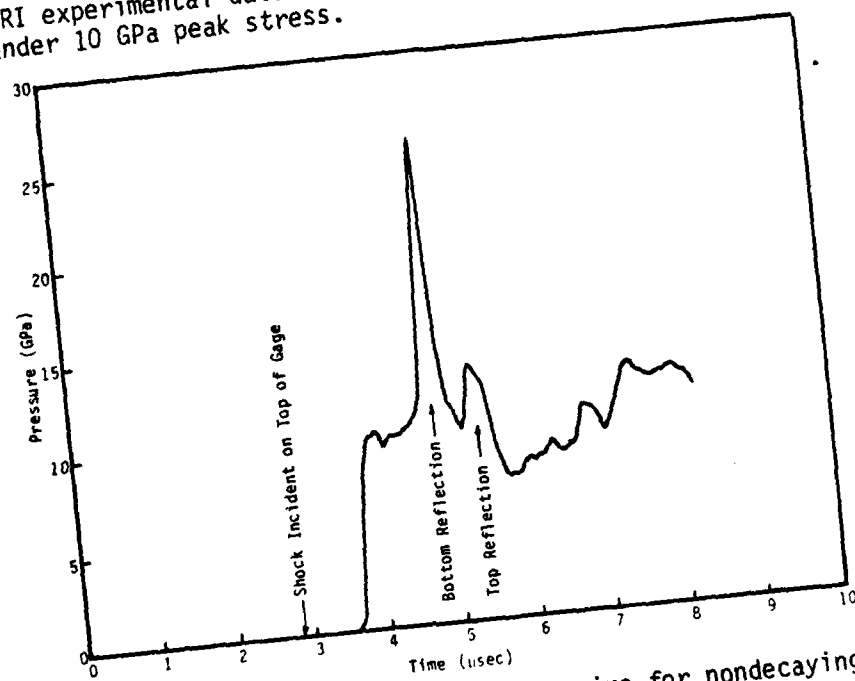
Aluminum Tube
15.75 mm OD
13.95 mm ID
Silastic Rubber
Insulator

(d)

Figure 1.9. Cylindrical gage designs--actual size.



(a) SRI experimental data for the brass/epoxy cylindrical gage under 10 GPa peak stress.



(b) Computed pressure around center wire for nondecaying 10 GPa pressure wave.

Figure 1.10. Experimental and computed response of the brass/epoxy cylindrical gage.

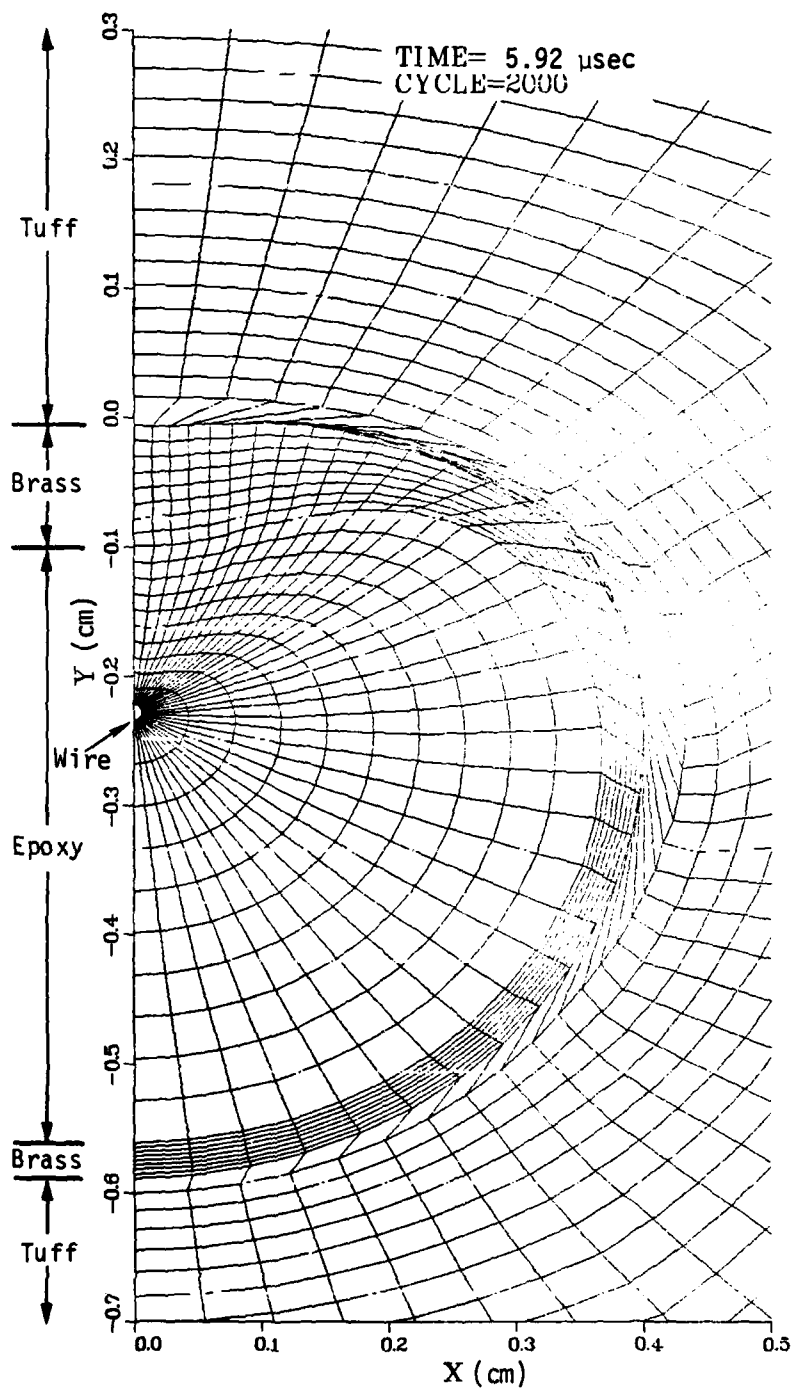


Figure 1.11. Grid plot at 5.92 μ sec--brass/epoxy cylindrical gage.

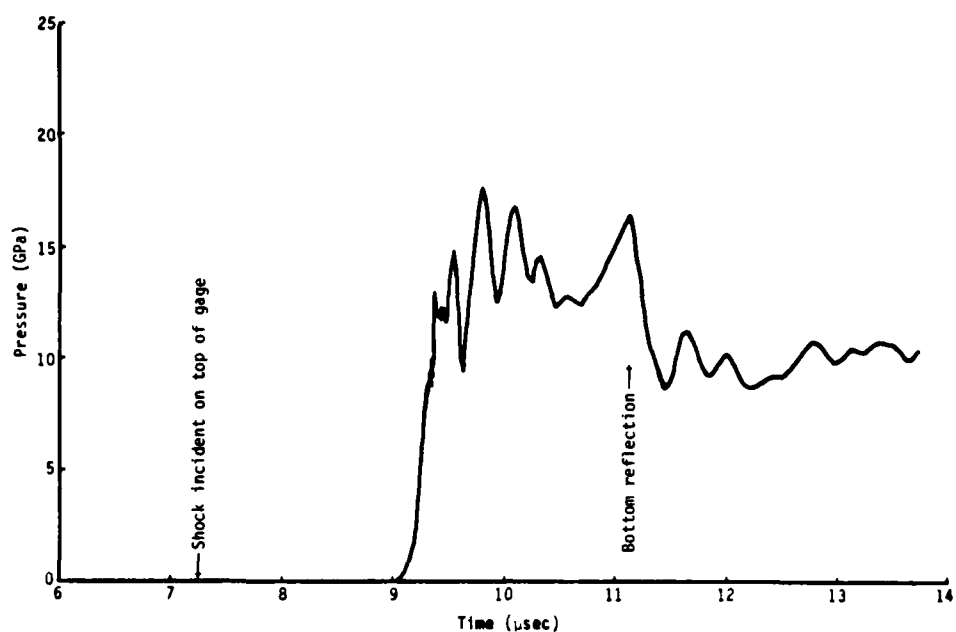
of the incident wave) while the bottom side has remained circular. The piezo-resistive wire has moved toward the top of the brass tube, suggesting that shorting of the wire to the tube is a possible failure mechanism for this gage.

After reviewing the experimental and computational results, SRI designed a new gage in which the brass tube was replaced by a magnesium tube and the epoxy insulator was replaced by Teflon. The dimensions of the Mg/Teflon gage are given in Figure 1.9b. The larger diameter and increased wall thickness of this gage resulted primarily from the need to fabricate the magnesium tube by drilling out a magnesium rod.

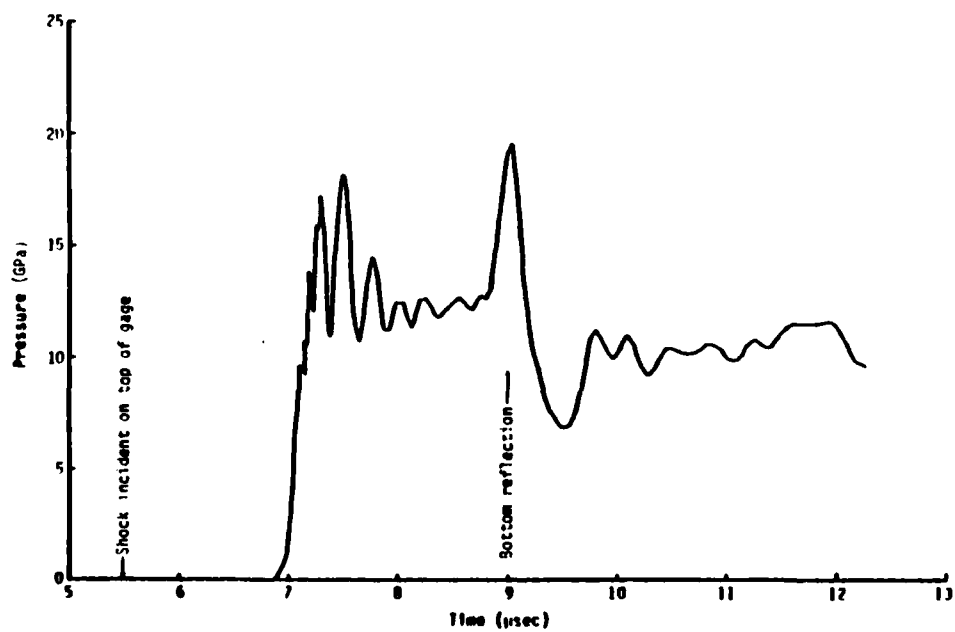
A STEALTH calculation was made for the Mg/Teflon gage which had the same boundary conditions as the brass/epoxy gage calculation but much coarser zoning. The grid shown in Figure 1.11 is finely zoned and, as a consequence, the brass/epoxy calculation suffered from small time steps and severe zone distortion at the material interfaces which prevented us from running the calculation to very late problem times. For the Mg/Teflon gage, we used about half as many zones in an attempt to increase the time steps and reduce zone distortion. This allowed us to compute the gage response for a longer period of time while reducing the calendar time needed to run the problem.

The computed response of the Mg/Teflon gage is shown in Figure 1.12a. The average pressure around the piezoresistive wire for this gage differs substantially from that computed for the brass/epoxy gage. The sharp initial spike when the pressure reaches the wire rises with large oscillations to a peak of 17.5 GPa over a time period of about 0.5 μ sec. The following slow falloff is interrupted by a second rise which is the reflection from the Mg/Teflon interface at the bottom of the gage. Following the arrival of the reflected shock the computed average pressure falls to the 10 GPa level and oscillates about that value until the end of the calculation.

The large oscillations in the 9.5 to 10.5 μ sec time period are at least partly the result of the coarser zoning in this calculation. Without the oscillations, the peak gage pressure reached in this period would probably



(a) Mg/Teflon gage



(b) Al/Teflon gage

Figure 1.12. Average pressure around piezoresistive wire for the Mg/Teflon and Al/Teflon cylindrical gages.

have been on the order of 13 to 14 GPa. This is about 30 percent higher than the incident wave and seems to be related to the gage deformation and resultant compression of the Teflon. The gage deformation occurs almost entirely by 11 μ sec which is the time when the shock reaches the bottom of the gage. At this time, the original circular shape of the Mg tubing has become elliptical and the Teflon has been compressed into a 30 percent smaller volume (see Figure 1.13). At later times this gage shape is maintained and the gage moves at about the particle velocity of the soil.

Several Mg/Teflon gages were tested by SRI in December 1981 (Reference 4) using HE-generated pressure waves at the 10- and 17-GPa levels. The measured response of these gages differed substantially from that shown in Figure 1.11a. As predicted by the STEALTH calculation, the large reflection spike was mitigated but other features were present in the response curve which were difficult to interpret. At the higher stress level there was also some temporary shorting of the electrical signal through the Teflon to the magnesium tube. It is not known whether the shorting occurred from the center manganin wire or from the copper lead wires that are attached to the manganin and are closer to the metallic tube.

While the Mg/Teflon cylindrical gage was considered an improvement over the brass/epoxy gage, it presented a fabrication problem. Magnesium tubing can be made either by drilling rod stock in the laboratory or commercially by the extrusion process. The former is time-consuming and usually results in tubing with a nonuniform wall thickness. The extruded tubing must be special-ordered at high cost and with at least a three-month lead time. For this reason, the possibility of using a different material than magnesium was considered.

The next cylindrical gage design considered is shown in Figure 1.9c. For this gage, thin-walled aluminum tubing was used in place of the magnesium tubing. A STEALTH calculation was made for this gage with the same boundary conditions as used previously. The zoning was still coarse but a few more zones were used in the Teflon in an attempt to reduce the numerical oscillations in the gage response.

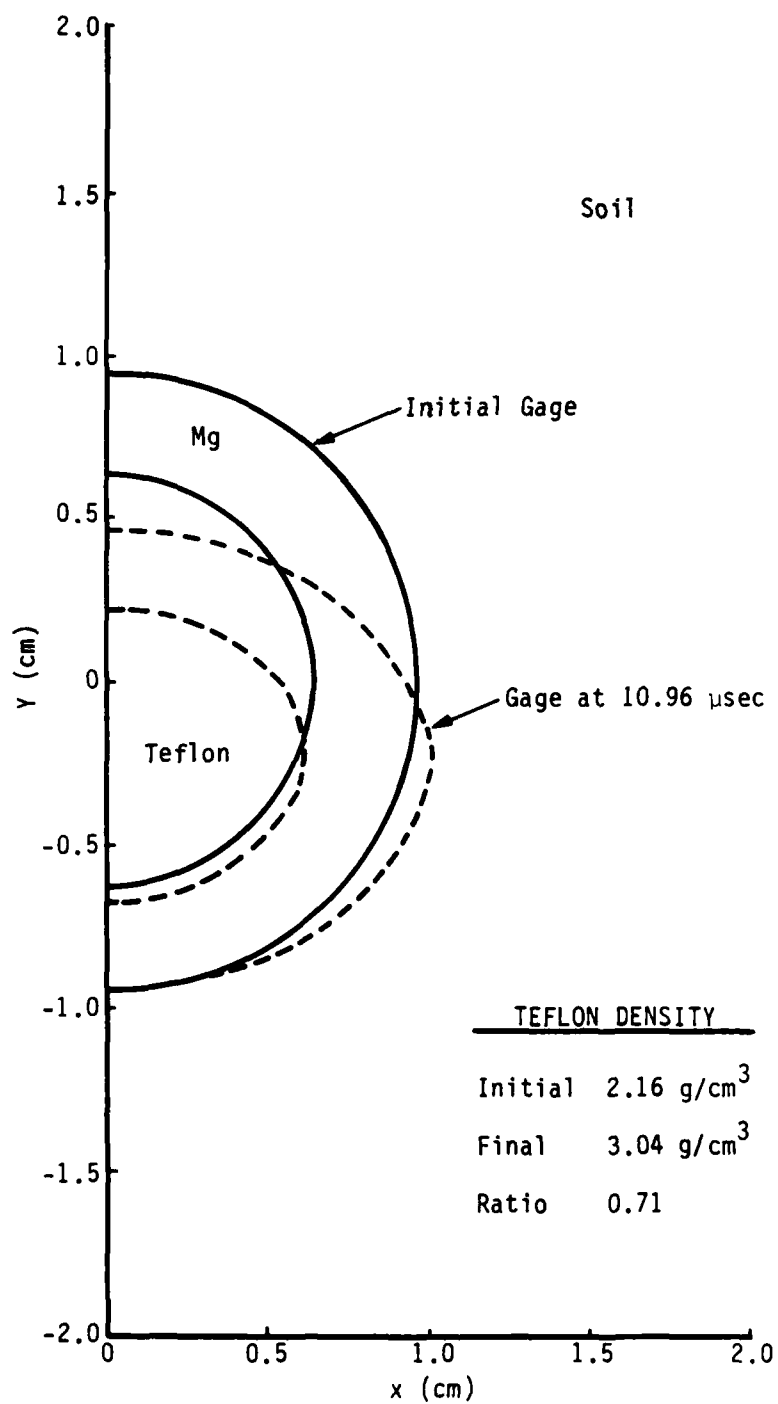


Figure 1.13. Deformation of the Mg/Teflon cylindrical gage.

The computed response of the Al/Teflon gage is shown in Figure 1.12b. It is quite similar to the response for the Mg/Teflon gage shown in Figure 1.12a. The initial rise reaches 18 GPa and the reflected shock has a higher peak at 20 GPa. The oscillations in the initial response are also somewhat smaller in magnitude but have a higher frequency because of the smaller zones used. As in the previous case, the gage deformation occurs almost entirely in the first 2 μ sec with the final shape determined by the time the incident wave reaches the bottom of the gage. In addition the final shape of the Teflon for this gage is almost identical to the final shape for the Mg/Teflon gage shown in Figure 1.13. At late time, this gage also moved at about the particle velocity of the soil.

The similarity of the computed response of the Mg/Teflon and Al/Teflon gages at the 10 GPa level suggests the use of magnesium tubing is not necessary. An attempt to experimentally confirm this result was made in March 1982. Several Al/Teflon gages were constructed and subjected to HE-generated pressure waves but good data were not obtained.

It was suspected that the poor experimental results with the Mg/Teflon and Al/Teflon gages was caused by increased conductivity in the Teflon at high pressures. For this reason, SRI changed the insulating material to silastic rubber. The Al/silastic gage design is shown in Figure 1.9d. It is slightly larger with the Al tubing having a 15.75 mm OD and 13.95 mm ID. The new gages were fielded in the HURON LANDING Event. Although there was some delay in recovering the data, these gages appeared to effective up to the 30 GPa stress level. Similar gages were also tested in the MINI JADE Event.

A STEALTH calculation was run for the Al/silastic gage with similar zoning and boundary conditions as the Al/Teflon gage. This calculation was run 5000 cycles to a problem time of nearly 20 μ sec. The computed gage response is shown in Figure 1.14. Comparing with Figure 1.12b, we see the response at early times is similar to that of the Al/Teflon gage. At later times, the pressure fluctuates about the expected value of 10 GPa. The pressure increase near 18 μ sec is a reflection from the side of the grid and should be disregarded.

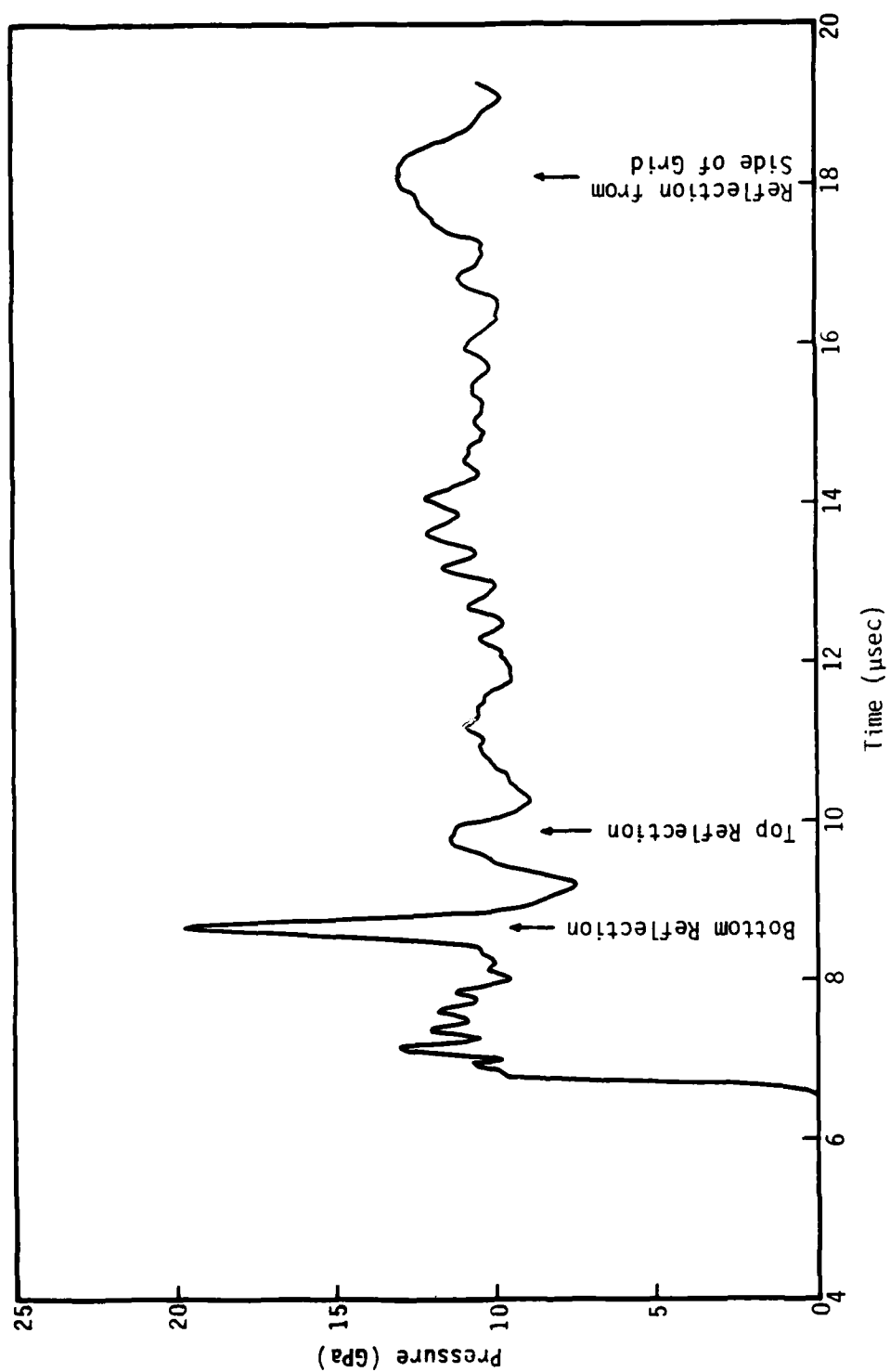


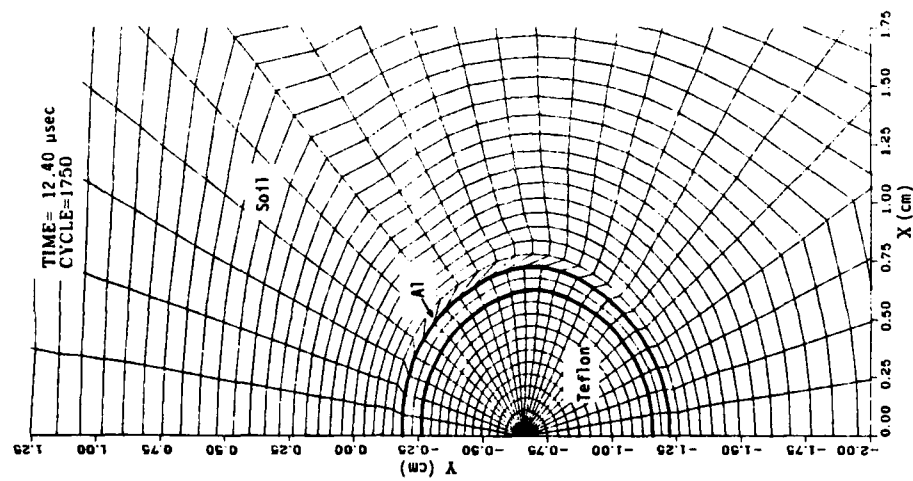
Figure 1.14. Average wire pressure to 19 μsec--Al/silastic cylindrical gage.

The Al/silastic gage deformed differently than the Al/Teflon gage. The shape of each gage at about 13 μ sec is shown in Figure 1.15. As discussed earlier, the Al/Teflon gage deformed into a near-elliptical shape (Figure 1.15a). The Al/silastic gage (Figure 1.15b) became more heart-shaped. This difference apparently occurs because the silastic rubber has a lower initial density than Teflon (1.37 g/cm^3 versus 2.16 g/cm^3 , respectively). Another difference was that the deformation continued with time. By the end of the calculation, the Al/silastic gage had a shape similar to that of the brass/epoxy gage shown in Figure 1.11.

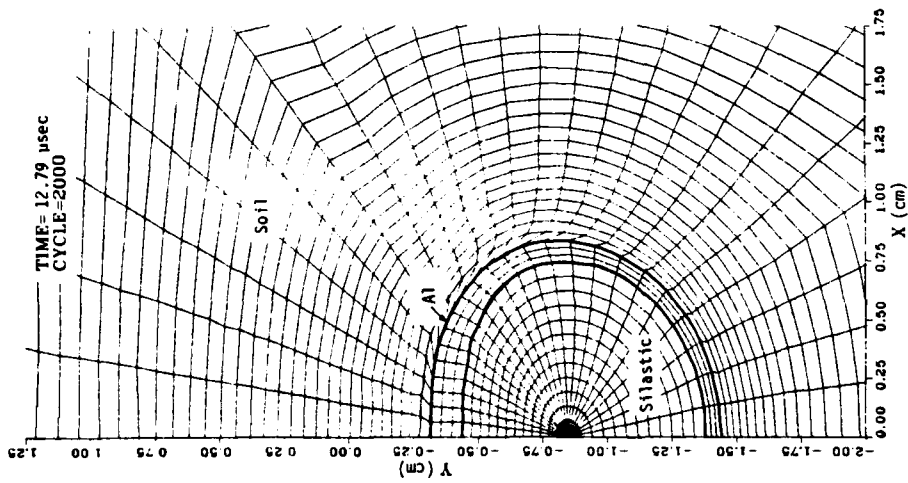
The distortion of the soil zones adjacent to the Al/silastic gage also increased with time even though this gage moved slightly faster than the surrounding soil. To determine what effect allowing the soil to slide around the gage would have on the gage response, we ran another STEALTH calculation with slidelines at the gage/soil interface. This calculation ran to 11 μ sec where it was stopped because of numerical problems that occurred with the slidelines at the top of the gage. Up to about 9 μ sec, the response of the Al/silastic gage was very similar in both calculations (with and without slidelines). Apparently soil slippage is not effective in shielding the gage from the free field. This is probably because the initial cylindrical shape of this gage ensures that the incident shock always impacts normally to the gage surface and is transmitted to the gage interior by what is close to a 1-D interaction.

Some general conclusions on cylindrical gage response can be drawn from the results of the 2-D STEALTH calculations for the four gage designs. Comparing the gage response curves for the brass/epoxy gage (Figure 1.10b), the Mg/Teflon gage (Figure 1.12a), the Al/Teflon gage (Figure 1.12b) and the Al/silastic gage (Figure 1.14), one sees the interactions are similar but their magnitude depends on the materials used in the gage.

The chronological sequence of interactions in each gage is as follows. When the incident stress wave first encounters the outside surface of the gage, a shock wave is reflected back into the soil and another wave transmitted into the tubing. A similar reflection and transmission also occurs at the metal/insulator interface. The combined interactions at both interfaces of the metal



(a) Grid plot at 12.40 μsec --
Al/Teflon gage.



(b) Grid plot at 12.79 μsec --
Al/silastic gage.

Figure 1.15. Deformation of the Al/Teflon and Al/silastic cylindrical gages.

tube determine the magnitude of the stress wave transmitted into the insulator. This stress wave passes over the piezoresistive wire and is recorded as the initial rise in the gage response curve.

This stress wave continues to travel through the insulator material until it reaches the side of the gage opposite the point of initial impact. Here a second pair of reflection and transmission interactions occur at the insulator/metal and metal/soil interfaces. A stress wave is transmitted into the undisturbed soil and another wave reflected into the now-compressed insulator material. The reflected wave travels across the gage. Its passage is recorded by the piezoresistive wire and appears as a sharp spike in the gage response curve.

When this wave reaches the side of the gage where the initial impact occurred, it results in a wave transmitted into the soil and another wave reflected into the insulator material. This wave is generally much weaker than the first reflected wave but can sometimes be seen as a second spike in the gage response curve. This sequence repeats several more times but each succeeding reflection is weaker and more difficult to see in the response curve. After the second reflection passes, the gage response appears to fluctuate in a random manner about the external soil pressure for slowly decaying shocks such as seen in underground nuclear tests.

The magnitude of the reflected and transmitted stress waves depends on the strength of the incident wave and on the gage materials. To first order, it is the ratio of the densities at the material interface. This is why the initial wave transmitted into the Teflon is stronger than the one entering the epoxy and silastic rubber. Similarly, the internal reflected waves are weaker with aluminum than with brass and weaker still with magnesium tubing.

It is also during the first two internal reflections that most of the gage deformation occurs. At later times, the gage shape changes slowly and the gage moves as a unit with a velocity close to the particle velocity in the surrounding soil. The degree of deformation seems to be related to the

density of the insulating material. With a high density insulator such as Teflon, the gage deforms more or less uniformly into an elliptical shape. With weak low-density insulating materials such as epoxy or silastic rubber, the deformation is mostly a flattening on the impacted side of the gage, giving a heart-shaped appearance.

The strong dependence of the early time gage response on the densities of the gage materials suggests that gage performance could be optimized by using materials that approximate the soil density. There is some theoretical support as well for this hypothesis. An analytic study of the response of rigid spherical gages made by Mow (Reference 5) suggests the best gage design will be the one whose average density is the same as the density in the surrounding soil. Mow also considered cylindrical gages but was unable to obtain an analytic solution although the same density considerations seemed to apply.

Mow's analysis, brought to our attention by Whitener (Reference 6), is generally supported by the results of the STEALTH calculations. The average density in the gages, in order of decreasing magnitude, was: brass/epoxy, 2.58 g/cm^3 ; Al/Teflon, 2.27 g/cm^3 ; Mg/Teflon, 1.93 g/cm^3 ; and Al/silastic, 1.66 g/cm^3 . The Mg/Teflon gage was closest to the soil density of 1.97 g/cm^3 . It had the weakest internal reflections and took the least time to come into equilibrium with the stress field in the surrounding soil. However, this gage as mentioned earlier was difficult to fabricate and performed poorly in HE tests made by SRI.

A materials parameter study was made to see if there were other material combinations that should be considered for future gage designs. For this study, aluminum or magnesium was used for the metal tube and calculations made with a variety of insulating materials, including Teflon, silastic rubber, epoxy and polyethylene. Tube thicknesses were also varied, including the use of aluminum foil (considered to have zero thickness in the calculations).

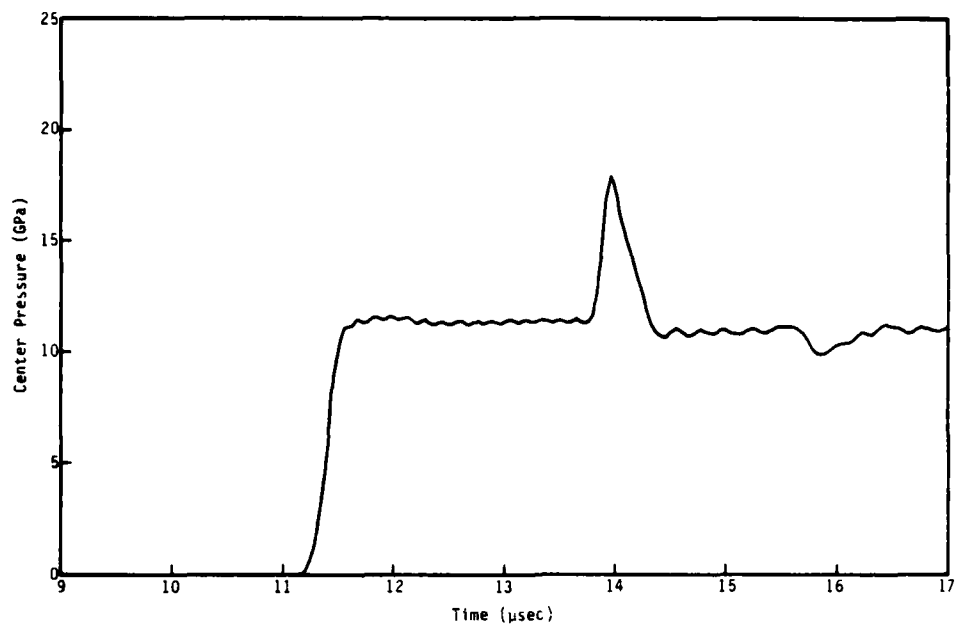
This study was made using a 1-D model of the cylindrical gage. This model represented a cut through the center of the gage. The metal tubing became two material plates with the tube thickness separated by an insulating

material with a dimension equal to the inside diameter of the gage. Soil was added both above and below this structure. A velocity boundary condition at one end of the soil was used to create a stress wave that impacted one side of the gage. The pressure at the center of the insulating material was edited to represent the gage response. Using this model allowed us to investigate a large number of gage material combinations without doing time-consuming 2-D STEALTH calculations.

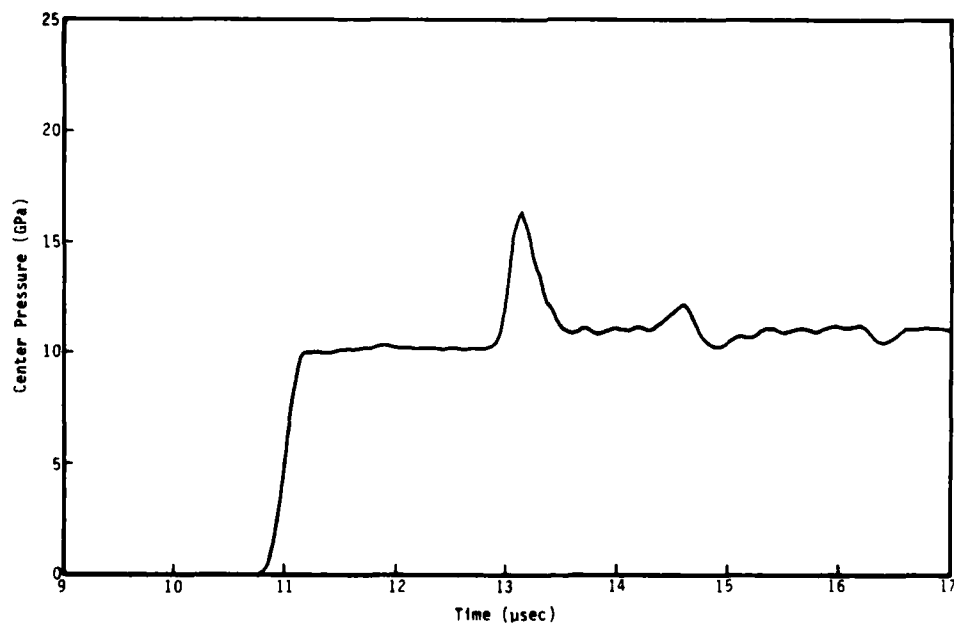
The response curves from the 1-D calculations had the same general features as those obtained from the 2-D calculations. For example, the 1-D response curves for Al/Teflon and Al/silastic are given in Figure 1.16. These should be compared with Figures 1.12b and 1.14, respectively. In both cases, one sees the initial rise, the spike in pressure representing the bottom reflection, and a second reflection. The timing is also similar with the difference being that the pressure was edited at the center of the insulator in the 1-D calculations. In the 2-D case, the pressure around the wire was edited and the wire could move relative to the insulating material.

The results with magnesium tubing were not as close to the 2-D case as with aluminum. The 1-D result for the Mg/Teflon gage is shown in Figure 1.17a. The reflection spike has been reduced and broadened compared to the result shown in Figure 1.12a. The magnesium was relatively thick for this case. A calculation of Mg/Teflon with a metal thickness of 0.09 cm (the same as the aluminum tubing thickness) is shown in Figure 1.17b. This case has a narrower spike and shows the advantage of going to thinner tubing to reduce the internal gage reflections. Other aluminum/insulator combinations and magnesium/insulator combinations gave results similar to those shown in Figures 1.16 and 1.17, respectively.

One function of the metal tube in the cylindrical stress gage is to provide an electrical shield to prevent EMP currents in the gage electrical conductors. This function could be satisfied if the insulator were wrapped with aluminum foil such as was done in the final TDR gage design. Some 1-D calculations were made for foil-wrapped gages. The results for foil/Teflon and foil/

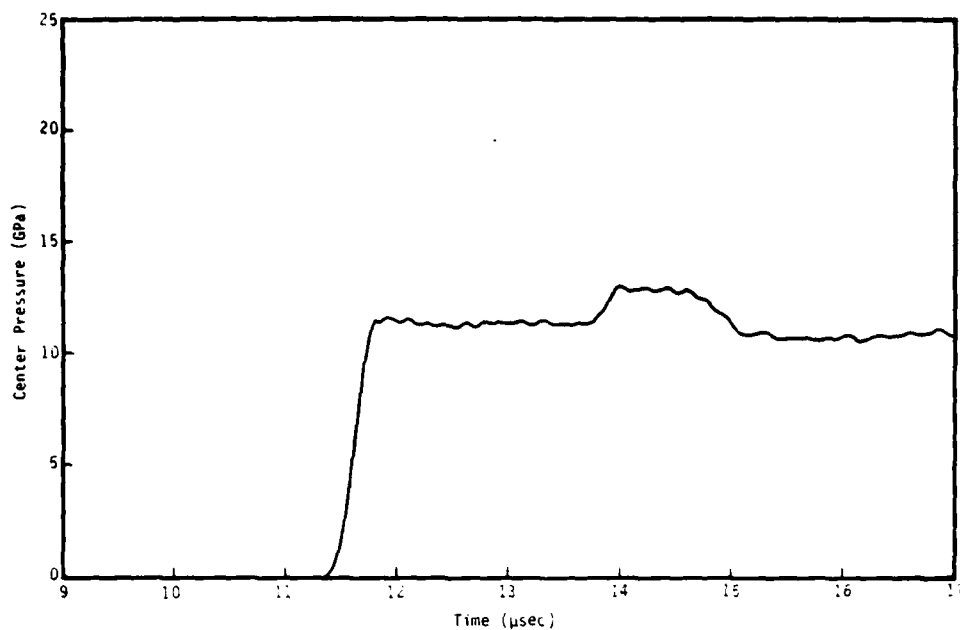


(a) Al/Teflon gage

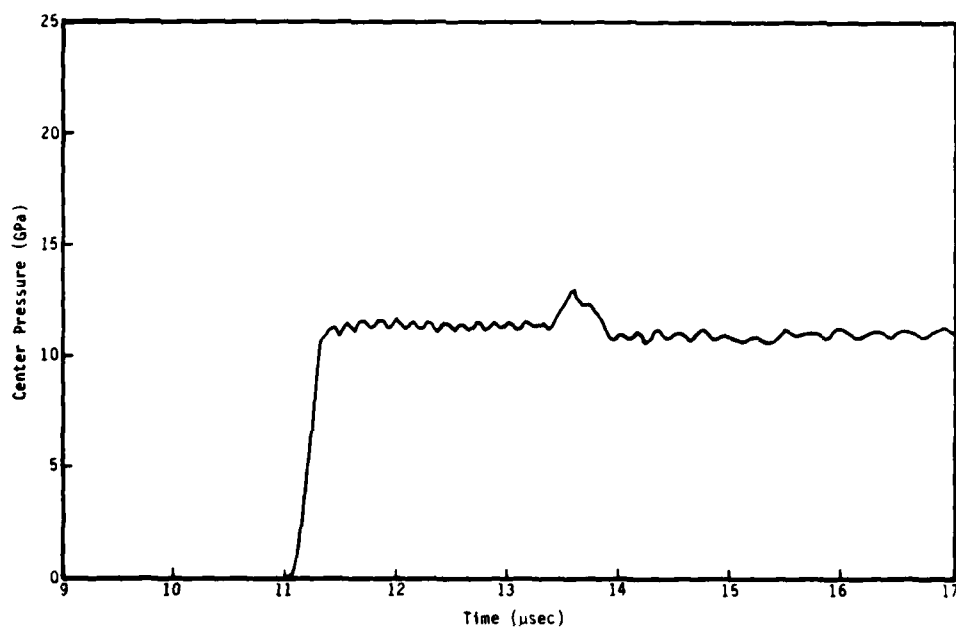


(b) Al/silastic gage

Figure 1.16. Center pressure from 1-D calculations of the Al/Teflon and Al/silastic cylindrical gages.



(a) Mg/Teflon gage--thick tubing



(b) Mg/Teflon gage--thin tubing

Figure 1.17. Effect of Mg thickness on center pressure of Mg/Teflon gage (from 1-D calculations).

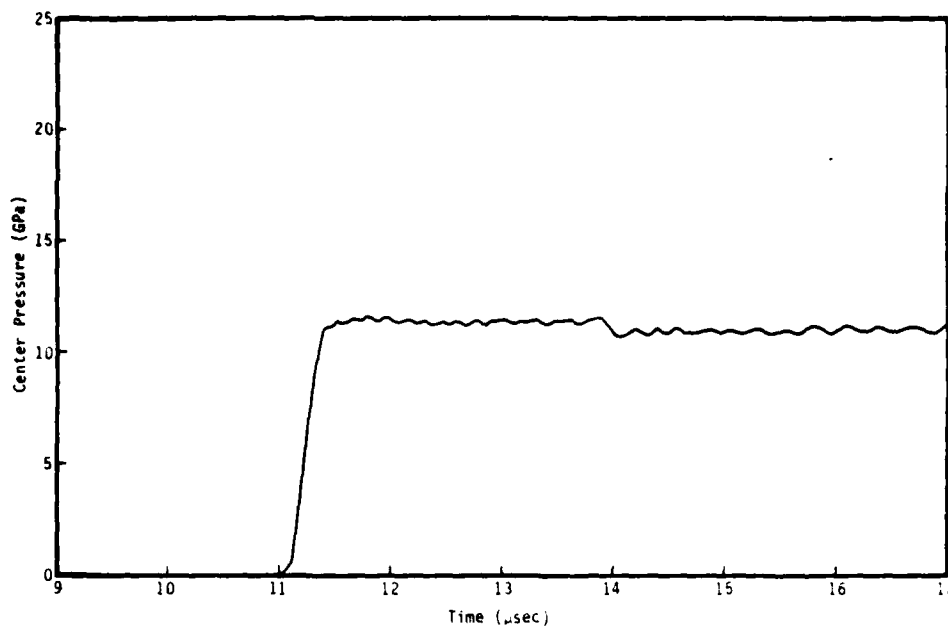
silastic gages are shown in Figure 1.18. These combinations give response curves with greatly reduced internal reflections compared to the gages which use metal tubing. The construction and testing of several foil-wrapped gages should be done to see if this is a practical design.

1-3 FLAT PACK STRESS GAGE

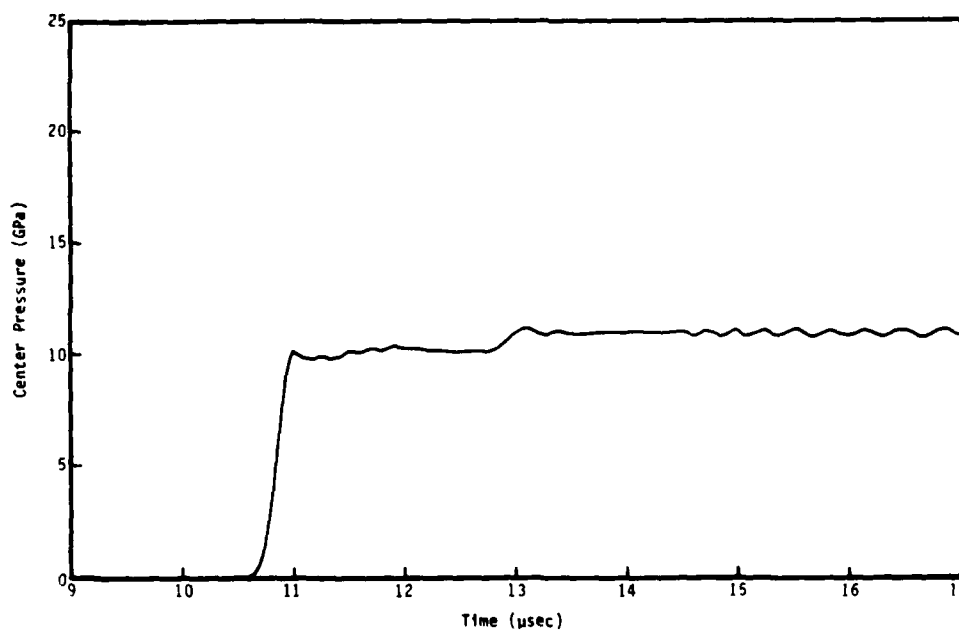
The flat pack stress gage is also used by SRI International to make measurements in the 10 to 30 GPa stress regime. A typical flat pack gage is shown in Figure 1.19. The gage consists of two thin steel plates about 6 cm in width and 5 or more meters long. Between the plates at one end is a manganin or ytterbium piezoresistive element. Four flat copper conductors extending the length of the plates connect to the element and provide an electrical path for a measurement of the element resistance as a function of time. The electrical circuit is the same as that used for the cylindrical stress gage (see Figure 1.8). The element and the conductors are insulated from the steel plates by Kapton tape or epoxy. The entire assembly is held together by welded seams around the edges of the steel plates.

Flat pack gages will be fielded on the MISTY JADE Event. They have been used in a number of recent underground tests, including the HURON LANDING and MINI JADE Events, as well as in large HE experiments such as the Mill Race Event and the Silo Test Program series. These gages are also used in HE calibration tests of other gages. For example they were used in the SRI HE tests of the cylindrical stress gage and the TDR particle velocity gage.

Flat pack gages typically have a very noisy initial response followed by a long slow decay. The initial "ringing" can reach a magnitude up to two or three times the incident stress wave. After the initial transient period, the gage is thought to give a fairly accurate measurement of the stress field in the surrounding soil if it has been carefully oriented so the incident stress wave impacts normal to the flat side of the gage. At late times, the gage may fail for mechanical reasons (breaks in the conducting wire etc.) or the gage element may bend or elongate adding a strain component to the gage response.



(a) Al foil/Teflon gage



(b) Al foil/silastic gage

Figure 1.18. Center pressure from 1-D calculations of the Al foil/Teflon and Al foil/silastic cylindrical gages.

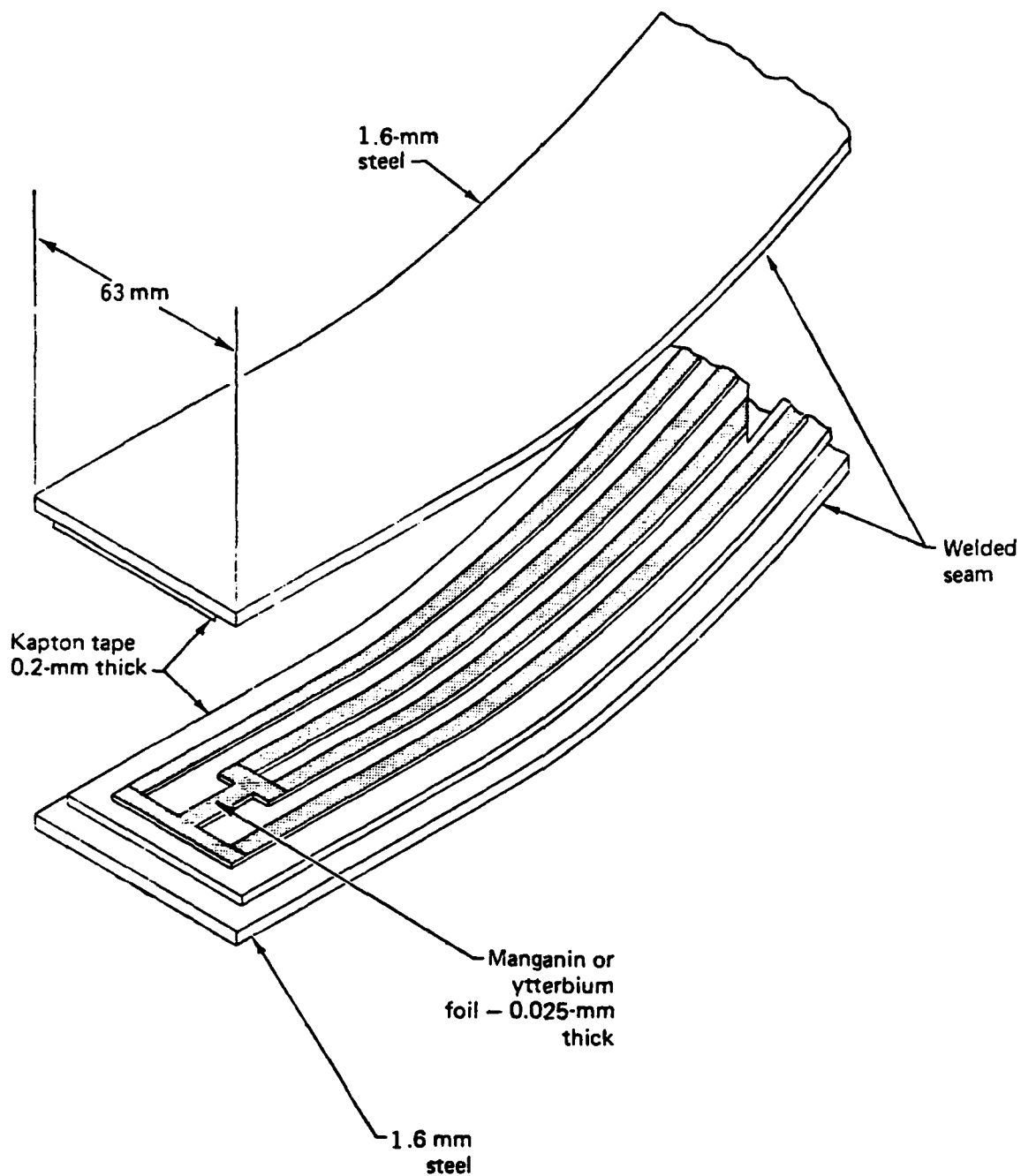


Figure 1.19. Schematic of flat pack stress gage.

While we devoted most of our effort to the TDR and cylindrical gages, some 1-D STEALTH calculations were made of the flat pack gage in an attempt to find the cause for its initial transient response. We modeled the gage as two metal plates surrounding a Teflon center region. Boundary conditions were used to generate a pressure wave incident on one side of this assembly and the pressure in the center of the gage was edited as a function of time.

Some results from these calculations are shown in Figure 1.20. The free field stress, a slowly decaying 9 GPa stress wave, is shown in Figure 1.20a. This wave was incident on a gage made of two 1.6 mm steel plates separated by 0.5 mm of Teflon. The computed pressure at the center of the gage is shown in Figure 1.20c. Shock reflections between the two steel plates raised the center pressure to an initial peak over 25 GPa. This high pressure decayed rapidly as the Teflon expanded and pushed the plates apart. The plates then were pushed closer again but in the second oscillation the center pressure reached a peak of only 13 GPa followed by 10 GPa and 9 GPa for the third and fourth oscillations, respectively. The calculation was continued for another 5 μ sec and subsequent oscillations were much smaller with the late time gage response approximately the same as the free field stress.

As a test to see if changing the plate material would reduce the "ringing", a similar 1-D calculation was made with aluminum plates of the same 1.6 mm thickness. The center pressure for this case is shown in Figure 1.20b. Only one large oscillation occurred which peaked at 14 GPa. After this time, the center pressure approximated the free field stress.

Because of the widespread use of the flat pack gage, additional calculations are needed to fully understand the internal dynamics of this gage. These should be 2-D calculations because the 1-D calculation reported here ignores several features of the gage construction that may affect the gage response. For example, the welded seams will prevent the metal plates from moving independently of each other. If 2-D calculations confirm changes in the gage materials will improve the gage response, then prototype gages should be constructed and tested to uncover any fabrication or other problems in the modified design.

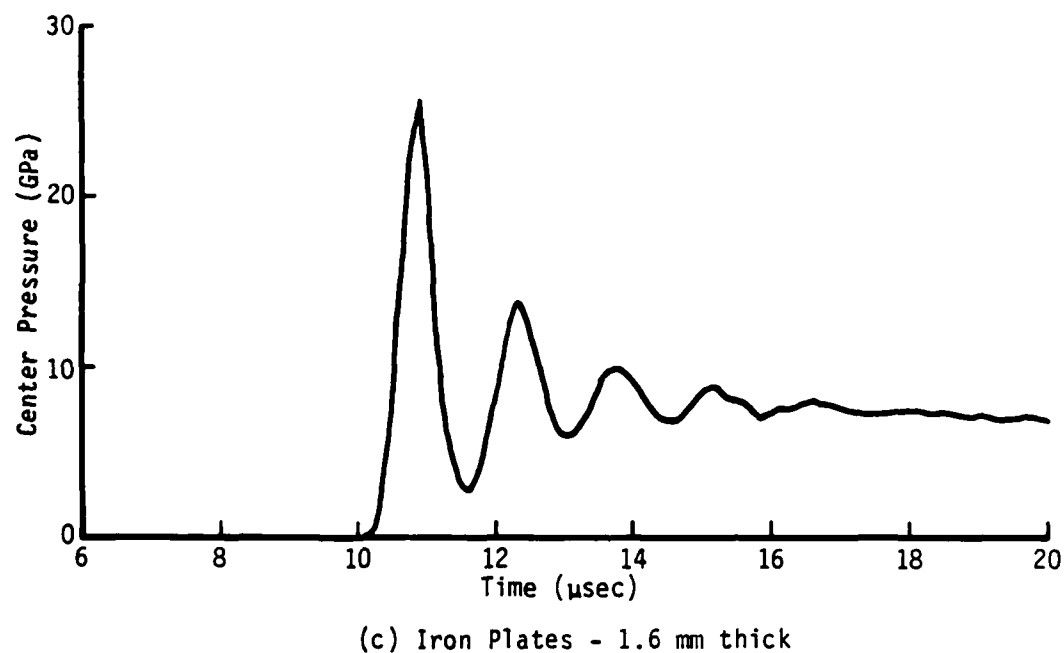
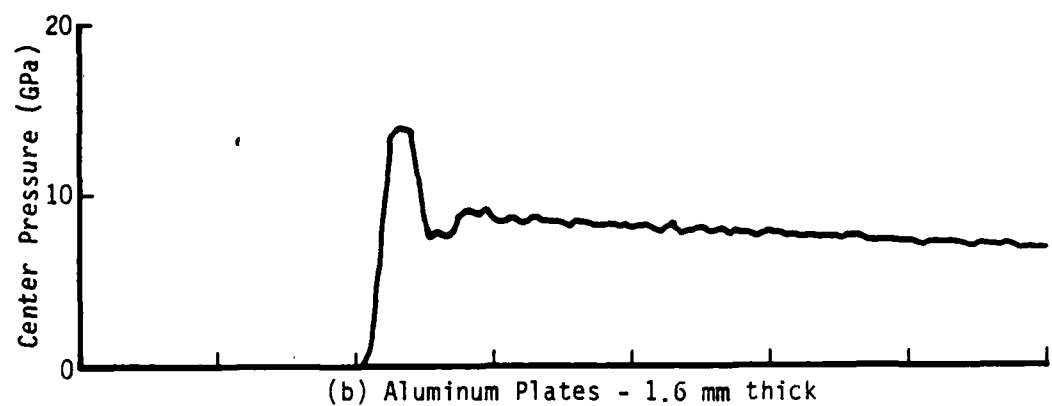
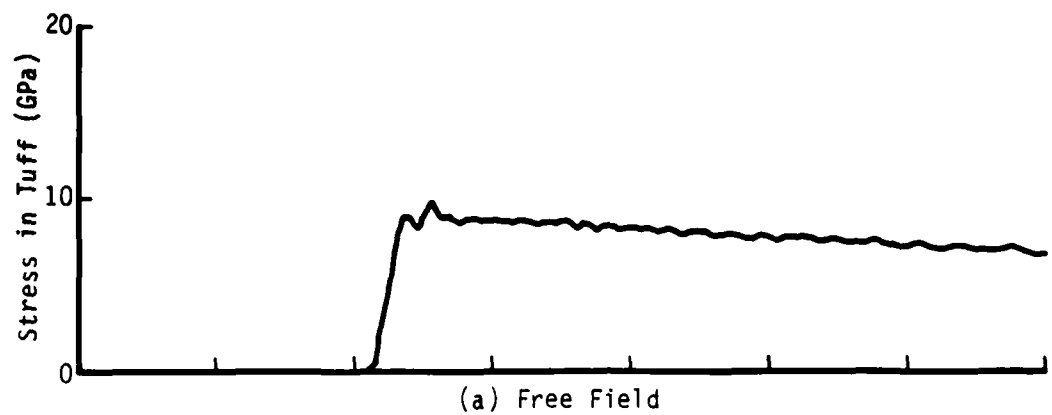


Figure 1.20. Effect of material variation on flat pack gage response.

SECTION 2

TDR PARTICLE VELOCITY GAGE

2-1 AL/SILICA GAGE WITH AL TUBING

Our first STEALTH calculation of the TDR gage was for the design shown in Figure 1.1a. An enlarged view giving the gage dimensions is shown in Figure 2.1. This design has an aluminum flyer plate 5.06 cm in radius and 0.66 cm in thickness. This plate is at the end of two concentric thin-wall aluminum tubes about 25 cm in length which are the conductors through which the electrical signals are transmitted. The larger tube has an inner radius of 3.80 cm and the smaller an inner radius of 0.64 cm. The wall thickness is 0.10 cm for both tubes. The remaining volume inside the tubes is filled with fused silica, an insulating dielectric material.

Figure 2.1 also schematically represents the STEALTH problem. An axisymmetric grid with an axial dimension of 20 cm and a radial extent of 21.5 cm was set up. The gage was placed along the axis 5 cm from the top of the grid. The remainder of the grid was filled with soil. A pressure boundary condition of the form

$$P = P_0 e^{-t/t_0}$$

with $P_0 = 10$ GPa and $t_0 = 30$ μ sec was imposed at the top of the grid to generate a planar pressure wave that is incident on the flyer plate of the gage. The remaining grid boundaries are fixed walls, i.e., the points attached to the boundary may slide along the boundary but cannot cross it.

Each material in the STEALTH calculation has an equation of state of the form

$$P = A\mu + B\mu^2 + C\mu^3 + TE/V$$

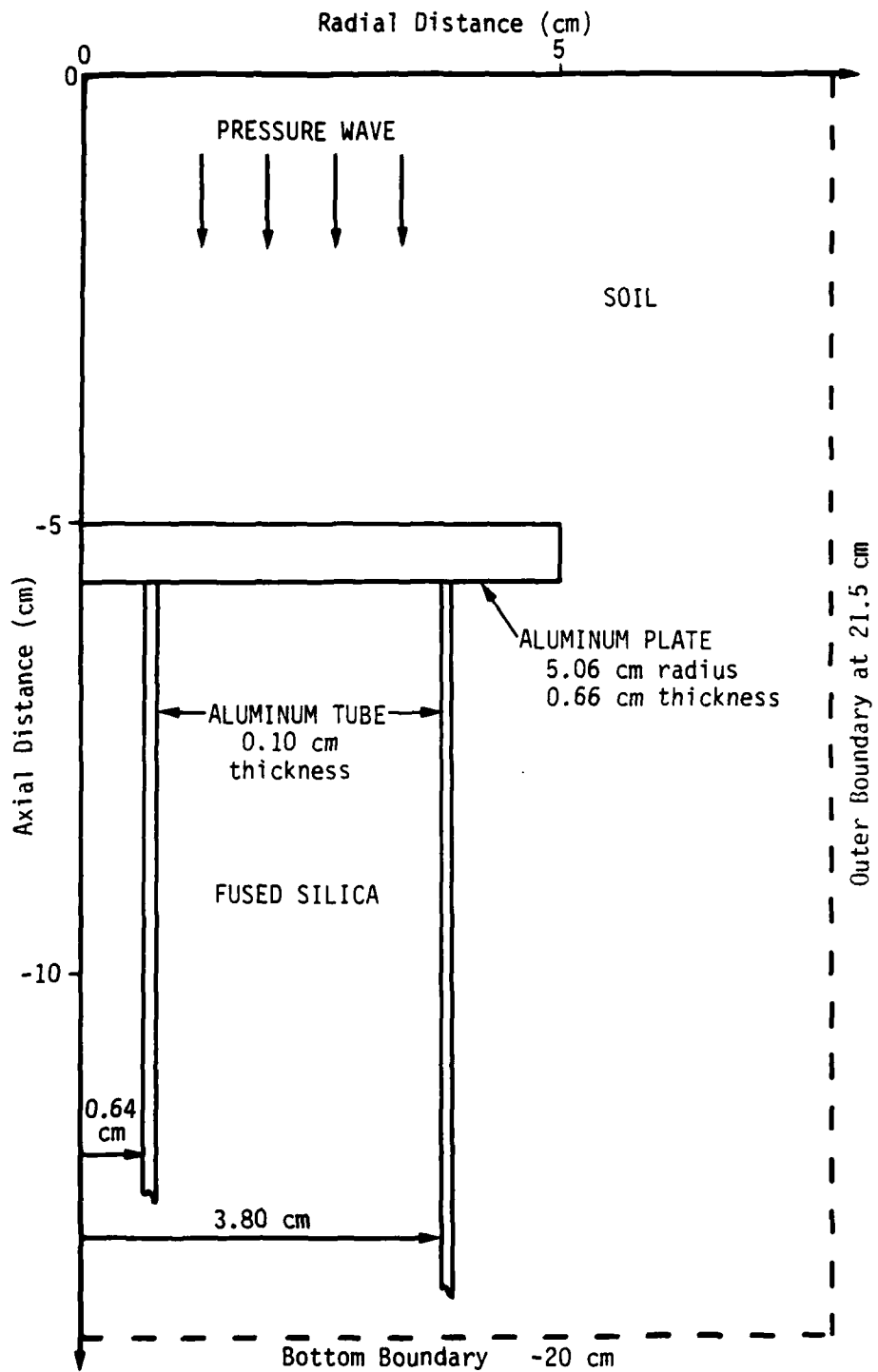


Figure 2.1. Dimensions and problem setup for the Al/silica TDR gage.

where E = Energy density (10^5 joules)

V = Relative volume = ρ_0/ρ

ρ = Density (g/cm^3)

ρ_0 = Initial density (g/cm^3)

$$\mu = \frac{\rho}{\rho_0} - 1$$

A, B, C, Γ = Constants.

The constants A, B, C, Γ and ρ_0 along with the shear modulus and yield strength for each material are listed in Table 2.1.

A portion of the zoning in the STEALTH grid is shown in Figure 2.2. The darkened lines denote the boundaries of the TDR gage. In the radial direction, four zones equal in ΔX were used to define the aluminum tubes. These were the smallest zones in the problem. The adjacent epoxy and soil zones were increased geometrically moving away from the tubes. The largest zones occurred at the outer boundary of the grid (not shown in Figure 2.2). In the axial direction, six zones with equal ΔY were used to define the flyer plate. Geometrically increasing zoning was then used above and below the plate. The number of zones in each grid directions and the geometric ratios used are listed in Table 2.2. The entire grid had 96 radial lines and 48 axial lines for a total of 4608 grid points.

This STEALTH calculation was run 700 cycles to a final problem time of 23.84 μsec . The time evolution of the problem will be briefly described by a series of contour plots showing what happens as the incident pressure wave sweeps over the TDR gage. More detailed information is available in the STEALTH output.

The pressure boundary condition imposed on the top surface of the grid propagates a pressure wave through the tuff which reaches the flyer plate of the gage at about 13 μsec . The position of this wave at 12.29 μsec can be seen in Figure 2.3. This pressure contour plot shows the boundary condition has indeed generated a planar wave which is about 9 GPa in magnitude when it reaches the flyer plate.

Table 2.1. Equations of state for gage calculations.

$$P = A\mu + B\mu^2 + C\mu^3 + \Gamma E/V$$

$$\mu = \frac{\rho}{\rho_0} - 1 \quad V = \text{Relative Volume}$$

| Material | ρ_0 (g/cm ³) | A (GPa) | B (GPa) | C (GPa) | Γ $\left(\frac{\text{GPa}}{\text{KJ}}\right)$ | Shear Modulus (GPa) | Yield Strength (GPa) |
|--------------------|----------------------------------|------------|------------|------------|---|---------------------------|----------------------------|
| Brass | 8.45 | 120.0 | 200.0 | 290.0 | 2.2 | 38.0 | 0.17 |
| Epoxy | 1.20 | 8.6 | 13.0 | 25.0 | 1.0 | 2.6 | 0.0 |
| Iron | 7.85 | 160.0 | 520.0 | 5200.0 | 1.7 | 82.0 | 0.8 |
| Teflon | 2.16 | 4.4 | -12.0 | 110.0 | 0.4 | 0.54 | 0.0 |
| Tuff | 1.97 | 10.0 | 8.0 | 0.0 | 1.8 | 4.0 | 0.0 |
| Aluminum | 2.70 | 76.7 | 128.3 | 125.1 | 2.0 | 27.6 | 0.263 |
| Magnesium | 1.745 | 36.0 | 23.0 | 20.0 | 1.46 | 17.0 | 0.13 |
| Fused Silica | 2.20 | 36.8 | 0.0 | 0.0 | 0.90 | 31.2 | 0.0 |
| Silastic Rubber | 1.372 | 6.5 | 24.0 | 58.0 | 1.4 | 0.0 | 0.0 |
| Polyethylene | 0.96 | 7.0 | 21.7 | -1.0 | 0.87 | 0.0 | 0.0 |

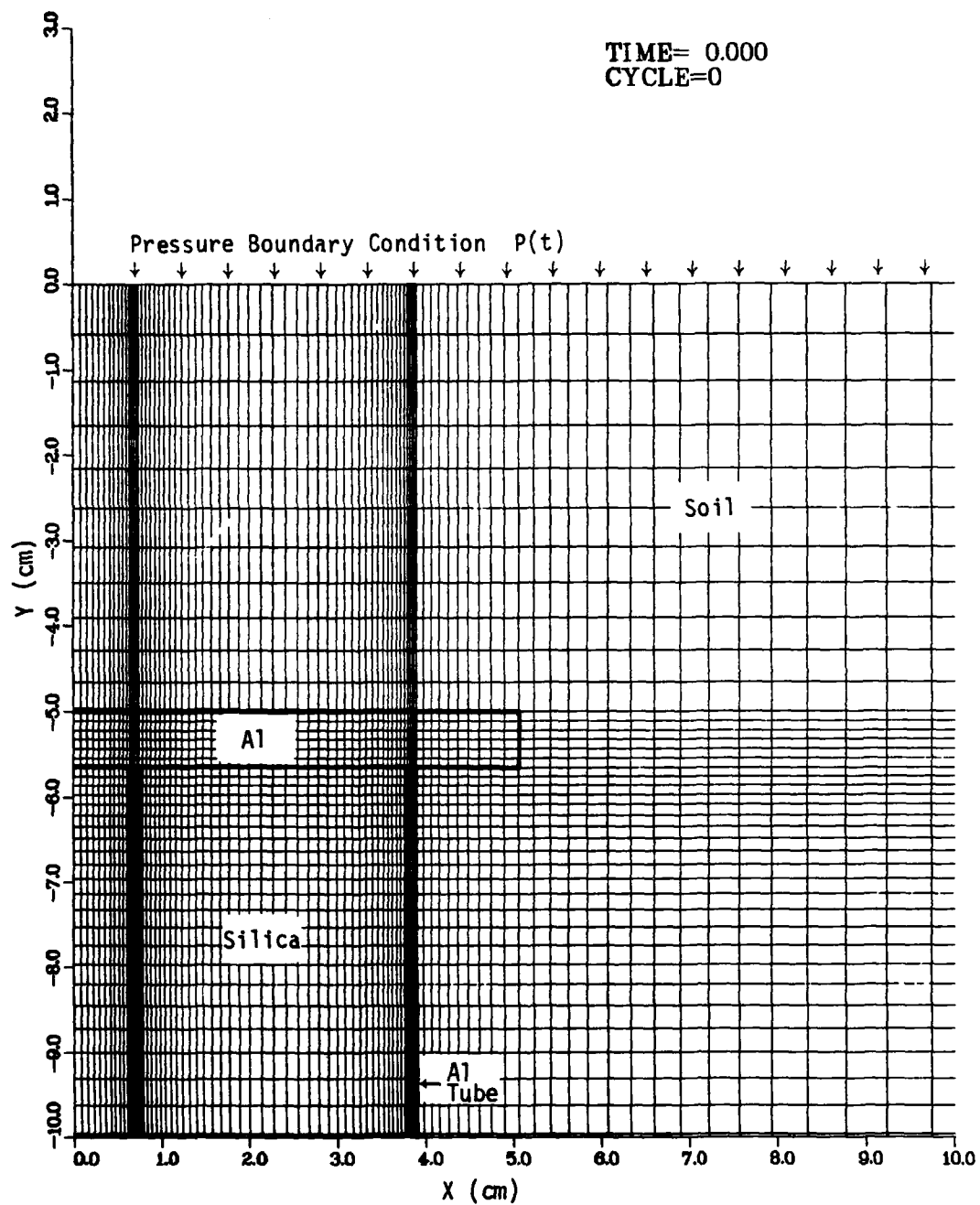


Figure 2.2. Initial grid for the Al/silica TDR gage.

Table 2.2. Initial zoning for the TDR gage problems with Al tubing.

RADIAL ZONING

| Inner Radius (cm) | Outer Radius (cm) | No. of Zones | Geometric Ratio (σ) |
|-------------------|-------------------|--------------|------------------------------|
| 0.0 | 0.64 | 11 | 0.93 |
| 0.64 | 0.7416 | 4 | 1.00 |
| 0.7416 | 2.2686 | 19 | 1.07 |
| 2.2686 | 3.7956 | 19 | 0.93 |
| 3.7956 | 3.8972 | 4 | 1.00 |
| 3.8972 | 21.52 | 38 | 1.08 |

AXIAL ZONING

| Bottom (cm) | Top (cm) | No. of Zones | Geometric Ratio (σ) |
|-------------|----------|--------------|------------------------------|
| -13.4884 | -5.66 | 30 | 0.95 |
| - 5.66 | -5.0 | 6 | 1.00 |
| - 5.0 | 0.0 | 11 | 1.06 |

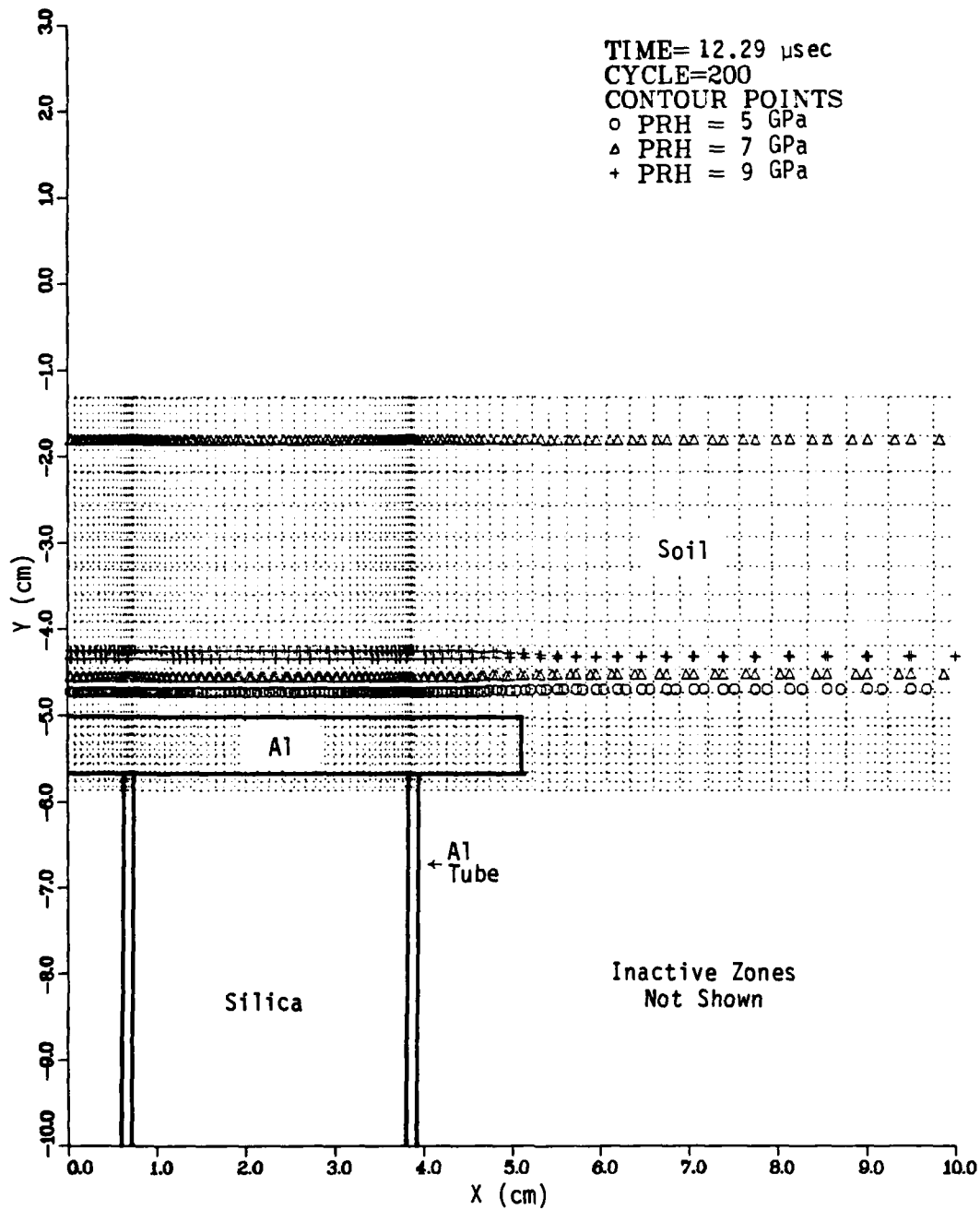


Figure 2.3. Pressure contour plot at 12.29 μ sec--
 A1/silica TDR gage.

After the incident pressure wave hits the flyer plate, a high-pressure reflection region develops. This can be seen in Figure 2.4 which is a pressure contour plot at 14.80 μ sec. By this time, the pressure wave has passed through the flyer plate and into the fused silica-filled aluminum tubes which provide the electrical path between the flyer plate and the recording instrumentation. Figure 2.5 is a pressure contour plot at 16.98 μ sec. The high-pressure reflection region has moved upward into the tuff above the flyer plate. Another high-pressure region has also developed in the fused silica below the flyer plate. Significant material motion is beginning to occur with the flyer plate now displaced downward by about 0.4 cm.

The pressure wave continues to propagate downward in the grid until the end of the calculation. The shock velocity was higher in the fused-silica regions than in the surrounding tuff and the wave front propagates further inside the gage than in the tuff. This can be seen in Figures 2.6, 2.7, and 1.4 which give the computed pressure contours at 19.2, 21.5, and 23.8 μ sec, respectively. This difference in shock velocity causes a transverse pressure gradient across the outer aluminum tube of the TDR gage which is responsible for the bending of the outer tube seen in Figure 1.4.

The STEALTH grid at the end of the calculation is shown in Figure 2.8. This figure shows a little more clearly the bending of the outer Al tube. The inward bend at the point the tube attaches to the flyer plate is not real but an artifact of the calculation. No slide lines were used so the tube had to remain tied to the corresponding vertical grid lines in the flyer plate whereas in reality it would probably slide outward. Figure 2.8 also shows some bending at the outer edge of the flyer plate and that the plate has not moved as much as the soil. The velocity of the Al plate is compared with the free-field soil velocity in Figure 1.3 and shows the plate velocity is about 10 to 15 percent less than the soil particle velocity.

In analyzing the results of this calculation, it was also noticed that the pressure boundary condition at the top of the tuff region was affected by the reflected shock wave from the flyer plate of the TDR gage. When the reflected shock reached the top boundary of the grid, it caused a

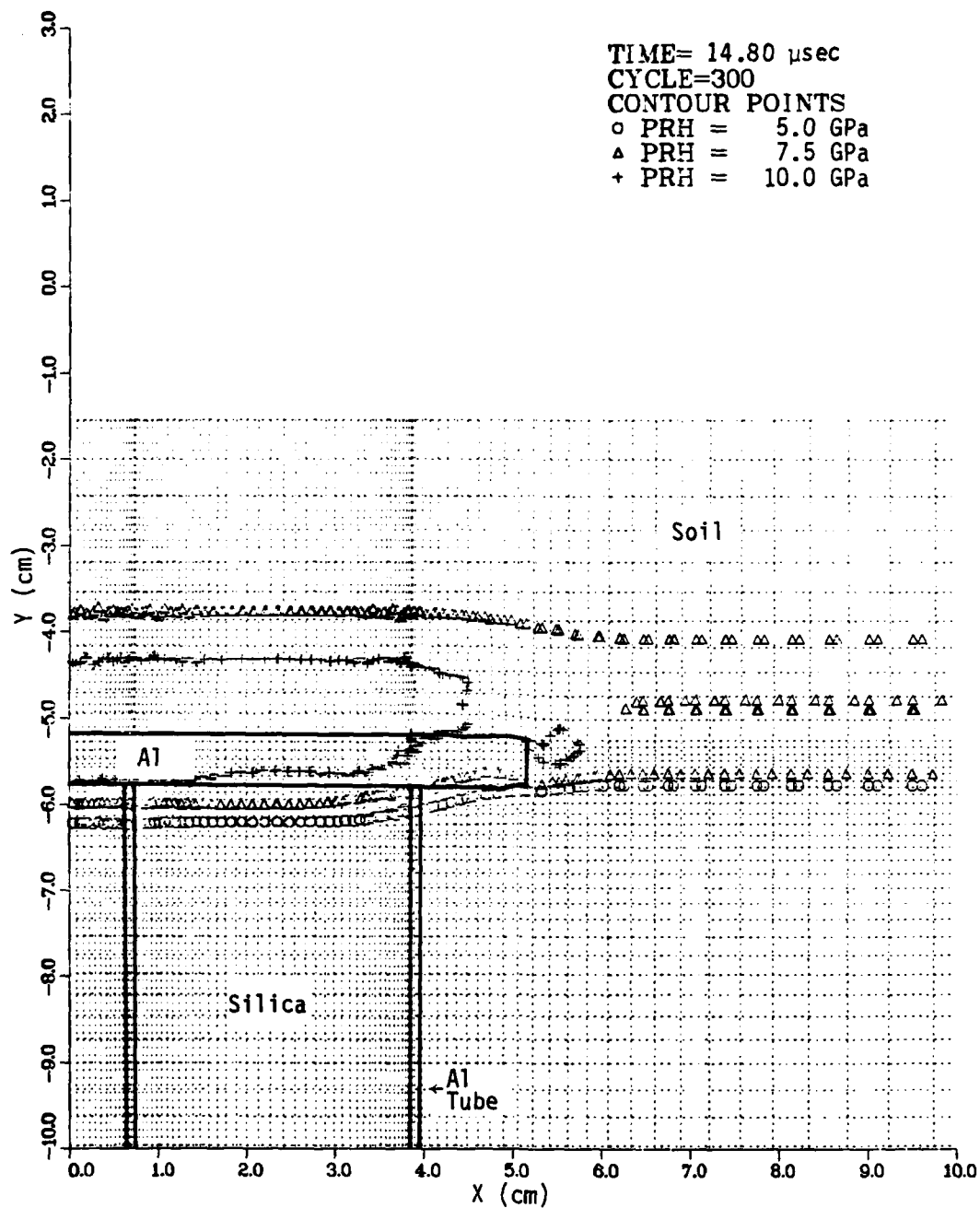


Figure 2.4. Pressure contour plot at 14.80 μ sec--
 Al/silica TDR gage.

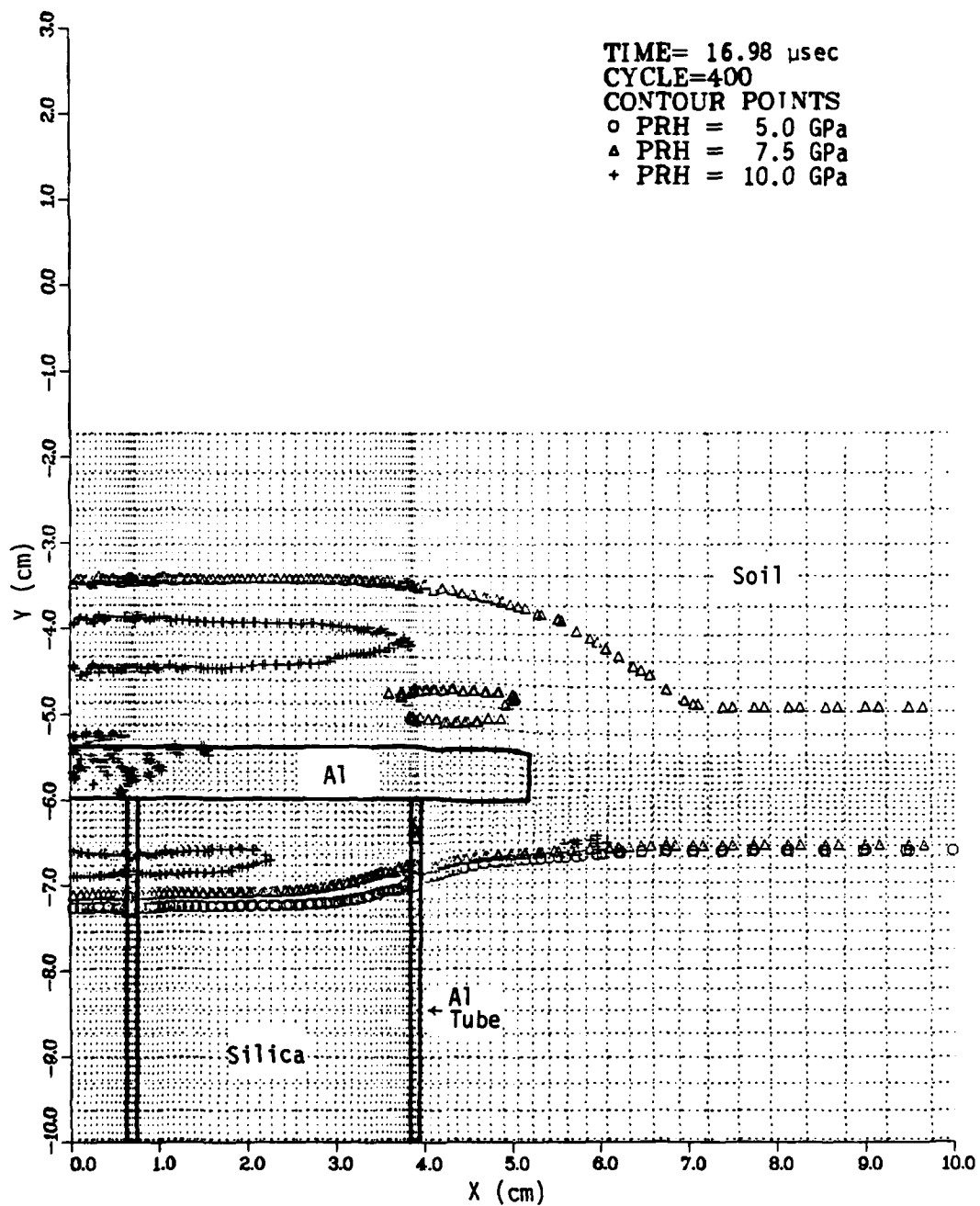


Figure 2.5. Pressure contour plot at 16.98 μ sec--
 Al/silica TDR gage.

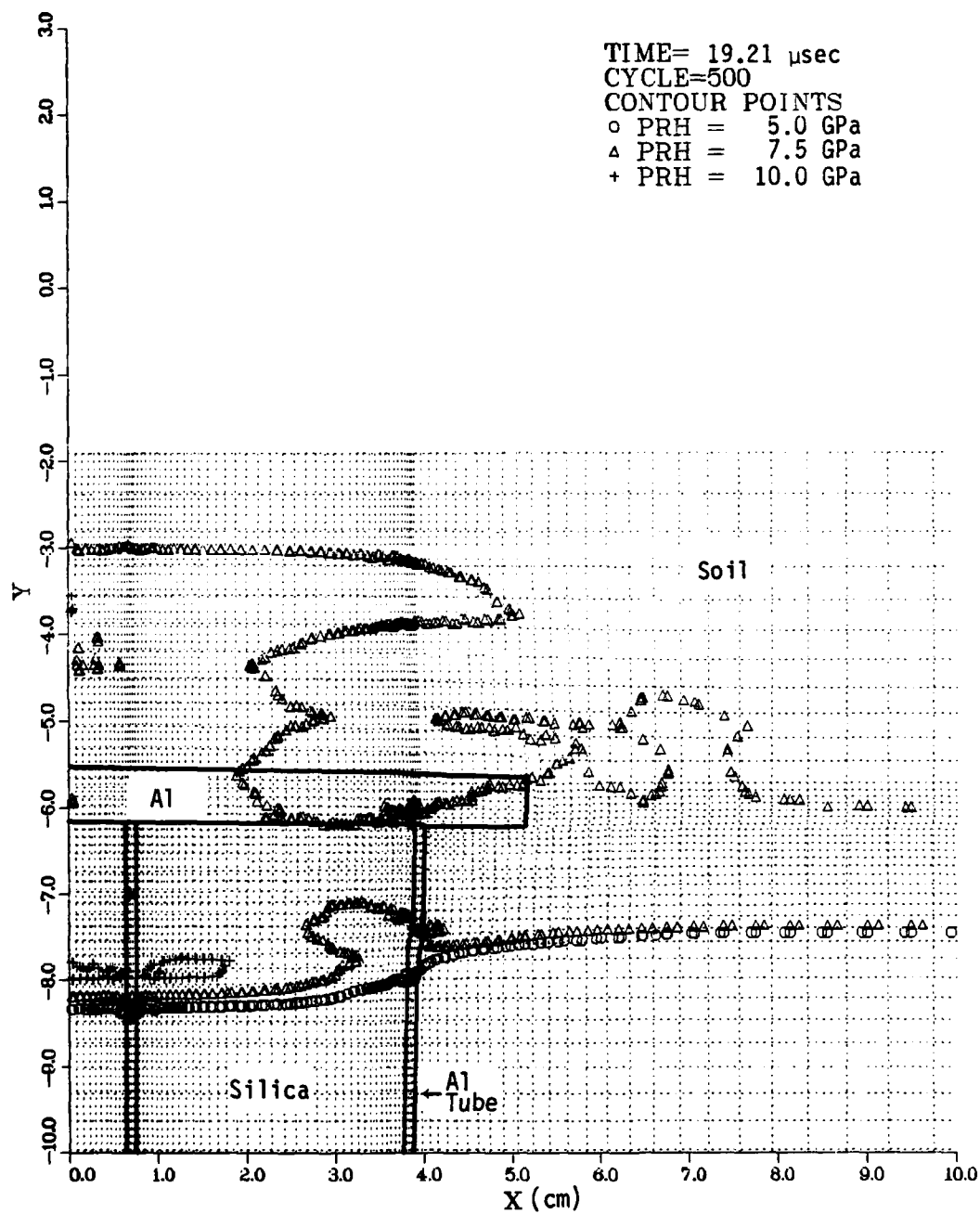


Figure 2.6. Pressure contour plot at 19.21 μ sec--
 Al/silica TDR gage.

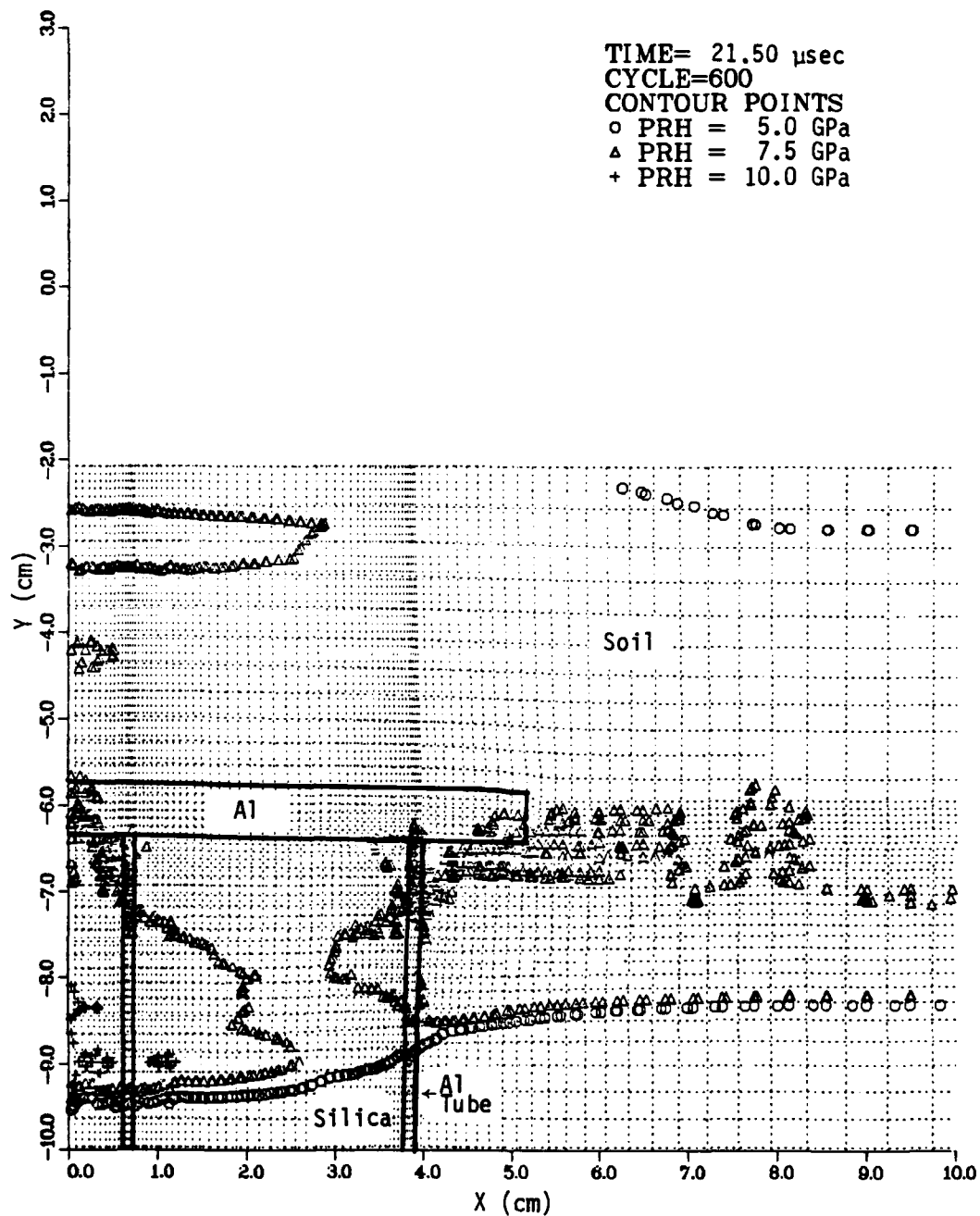


Figure 2.7. Pressure contour plot at 21.50 μ sec--
 Al/silica TDR gage.

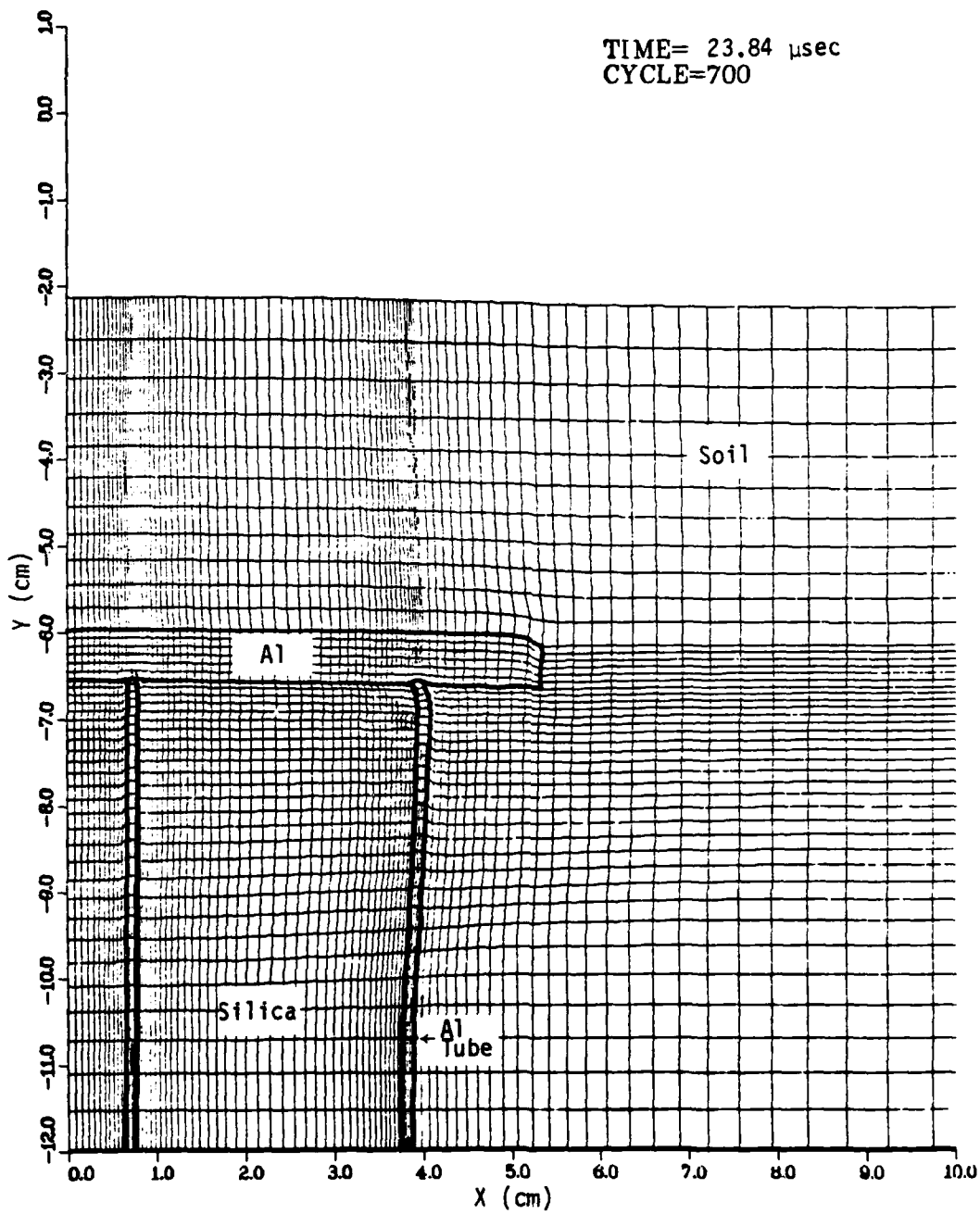


Figure 2.8. Grid plot at 23.84 μ sec--
Al/silica TDR gage.

temporary decrease in the boundary velocity when compared to the free field velocity. The effect was greatest along the axis of symmetry and diminished with radial distance with the result that the top surface of the problem is no longer a flat plane. At 23.84 μsec , the downward movement is 2.13 cm along the axis and 2.26 cm at a radius of 21.5 cm.

In view of the computational results and the practical difficulty of fabricating fused silica, a prototype of this version of the TDR gage was not built.

2-2 MG/TEFLON GAGE WITH AL TUBING

It was felt, after analyzing the results of the TDR gage calculation discussed in the previous section, that the gage response could be improved by changing the materials used in the gage. The redesigned gage (see Figure 1.2b) has the same dimensions as shown in Figure 2.1 but used magnesium as the flyer plate material instead of aluminum and Teflon as the dielectric material in place of fused silica. The equation-of-state data for these materials are given in Table 2.1. Magnesium was chosen because its density at 1.75 g/cm^3 was closer to typical soil densities than aluminum and its use might result in the flyer plate following the soil motion more closely. Teflon has about the same density as fused silica but it is much easier to fabricate and also has a lower shock velocity at 10 GPa.

Other than the material changes, the second STEALTH calculation was set up identically to the first calculation. The initial STEALTH grid used the zoning listed in Table 2.2 and shown in Figure 2.2. The boundary condition was also the same. We considered changing from a pressure to a velocity boundary condition but decided not to in order to be able to directly compare the results of the two calculations.

This STEALTH calculation was run 700 cycles to a final problem time of 24.66 μsec . As before, a few contour plots will be used to describe the time evolution of the calculation. Because the same boundary condition was used, the wave propagation is the same until the incident wave hits the flyer plate at about 13 μsec (see Figure 2.3).

By 15.07 μsec , the pressure wave has passed through the flyer plate and into the Teflon. A contour plot at this time is shown in Figure 2.9 and should be compared to Figure 2.4. Note that there is a shock reflection from the Mg plate but it is much weaker than that from the Al flyer. In fact, by 17.49 μsec , the reflected shock in the tuff cannot be seen in the contour plot (compare Figure 2.10 to Figure 2.5 but note change of contour scale). There is a high-pressure region in the Teflon just below the flyer plate but again it is significantly smaller than in the Al/silica case.

The pressure wave continues to propagate downward in both the tuff and Teflon until the end of the calculation. At the final time, the wave front is at approximately the same position in both the dielectric and the soil as shown in the contour plot at 24.66 μsec (Figure 1.5). This is a great improvement over the previous result (Figure 1.4) and justifies the change to Teflon. However, the shock wave does travel faster in the Al tubing than in the soil.

The STEALTH grid at 24.66 μsec is shown in Figure 2.11. Because the pressure contours are relatively flat, there is less bending of the outer Al tube than before (see Figure 2.8). There is still some distortion at the outer edge of the flyer plate but the plate is no longer lagging behind the soil. The velocity of the bottom of the Mg flyer plate is now very close to the soil particle velocity (see Figure 1.3) so the accuracy of the gage has been improved by changing the flyer plate material to magnesium.

The STEALTH results showed the Mg/Teflon TDR gage to be a significant improvement over the Al/silica design. However, there were still some problems with the use of Al tubing to provide the electrical path to the flyer plate. Before this calculation was completed, it was decided to replace the Al tubes by Al foil in the prototype TDR gage.

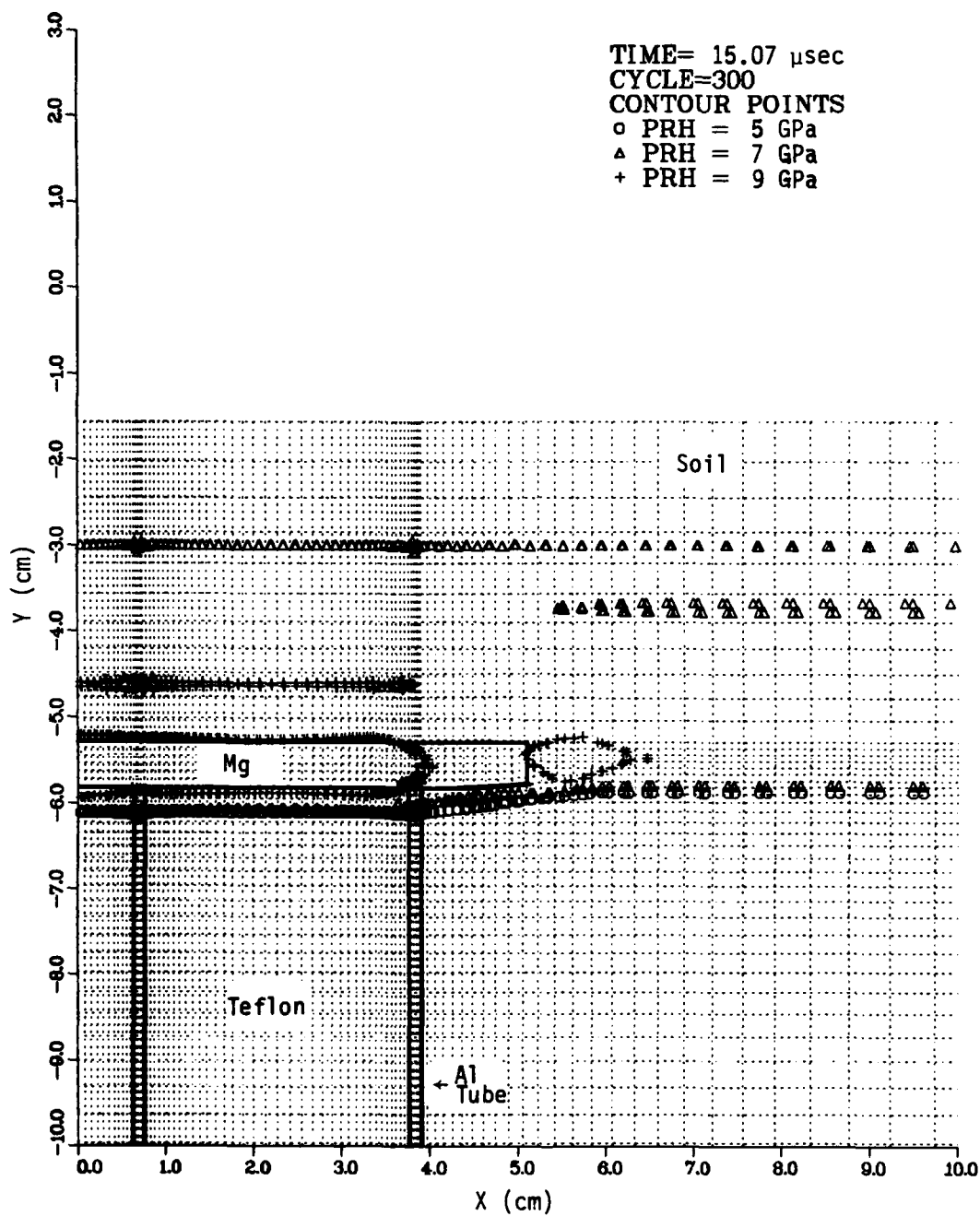


Figure 2.3. Pressure contour plot at 15.07 μ sec--
 Mg/Teflon TDR gage with Al tubing.

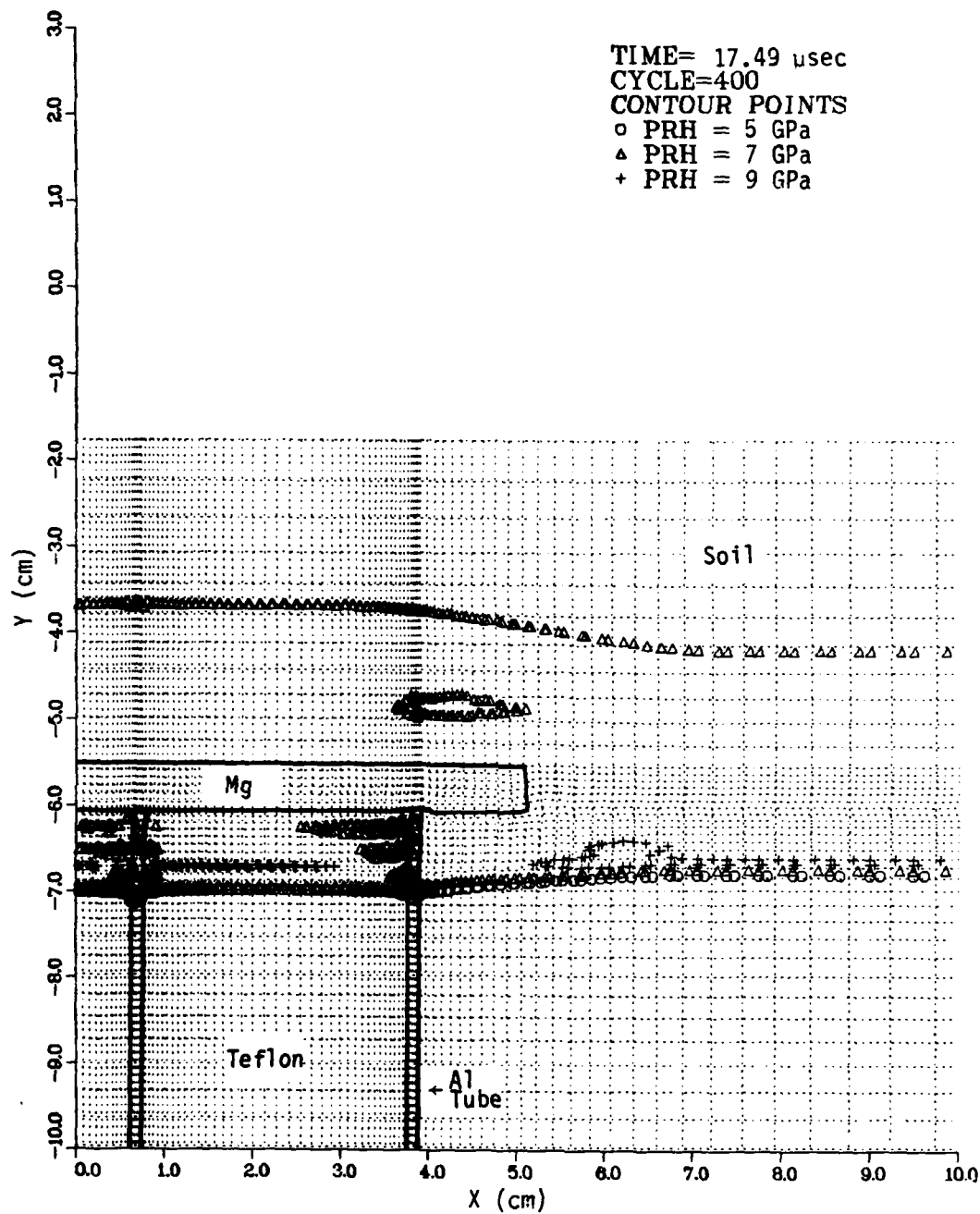


Figure 2.10. Pressure contour plot at 17.49 μ sec--
 Mg/Teflon TDR gage with Al tubing.

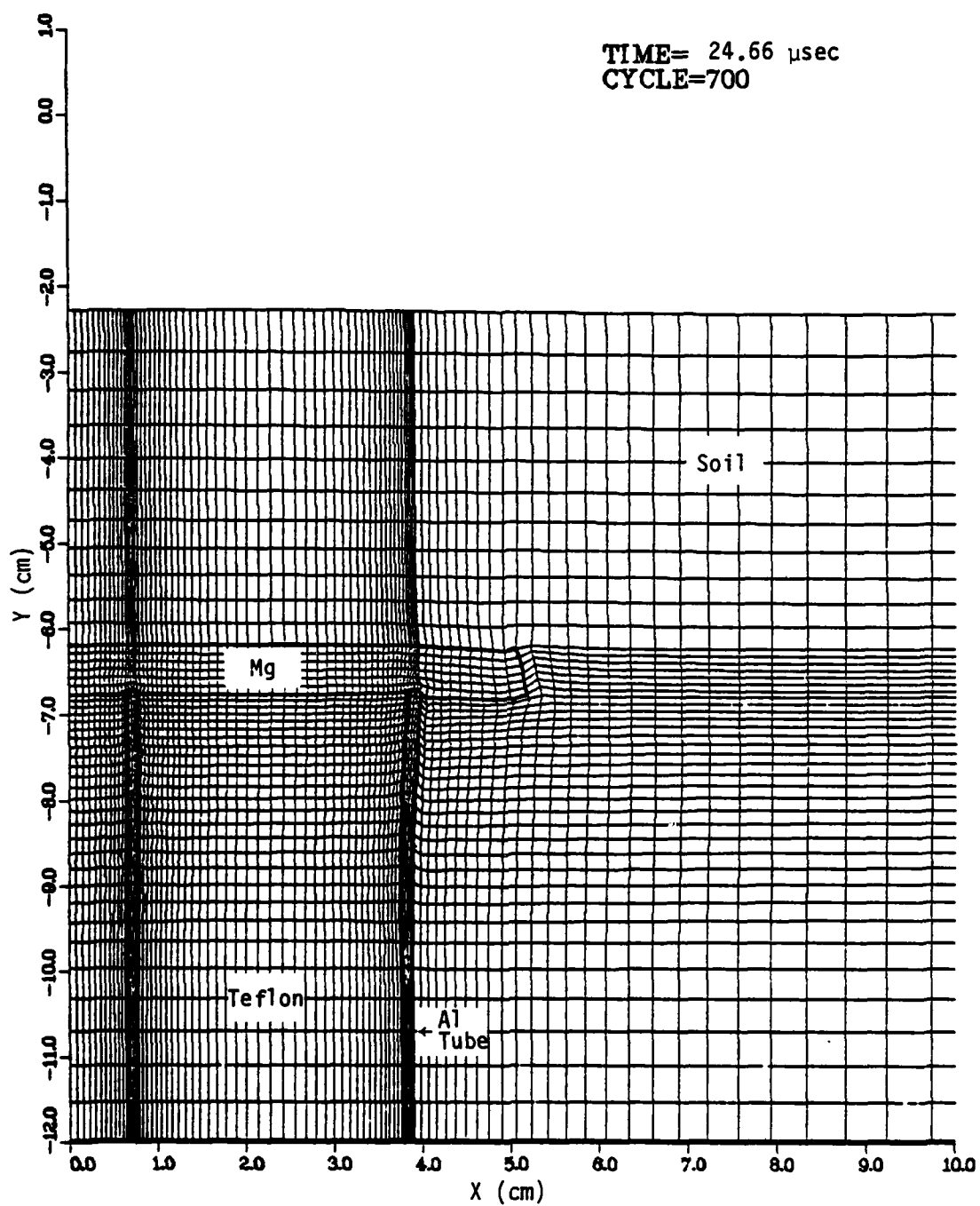


Figure 2.11. Grid plot at 24.66 μ sec--Mg/Teflon TDR gage with Al tubing.

The third design for the TDR particle velocity gage is shown in Figure 1.2c. This gage is similar to the gage discussed in Section 2.2 but has a smaller diameter flyer plate and used aluminum foil conductors to provide the electrical path to the flyer plate. Another change is that the outer Al foil is covered by a thin protective layer of Teflon.

The upper portion of the initial grid for the STEALTH calculation of this gage is shown in Figure 2.12. The entire grid is symmetric about the Y axis. It extends from $Y=0$ to $Y=100.64$ cm and from zero to 20 cm in radius. The axial dimension was made much larger than in the other two calculations so this one could be run to a longer problem time without the results being affected by reflections from the top or bottom of the grid.

The darkened grid lines in Figure 2.12 denote the gage boundaries. The Mg plate goes from $Y=60.0$ cm to $Y=60.64$ cm and has an outer radius of 3.85 cm. The Teflon dielectric is a cylinder of outer radius 3.50 cm that extends from $Y=0$ to $Y=60$ cm. The remainder of the grid is filled with tuff.

In the real gage, the aluminum foil conductors are in the Teflon dielectric at radii of 0.5 cm and 3.18 cm. Because the foils are very thin they are not included in the calculational grid. This allowed us to use larger and more uniform zoning in the radial direction than in our previous TDR gage calculations. In particular, there are no long thin zones (high aspect ratio) in the grid shown in Figure 2.12. Such zones typically lead to small time steps in explicit calculations because of the Courant stability condition.

The Mg flyer plate has 12 zones with equal ΔX in the radial direction and 4 zones with equal ΔY in the axial direction. These are the smallest zones in the grid. Beyond the outer radius of the flyer plate, the radial zone size increases geometrically to the outer boundary. In the axial direction the zone sizes increase geometrically both above and below the flyer

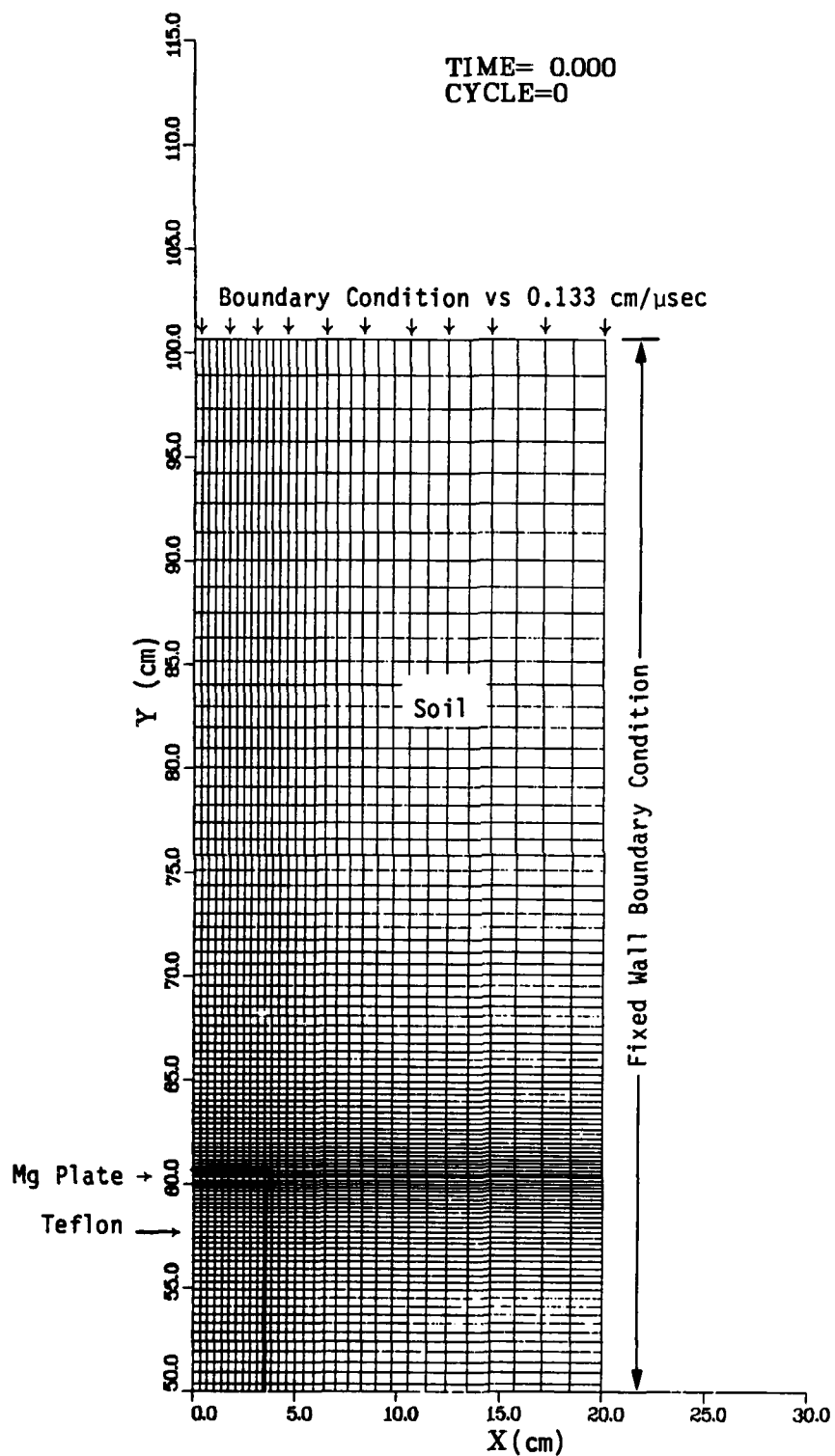


Figure 2.12. Initial grid for the Mg/Teflon TDR gage with Al foil.

plate. The number of zones in each portion of the grid and the geometric ratios used are listed in Table 2.3. The entire grid has 32 radial lines and 134 axial lines for a total of 4288 grid points.

The stress wave incident on the gage is generated by a velocity boundary condition at the top of the grid (see Figure 2.12). This is a different boundary condition than used in the two previous TDR gage calculations. It results in a 10.5 GPa pressure wave with no decay that moves downward at 0.42 cm/ μ sec. This wave reaches the top of the TDR gage at about 95 μ sec. A pressure contour plot at 97.4 μ sec is shown in Figure 2.13. It shows the shock has just propagated through the Mg plate at this time. Also, there is a weak reflected shock (about 12.5 GPa) moving upward in the soil above the plate.

By 129.3 μ sec, the incident wave has swept over 13 cm of the gage. A pressure contour plot at this time is shown in Figure 2.14. The wave front is at nearly the same position in the Teflon and the soil as desired. There are some weak reflected shocks in the Teflon (possibly caused by numerical noise) but no disturbance caused by the presence of the gage is apparent in the soil. Also note the position of the Mg flyer plate at this time. The bottom of the plate, initially at Y=60.0 cm, has moved downward to 55.8 cm. The Teflon between the plate and the shock front has been compressed about thirty percent and is also beginning to expand outward just behind the plate.

This calculation was run to a problem time of 152.9 μ sec. At that time, the pressure front had reached about Y=37 cm as shown in Figure 1.6. The flyer plate had moved downward about 7 cm to Y=53 cm. The calculation was stopped at this time because the distorted Teflon zones just behind and near the outer edge of the flyer plate had considerably reduced the problem time step.

The distortion near the flyer plate can be seen more clearly in Figure 2.15. This grid plot shows the flyer plate has been bent into a convex downward shape. The outer radius of the plate has also increased to about 4.1 cm. The Teflon just behind the plate has been squeezed outward into a

Table 2.3. Initial zoning for the Mg/Teflon TDR gage with Al foil.

RADIAL ZONING

| Inner Radius (cm) | Outer Radius (cm) | No. of Zones | Geometric Ratio (σ) |
|-------------------|-------------------|--------------|------------------------------|
| 0.0 | 3.85 | 11 | 1.0 |
| 3.85 | 20.0 | 20 | 1.08 |

AXIAL ZONING

| Bottom (cm) | Top (cm) | No. of Zones | Geometric Ratio (σ) |
|-------------|----------|--------------|------------------------------|
| 0.0 | 60.0 | 69 | 0.96 |
| 60.0 | 60.64 | 4 | 1.0 |
| 60.64 | 100.64 | 60 | 1.04 |

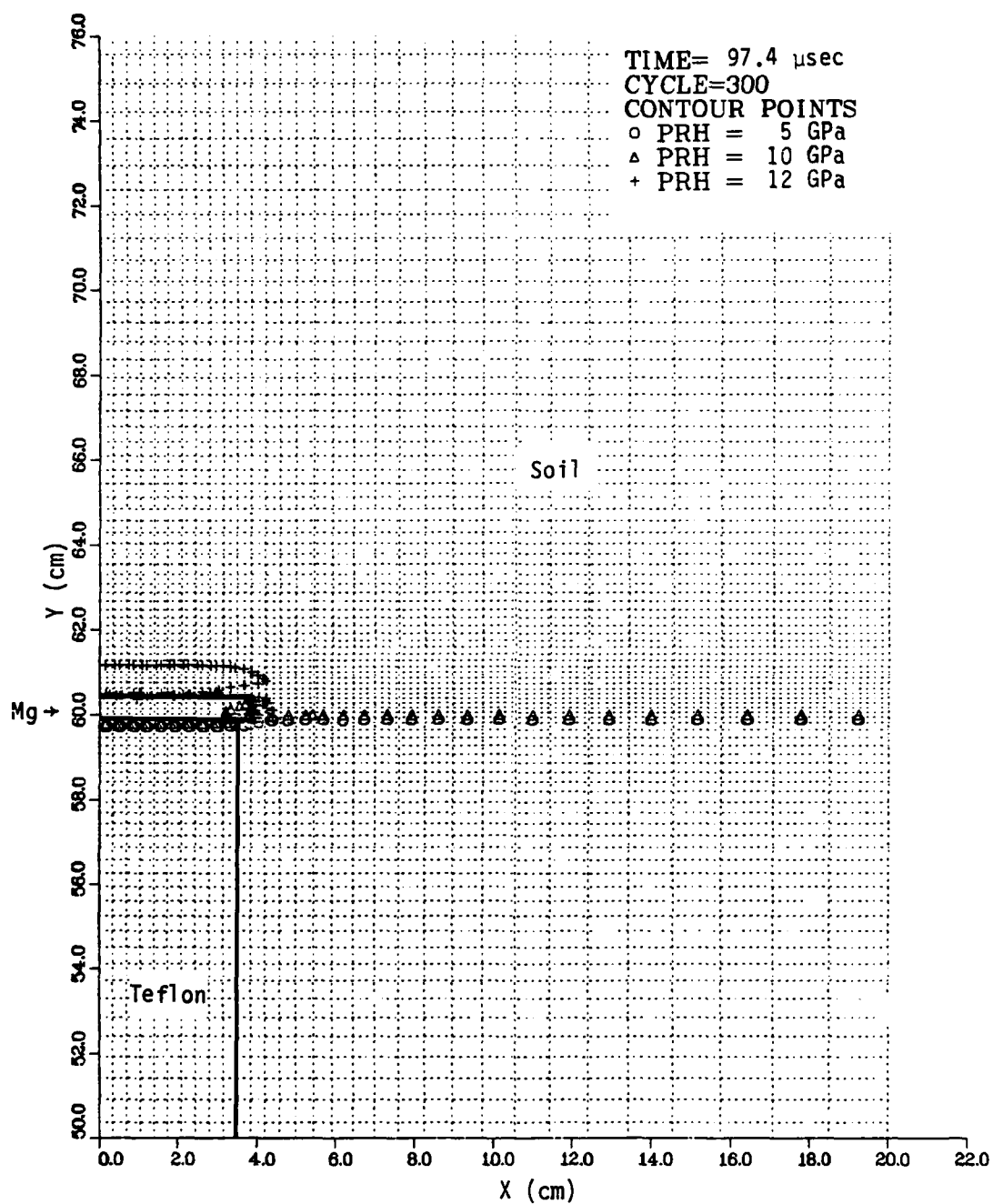


Figure 2.13. Pressure contour plot at 97.40 μ sec--
 Mg/Teflon TDR gage with Al foil.

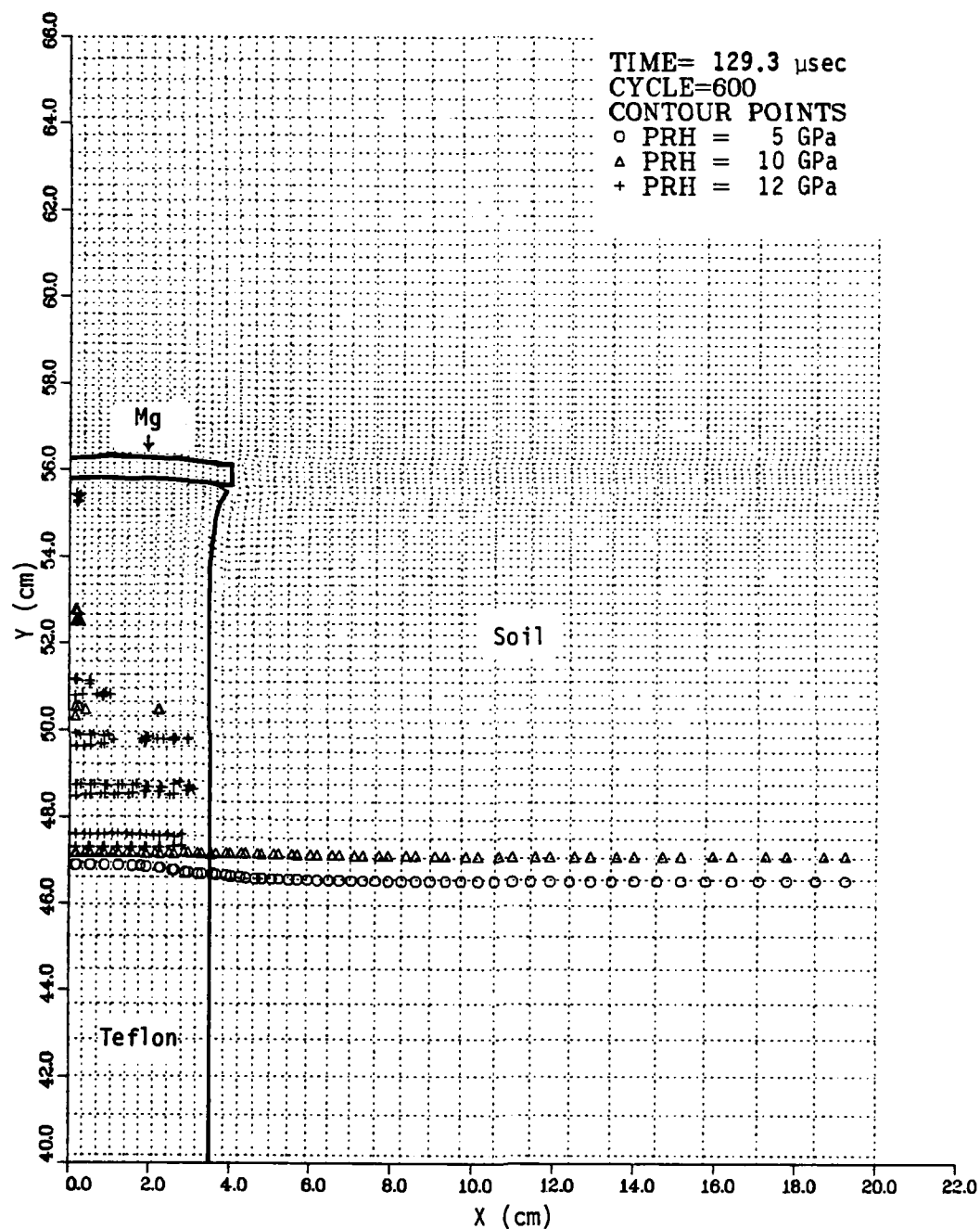


Figure 2.14. Pressure contour plot at 129.3 μ sec--
Mg/Teflon TDR gage with Al foil.

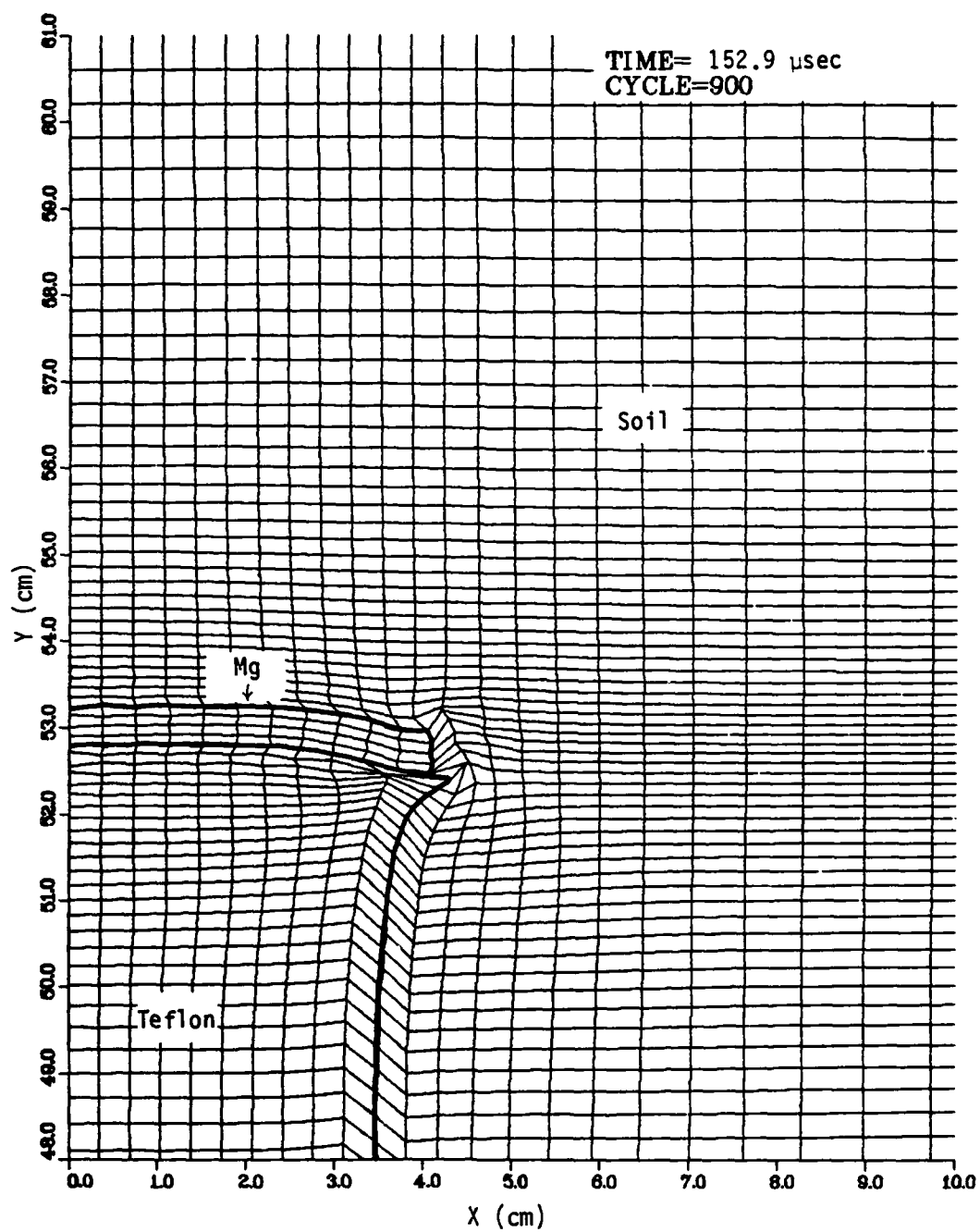


Figure 2.15. Grid plot of flyer plate region at 152.9 μ sec--
Mg/Teflon TDR gage with Al foil.

bell shape with the outer edge of the Teflon now beyond the outer radius of the flyer plate. Another interesting result shown in Figure 2.15 is that the horizontal grid lines are displaced upward as they cross from the soil into the Teflon. This is apparently caused by the difference between the tuff and Teflon equations of state. At 10 GPa, Teflon has approximately the same shock velocity as tuff but a lower particle velocity. This difference causes the Teflon to move more slowly than the soil.

The displacement of the shock front and the bottom of the flyer plate relative to the original position of the bottom of the flyer plate is shown in Figure 1.7. After the shock reached the bottom of the flyer plate at about 97 μ sec, both the shock front and the flyer plate moved downward at a constant velocity as expected. By the end of the calculation, the shock front had traveled about 27 cm into the Teflon and the plate had moved nearly 7 cm.

Prototypes of this version of the TDR particle velocity were constructed and tested in HE experiments at SRI International in December 1981 (Reference 2). The measured plate and shock front displacements were comparable to those shown in Figure 1.7. Several other HE tests were made during 1982 prior to these gages being used on the HURON LANDING and MINI JADE Events.

SECTION 3 CYLINDRICAL STRESS GAGE

3-1 BRASS/EPOXY GAGE

The first SRI cylindrical stress gage was made with thin-walled brass tubing and used epoxy as the insulating material (see Figure 1.9a). The grid for the STEALTH calculation of this gage is shown in Figure 3.1. The gage, centered at $X=0$ and $Y=0$, is surrounded by soil through which a downward-moving pressure wave will propagate and pass over the gage. The STEALTH grid is a planar cross section through the soil and the gage, only half of which needs to be included in the grid because of symmetry.

The zoning for the STEALTH grid is listed in Table 3.1. The grid lines are of two types. Radial lines with 5° spacing extend from the gage center to the outer grid boundary. The grid is completed with semicircular lines inside the gage. These lines transition in the soil from semicircles at the gage outer boundary to straight lines that define the outer boundary of the grid.

An expanded view of the gage region at the start of the calculation is shown in Figure 3.2. The zones in the brass had equal spacing in the radial direction (equal ΔR). The epoxy zones also had equal ΔR and were mass-matched (equal $\rho\Delta R$) to the brass zones. The tuff zones were mass-matched at the brass-tuff interface and then were geometrically increased along the radial lines by the ratio necessary to reach the grid outer boundary. The geometric ratio differed for each radial line; the ratios varied from 1.06 to 1.08.

The piezoresistive wire is represented by the small semicircle at the center of the gage in Figure 3.2. The wire is included in the calculation as a rigid body boundary condition which responds to stresses in the surrounding epoxy zones. The net force on the wire is calculated each cycle, converted to

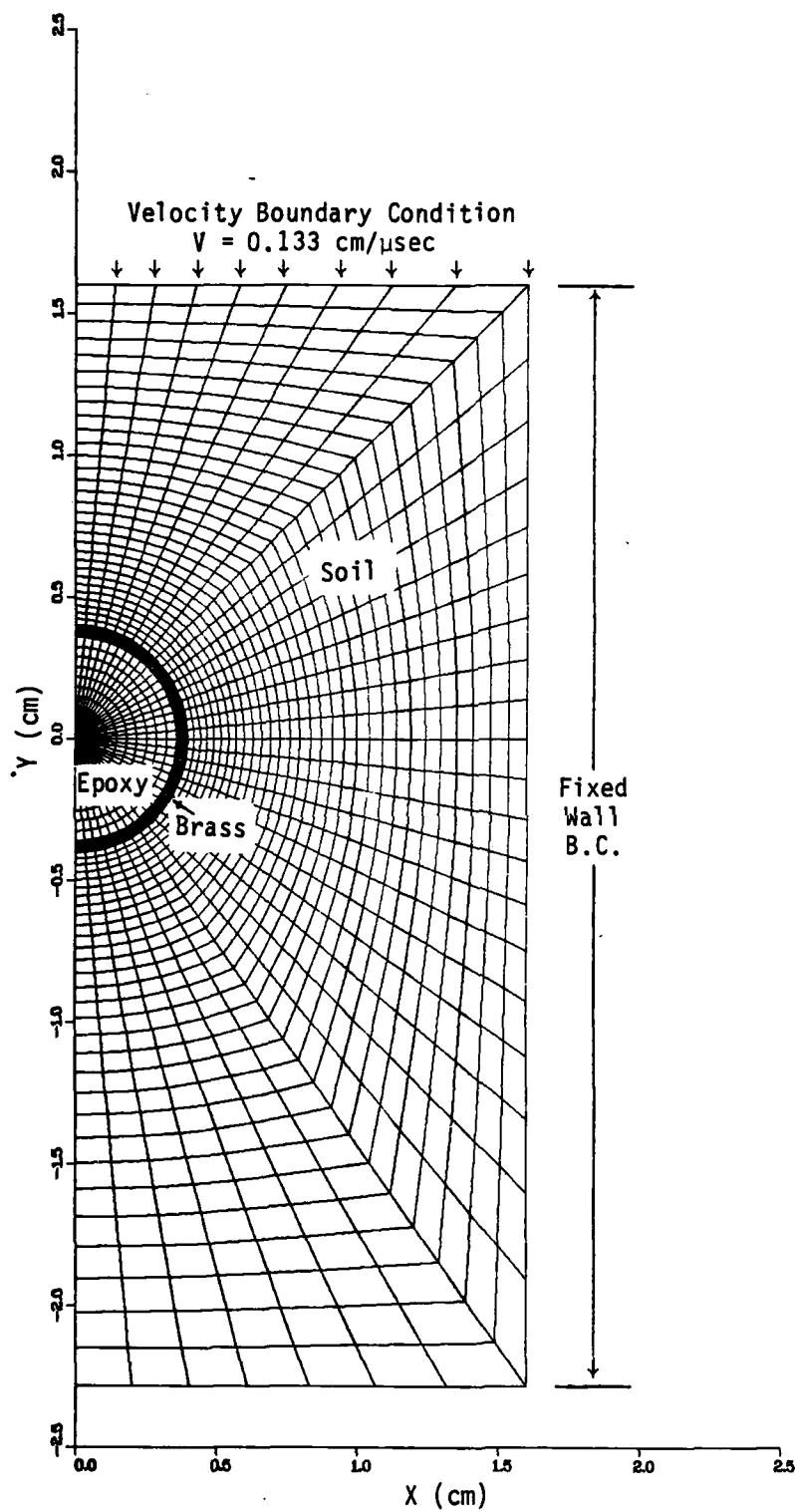


Figure 3.1. Initial grid for the brass/epoxy cylindrical gage.

Table 3.1. Zoning for cylindrical gage calculations.

| | Brass/Epoxy | Mg/Teflon | Al/Teflon | Al/Silastic |
|--------------------------------------|-------------|-----------|-----------|-------------|
| Wire Radius (cm) | 0.00635 | 0.00635 | 0.00635 | 0.00635 |
| Inner Tube Radius (cm) | 0.36 | 0.625 | 0.635 | 0.6975 |
| Outer Tube Radius (cm) | 0.40 | 0.950 | 0.711 | 0.7875 |
| Average Density (g/cm ³) | 2.58 | 1.93 | 2.27 | 1.66 |
| Top of Grid (cm) | 1.60 | 4.0 | 3.0 | 3.0 |
| Bottom of Grid (cm) | -2.285 | -6.298 | -5.196 | -5.196 |
| Right Side of Grid (cm) | 1.60 | 4.0 | 3.0 | 3.0 |
| Number of Radial Lines | 37 | 25 | 25 | 25 |
| Spacing (degrees) | 5 | 7.5 | 7.5 | 7.5 |
| Number of Circular Lines | 49 | 40 | 40 | 45 |
| Wire | 1 | 1 | 1 | 1 |
| Insulator | 10 | 10 | 12 | 12 |
| Metal | 8 | 4 | 2 | 3 |
| Soil | 30 | 25 | 25 | 29 |
| Grid Points | 1813 | 1000 | 1000 | 1125 |

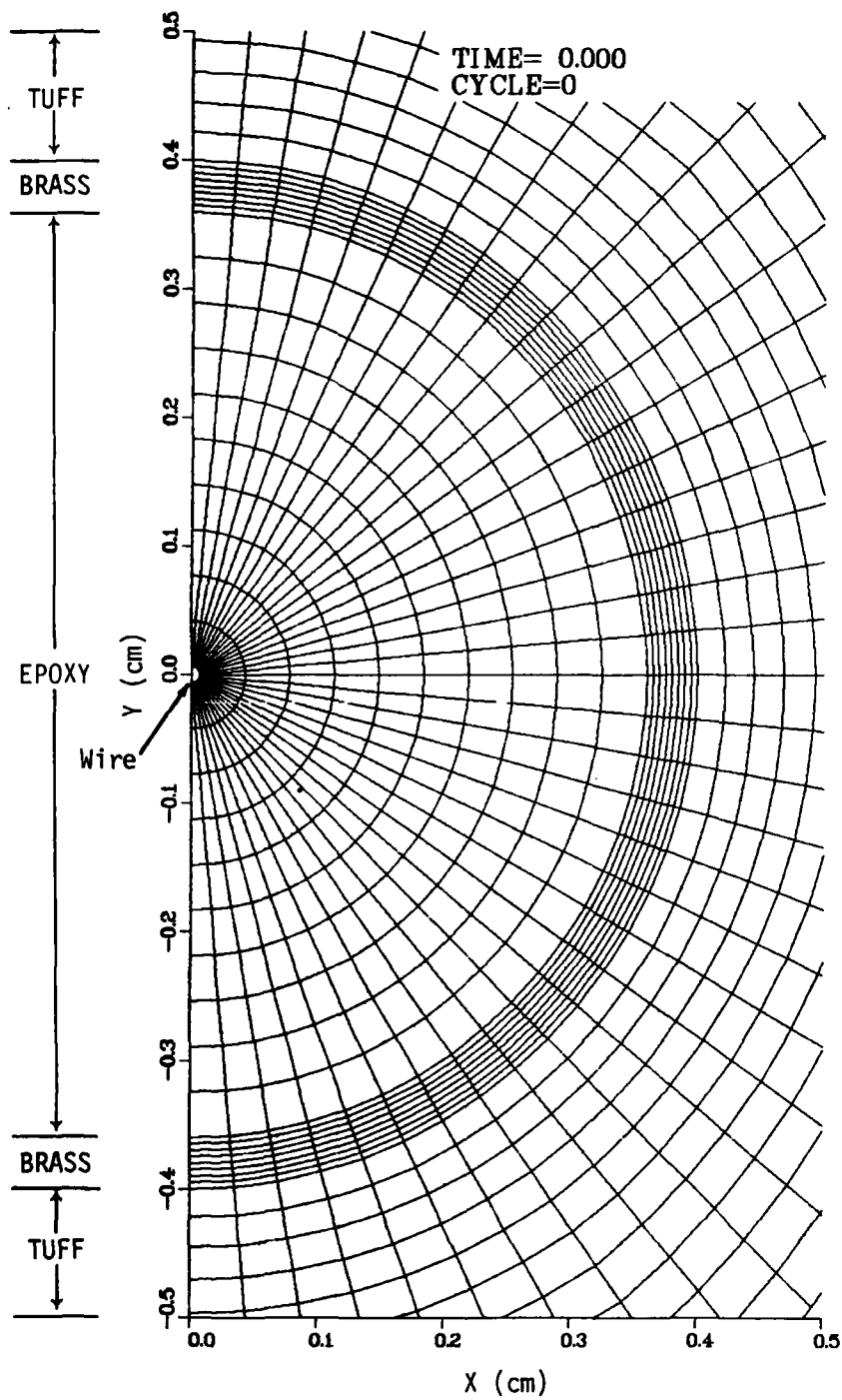


Figure 3.2. Initial zoning of gage region--brass/epoxy cylindrical gage.

an acceleration and integrated with time to obtain the wire velocity. This velocity is assigned to all the boundary grid points defining the wire shape. These points are then moved each cycle a distance equal to the velocity times the cycle time step. The details of this algorithm are given in the Appendix.

The velocity boundary condition at the top of the grid (see Figure 3.1) generates a 10.5 GPa shock wave that moves downward at 0.42 cm/ μ sec. At 2.51 μ sec, the pressure wave has nearly reached the top of the gage as shown in the grid velocity plot (Figure 3.3) and the pressure contour plot (Figure 3.4) at this time. The pressure contours show the wave is not quite planar. The 10 GPa contour lags behind on the right side of the grid. We believe this is a zoning effect caused by the abrupt change in zone shape along the 45° line connecting the gage center with the upper right corner of the grid.

Initially we computed the interaction of the incident pressure wave and the gage using a pure Lagrange grid in which the mass in each zone remains constant throughout the calculation. This method led to the two types of zone distortion shown in Figure 3.5. One was distortion in the zones on each side of the brass-tuff and brass-epoxy interfaces (see Figure 3.5a). The second and more severe case was distortion of the small epoxy zones around the piezo-resistive wire (see Figure 3.5b). At a problem time of 4.5 μ sec, the problem time step dropped sharply when boundary crossings occurred in several of the epoxy zones below the wire. The calculation was stopped after this occurred.

The calculation was restarted at 2.51 μ sec (before the shock wave reached the gage) using one of the standard STEALTH rezone options. In this scheme, each interior grid point in the epoxy region is rezoned every ten cycles. (The points rezoned on a given cycle are chosen so that no adjacent points are rezoned on the same cycle.) The rezoned point is moved so that a straight radial grid line is maintained between the center wire and the epoxy-brass interface. The same scheme was used for the interior points in the brass to maintain a straight line between the epoxy-brass and brass-tuff interfaces. The points defining the epoxy-brass and brass-tuff interfaces are not rezoned. These boundaries continue as Lagrange interfaces so no material mixing occurs.

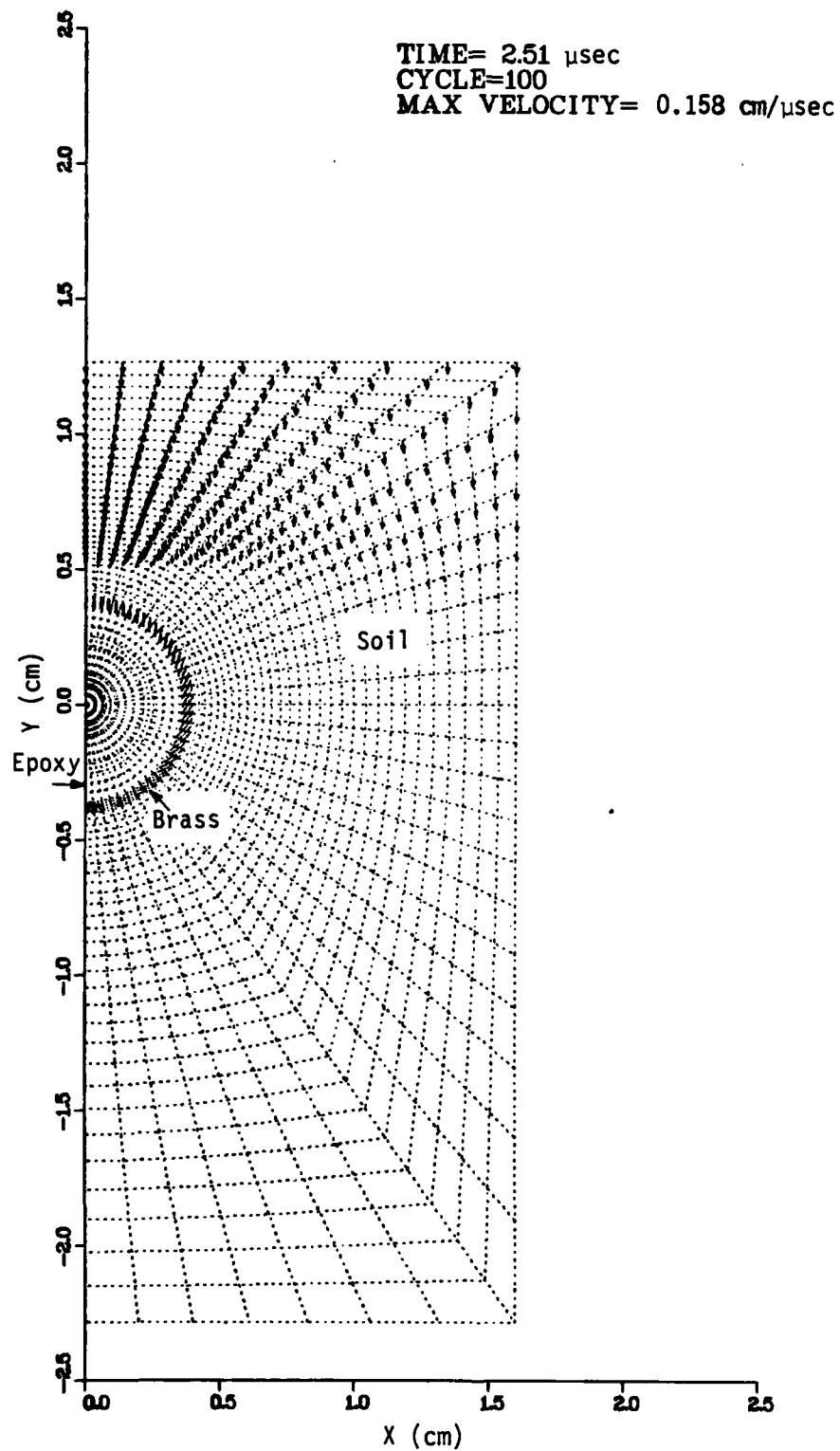


Figure 3.3. Grid-velocity plot at 2.51 μ sec--
brass/epoxy cylindrical gage.

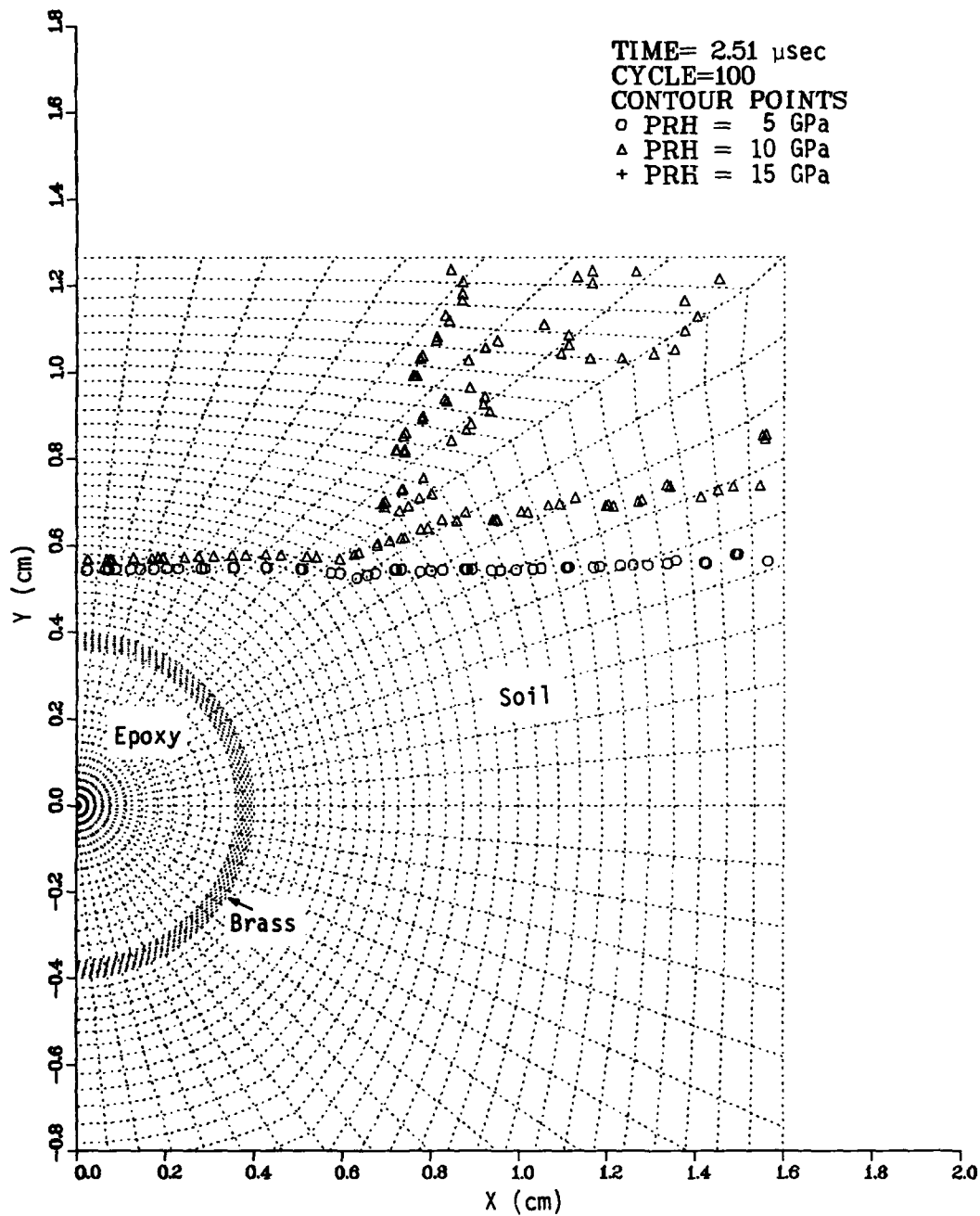
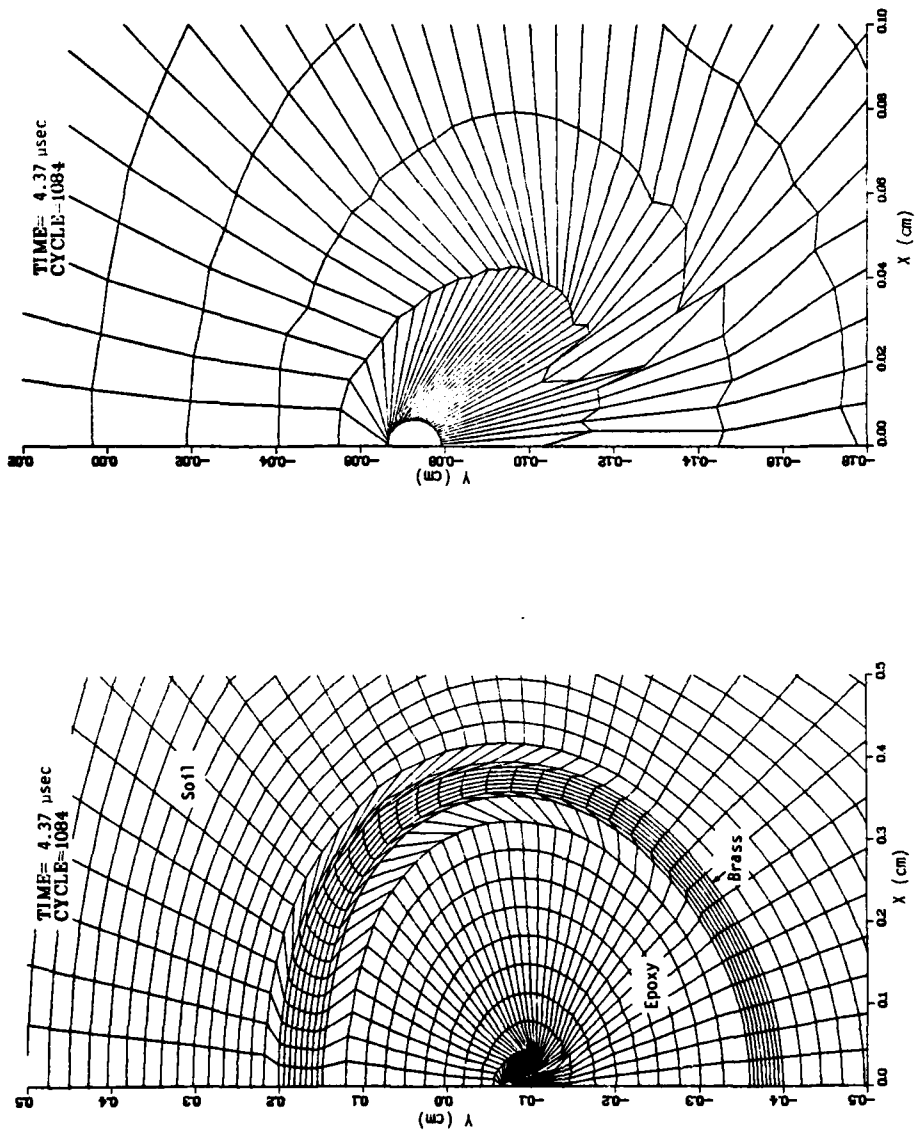


Figure 3.4. Pressure contour plot at 2.51 μ sec--brass/epoxy cylindrical gage.



(a) Distortion at brass/tuff and brass/epoxy interfaces

(b) Distorted zones around center wire

Figure 3.5. Grid distortion in Lagrange calculation of brass/epoxy cylindrical gage.

The efficacy of this rezone method can be seen in Figure 1.11 which shows the gage grid lines at 5.91 μsec . The epoxy zones around the wire are still the smallest zones in the grid but now are very regular and not causing time step problems. No rezoning was done in the tuff and it was in the tuff zones just outside the brass that time step problems eventually developed. This difficulty and some possible solutions will be discussed later.

The STEALTH problem with rezoning in the gage was run 2000 cycles to a problem time of 5.92 μsec . The time evolution of the interaction of the gage with the incident pressure wave will be illustrated by a series of pressure contour plots. More detailed information is available in the STEALTH output.

The incident shock wave reaches the gage at approximately 2.9 μsec . By 3.46 μsec , the pressure wave has swept over the upper quarter of the gage and has been transmitted through the brass cylinder into the epoxy. The pressure contours at this time are shown in Figure 3.6. There are several points of interest in this figure. One is the continued planar shape of the 5 GPa contour (small circles) in both the wet tuff and, although lagging somewhat behind, in the epoxy. Also note that while there are higher pressures in the brass (some over 15 GPa), the epoxy pressures are all under 10 GPa. There is also a high-pressure region in the tuff above the brass outlined by the 15 GPa contour (small crosses). The peak pressures in this region are about 20 GPa or double the incident wave. This region represents a reflection of the incident wave off the brass cylinder.

The pressure wave reaches the piezoresistive wire at about 3.7 μsec and the bottom of the gage at about 4.5 μsec . Figure 3.7 shows the pressure contours at 4.43 μsec . Note the pressure wave in the tuff is only about three-quarters of the way past the gage. The wave has traveled faster inside the gage because of the higher sound speed in the epoxy. An interior reflection off the bottom of the brass tube is forming in the region of the epoxy denoted by the small crosses in Figure 3.7. This reflected shock becomes quite strong reaching over 25 GPa.

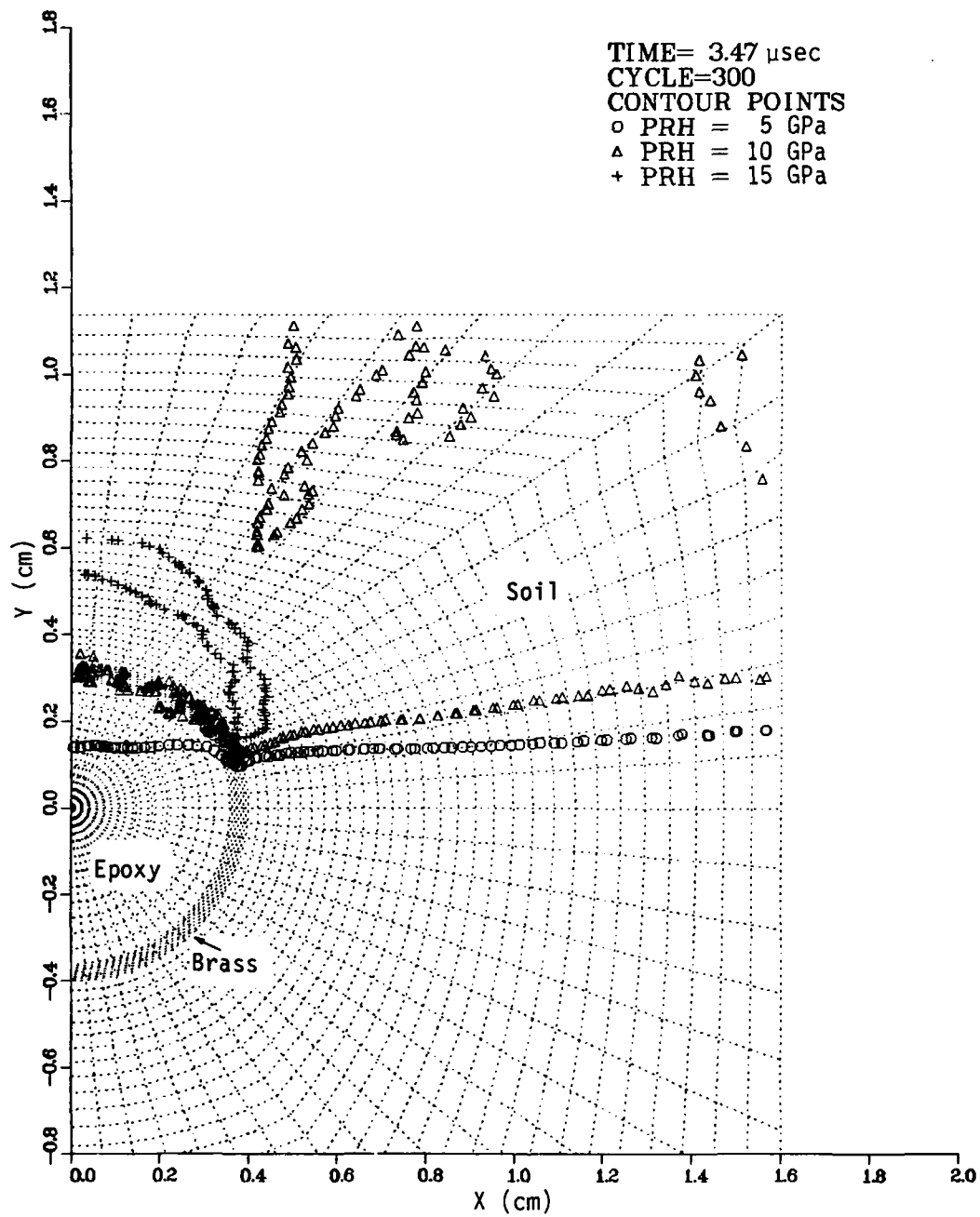


Figure 3.6. Pressure contour plot at 3.47 μ sec--
brass/epoxy cylindrical gage.

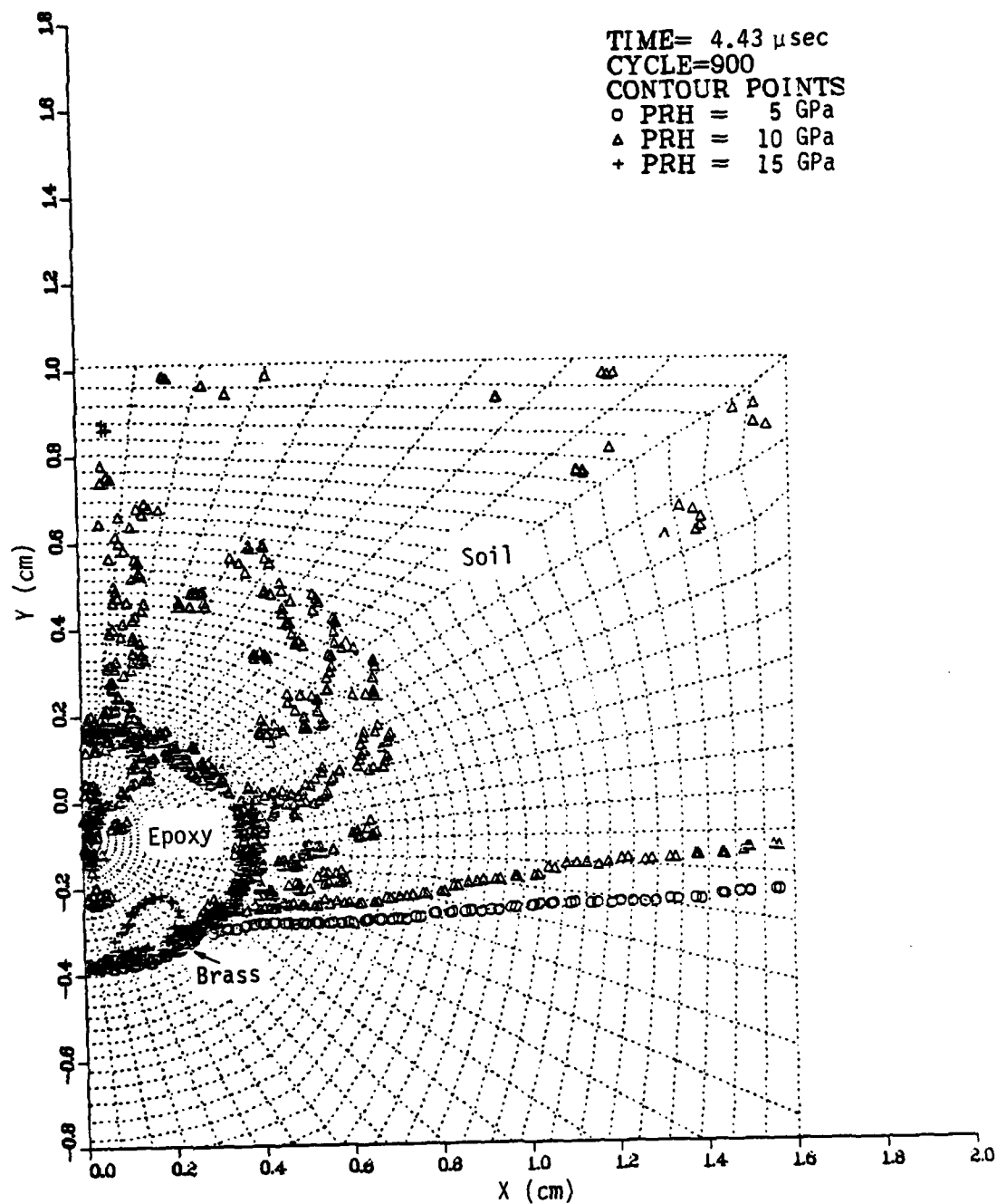


Figure 3.7. Pressure contour plot at 4.43 μ sec--brass/epoxy cylindrical gage.

By 4.74 μsec , the reflected shock has traveled upward and reached the piezoresistive wire (see Figure 3.8). By 5.00 μsec , it is at the top of the brass tube (see Figure 3.9). A weak reflection then occurs which travels downward toward the bottom of the gage (Figure 3.10). In addition, a nearly spherical wave is transmitted into the tuff. This wave has moved further into the tuff at 5.92 μsec (Figure 3.11). The pressure inside the gage is fairly uniform at this time.

The STEALTH grid at 5.92 μsec is shown in Figure 1.11. While the rezone scheme kept the brass and epoxy zones very regular, severe distortion occurred in the tuff zones at the brass-tuff interface. The top surface of the gage moved less than the adjacent tuff and, as a result, the tuff tried to slide around the upper portion of the gage. However, the brass-tuff interface was not a slide line so the radial lines had to remain connected leading to the distorted tuff zones seen in Figure 1.11. In retrospect, this problem could have been avoided in one of two ways. A slide line could have been used at the brass-tuff interface. It wasn't because for our initial calculation we wanted to do as straightforward a calculation as possible to have a basis for a future calculation using one or more slide lines.

The second thing that could have been done was to use a rezone scheme in the tuff similar to that used inside the gage. Because the tuff zones were determined initially by geometric ratios, the standard STEALTH rezoner could not have been used. However, we could have programmed into STEALTH a rezoner which would have kept straight radial lines in the tuff and maintained the geometric zoning. This scheme would also have allowed the soil to move around the gage without the complication of a slide line. This was not done because, this being our first cylindrical gage calculation, we did not anticipate this problem.

We did continue the brass/epoxy gage calculation to later problem times by converting from a fine-zoned to a coarse-zoned grid. The grid at 5.0 μsec was dezoned by removing approximately every other semicircular grid line and two out of every three radial grid lines (from 5° spacing to 15° spacing where possible). This reduced the grid from 37 by 49 lines to 14 by 25 lines. The dezoned grid is shown in Figure 3.12.

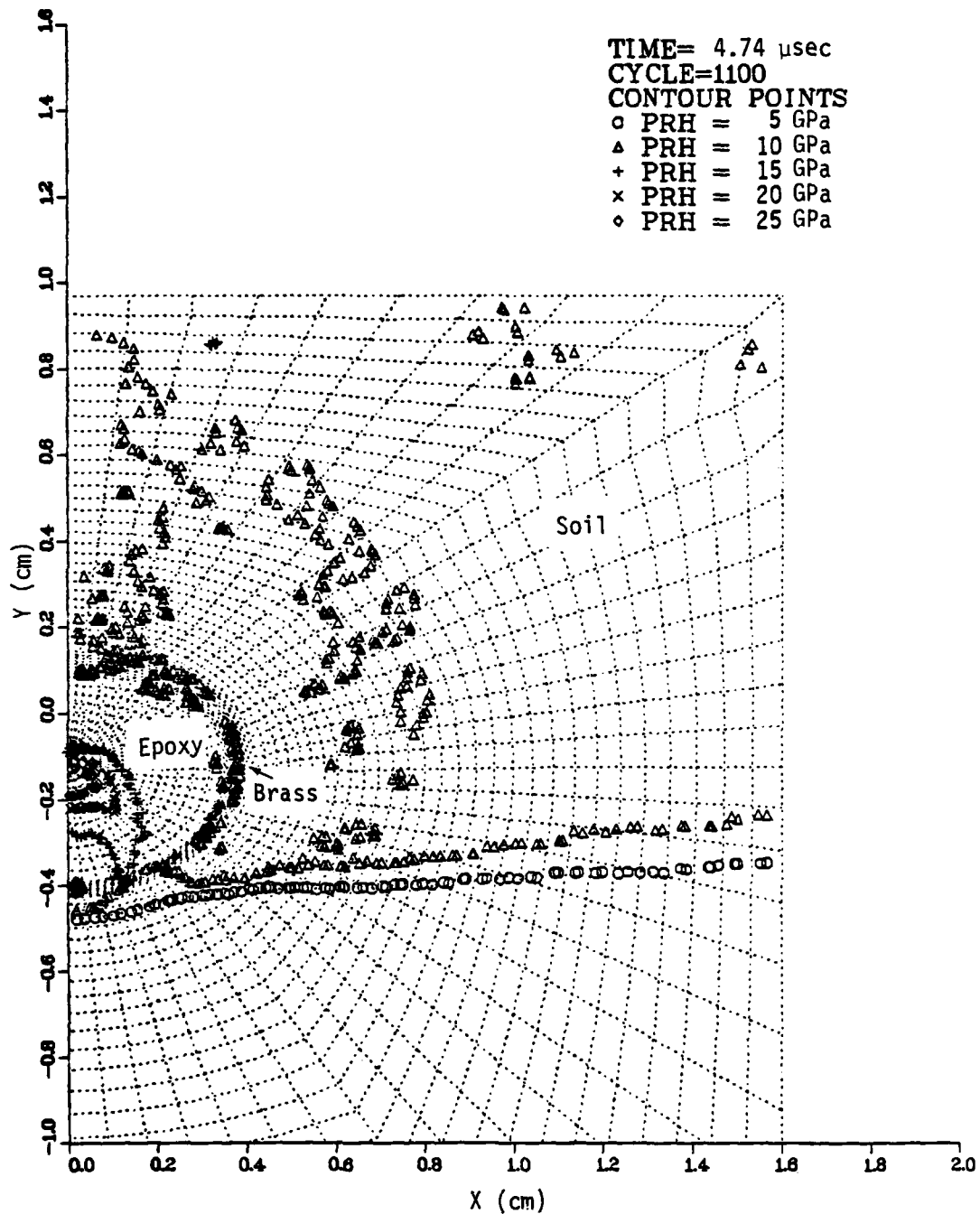


Figure 3.8. Pressure contour plot at 4.74 μ sec--brass/epoxy cylindrical gage.

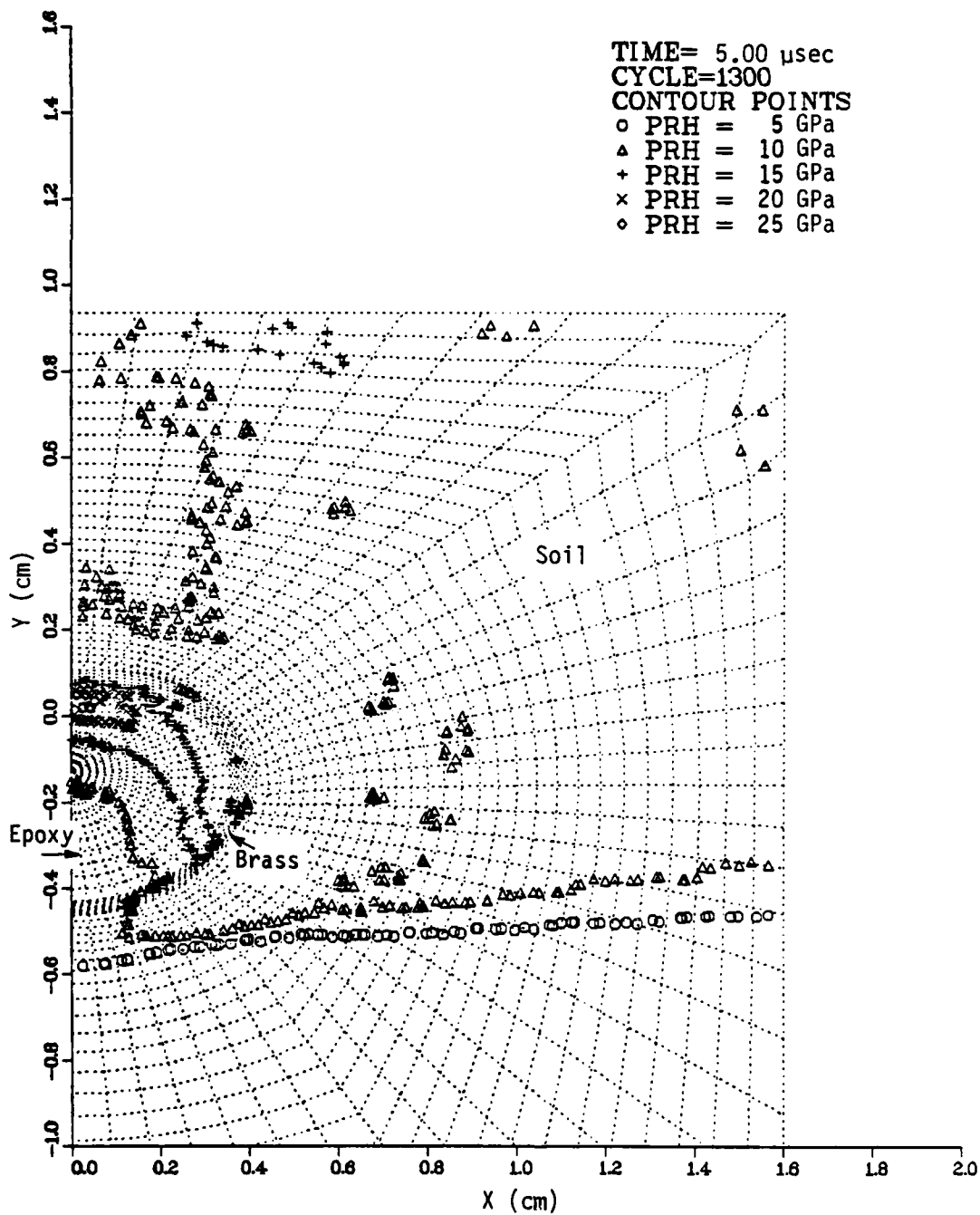


Figure 3.9. Pressure contour plot at 5.00 μ sec--brass/epoxy cylindrical gage.

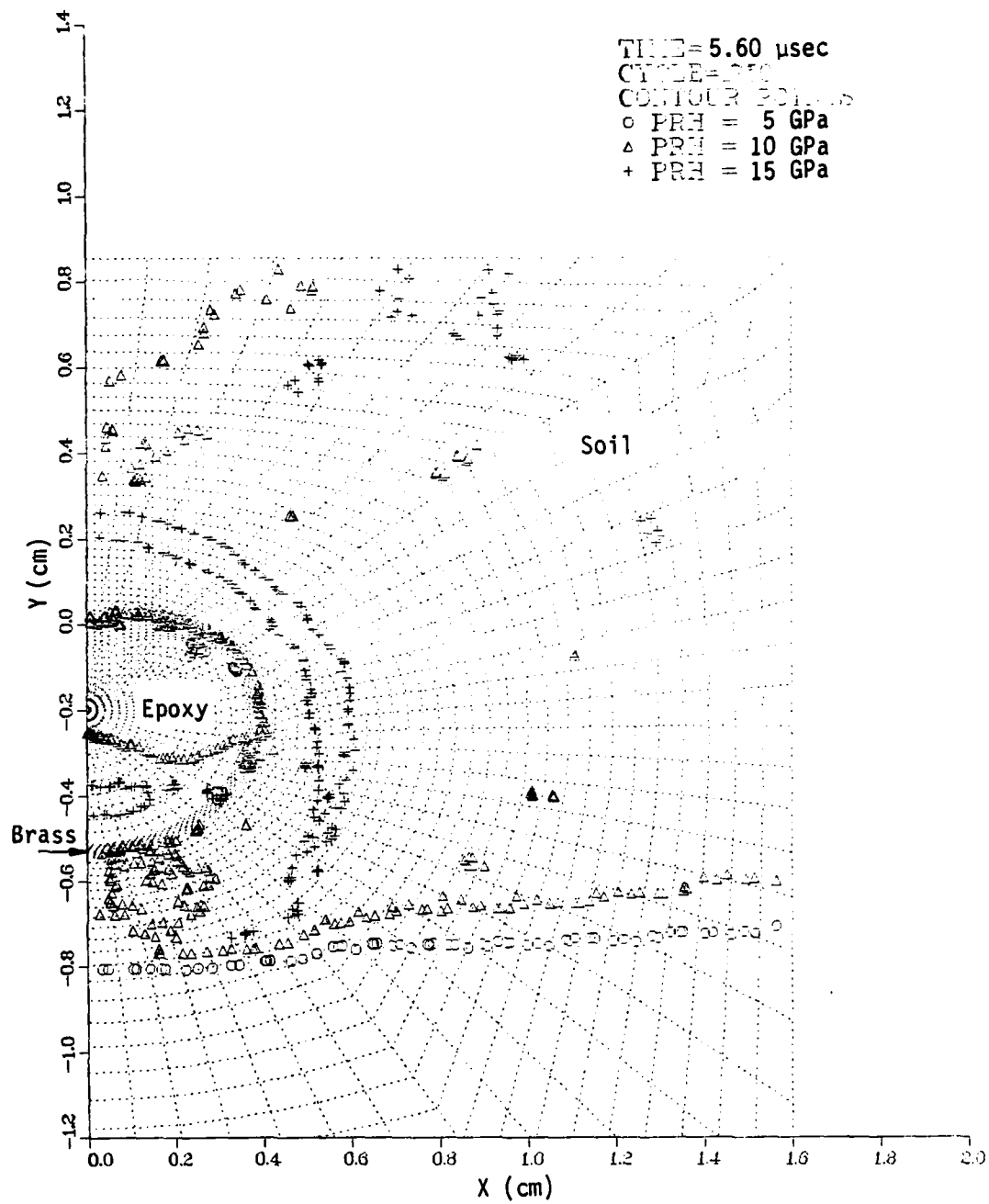


Figure 3.10. Pressure contour plot at 5.60 μ sec--brass/epoxy cylindrical gage.

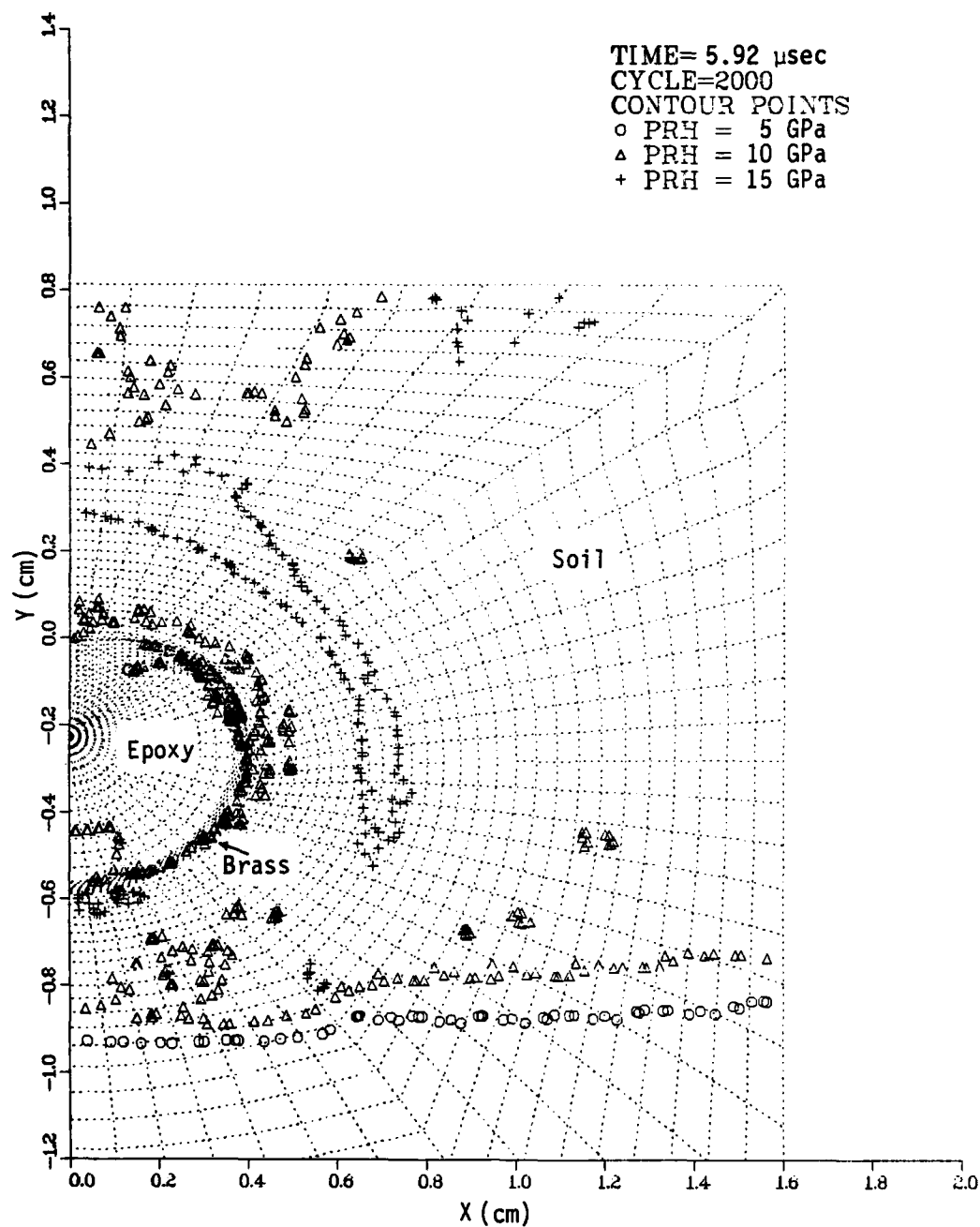


Figure 3.11. Pressure contour plot at 5.92 μ sec--
brass/epoxy cylindrical gage.

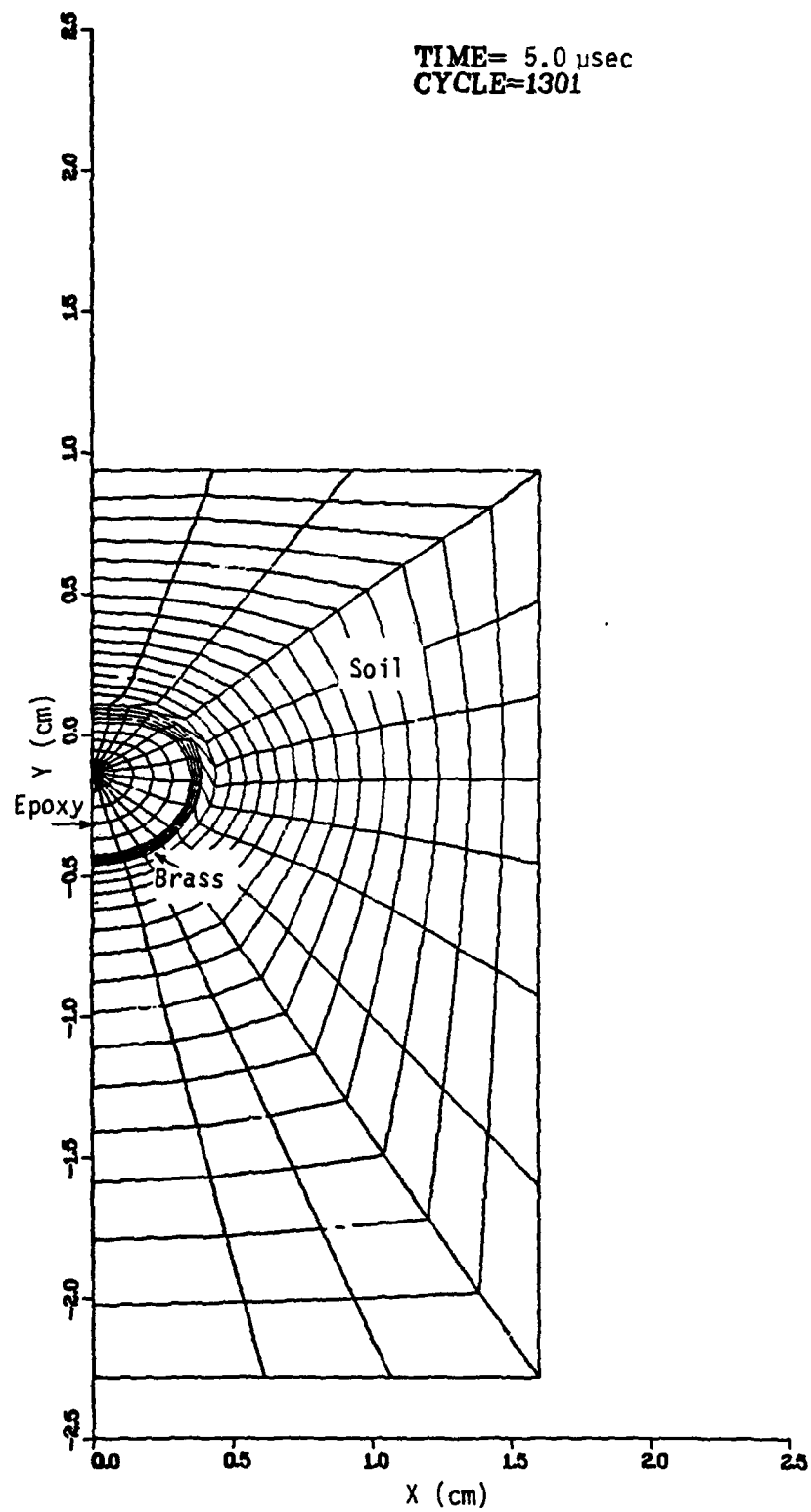


Figure 3.12. Dezoned grid at 5.0 μ sec--
brass/epoxy cylindrical gage.

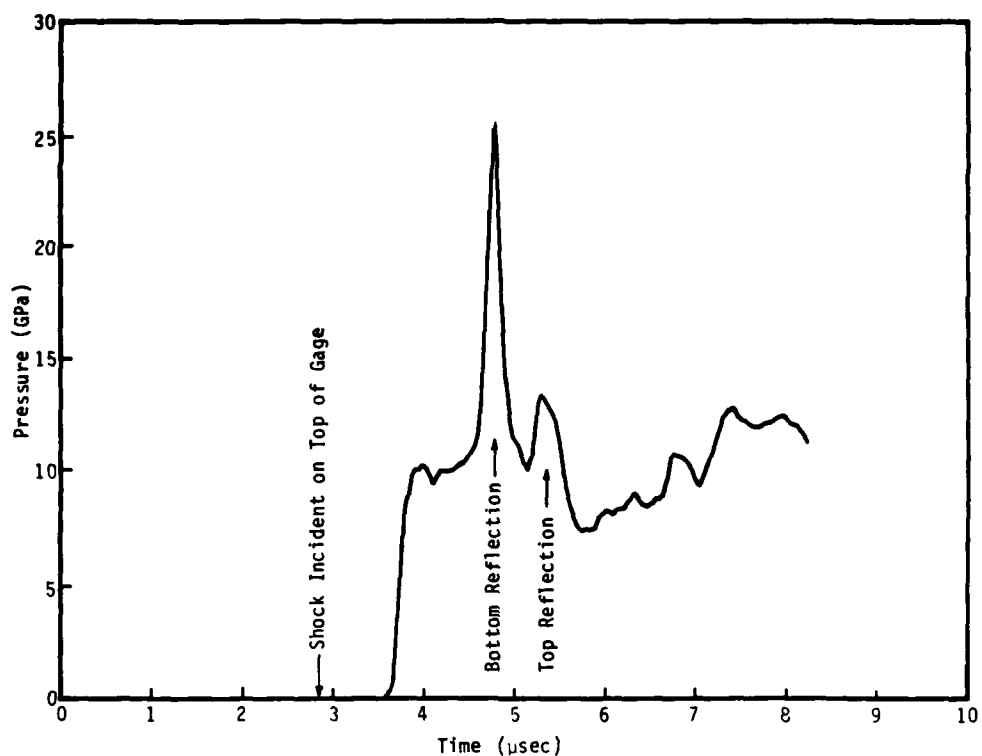
This dezoning increased the average zone size and the time step by about a factor of four. We also initiated a rezone in the first eight rows of tuff zones surrounding the brass tube. With these changes, we were able to continue the calculation to a problem time of 8.23 μsec . At this time the piezoresistive wire came in contact with the upper inner surface of the brass tube and the calculation had to be stopped.

Throughout the STEALTH calculation, the average pressure around the piezoresistive wire was edited for comparison with the experimental gage response. We also edited the wire velocity. Those results are shown in Figures 3.13a and 3.13b, respectively. These figures together with the pressure contour plots in Figures 3.6 to 3.11 give a good description of the internal gage dynamics.

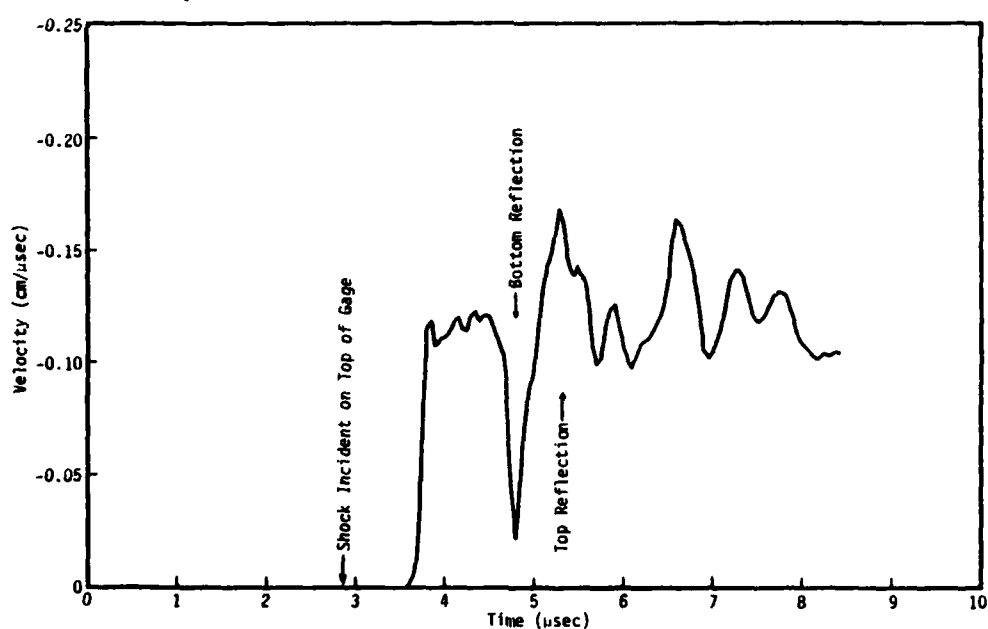
While the incident shock hits the top of the gage at 2.9 μsec , it takes an additional 0.8 μsec to reach the center of the gage. Both the wire pressure and velocity plots show the arrival of the incident pressure wave at 3.7 μsec . After a sharp rise the wire pressure is raised to the loading pressure of 10 GPa and remains at this value for nearly a microsecond. The wire velocity during this period averages -0.12 cm/ μsec , slightly slower than the boundary condition velocity of -0.133 cm/ μsec .

Then the reflected shock from the bottom of the brass tube passes over the wire raising the average pressure to a sharp peak of 25 GPa at about 4.8 μsec . The reflected shock, traveling upward, decelerates the wire to a velocity of about -0.02 cm/ μsec . Next the wire is accelerated by the shock reflection from the top of the gage to a velocity of -0.17 cm/ μsec . This secondary reflection is much weaker as indicated by the peak wire pressure of 13 GPa at 5.3 μsec . Additional reflections occurring at later times produce more oscillations in the wire velocity. However, these reflections are less apparent in the average pressure possibly because of the coarser zoning used after the grid was dezoned.

Some experimental data obtained from SRI (Ref. 3) is shown in Figure 1.10a. This is the measured response for a brass/epoxy gage under 10 GPa high-explosive loading. The computed response from Figure 3.13a is reproduced as Figure 1.10b



(a) Average pressure around piezoresistive wire



(b) Velocity of piezoresistive wire

Figure 3.13. Wire pressure and velocity--brass/epoxy cylindrical gage.

for easy comparison. Both the measured and computed response curves show the same pattern--an initial rise, a plateau, a sharp spike, then increasingly smaller oscillations at later times. The timing and ratio of the peak-to-plateau pressures are quite similar in both cases giving us confidence that the STEALTH results are a good numerical simulation of the cylindrical gage.

Both the computed and experimental initial gage response varies substantially from the incident pressure. The deviation at later times is less but contains oscillatory behavior that one would like to eliminate. These differences are caused partly by the internal dynamics of the gage and also by the effect of the gage on the surrounding soil. Looking at Figure 1.11 or Figure 3.12, one would be tempted to say the brass/epoxy gage does not move with the soil. This conclusion is only partially true because one must also consider the gage deformation.

As the incident stress becomes lower, less gage deformation will occur. In the limit, the gage moves as a rigid body and the outer shape does not change when moved downward by an incident pressure wave hitting the top of the gage (see Figures 3.14a and b). This is the case considered analytically by Mow (Reference 5) for spherical gages. Let us consider what happens to the side point of the gage (point SP in Figure 3.14). If the gage moves as a rigid body, the side point might move the same distance as a free field soil point at the same depth or it might move more or less. We could use the relative motion of these points to answer the question of whether the gage moves with the soil.

Suppose the side point moves with the soil, i.e., has the same displacement as a free field soil point (after an initial transient period). If the gage is a rigid body then all the points on the outer surface of the gage will have this same displacement (see Figure 3.15a). However, only the point SP will have the same displacement as the soil. Points on the top surface of the gage will be displaced less than corresponding free field points in the soil and those on the bottom surface will be displaced more if the gage is truly a rigid body.

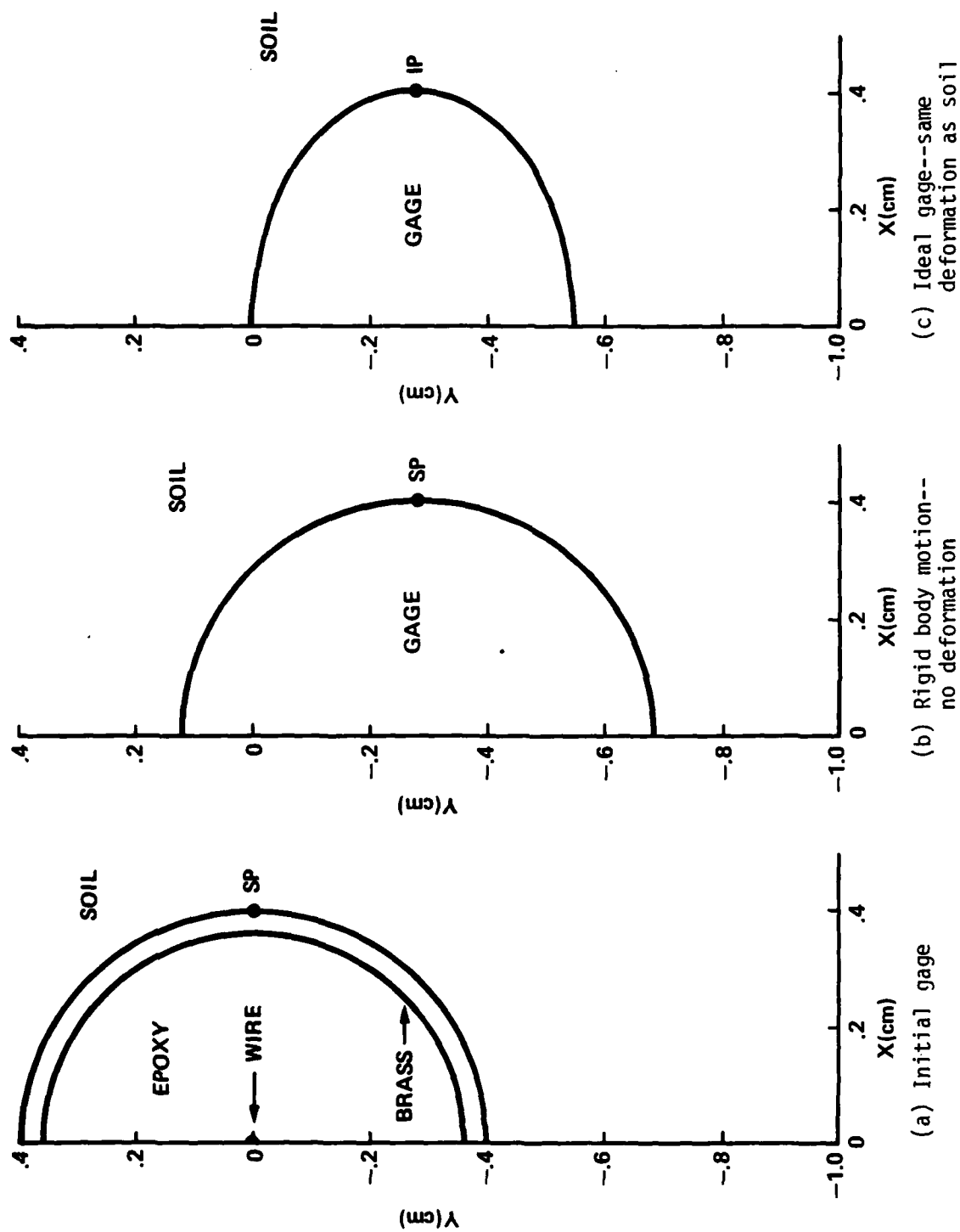


Figure 3.14. Models for cylindrical gage deformation.

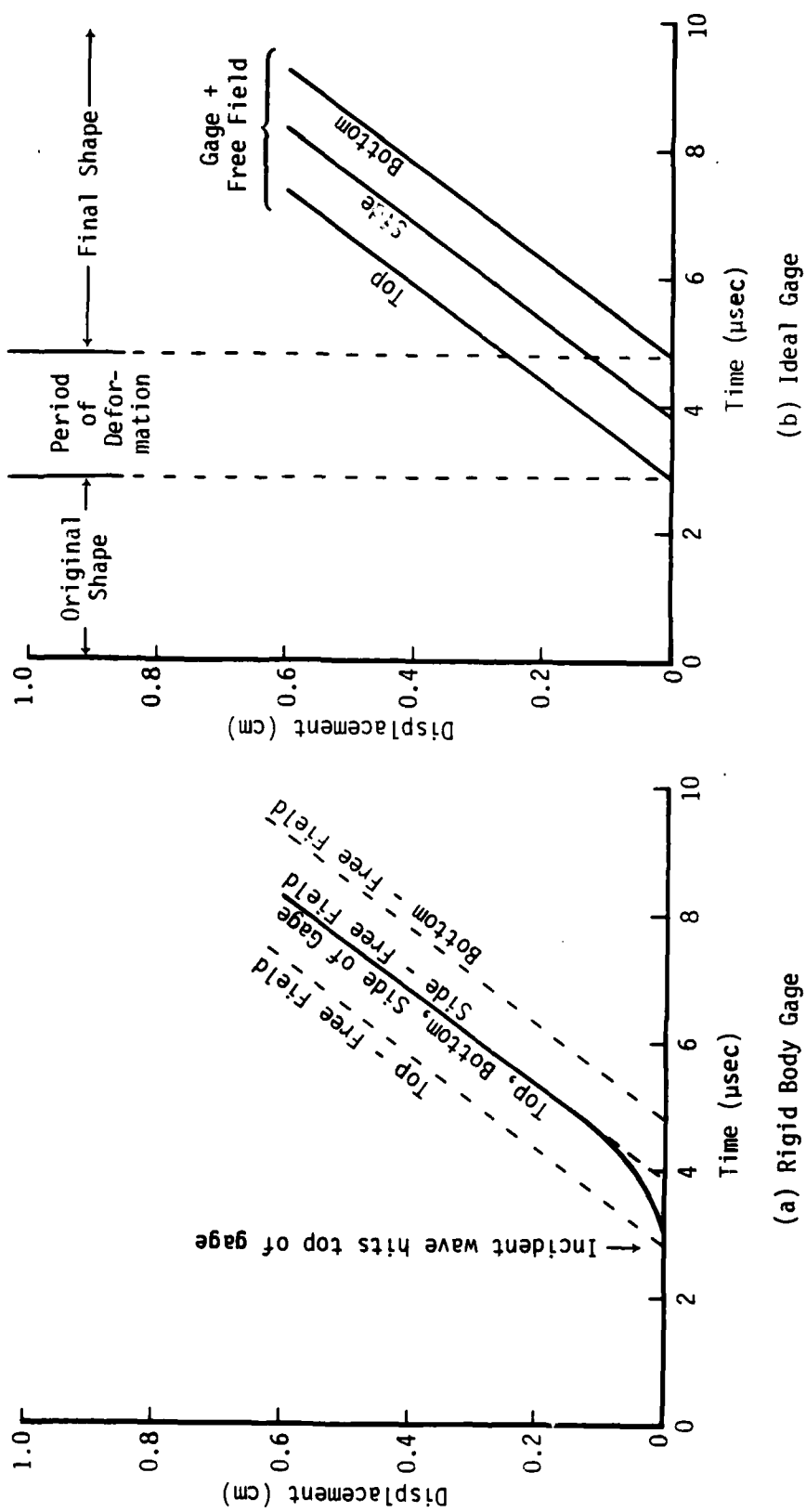


Figure 3.15. Displacement versus time for rigid body and ideal cylindrical gages.

Let us define an "ideal cylindrical gage" as one whose outer surface has the same displacement with time as corresponding free field points in the soil. Assume this gage is loaded by a constant pressure wave as in our STEALTH calculation. This gage would begin to deform when the incident wave hit the top of the gage. Deformation would continue as the wave passed over the gage but stop after the wave reached the bottom of the gage. From then on, the outer gage shape would not change as the gage moves downward with the particle velocity in the soil. The displacement for the top, side, and bottom of this gage is shown in Figure 3.15b.

With a constant soil velocity behind the shock front, the final shape for the ideal gage will be an ellipse, as shown in Figure 3.14c, with the following major and minor axes:

$$\begin{aligned} r_{\text{major}} &= R_o \\ r_{\text{minor}} &= R_o \left(1 - \frac{v_p}{v_s} \right) \end{aligned}$$

where R_o = original gage outer radius
 v_p = particle velocity in soil
 v_s = shock velocity in soil.

For the STEALTH calculation with a 10 GPa wave in tuff,

$$v_p = 0.133 \text{ cm}/\mu\text{sec}$$

$$v_s = 0.421 \text{ cm}/\mu\text{sec}$$

and $r_{\text{minor}} = 0.68 R_o$.

The deformation of the brass/epoxy cylindrical gage is shown at three times in Figure 3.16. The outer boundary of the corresponding ideal gage is shown as a dashed line for each case. At 4.74 μsec , the incident shock has just passed over the gage. The outer brass surface is still very close to the ideal shape. The displacement is the same at the top of the gage. The

AD-A147 486

HYDRODYNAMICS CALCULATIONS FOR MINI JADE GAGES(U)
SCIENCE APPLICATIONS INC LA JOLLA CA R N SCHLAUG
29 JUL 83 SAI-001-83-506-LJ DNA-TR-81-300

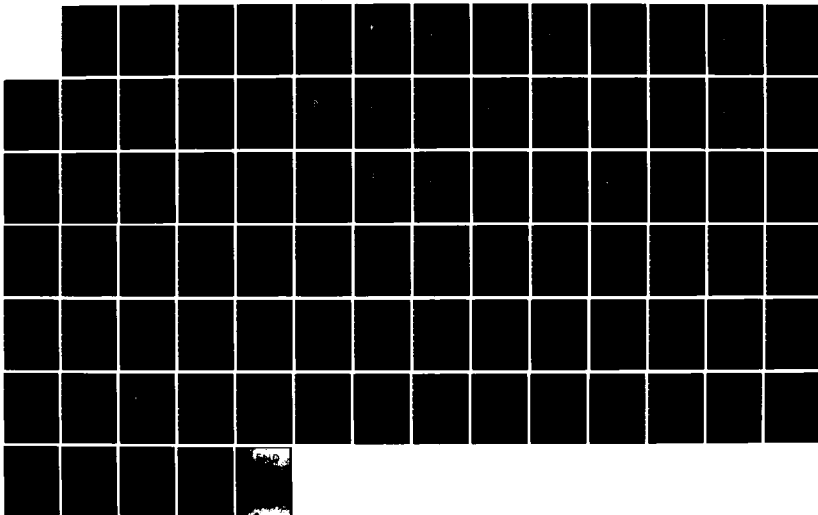
2/2

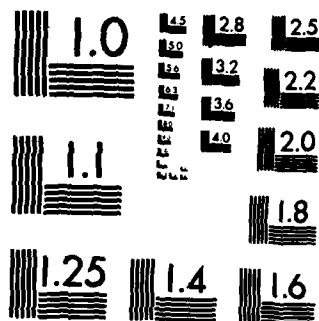
UNCLASSIFIED

DNA001-81-C-0167

F/G 18/3

NL





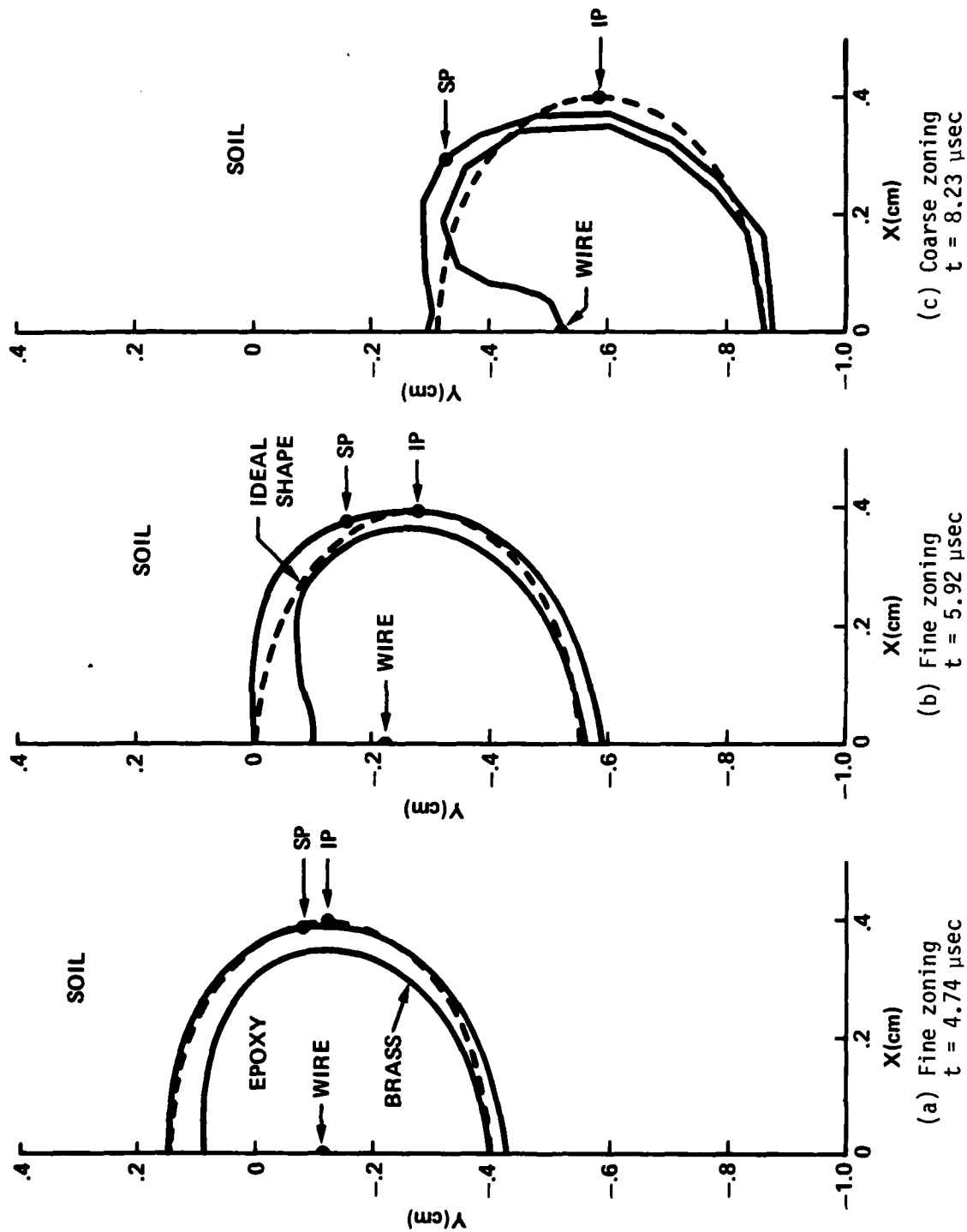


Figure 3.16. Deformation of brass/epoxy cylindrical gage.

bottom of the real gage has moved ahead because of the faster shock speed in the epoxy (see Figure 3.7). The side point SP has moved less than the ideal side point IP and has also moved slightly inward. The brass tube also has become thicker at the top.

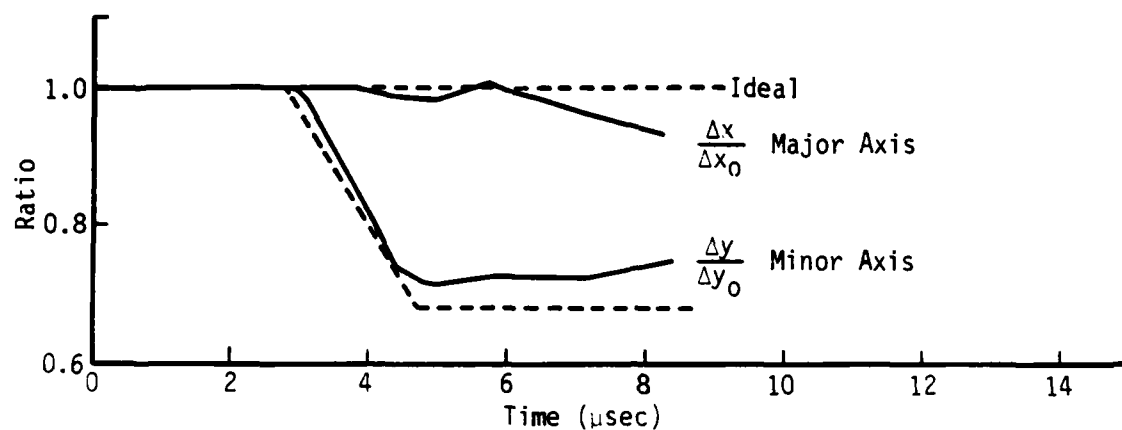
At 5.92 μ sec, the end of the fine-zoned calculation, the gage has deformed further. The gage is not elliptical but heart-shaped, bulging out in the upper quadrant. On axis, the displacement is about ideal at the top of the gage but too large at the bottom. The side point SP has slipped further behind IP which is the reason for the zone distortion at the brass/tuff interface shown in Figure 1.11. The tube is becoming still thicker at the top of the gage and thinner at the bottom (0.093 cm at the top and 0.027 cm at the bottom, compared to the original 0.04 cm).

The gage shape at 8.23 μ sec, the end of the coarse-zoned extension of the STEALTH calculation, is also shown in Figure 3.16. The deformation has continued further in the same manner. The brass tube has become very thick at the top, so thick that the tube came in contact with the center wire. The overall displacement is still, however, very close to that of an ideal gage.

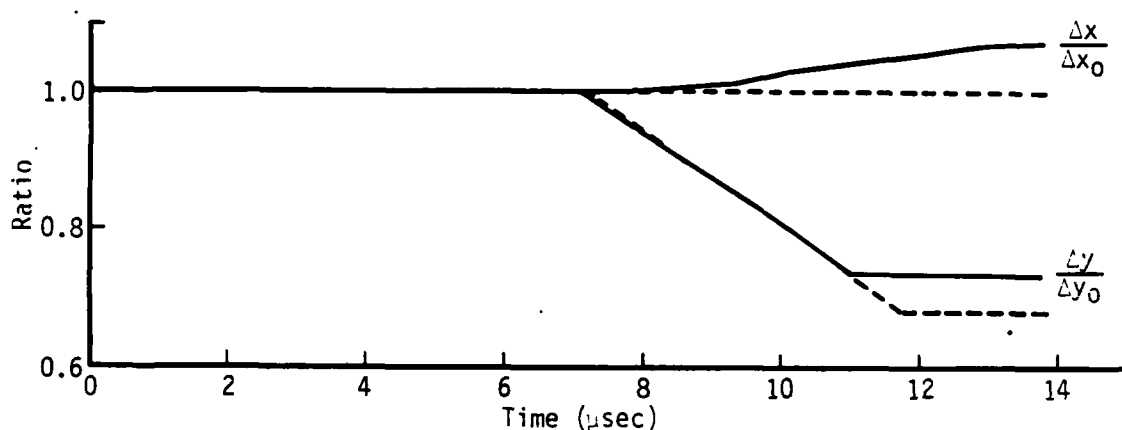
The gage deformation with time is summarized in Figure 3.17a. The major and minor axes divided by the original gage radius are compared with the corresponding values for the ideal gage. The major axis initially contracts slightly, then expands to about the ideal value and finally goes into a contraction phase that continues to the end of the calculation. The minor axis exhibits near-ideal behavior contracting to $0.71 R_0$ at 5.0 μ sec compared to the ideal $0.68 R_0$. The minor axis then expands slowly to $0.75 R_0$ at the end of the calculation.

3-2 MG/TEFLON GAGE

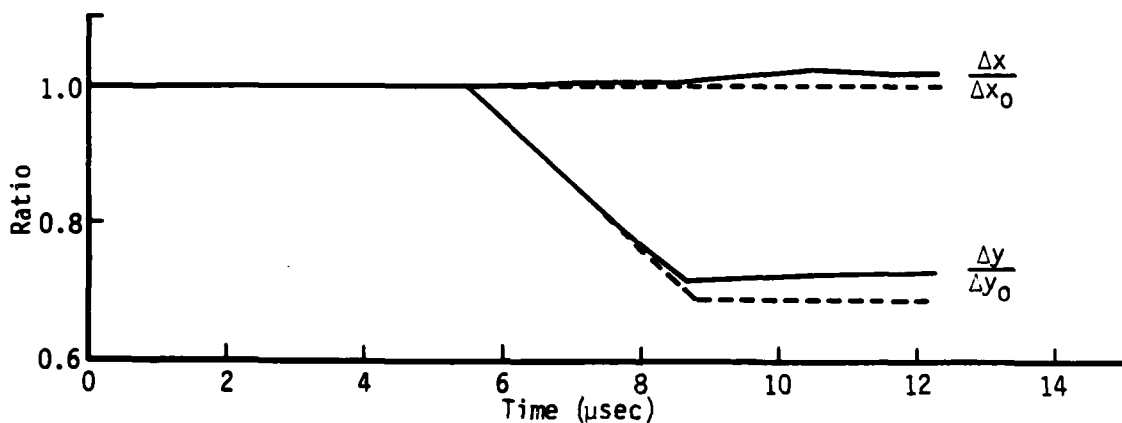
After reviewing the experimental and computational results for the brass/epoxy gage, SRI designed a new cylindrical gage in which the brass tube was replaced by a magnesium tube and the epoxy insulator was replaced by Teflon. The dimensions for the Mg/Teflon gage are given in Figure 1.9b. The



(a) Brass/Epoxy Gage



(b) Mg/Teflon Gage



(c) Al/Teflon Gage

Figure 3.17. Change in gage major and minor axes versus time.

larger size and increased wall thickness resulted primarily from the need to fabricate the magnesium tube by drilling out a magnesium rod.

The initial grid for the STEALTH calculation is shown in Figure 3.18. An expanded view of the gage region is shown in Figure 3.19. As in the previous calculation, the grid represents a planar cross section through the soil and the gage, which is centered at $X=0$ and $Y=0$. The darkened semicircles denote the inner and outer boundaries of the Mg tubing. The material inside the tubing is Teflon; the remainder of the grid is tuff. The piezoresistive wire is represented by a rigid body boundary condition at the center of the gage which is moved according to the algorithm described in the Appendix.

The grid zoning is listed in Table 3.1. This zoning is similar to that used for the brass/epoxy gage but significantly coarser. The radial lines are now spaced 7.5° apart. Four fewer semicircular lines are used in the gage and five fewer in the tuff. The use of fewer zones, combined with the larger gage diameter and outer grid dimensions, increases the average zone size significantly. This larger zoning was used in an attempt to increase the average time step and hopefully reduce zone distortion. This allowed us to run to a longer problem time in less calendar time and obtain a longer calculated response to compare with the experimental data.

The STEALTH calculation was run 1500 cycles to a problem time of $13.73 \mu\text{sec}$. As in the previous calculation, a velocity boundary condition was used at the top of the grid (see Figure 3.18) to generate a 10.5 GPa shock wave that moves downward at $0.42 \text{ cm}/\mu\text{sec}$. Because of the larger distance involved, it takes $7.25 \mu\text{sec}$ for this wave to reach the top of the gage. A pressure contour plot of the grid just before the wave hits the gage is shown in Figure 3.20.

The pressure contours at $9.41 \mu\text{sec}$ are shown in Figure 3.21. At this time, the wave is just past the center of the gage. The shock continues to move downward through the gage and reaches the bottom of the gage at $10.96 \mu\text{sec}$ (see Figure 3.22). The shock is well past the gage by $11.91 \mu\text{sec}$

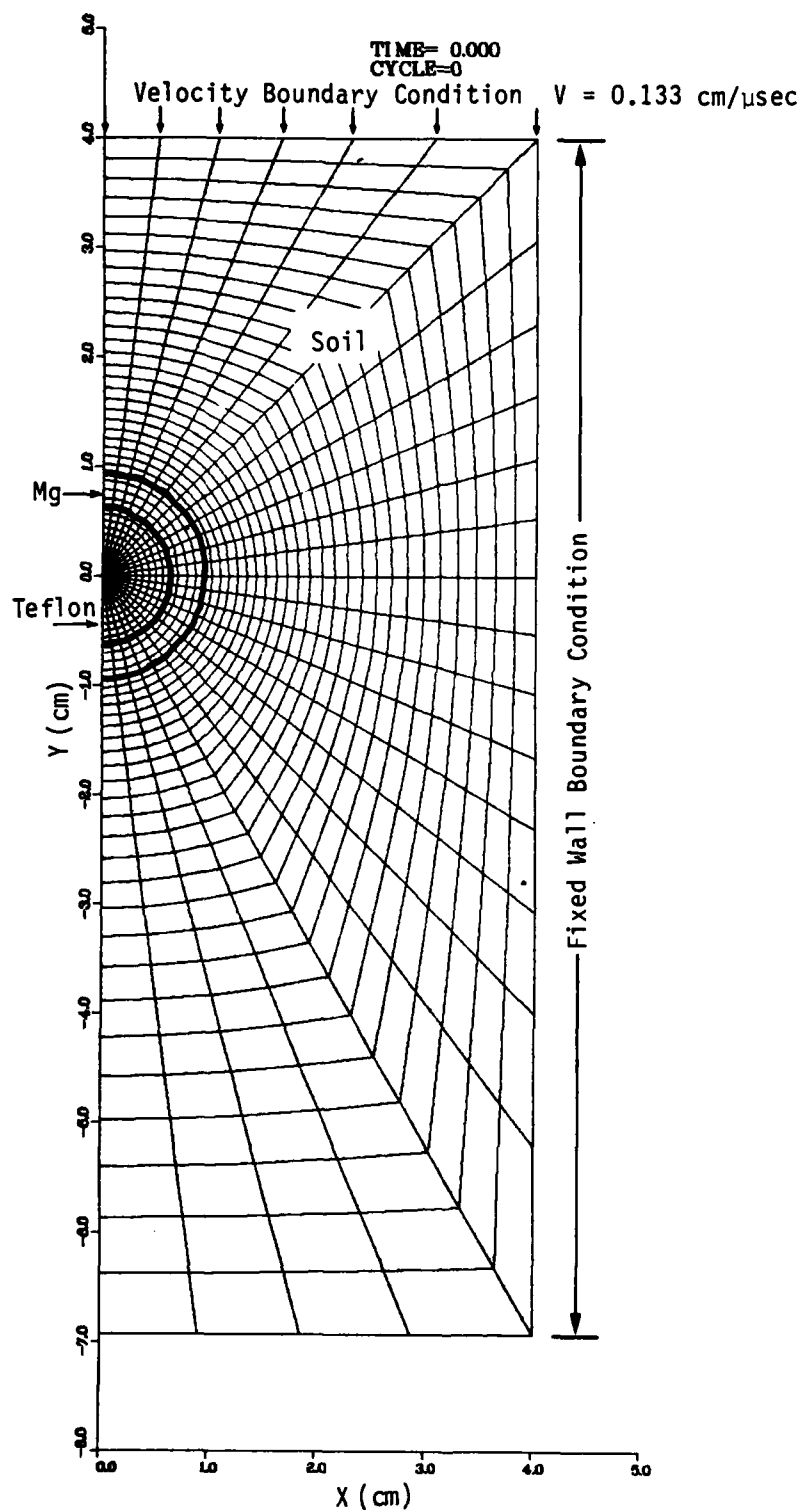


Figure 3.18. Initial grid for the Mg/Teflon cylindrical gage.

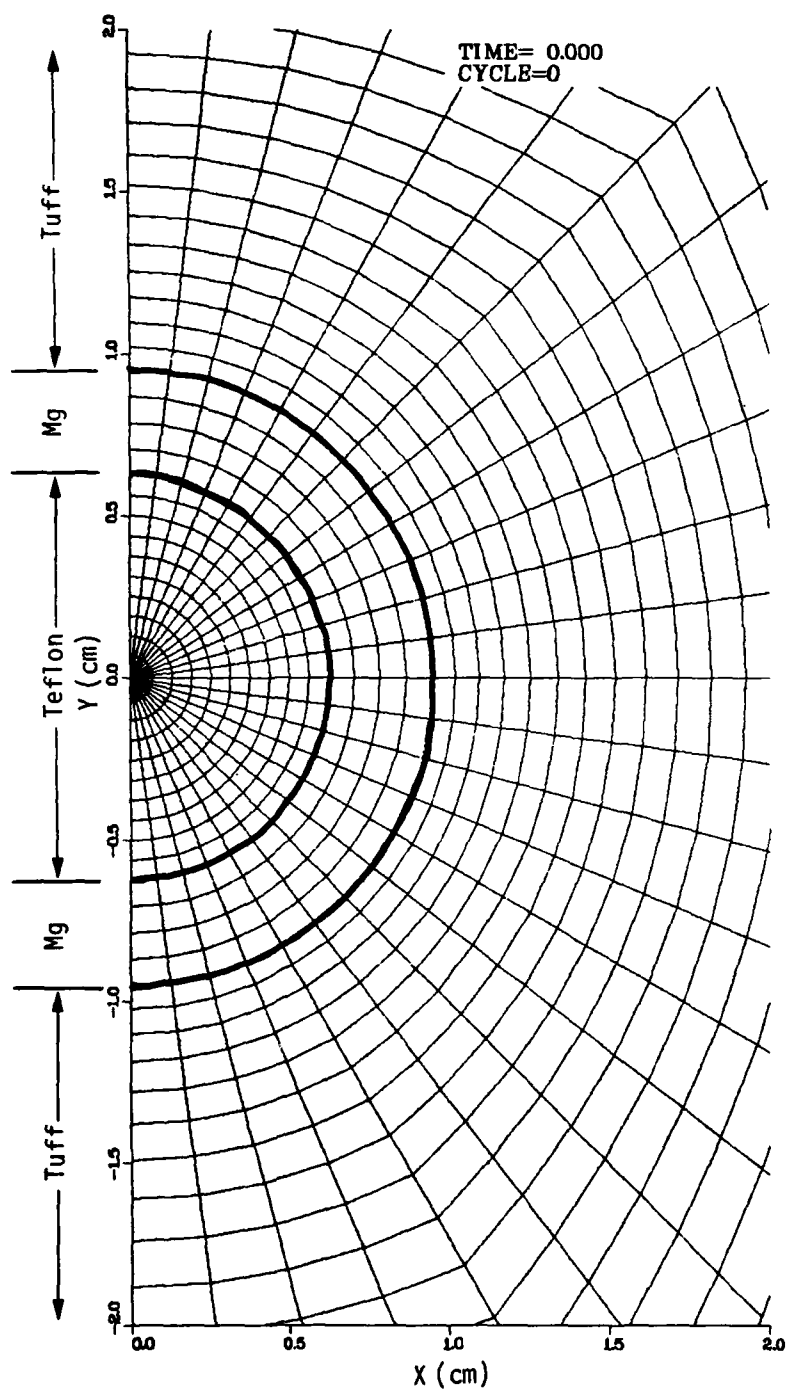


Figure 3.19. Initial zoning of gage region--Mg/Teflon cylindrical gage.

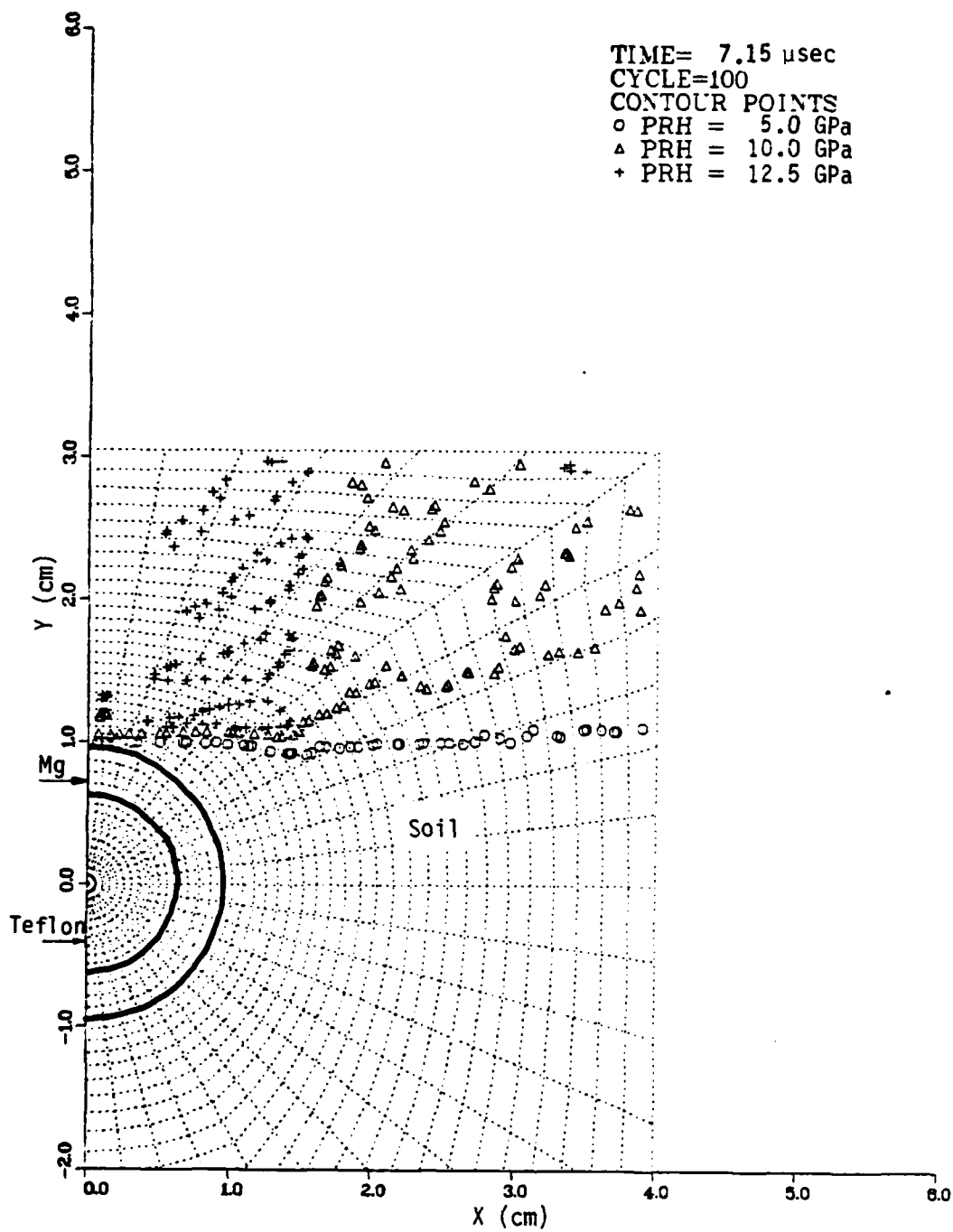


Figure 3.20. Pressure contour plot at 7.15 μ sec--
 Mg/Teflon cylindrical gage.

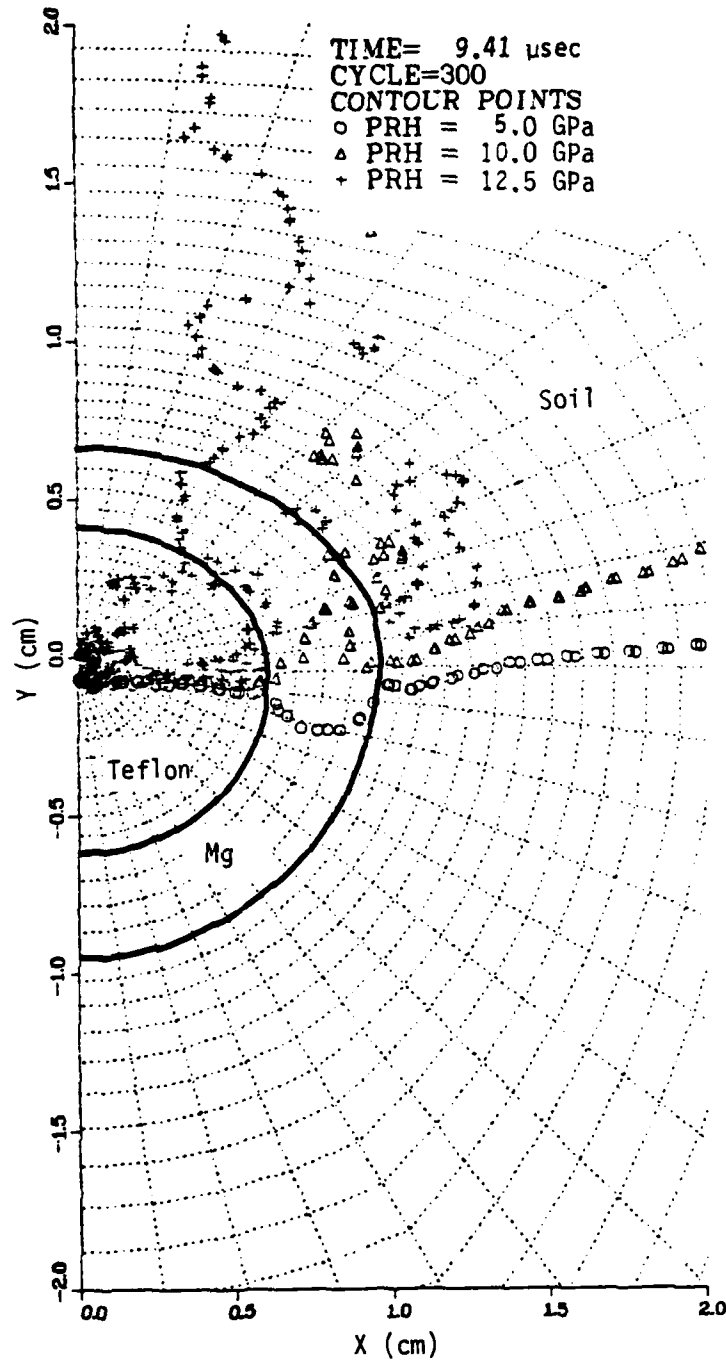


Figure 3.21. Pressure contour plot at 9.41 μ sec--
 Mg/Teflon cylindrical gage.

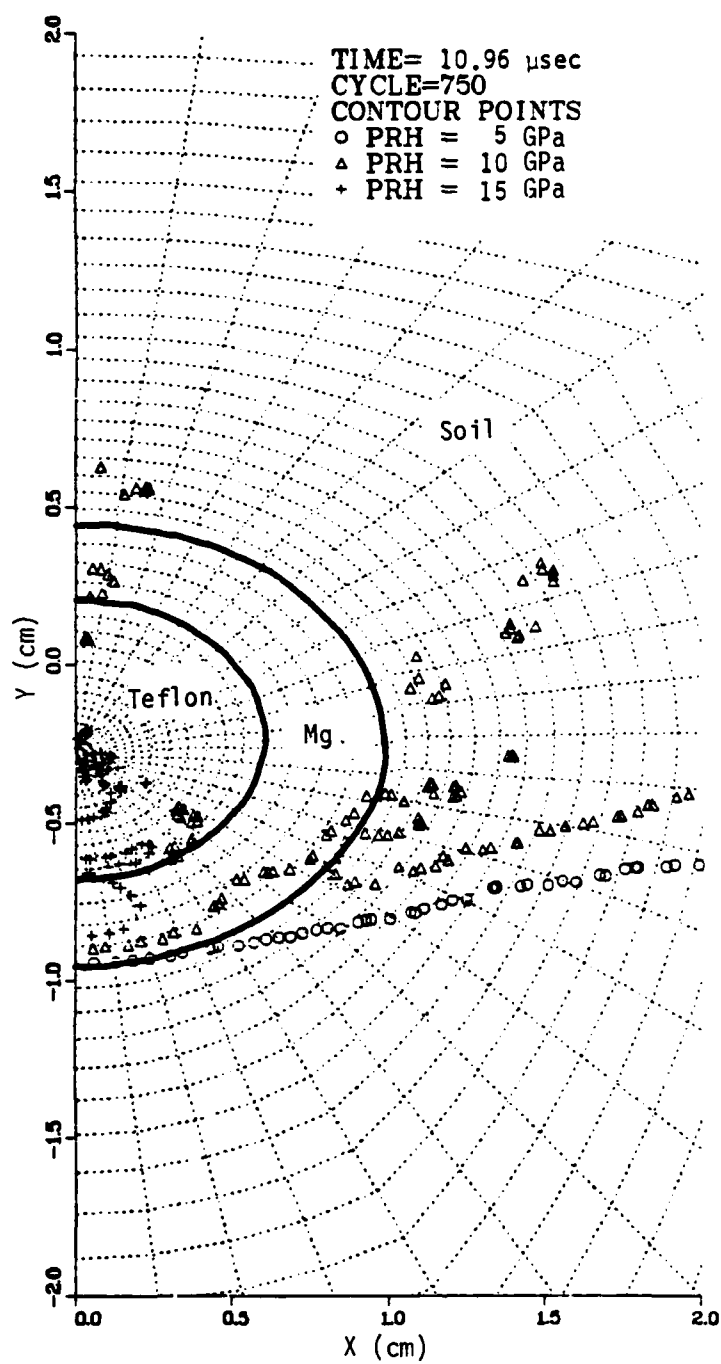


Figure 3.22. Pressure contour plot at 10.96 μ sec--
 Mg/Teflon cylindrical gage.

as shown in Figure 3.23. It continues moving downward in the grid until the end of the calculation at 13.73 μ sec. A grid plot of the gage region at this time is shown in Figure 3.24.

In general, these plots show the Mg/Teflon gage is much less of a perturbation in the soil than the brass/epoxy gage. There is no strong early time reflection from the top of the gage and no late time diffraction wave. Even the reflected shock from the bottom of the gage (shown in Figure 3.22) is considerably weaker reaching only about 16 GPa. The distortion in the tuff zones at the Mg/tuff interface in Figure 3.24 indicates that the outer surface of the gage is moving slightly faster than the adjacent soil.

The average pressure around the piezoresistive wire and the average wire velocity throughout the calculation are shown in Figures 3.25a and 3.25b, respectively. While the incident shock reaches the top of the gage at about 7.2 μ sec, it is nearly 2 μ sec later before pressures are seen around the center wire. The average wire pressure begins to rise sharply at about 9.2 μ sec and reaches a peak of 17.5 GPa at 9.8 μ sec. The pressure then falls to about 12.5 GPa at 10.5 μ sec before rising to a second peak of 16.5 GPa at a time of 11.1 μ sec. This peak is the reflection of the incident wave from the Teflon/magnesium interface at the bottom of the gage. Following arrival of the reflected shock, the pressures fall to the 10 GPa level and oscillate about that value to the end of the calculation. The large oscillations in the 9.5 to 10.5 μ sec time period are at least partly the result of the coarse zoning in this problem. Without these oscillations, the peak pressure in this time period would probably have been on the order of 14 to 15 GPa.

The wire velocity, shown in Figure 3.25b, shows similar oscillations slightly earlier in time. We feel these fluctuations are related to the larger zones around the wire in this calculation compared to the brass/epoxy calculation. With the algorithm we are using, pressures in the zones at the top of the wire accelerate the wire downward until counterpressures build up in the zones at the bottom of the wire. The larger these zones are, the longer the time it takes for them to be compressed. This time delay leads to an overshoot with higher pressures than there should be in the bottom zones.

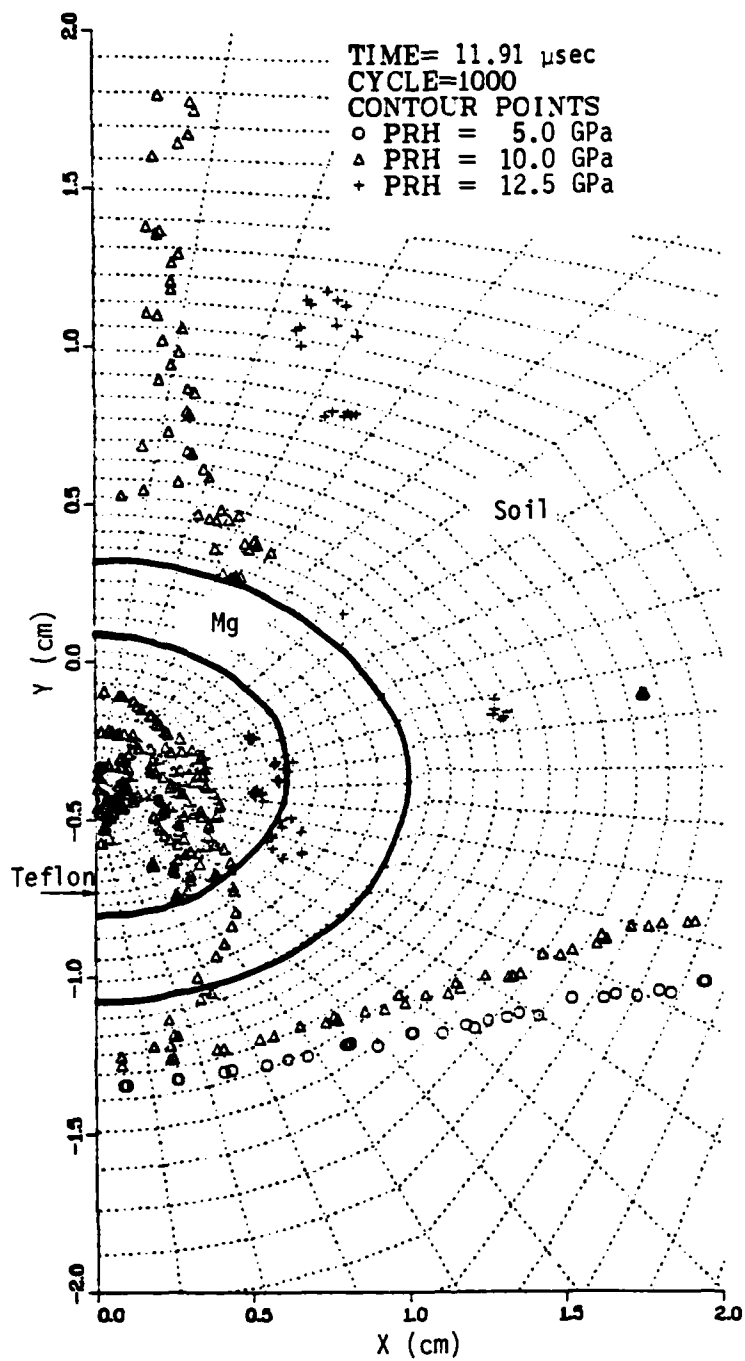


Figure 3.23. Pressure contour plot at 11.19 μ sec--
 Mg/Teflon cylindrical gage.

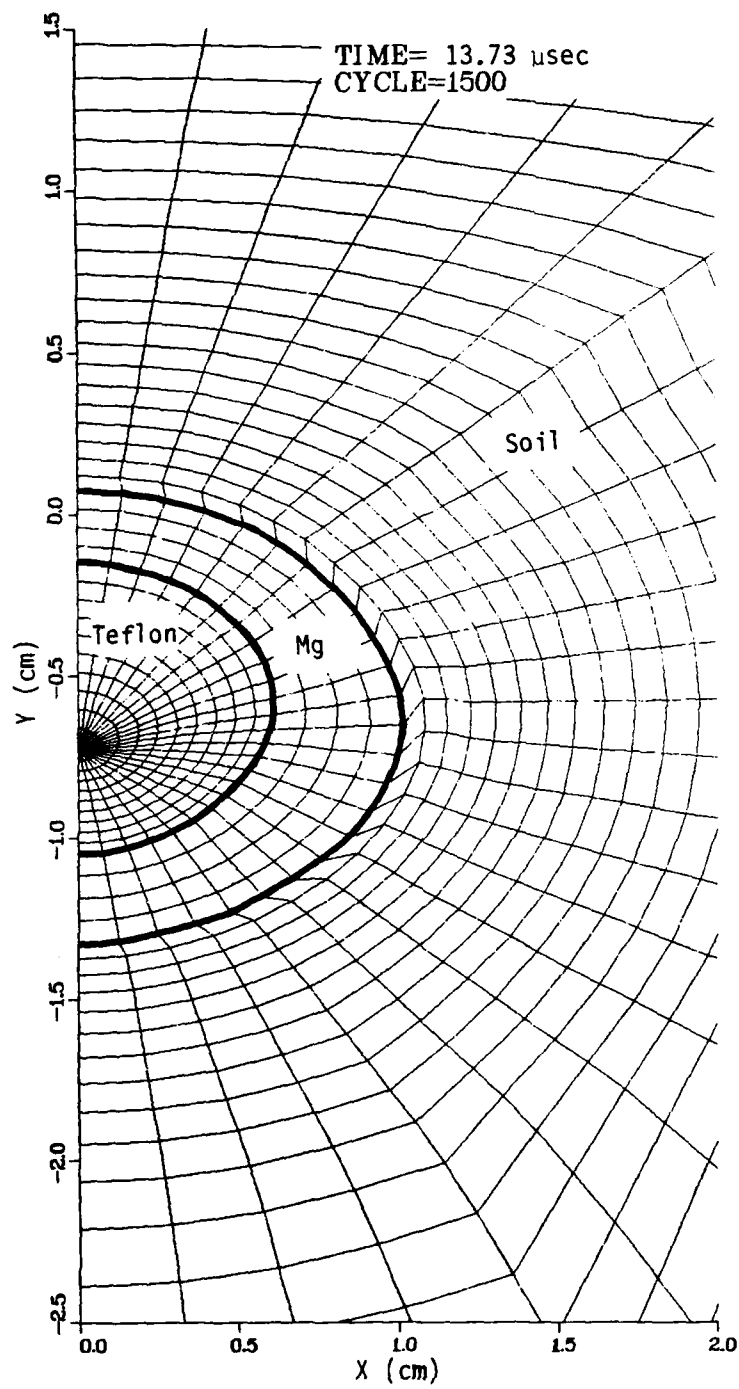
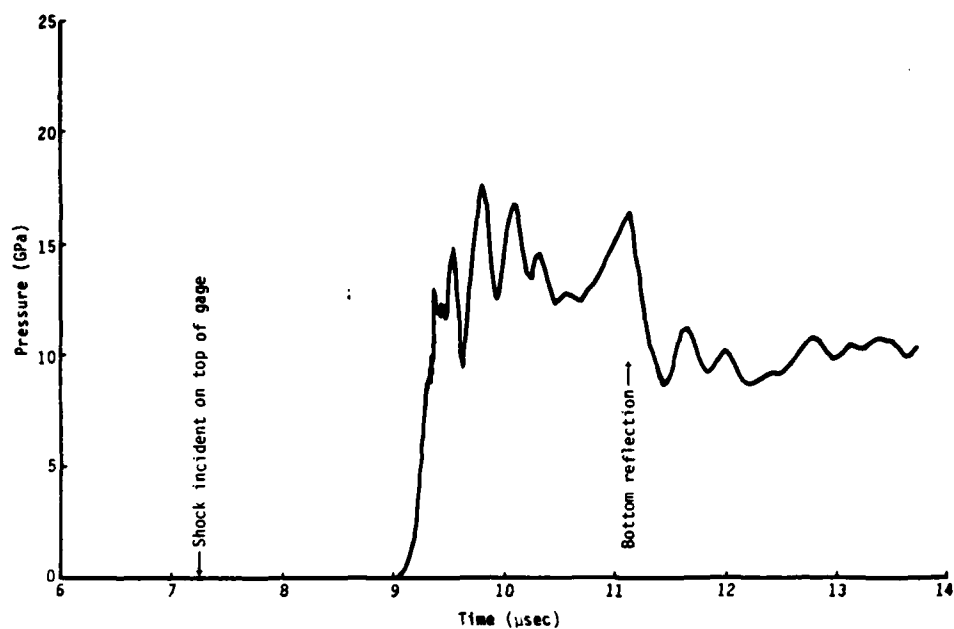
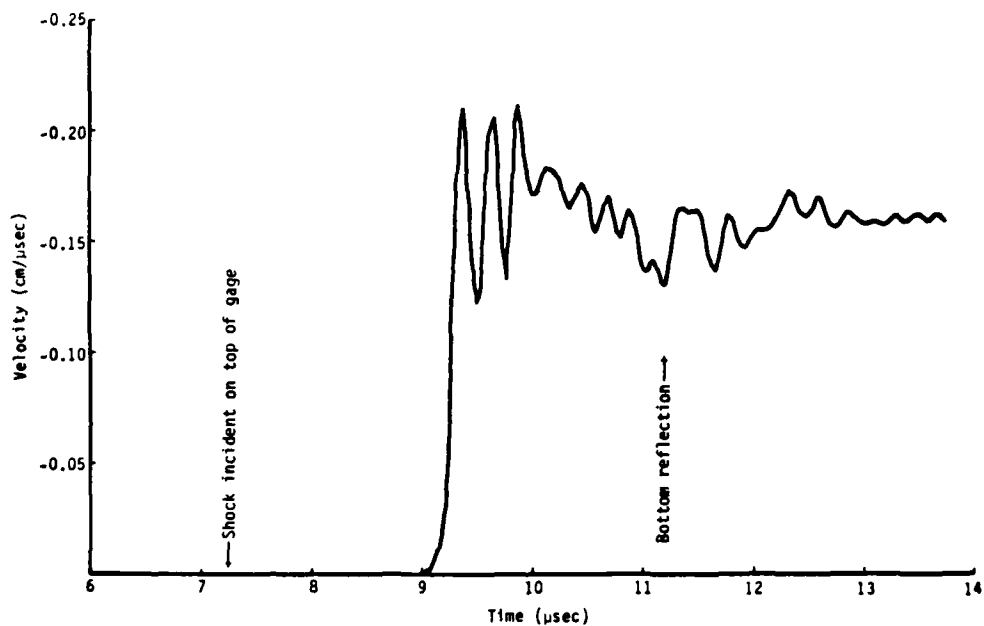


Figure 3.24. Grid plot of gage region at 13.73 μ sec--
Mg/Teflon cylindrical gage.



(a) Average pressure around piezoresistive wire



(b) Velocity of piezoresistive wire

Figure 3.25. Wire pressure and velocity--Mg/Teflon cylindrical gage.

Then the condition of high pressures at the top of the wire and low pressures at the bottom changes to low pressures at the top and high pressures at the bottom. It takes a few cycles of this behavior before enough damping occurs to reduce the oscillations. They become much smaller as the calculation progresses but are never entirely eliminated. A modification made to the wire motion algorithm for later calculations would not have significantly reduced the pressure oscillations if it had been used for this gage (see the Appendix).

The deformation of the Mg/Teflon gage is much closer to the postulated deformation of the ideal cylindrical gage than was the case for the brass/epoxy gage. The deformation process is shown in Figure 3.26 which gives the initial gage shape, the shape at 10.96 μsec when the shock reached the bottom of the gage, and the shape at 13.73 μsec , the end of the STEALTH calculation. The dashed line represents the outer boundary of the ideal gage.

We see that the deformed Mg/Teflon gage is very nearly elliptical in shape as would be an ideal gage. The change in the major and minor axes with time is shown in Figure 3.17b. The minor axis contracts along the path predicted for the ideal gage to $0.74 R_0$ at 11 μsec and remains at about this value to the end of the calculation. While the minor axis did not reach the predicted $0.68 R_0$, deformation did stop when the shock wave reached the bottom of the gage. What happened was that the shock was transmitted more quickly through the gage than in the surrounding soil. The major axis exhibits somewhat nonideal behavior, growing slowly with time to $1.07 R_0$ at the end of the calculation.

Returning to Figure 3.26, we can see how these differences change the gage shape from the ideal shape. At 10.96 μsec , the top of the gage has moved with the soil. The side point SP has moved slightly more than the ideal side point IP. The bottom of the gage is just beginning to move but in the ideal case this would not occur until about 11.8 μsec . At the end of the calculation, we have a very similar situation. The top of the gage has moved with the soil. The side point is still ahead and has moved noticeably outward. The bottom of the gage is now clearly ahead of its ideal position. Even so, the shape at 13.73 μsec is very close to that at 10.96 μsec .

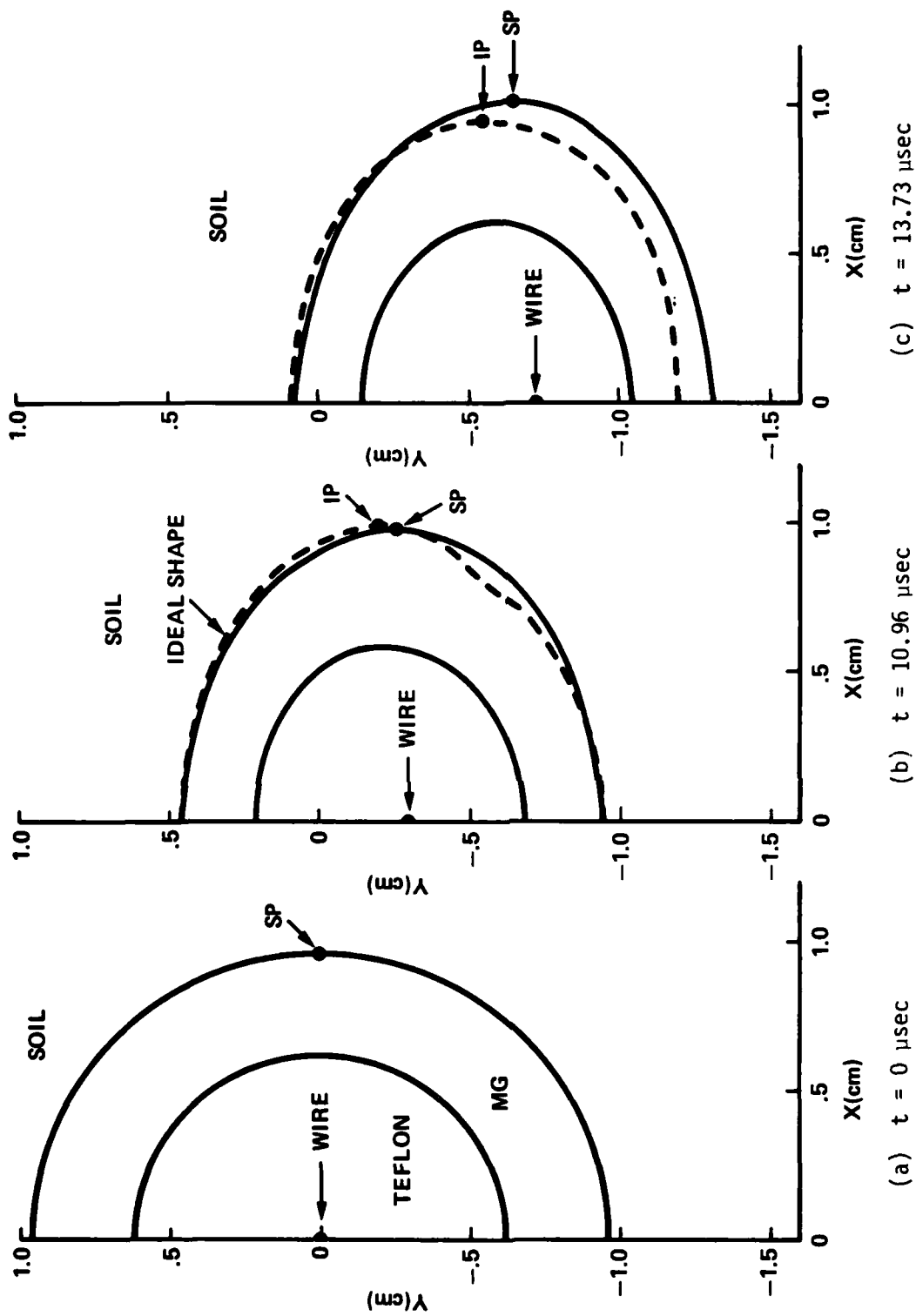


Figure 3.26. Deformation of Mg/Teflon cylindrical gage.

Looking inside the gage, we find the Teflon has been compressed about 30 percent to an average density of 3.04 g/cm^3 . With the Teflon equation of state used in the calculation, a 30-percent compression is about what one should get for a 10 GPa shock. The higher pressures near 15 GPa seen around 10 μsec occur because the compression is higher during the period the shock front is moving through the gage. For example, at 9.41 μsec (see Figure 3.21), about half the Teflon is in its original state and half has been compressed. The Teflon behind the shock has an average density about 3.25 g/cm^3 which corresponds to a Hugoniot pressure of 14 GPa, about what was seen around the center wire.

The calculated velocity of the piezoresistive wire is shown in Figure 3.25b. It is significantly faster than the particle velocity in the soil, averaging about $-0.16 \text{ cm}/\mu\text{sec}$. This is the opposite case than for the brass/epoxy gage for which the wire was found to move more slowly ($-0.11 \text{ cm}/\mu\text{sec}$) than the soil. However, it appears that it would be at least 7 to 10 more μsec before the piezoresistive wire would come into contact with the magnesium tubing and cause gage failure. The modified wire motion algorithm used in later calculations would probably have given an average velocity 10 to 20 percent lower than shown in Figure 3.25b (see the Appendix).

Several Mg/Teflon gages were tested by SRI in December 1981 (Reference 4) using HE-generated pressure waves at the 10- and 17-GPa levels. The measured response of these gages differed substantially from the response (Figure 3.25a) predicted by the STEALTH calculation. In particular, the large reflection spike was mitigated but other features were present in the response curve which were difficult to interpret. At the higher stress level there was also some temporary shorting of the electrical signal through the Teflon to the magnesium tube. It is not known whether the shorting occurred from the center manganin wire or from the copper lead wires that are attached to the manganin and are closer to the metallic tube.

While the Mg/Teflon cylindrical gage was considered an improvement over the brass/epoxy gage, it presented a fabrication problem. Magnesium tubing can be made either by drilling rod stock in the laboratory or commercially by the extrusion process. The former is time-consuming and usually

results in tubing with a variable nonuniform wall thickness. The extruded tubing must be special-ordered at high cost and with at least a three-month lead time. For this reason, the possibility of using a different material than magnesium was considered.

3-3 AL/TEFLON GAGE

The next cylindrical gage design considered was similar to the Mg/Teflon gage but used thin-walled aluminum tubing in place of the magnesium tubing. The dimensions for the Al/Teflon gage are given in Figure 1.9c. The use of the Al tubing reduced the gage OD to 1.42 cm compared to 1.90 cm for the Mg/Teflon design.

The initial grid for the Al/Teflon gage calculation is shown in Figure 3.27 with an expanded view of the gage region given in Figure 3.28. The region inside the tubing contains Teflon; the region outside is tuff. The grid zoning is listed in Table 3.1. This grid is less coarsely zoned than the grid used in the Mg/Teflon calculation. It has the same number of grid points (1000) but the outer dimensions are smaller because the Al/Teflon gage is smaller. We made the Teflon zoning finer by using 12 semicircular lines, instead of 10. Two less lines were used to describe the Al tubing because of its smaller wall thickness. The radial lines were spaced every 7.5° as in the Mg/Teflon calculation. Also as before, the piezoresistive wire at the center of the gage was included as a rigid body boundary condition.

The STEALTH calculation was run 1750 cycles to a problem time of 12.25 μsec . We used the same velocity boundary condition at the top of the grid as in the previous cylindrical gage problems. This boundary condition generates a downward-moving 10.5 GPa pressure wave that takes about 5.4 μsec to reach the top of the gage (see Figure 3.29). The wave reaches the center of the gage at 7.2 μsec as shown in the pressure contour plot at this time (Figure 3.30). The shock wave continues to move downward reaching the bottom of the gage at about 8.6 μsec as shown in Figure 3.31. This plot also shows the reflected shock that originates at the Al/Teflon interface at the bottom of the gage. It is quite strong at this time (over 20 GPa) but the peak

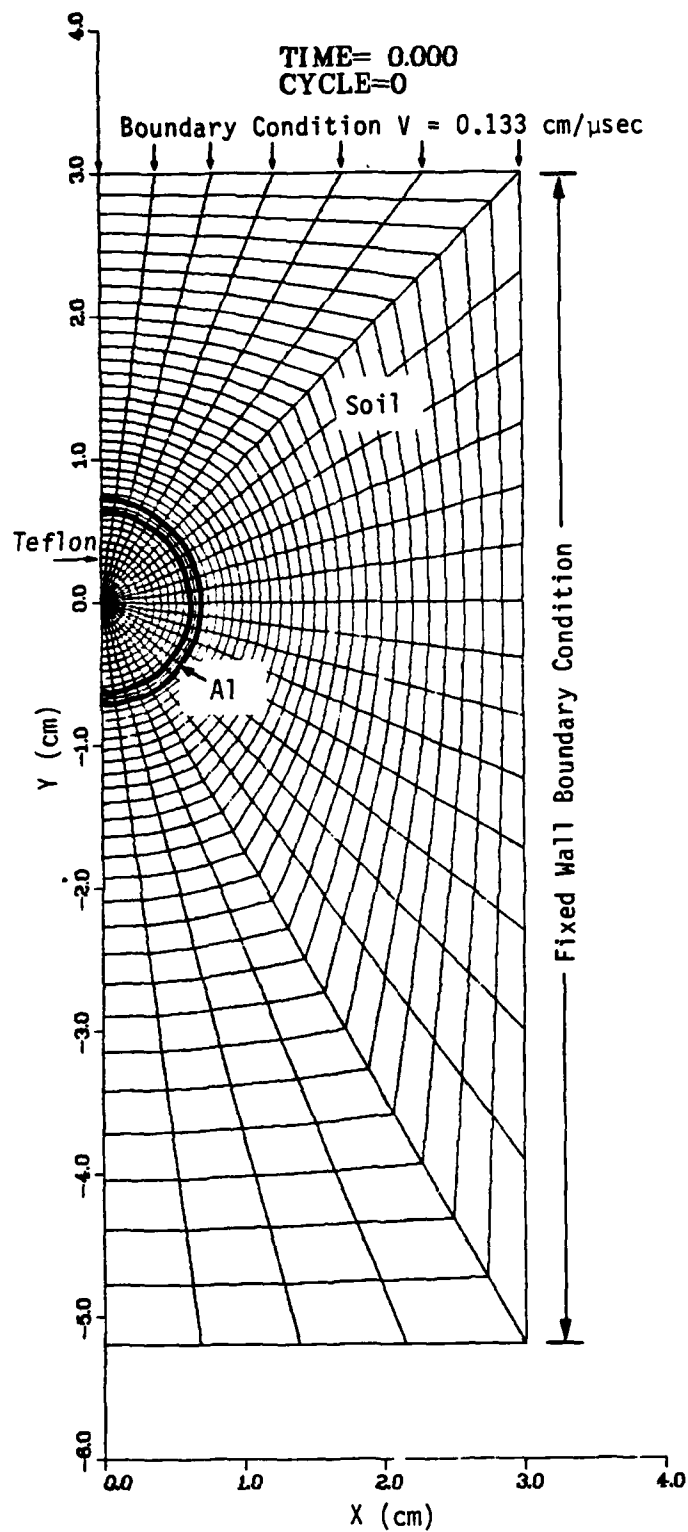


Figure 3.27. Initial grid for the Al/Teflon cylindrical gage.

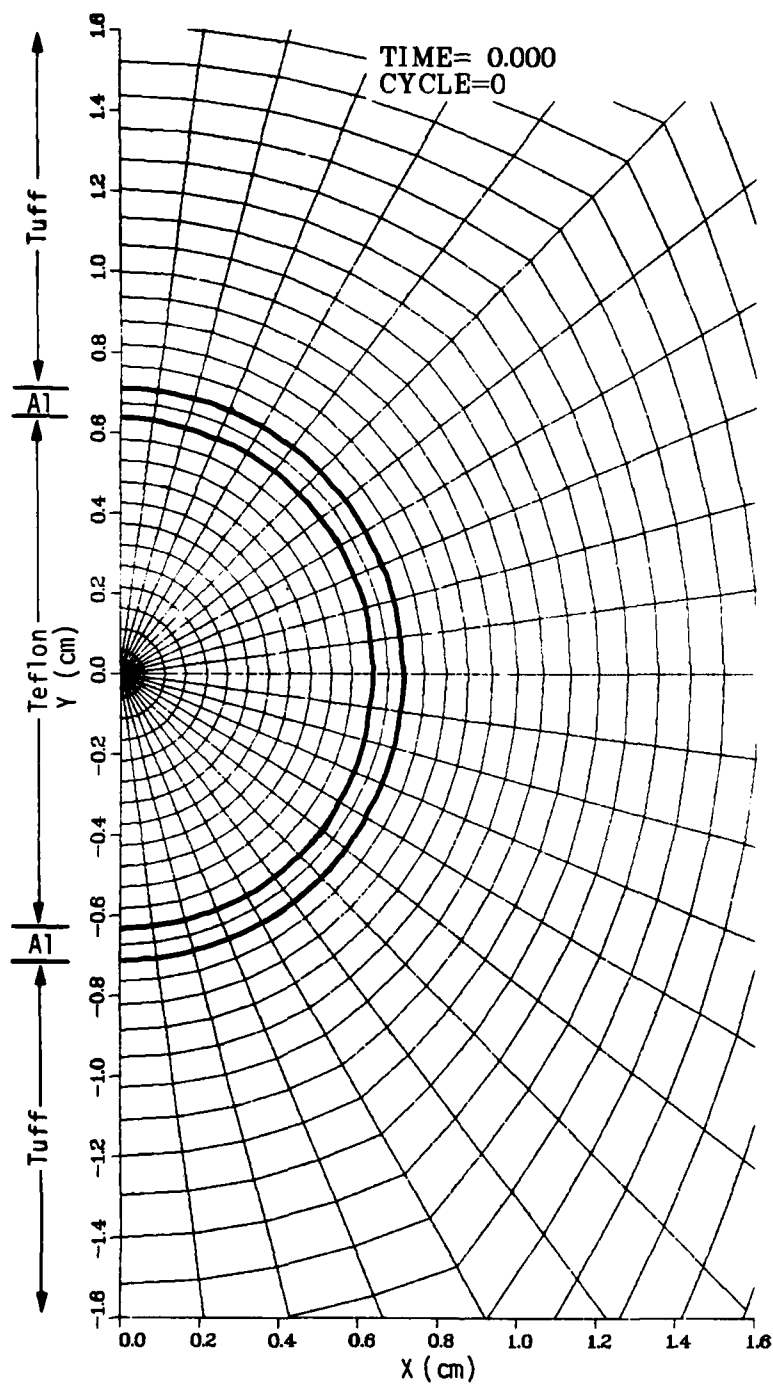


Figure 3.28. Initial zoning of gage region--Al/Teflon cylindrical gage.

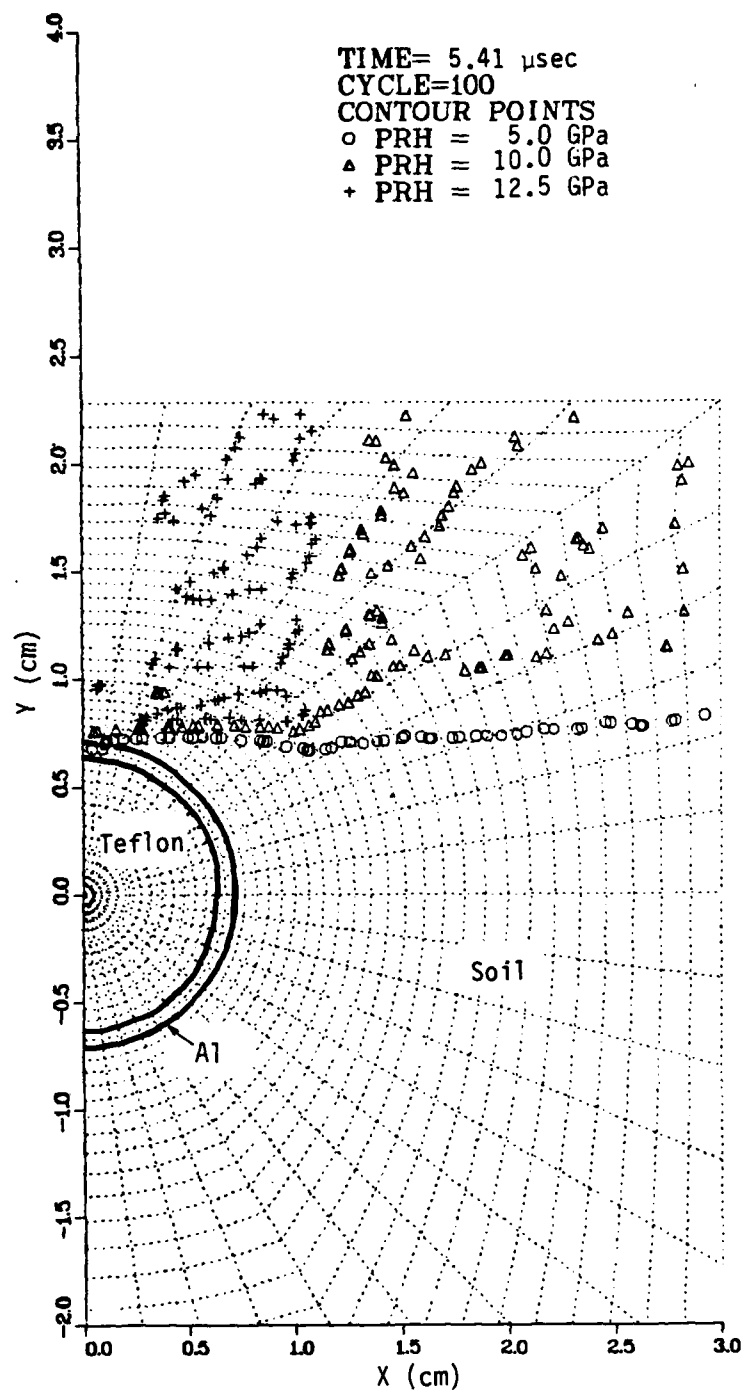


Figure 3.29. Pressure contour plot at 5.41 μ sec--
Al/Teflon cylindrical gage.

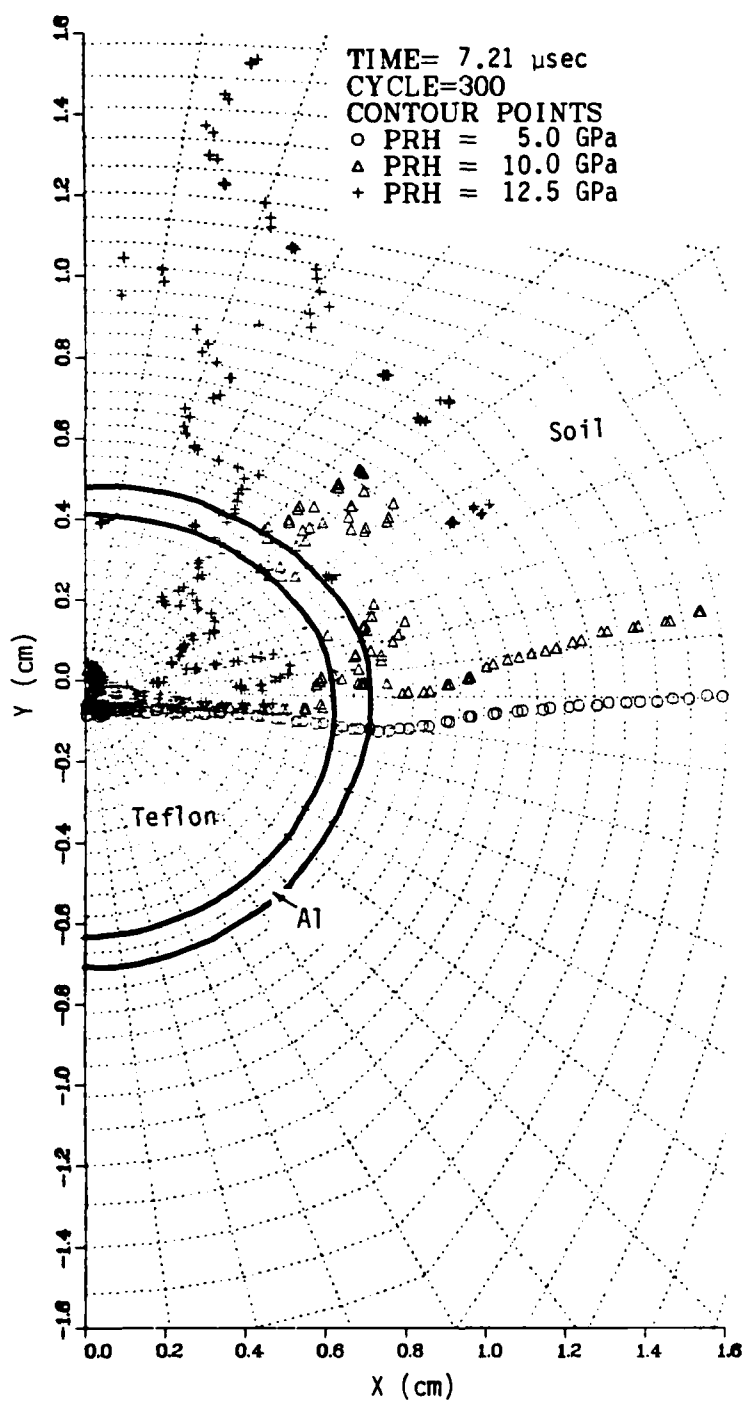


Figure 3.30. Pressure contour plot at 7.21 μ sec--
Al/Teflon cylindrical gage.

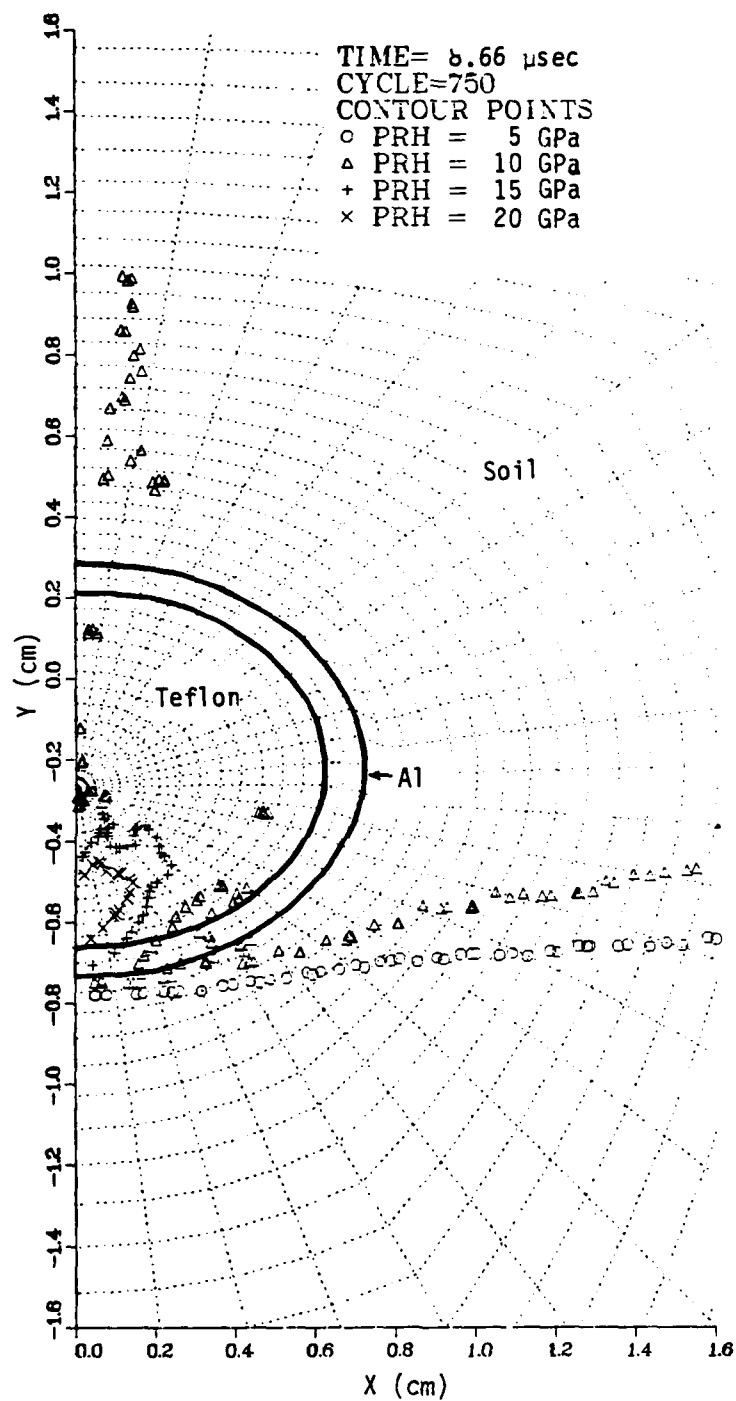


Figure 3.31. Pressure contour plot at 8.66 μ sec--
Al/Teflon cylindrical gage.

pressure diminishes as the shock expands upward into the Teflon. It is only 14 GPa just before hitting the upper portion of the Al tubing as shown in the contour plot at 9.55 μ sec (Figure 3.32).

This calculation was continued to a problem time of 12.25 μ sec. At this time the stress wave is well beyond the bottom of the gage (see Figure 3.33). A grid plot of the gage region at the end of the calculation is shown in Figure 3.34. As in the Mg/Teflon gage, the piezoresistive wire has drifted toward the bottom of the gage. We also see from the twisted grid lines just outside the Al tubing that the top of the gage is moving somewhat slower than the surrounding soil. (The grid lines in the Teflon and aluminum are kept straight by the STEALTH rezone subroutine but no rezone is done in the soil.) In contrast, the top of the Mg/Teflon gage moved slightly faster than the soil (see Figure 3.24).

In general, the Al/Teflon gage responds to the incident loading quite similarly to the Mg/Teflon gage. Comparing the contour plots for the Mg/Teflon gage shown in Figures 3.20 to 3.23 with those for the Al/Teflon gage (Figures 3.29 to 3.32) shows no qualitative differences. For both of these gages, there is no strong reflection from the top surface and no late time diffraction wave as seen for the brass/epoxy gage (Figures 3.6 to 3.11).

The average pressure around the piezoresistive wire and the average wire velocity as a function of time are shown in Figures 3.35a and 3.35b, respectively. While the pressure wave hits the top of the gage at about 5.5 μ sec (see Figure 3.29), it is nearly 1.5 μ sec later before a signal is seen at the center wire. The average wire pressure begins to rise sharply at about 7.0 μ sec and reaches a peak around 18 GPa at 7.5 μ sec. The average pressure then falls to about 12 GPa and maintains this level until 8.8 μ sec when the reflected shock arrives. This shock peaks at nearly 20 GPa at 9.0 μ sec and is followed by a decline to about 7 GPa at 9.5 μ sec. The average wire pressure then rises to the 10 GPa level and oscillates about that value to the end of the calculation.

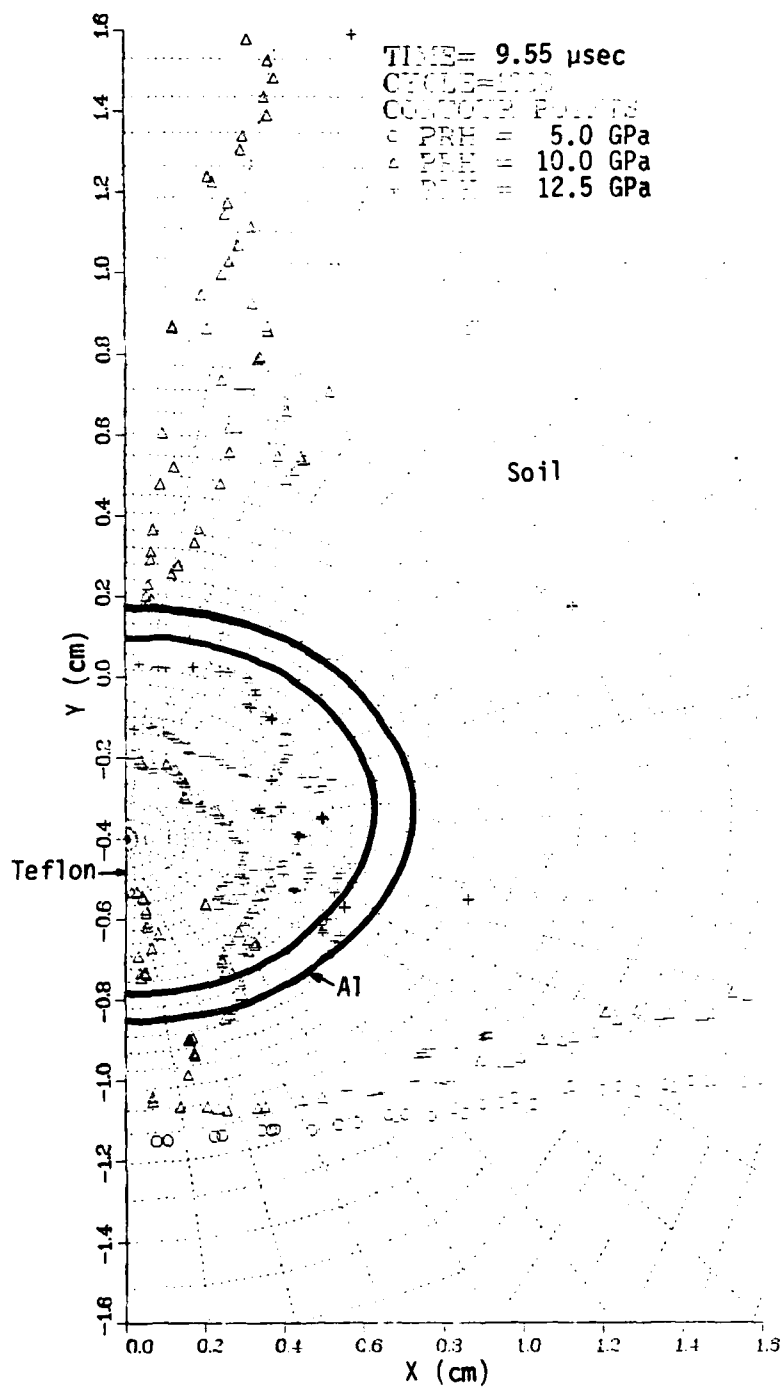


Figure 3.32. Pressure contour plot at 9.55 μ sec--
 A1/Teflon cylindrical gage.

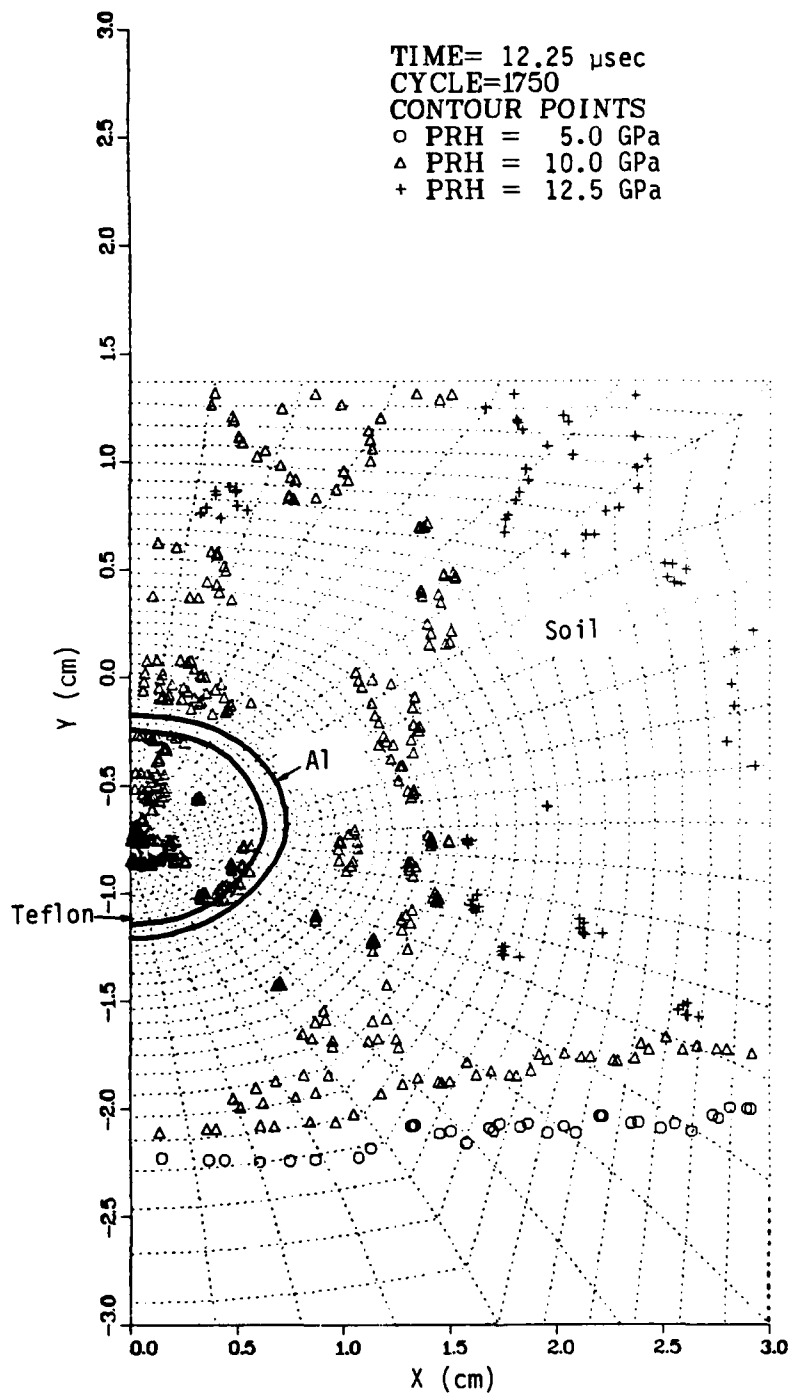


Figure 3.33. Pressure contour plot at 12.25 μ sec--
Al/Teflon cylindrical gage.

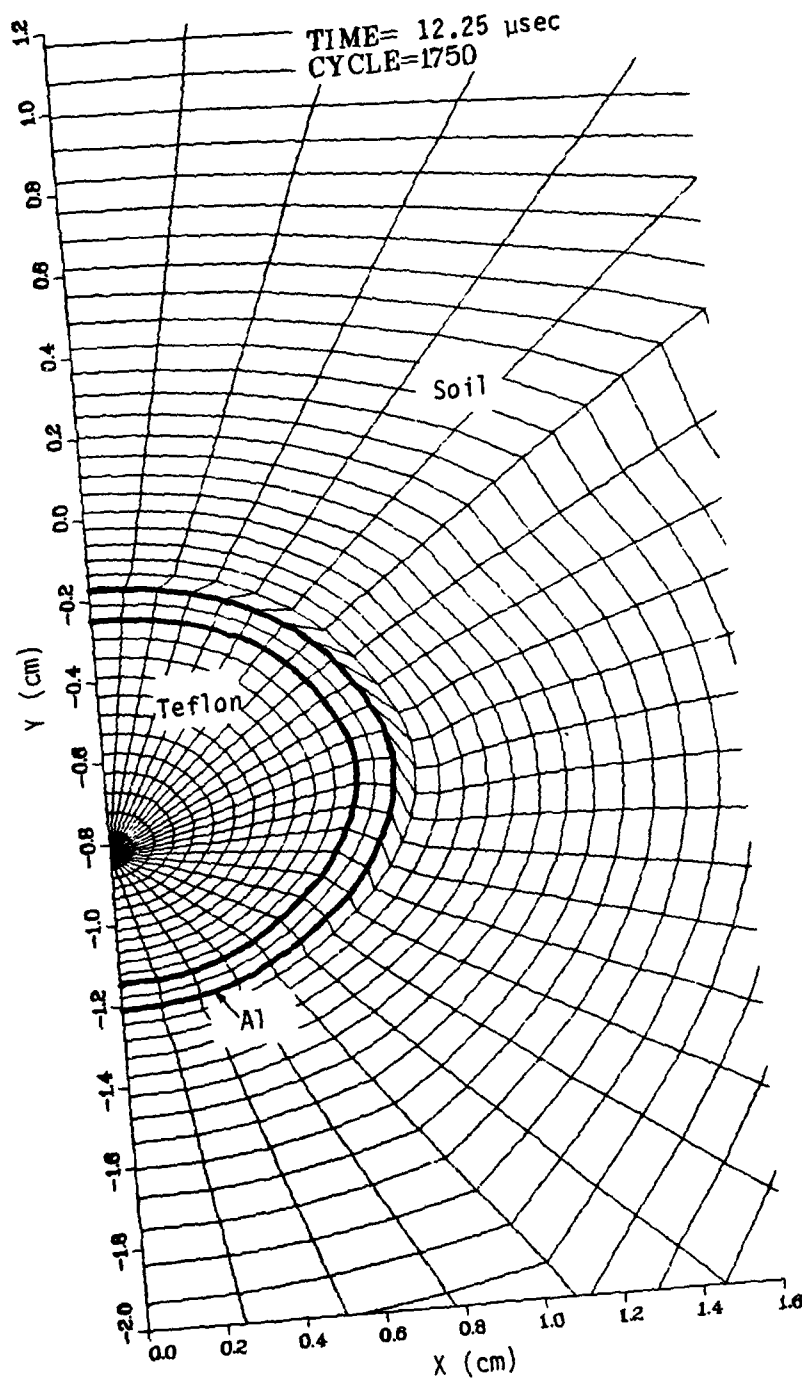
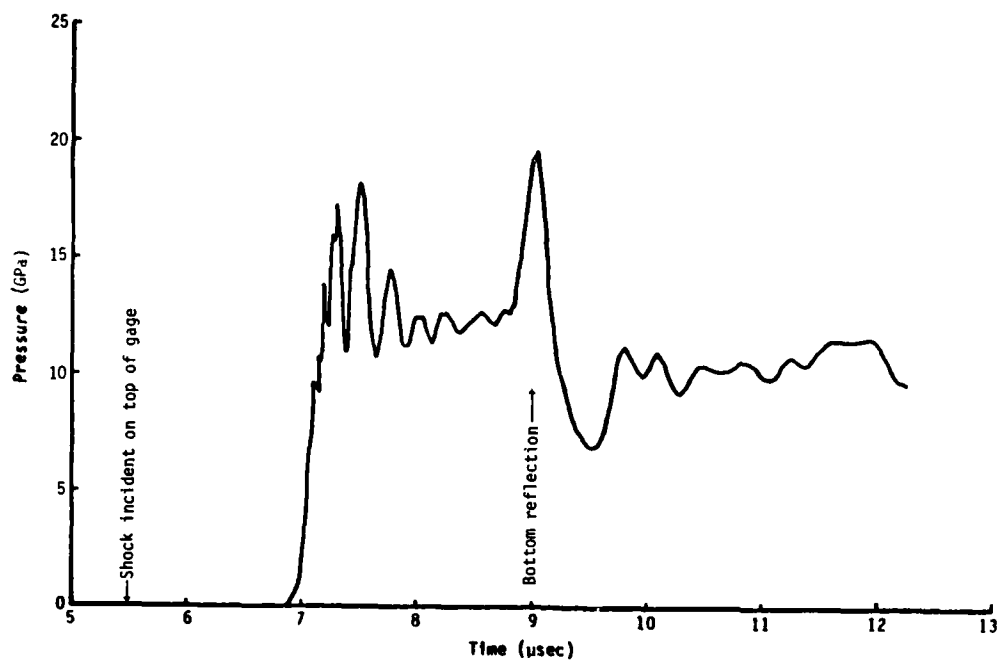
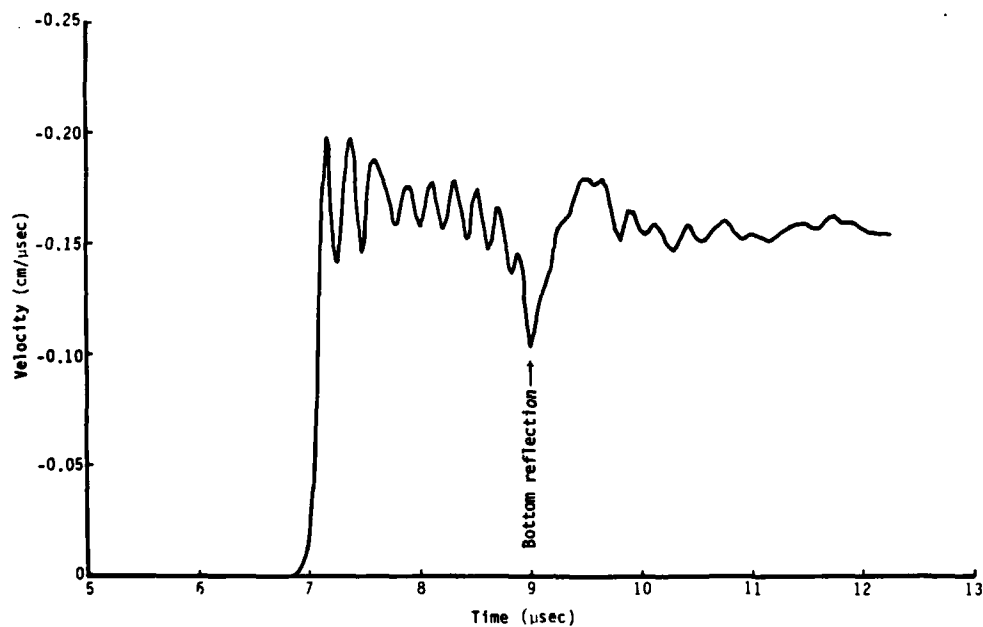


Figure 3.34. Grid plot of gage region at 12.25 μ sec--
Al/Teflon cylindrical gage.



(a) Average pressure around piezoresistive wire



(b) Velocity of piezoresistive wire

Figure 3.35. Wire pressure and velocity--Al/Teflon cylindrical gage.

The early time numerical oscillations seen in the Mg/Teflon gage calculation also occur in this calculation. These fluctuations, due in part to the coarse grid zoning, are somewhat smaller in the Al/Teflon gage because of the extra zones used in the Teflon region (compare Figure 3.35 with Figure 3.25). If we average out the oscillations in Figure 3.35a, the average wire pressure from 7 to 8 μsec is about 14 to 15 GPa, about what was seen in the Mg/Teflon gage.

The deformation of the Al/Teflon gage is shown in Figure 3.36 which compares the initial gage shape with the shape at 8.66 μsec when the shock reached the bottom of the gage and at 12.25 μsec which was the end of the calculation. The dashed line represents the outer boundary of the ideal gage.

The Al/Teflon gage has deformed into an elliptical shape with most of the deformation occurring by 8.7 μsec . The change in the major and minor axes with time is shown in Figure 3.17c. The minor axis contracts along the expected path to $0.72 R_0$ which is very close to the ideal value and then increases slowly to the end of the calculation. The major axis remains close to R_0 throughout the calculation growing slowly to $1.02 R_0$ at 12.25 μsec . Of the four cylindrical gages, the final shape of the Al/Teflon gage is closest to the shape predicted for the ideal gage.

The displacement of the Al/Teflon gage is also close to the ideal displacement (see Figure 3.36). The top of the gage moves slightly less than predicted. The side point SP also lags somewhat. This reduced displacement of the top half of the gage is what causes the zone distortion at the Al/tuff interface seen in Figure 3.34. At the bottom of the gage, the displacement is slightly larger than for the ideal gage. Even so, the Al/Teflon gage again exhibits the closest to ideal behavior of the four gages for which 2-D STEALTH calculations were made.

The final Teflon compression for this gage is about 30 percent, almost identical to the Mg/Teflon gage. The final Teflon shape is also about the same for both gages as is the average wire velocity (0.16 cm/ μsec). Again, it appears that after another 7 to 10 μsec , the wire might come into contact

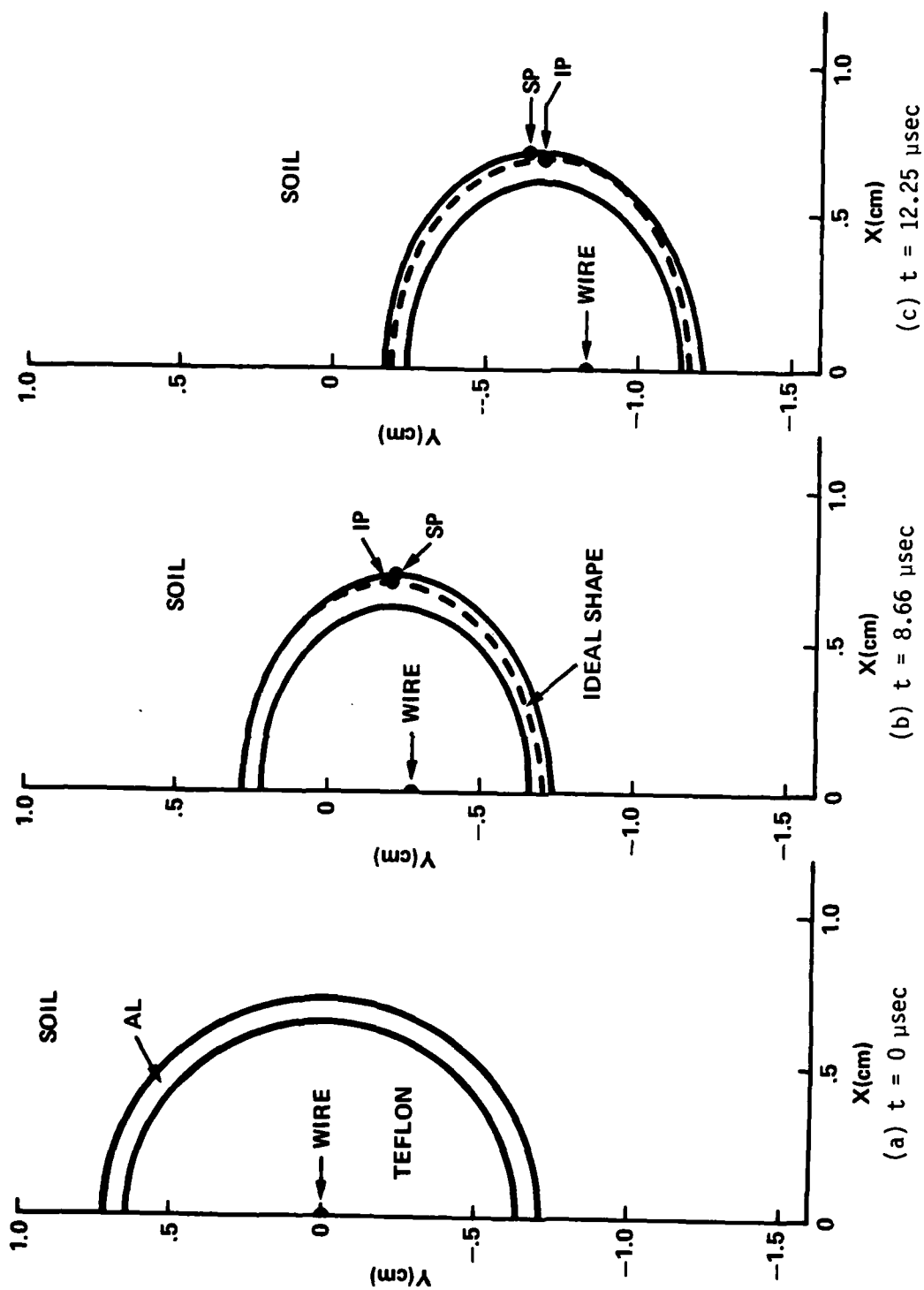


Figure 3.36. Deformation of Al/Teflon cylindrical gage.

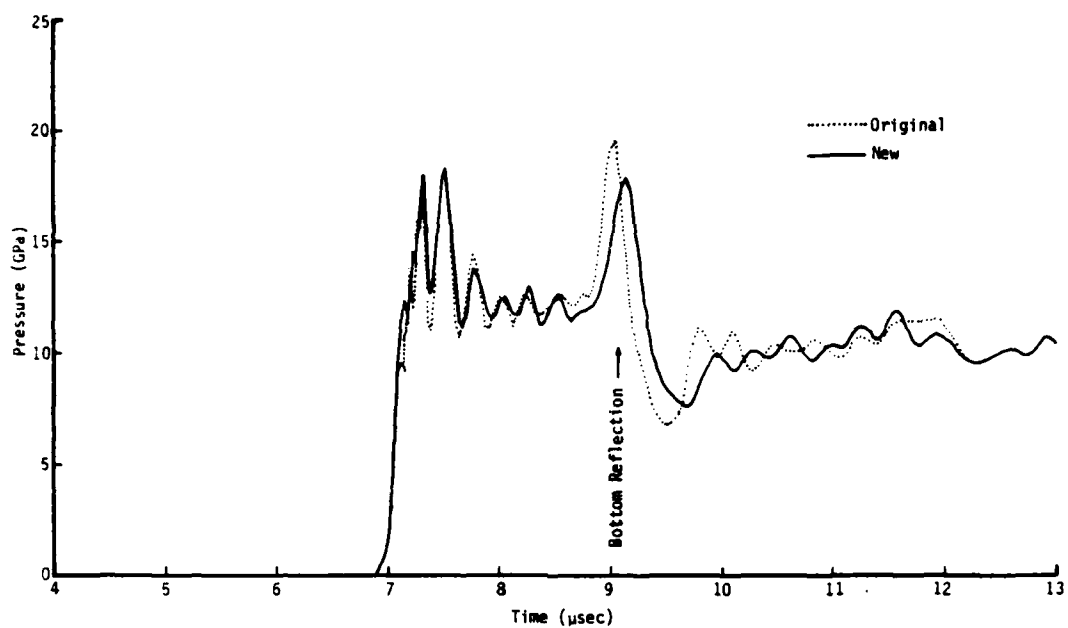
with the bottom of the Al tube. The velocity was found to be about 20 percent too high when the Al/Teflon gage was rerun with the modified wire motion algorithm (see the Appendix).

Several Al/Teflon gages were tested by SRI in March 1982 but no reliable data was obtained. The problem again seemed to be caused by increased conductivity in the Teflon at high pressures. No further tests were made of the Al/Teflon gage as SRI decided to use silastic rubber for the insulating material.

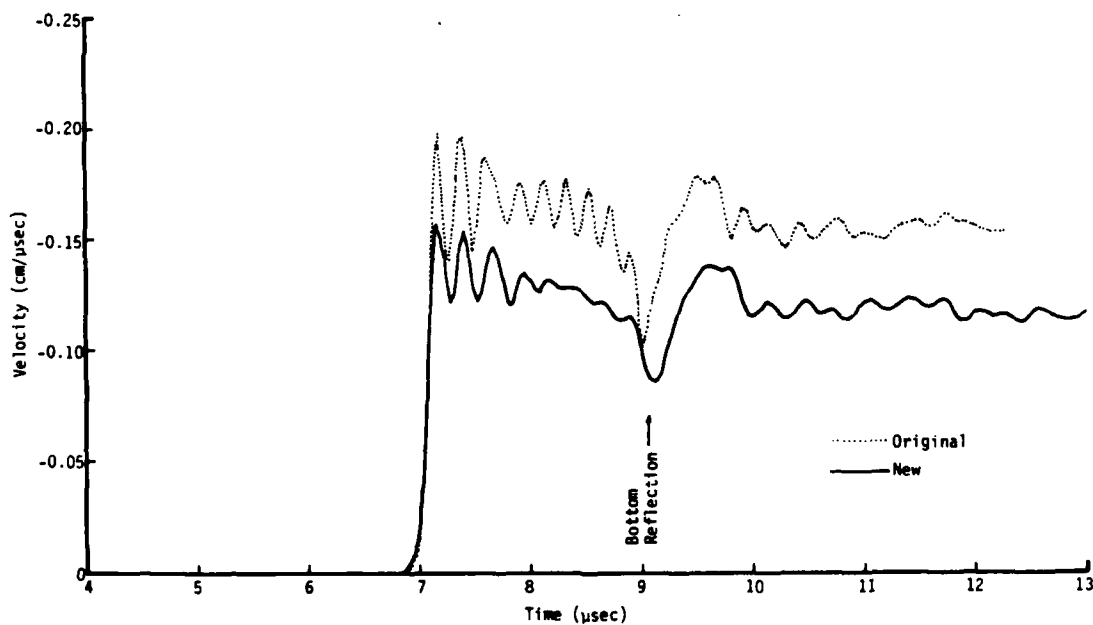
Before making a STEALTH calculation of the Al/silastic gage, an effort was made to find the source of the numerical oscillations in the gage response. A number of calculations were made with a "spider" grid similar to Figure 3.27 containing only soil. Various parameters were changed and the results compared to those from a rectangular grid. As a result of this study, the wire motion algorithm was changed. The gage wire was still treated as a rigid body and a net force computed from the stresses in the surrounding zones. The original algorithm assumed these forces acted perpendicular to the wire surface. The new algorithm defined a "centroid" surface connecting the midpoints of the adjacent grid lines and applied the stresses to this surface. The main difference is that as these zones distort, the angle with respect to the wire surface changes accordingly. This method only slightly reduced the numerical oscillations in the wire pressure but made a large difference in both the oscillations and the magnitude of the wire velocity. A description of the test calculations and the modified algorithm is given in the Appendix.

As a final test, the Al/Teflon gage calculation was rerun using the modified algorithm and with the newly released Version 4.1A of the STEALTH code. In all other aspects, the setup of the second Al/Teflon gage calculation was identical to the original calculation whose initial and boundary conditions are shown in Figure 3.27.

The results of the new calculation are compared to those of the first calculation in Figure 3.37. The average pressure around the piezoresistive wire is little changed (see Figure 3.37a). Both response curves have a



(a) Average pressure around piezoresistive wire.



(b) Velocity of piezoresistive wire.

Figure 3.37. Comparison of wire pressure and velocity for the two Al/Teflon gage calculations.

sharp initial rise to about 18 GPa followed by an oscillatory decline to the 12 GPa level. The bottom reflection spike is smaller in the new calculation at 18 GPa compared to 20 GPa and peaks slightly later in time. At later times, the average pressure in both calculations oscillates about the 10 GPa level, which is the value in the surrounding soil.

The wire velocity for the two calculations is compared in Figure 3.37b. Both curves have similar features--a sharp rise, then a slow decline until the reflected wave reaches the wire, a rebound and then oscillations about a constant value at later times. However, the velocities computed using the new algorithm are consistently about 20 percent smaller in absolute magnitude than those given by the old method. This slower motion of the wire results in it being further from the bottom of the gage. This is the reason for the difference in timing in the bottom reflections in the two calculations. In addition, the magnitude of the early time oscillations is greatly reduced.

Other aspects of the two calculations were very close. The deformation was nearly the same in both cases (compare Figure 1.15a from the second calculation to Figure 3.34). The only difference was in the position of piezoresistive wire which did not move as much in the new calculation because of the lower wire velocity. The fact that the average wire pressure was little changed by the fairly large change in wire velocity indicates the accuracy of the computed gage response is fairly insensitive to the details of the wire motion algorithm.

3-4 AL/SILASTIC GAGE

The final cylindrical gage design modeled by 2-D STEALTH calculations was made of thin-walled aluminum tubing with silastic rubber as the insulating material. The dimensions for this gage are shown in Figure 1.9d. It is very similar to the Al/Teflon gage but slightly larger in size.

The initial grid for the Al/silastic gage calculation is shown in Figure 3.38 with an expanded view of the gage region given in Figure 3.39. The grid zoning is listed in Table 3.1. The overall grid dimensions are the

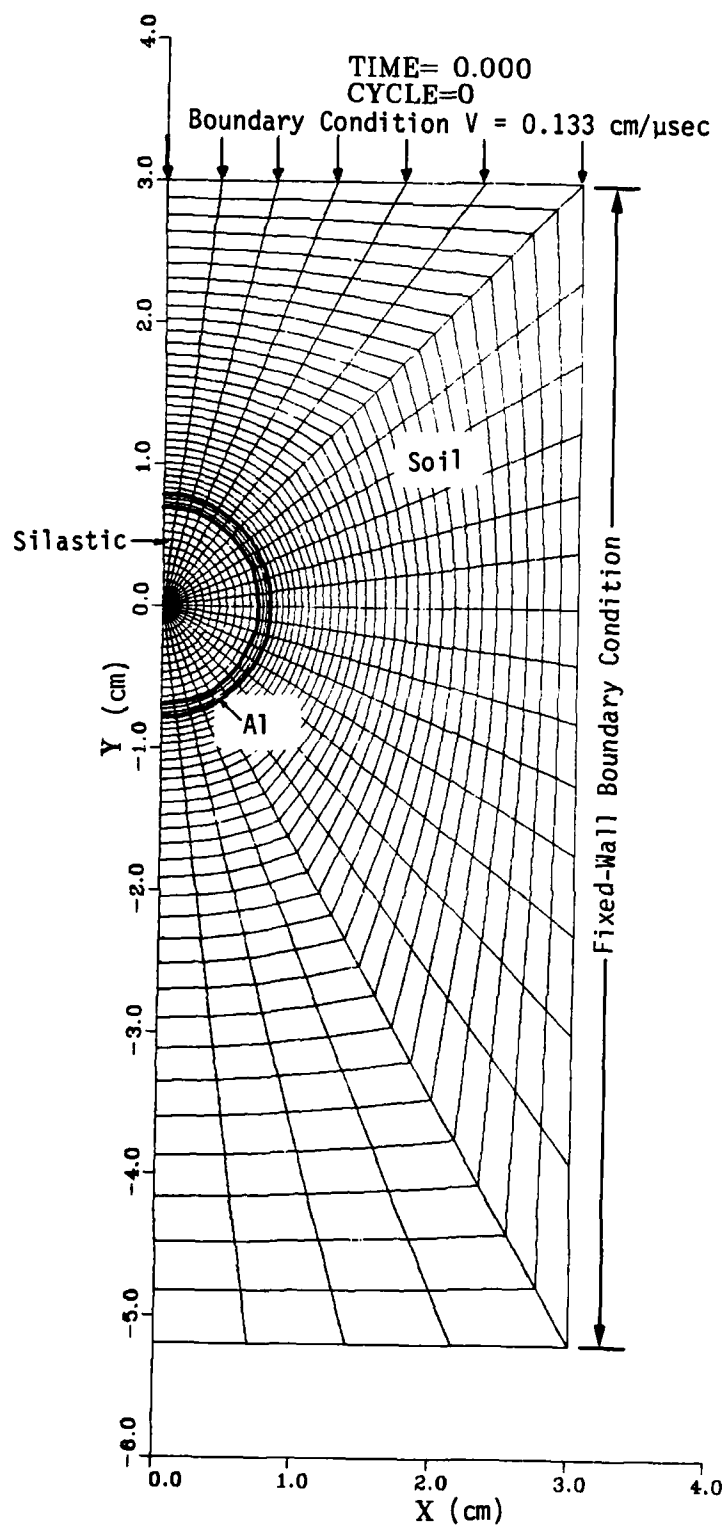


Figure 3.38. Initial grid for the Al/silastic cylindrical gage.

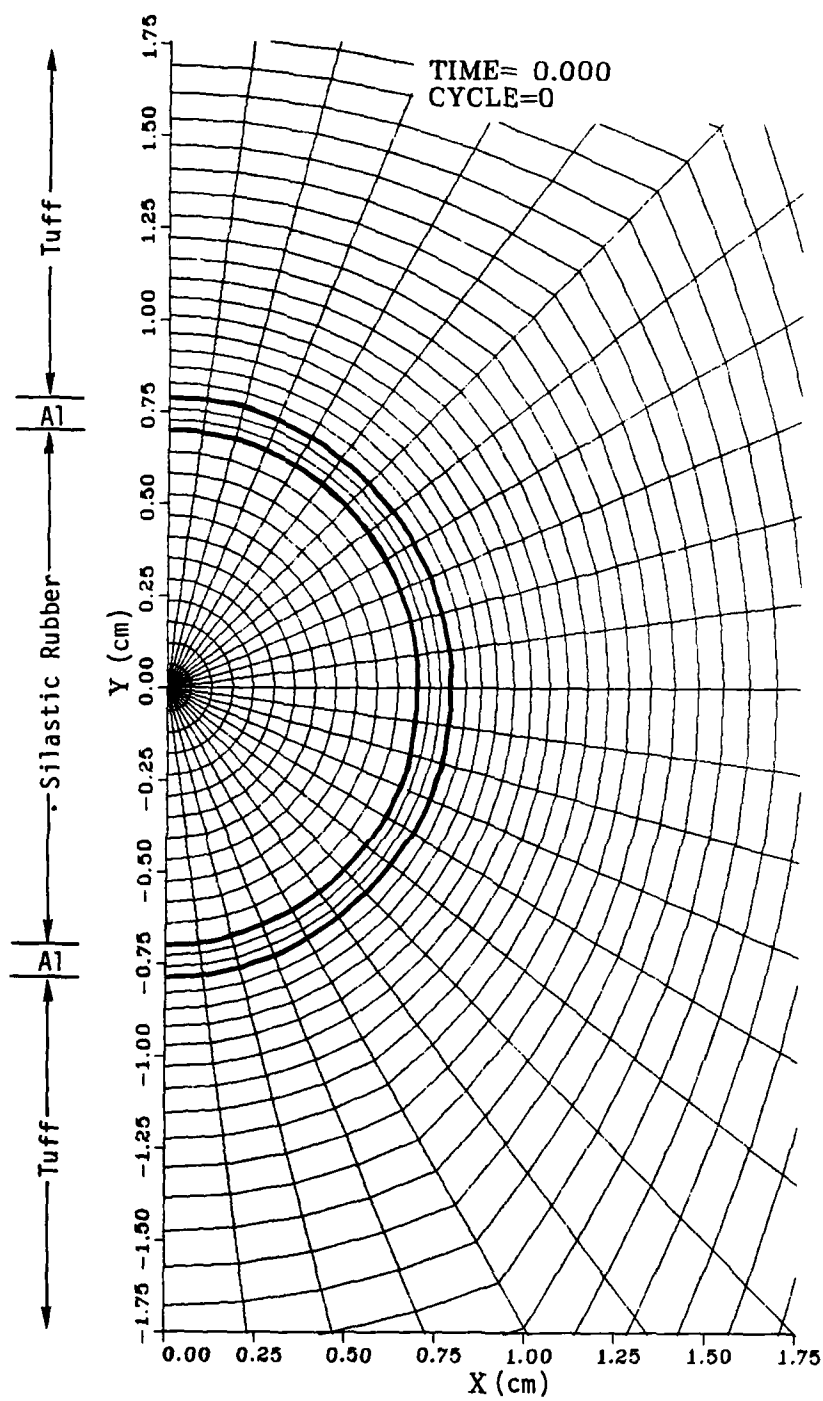


Figure 3.39. Initial zoning of gage region--Al/silastic cylindrical gage.

same as used for the Al/Teflon gage. However, the total number of grid points is larger (1125 versus 1000, respectively). The spacing of the rays emanating from the gage center was unchanged at 7.5° . The additional grid points were used to add one more semicircular grid line in the aluminum tubing and to decrease the zone thicknesses along the rays in the tuff. This somewhat finer zoning was needed to obtain mass matching at the Al/silastic and Al/tuff interfaces.

The STEALTH calculation of this gage was initially run 2000 cycles to a problem time of $12.79 \mu\text{sec}$. After analysis of the results to that time, the calculation was restarted and run an additional 3000 cycles to a problem time of $19.17 \mu\text{sec}$. This was done to obtain a long time response for this gage. The progress of this calculation will be illustrated by a sequence of pressure contour plots. Additional information is available in the STEALTH output.

The velocity boundary condition imposed on the top of the grid generates a downward-moving 10.5 GPa pressure wave that reaches the top of the gage at about $5.4 \mu\text{sec}$ (see Figure 3.40). This wave is transmitted into the interior of the gage and reaches the center wire at about $6.8 \mu\text{sec}$ as shown in Figure 3.41. The shock wave continues to move downward reaching the bottom of the gage at about $8.2 \mu\text{sec}$. The strong shock reflection that occurs at the silastic/aluminum interface can be seen moving upward at $8.5 \mu\text{sec}$ in Figure 3.42. This shock passes over the piezoresistive wire with a strength of about 20 GPa. It continues upward hitting the top of the gage where another weaker reflection occurs. This top reflection can be seen in the contour plot at $9.36 \mu\text{sec}$ shown in Figure 3.43. The reflected wave travels again to the bottom of the gage, passing over the gage wire on its way. A second reflection from the bottom must occur but is too weak to be seen clearly in a pressure contour plot.

After about $10 \mu\text{sec}$, the contour plots show little pressure variation inside the gage. This is illustrated in the contour plot at $14.3 \mu\text{sec}$ shown in Figure 3.44. By this time, the incident pressure wave has moved about

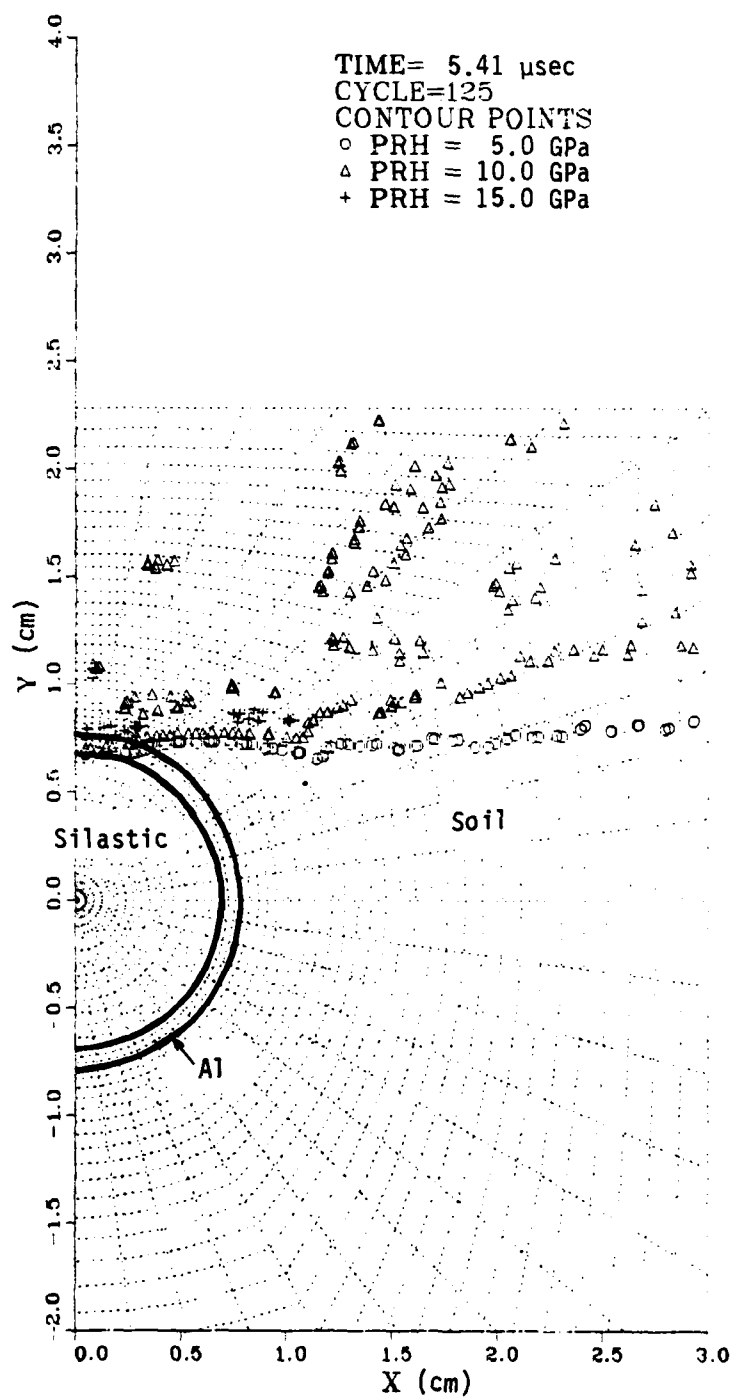


Figure 3.40. Pressure contour plot at 5.41 μ sec--Al/silastic cylindrical gage.

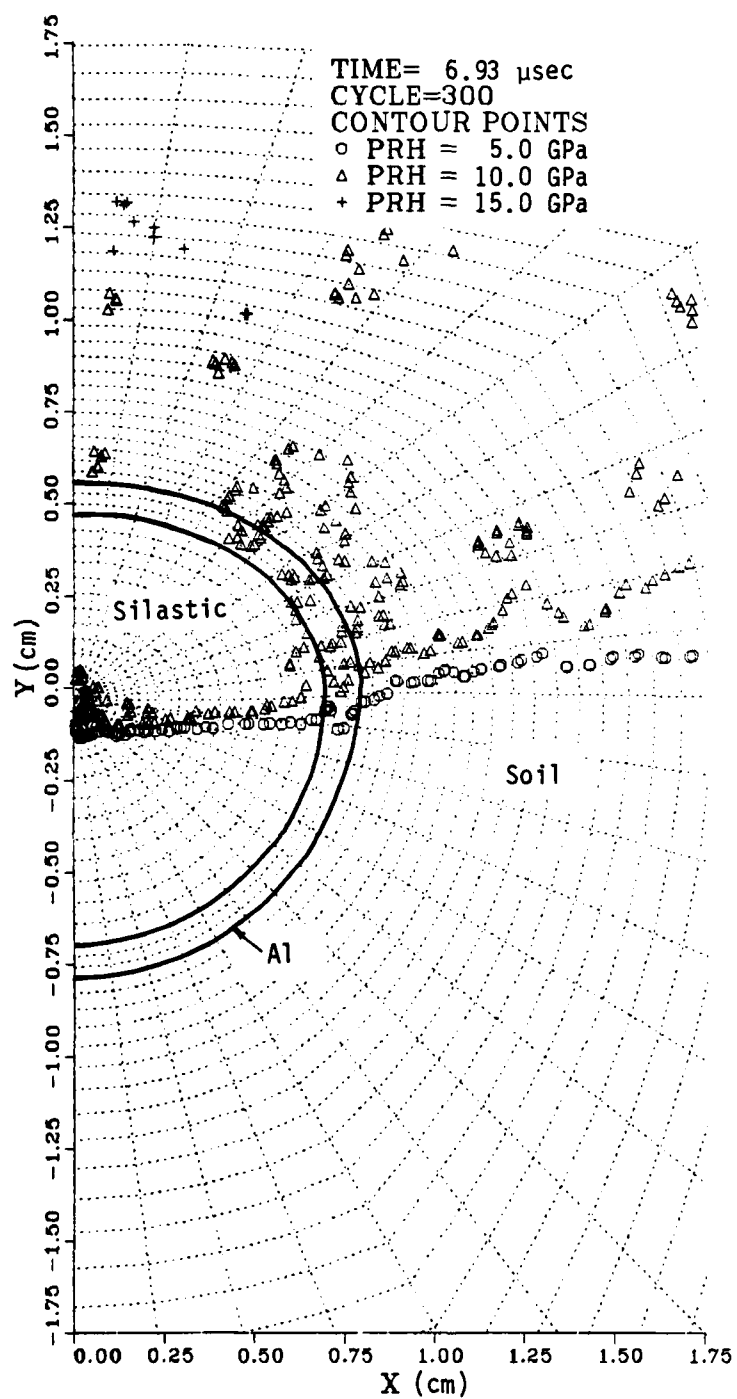


Figure 3.41. Pressure contour plot at 6.93 μ sec--Al/silastic cylindrical gage.

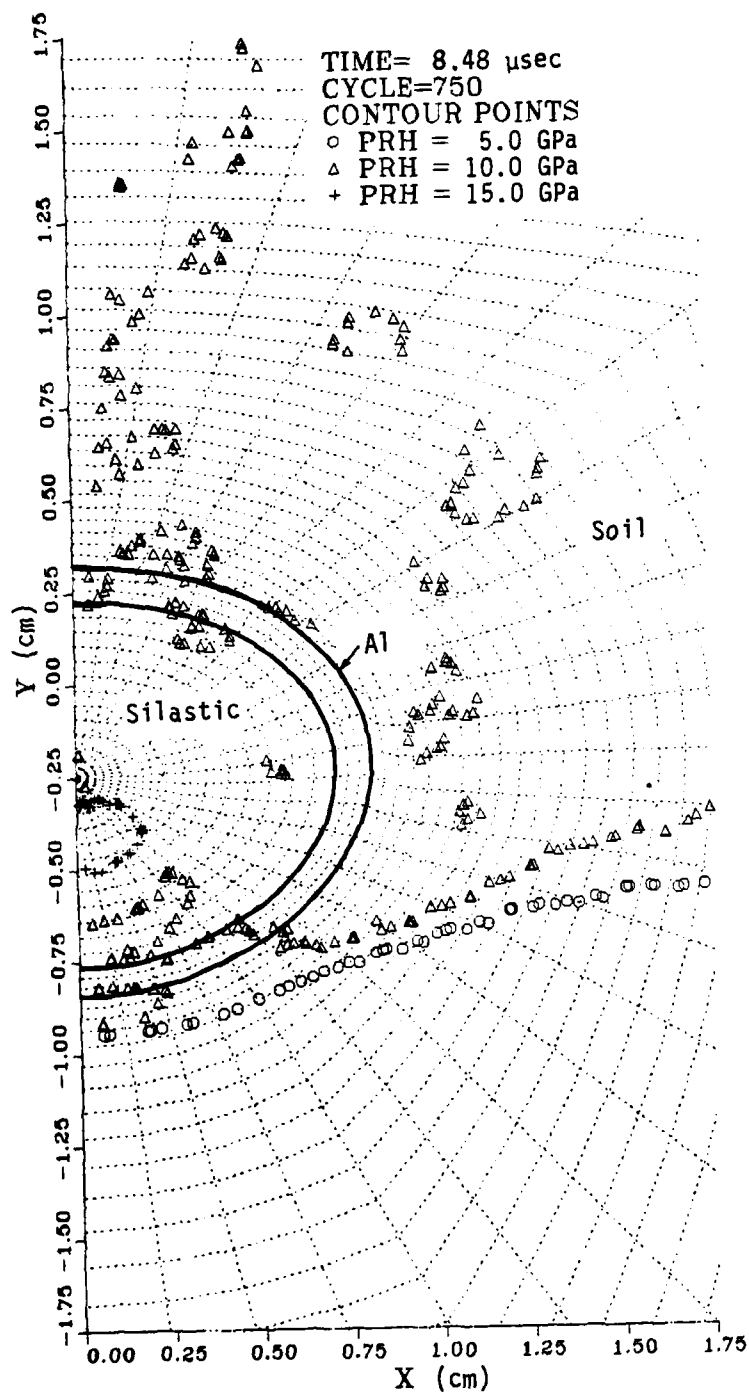


Figure 3.42. Pressure contour plot at 8.48 μ sec--Al/silastic cylindrical gage.

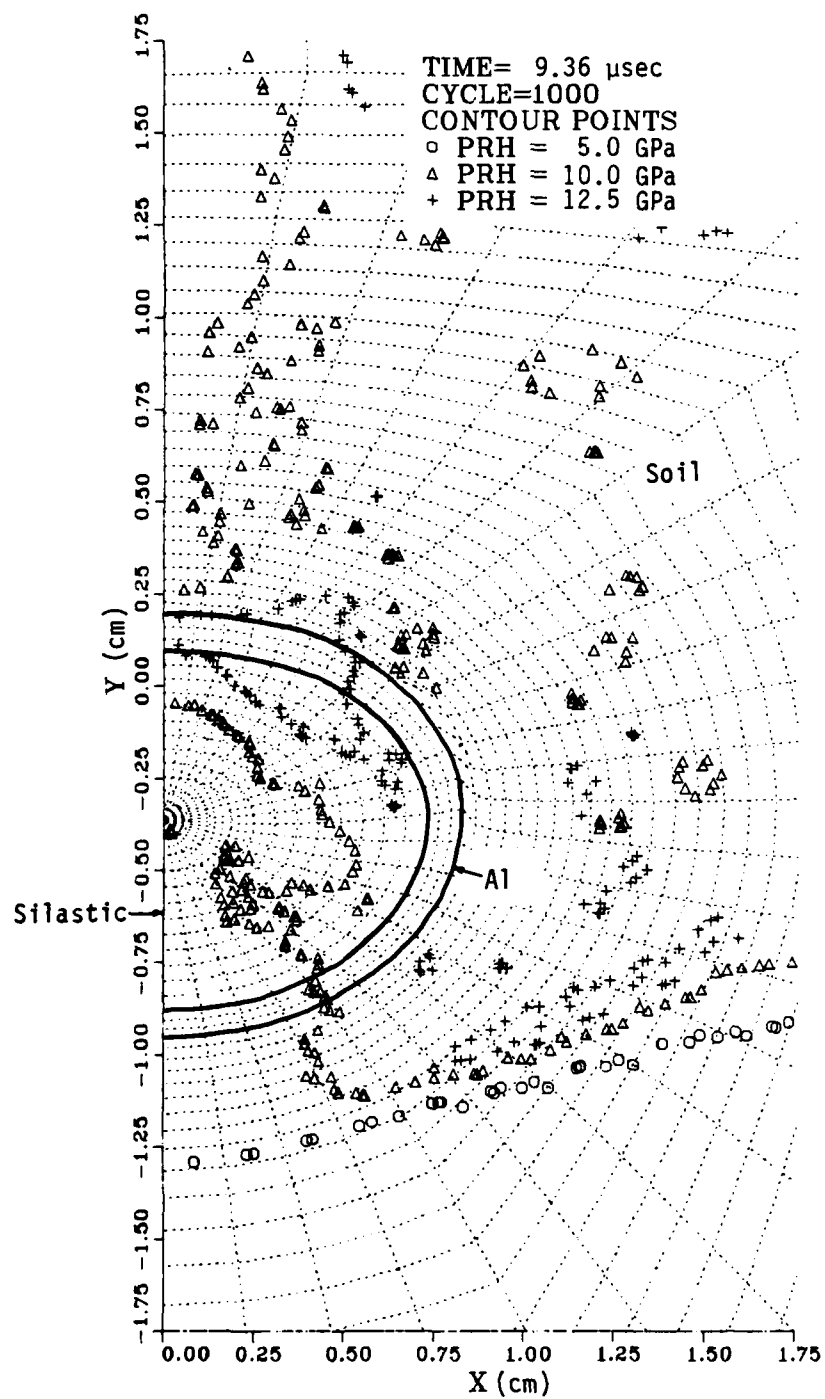


Figure 3.43. Pressure contour plot at 9.36 μ sec--Al/silastic cylindrical gage.

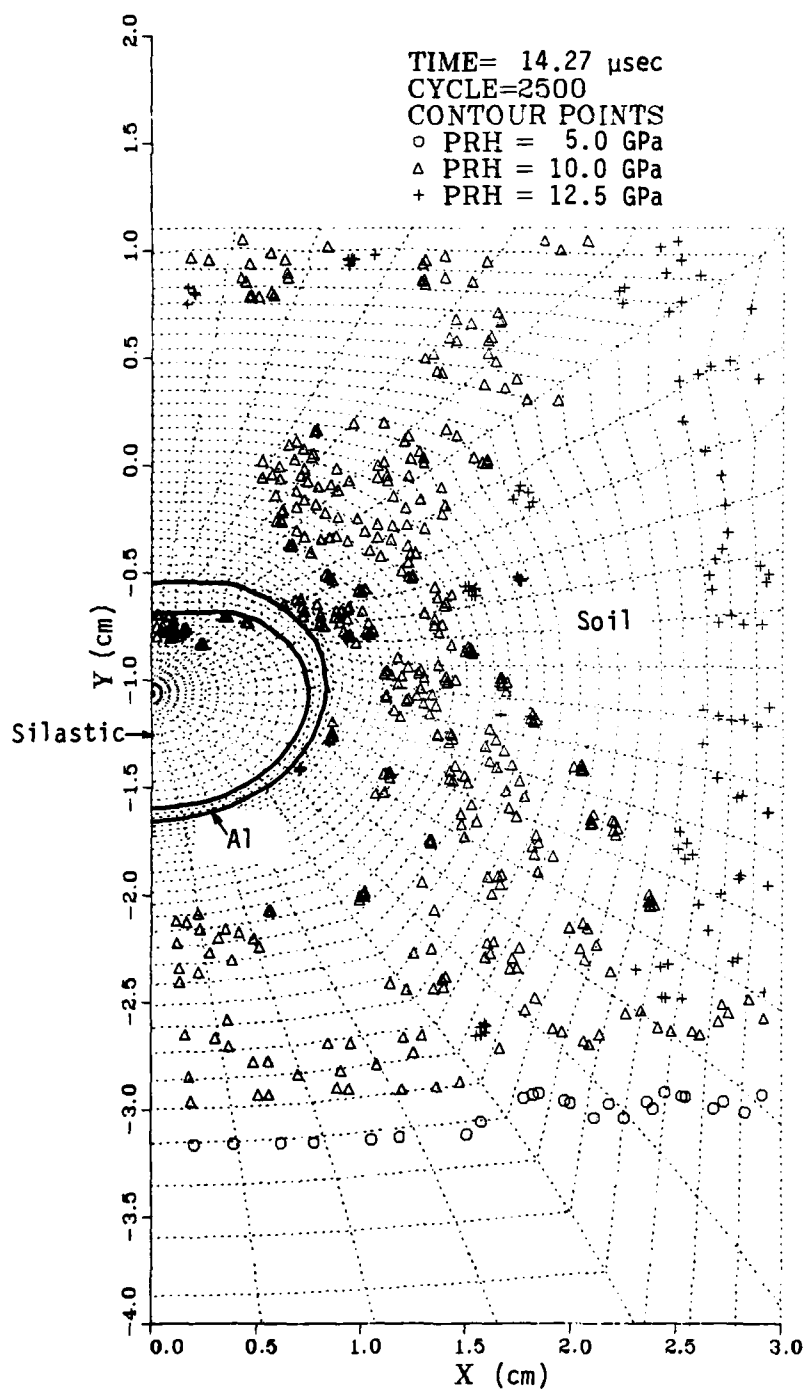


Figure 3.44. Pressure contour plot at 14.27 μ sec--Al/silastic cylindrical gage.

1.5 cm below the bottom of the gage. Some higher pressure regions above 12.5 GPa are seen along the right boundary of the grid, possibly a reflection from the fixed wall boundary condition at $x = 3.0$ cm. Pressures of about the same magnitude appear along the left grid boundary and in the gage response curve at about 18 μsec (see Figure 1.14). We think these side wall reflections are related and therefore are artifacts of the calculation and not physical phenomena. This could be checked by running another calculation in a larger grid (4-cm wide, for example) but this was not done.

The average pressure around the piezoresistive wire for the Al/silastic gage is shown as a function of time in Figure 1.14. The gage response is similar to that found with the Al/Teflon gage (see Figure 3.37a). The main difference between the two response curves is a shift in timing. The signal from the Al/silastic gage begins about 0.3 μsec earlier in time and the bottom reflection peaks about 0.45 μsec sooner. This time change is caused by two things. First, the Al/silastic gage is larger so the shock front reaches the upper gage surface earlier in time. Second, the shock velocity at 10 GPa is greater in silastic rubber than in Teflon (0.56 cm/ μsec versus 0.38 cm/ μsec) so the transmitted and reflected waves traverse the gage in less time.

Another difference between the response curves is that there is less overshoot and smaller fluctuations in the Al/silastic results in the time period between the initial rise and the arrival of the bottom reflection. This is the result of changing the insulating material from Teflon (density 2.16 g/cm³) to silastic (1.37 g/cm³). The larger density mismatch at the aluminum/silastic interface reduces the magnitude of the shock transmitted to the interior of the gage. The ratio of the initial densities of silastic and Teflon is 0.64; this is close to the ratio in peak pressures (13 GPa/18 GPa = 0.74) that occurs just after 7 μsec .

The wire velocity as a function of time for the Al/silastic gage is given in Figure 3.45. This curve is similar to Figure 3.37b with the same timing variations discussed above. Another difference is in the late time value about which the velocity fluctuates. It is about 0.143 cm/ μsec for the Al/silastic gage, slightly higher than the free field tuff value of 0.133 cm/ μsec , and also higher than the 0.12 cm/ μsec seen for the Al/Teflon gage.

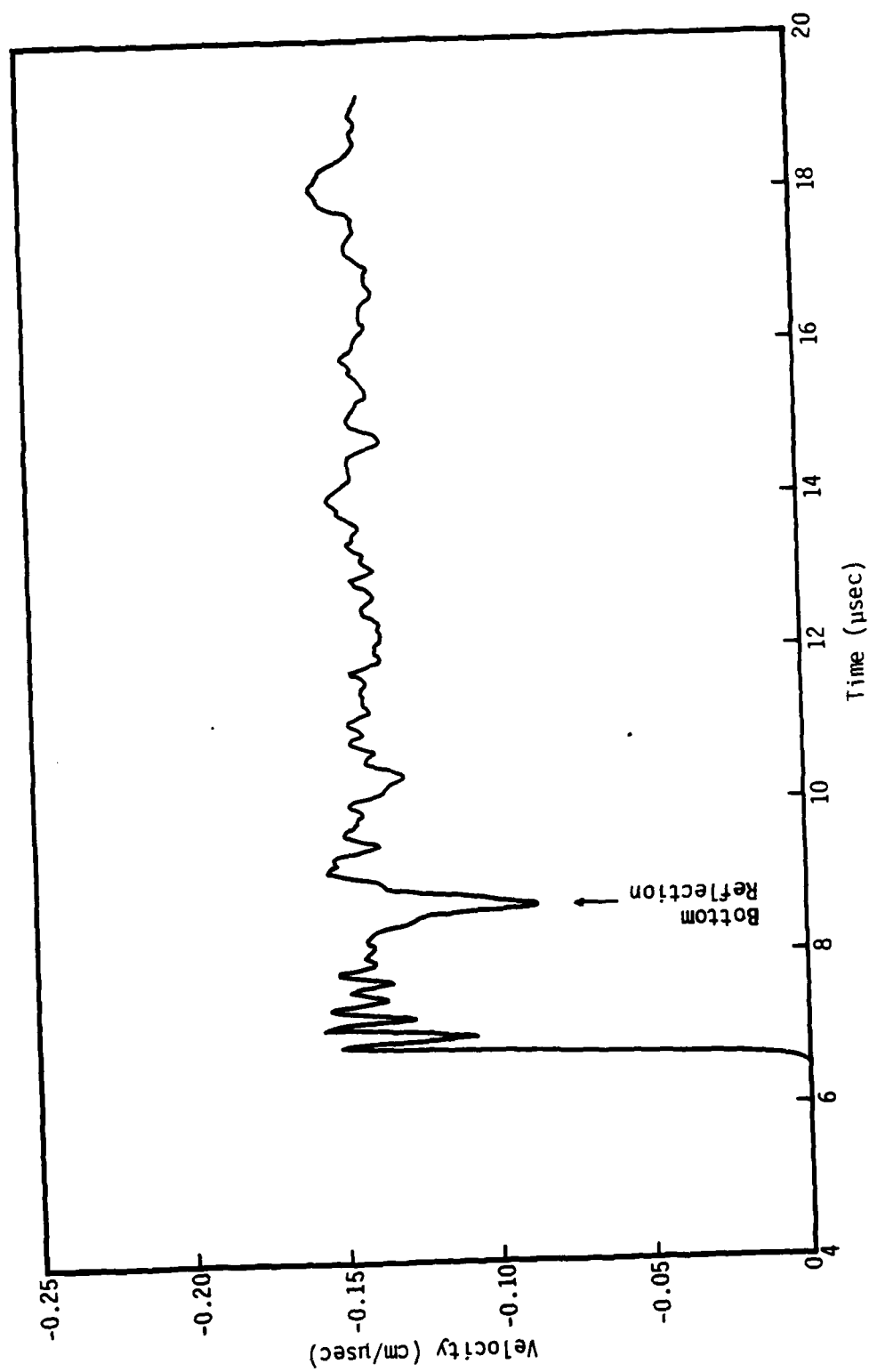


Figure 3.45. Wire velocity to 19 μsec--Al/silastic cylindrical gage.

A grid plot of the Al/silastic gage at 12.79 μsec is shown in Figure 1.15b for comparison with the Al/Teflon grid at about the same time shown in Figure 1.15a. The Al/Teflon gage deformed into a nearly elliptical shape while the Al/silastic gage became more heart-shaped like the brass/epoxy gage (see Figure 1.11). The Al/silastic gage at the end of the calculation is shown in Figure 3.46. The final shape is also similar to that of the brass/epoxy gage at late times (see Figure 3.16c). The heart-shaped deformation occurred in both gages for which the insulator material had a density less than the soil density and the elliptical shape for the two gages with an insulating material greater than the soil density.

A measure of the rate of deformation of the Al/silastic gage with time is given in Figure 3.47 which compares the major and minor axes of this gage with those for an ideal gage. The minor axis contracts along the expected path to $0.76 R_0$ and then decreases very slowly with time. At the end of the calculation, it is nearly at the theoretical value of $0.68 R_0$. The major axis increases to $1.07 R_0$ at a time of 11 μsec and then begins a slow decrease. (Similar plots for the other three cylindrical gages are given in Figure 3.17.)

The displacement and deformation of the Al/silastic gage at various times throughout the calculation is shown in Figure 3.48. The initial position and shape of the gage is given in Figure 3.48a. The gage at 9.36 μsec is shown in Figure 3.48b. This time is just after the incident wave has completely passed over the gage as shown in the pressure contour plot at the same time (Figure 3.43). The top of the gage has moved about as predicted while the bottom has been displaced more than the displacement in an ideal gage. This occurs because the shock wave traveled faster in silastic rubber than in soil and reached the bottom of the gage about 1 μsec before the shock in the soil. To this time, the gage has deformed approximately elliptically.

By 12.79 μsec , the gage shape has changed significantly (see Figure 3.48c). The aluminum tubing has begun to flatten at the top and also became thicker at the top than the bottom. The displacement at both the top and bottom is ahead of the ideal gage values but the side point SP is lagging behind the ideal side point IP.

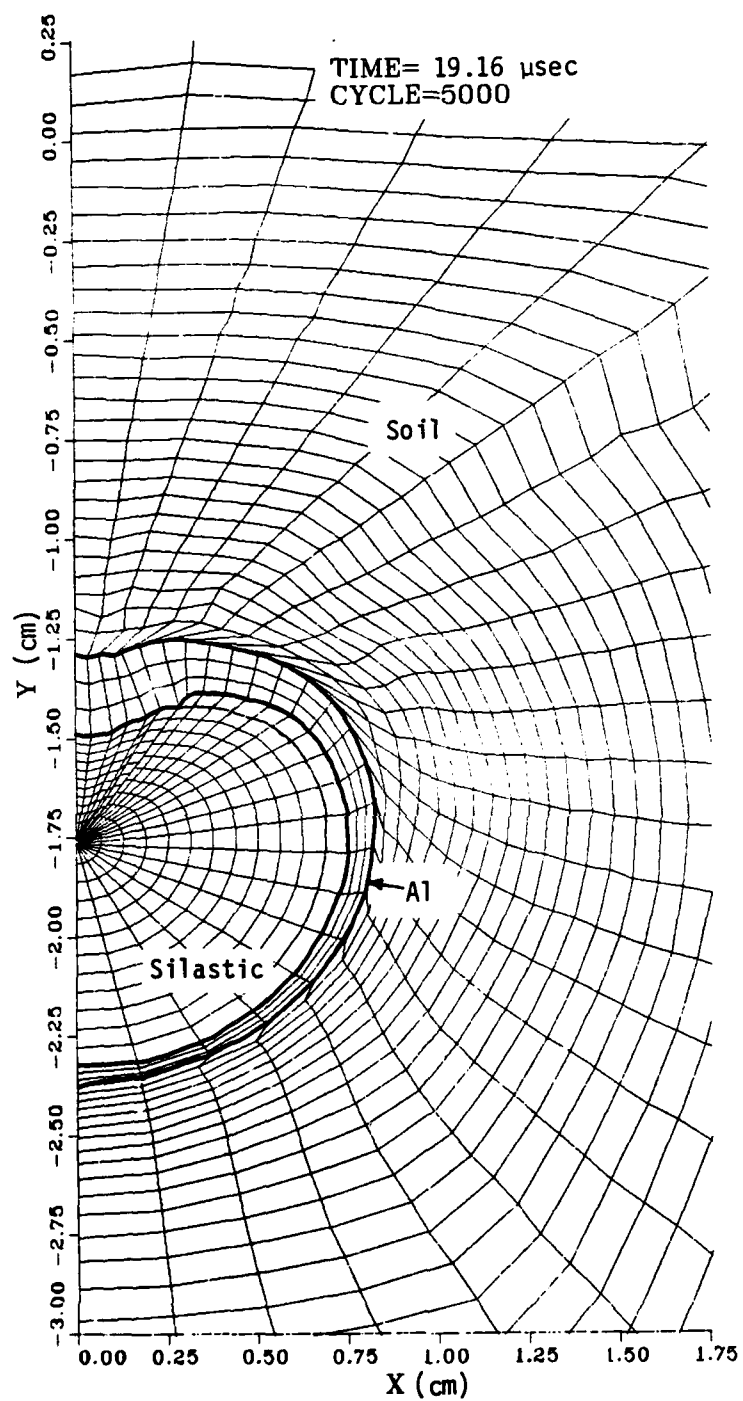


Figure 3.46. Grid plot at 19.16 μ sec--Al/silastic cylindrical gage.

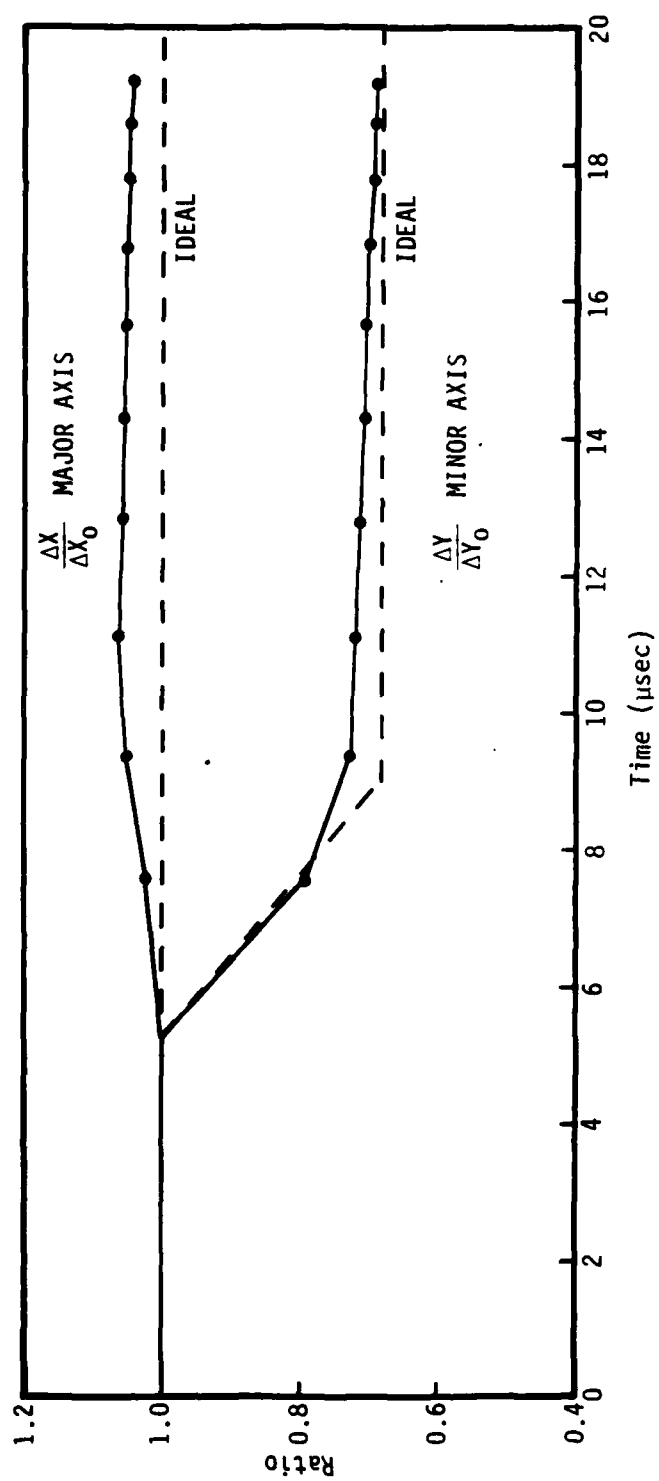


Figure 3.47. Change in major and minor axes of Al/silastic gage versus time.

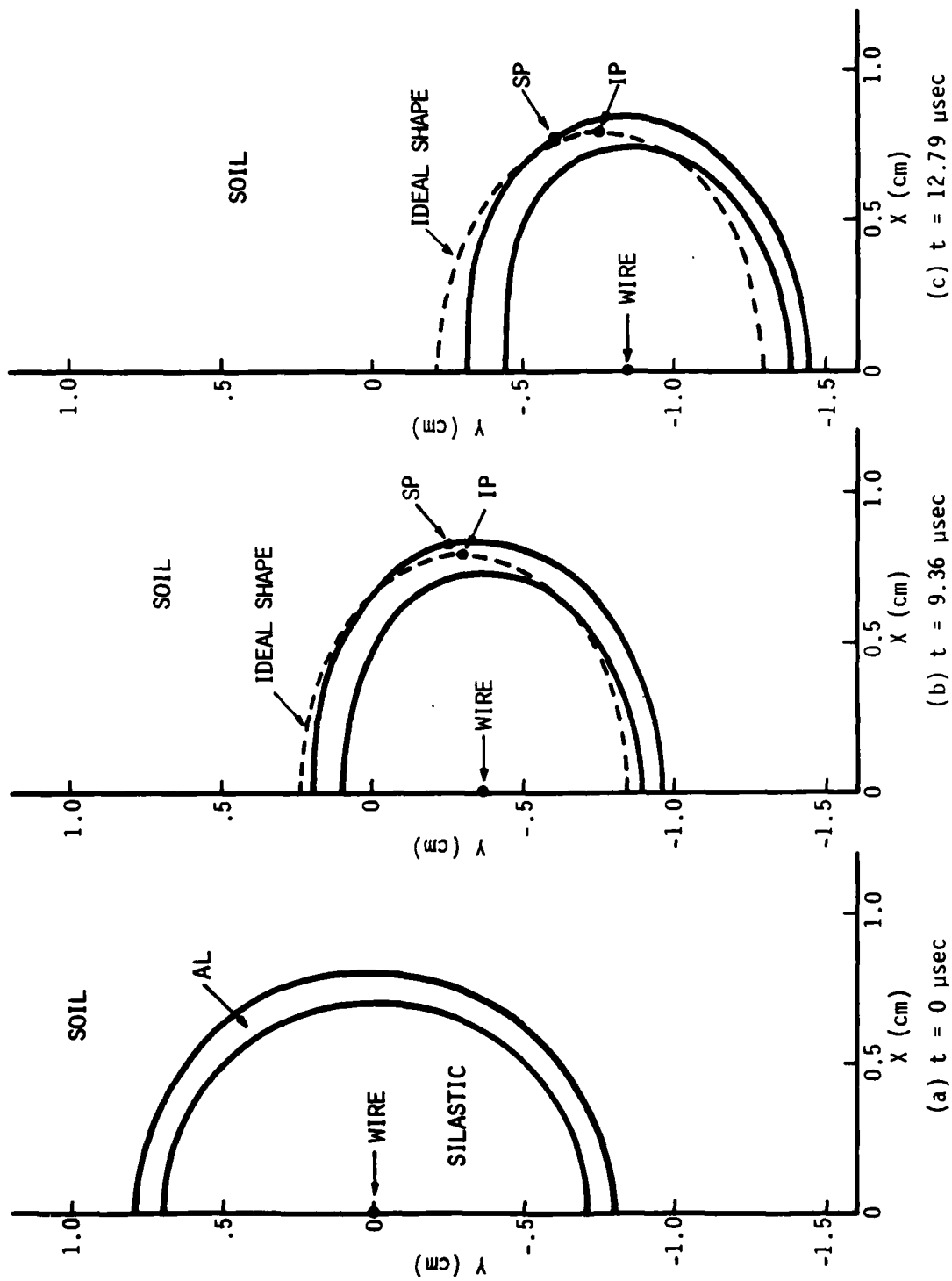


Figure 3.48. Deformation of Al/silastic cylindrical gage.

These trends continue at later problem times. The beginning of a concave region at the top of the gage can be seen at 15.64 μsec in Figure 3.48d. This depression is larger at 17.79 μsec (Figure 3.48e) and still larger at 19.16 μsec (Figure 3.48f). In contrast, the bottom of the gage remains nearly circular with a radius about equal to the initial radius of 0.79 cm.

Throughout the calculation, the top portion of the aluminum tubing continued to thicken while the bottom of the tube became progressively thinner. As a consequence, the side point SP moves around the top of the gage toward the y-axis and is displaced much less than the ideal side point IP.

After about 9 μsec , the top and bottom of the gage move at a velocity of about 0.15 cm/ μsec for the remainder of the calculation. This is faster than the soil particle velocity of 0.133 cm/ μsec and is the reason for the increasing difference between the displacement of Al/silastic gage and the ideal gage with time seen in Figure 3.48. The average velocity of the piezo-resistive wire is about 0.143 cm/ μsec (see Figure 3.45). This is faster than the soil particle velocity but slower than the top and bottom of the aluminum tubing. As a consequence, the displacement of the wire is less than that of the tubing and the wire is seen in Figure 3.48 to become closer to the top of the gage with time.

Another result of the heart-shaped deformation of this gage was the distortion of the soil zones adjacent to the soil/aluminum interface, particularly on the top half of the gage. This effect, while most pronounced at late times (Figure 3.46), can also be seen in the early part of the calculation (Figure 1.15b). We made a second 2-D calculation of the Al/silastic gage with slide lines at this interface to see what effect allowing the soil to slide around the gage would have on the gage response and deformation.

The initial grid for the slide line calculation had the same zoning as shown in Figure 3.38. The only difference was that two grid lines were used to describe the gage/soil interface. The grid points on these lines initially lie on top of each other but are free to move independently during the calculation. The motion of the points on each side of the interface is

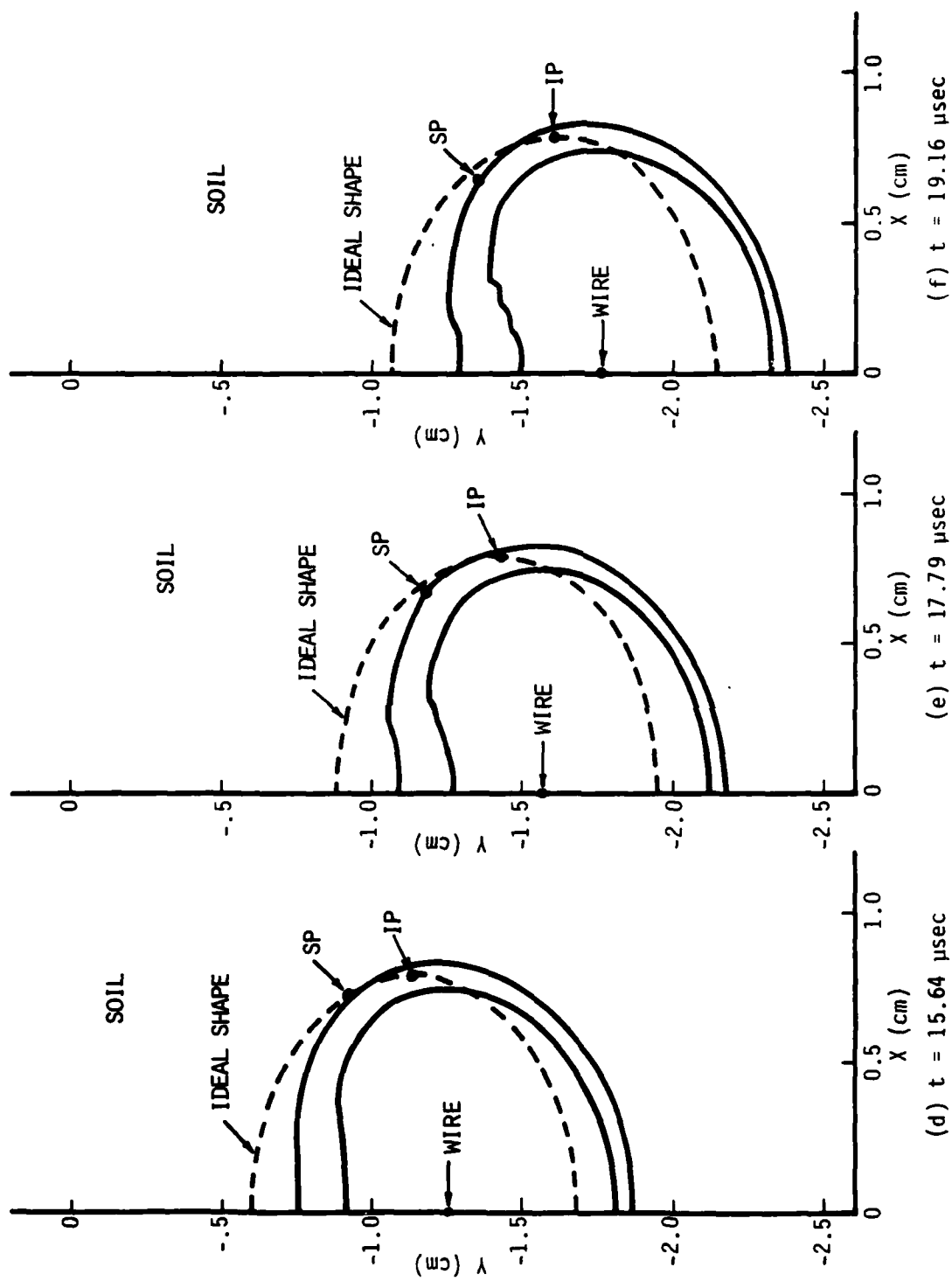


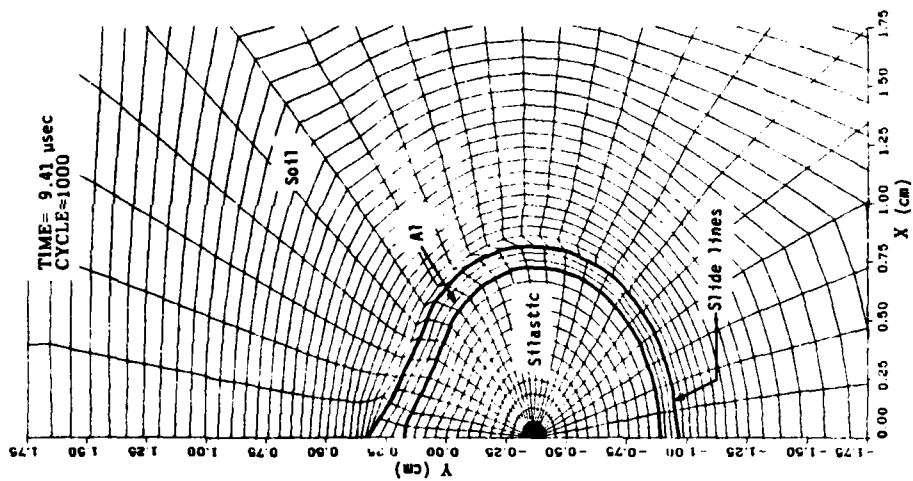
Figure 3.48. Deformation of Al/silastic cylindrical gage (continued).

computed under the assumptions that the slide lines are frictionless and cohesionless. In the STEALTH context, frictionless means that shear stresses from across the interface do not affect the motion tangential to the slide line of the grid points on the other side of the interface. Cohesionless means that the slide lines are free to separate without overcoming a finite binding force. Under these conditions only normal stresses are transmitted across the slide lines.

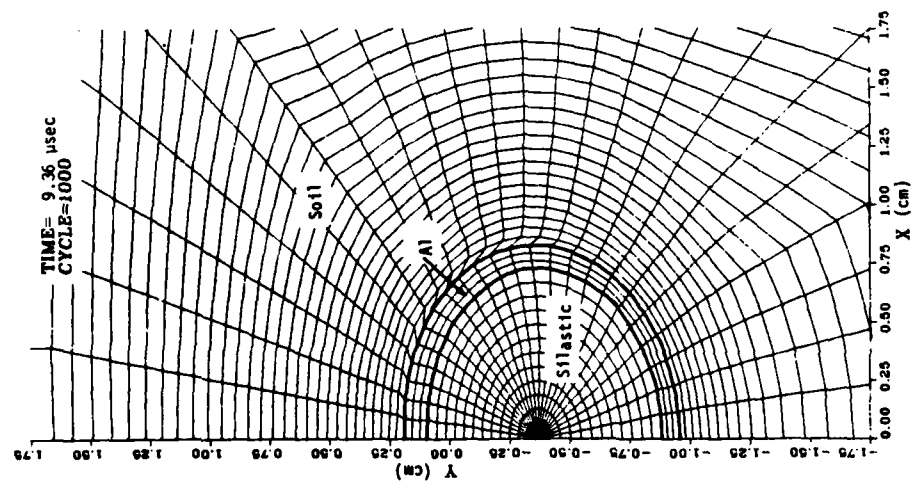
The slide line calculation was run 1500 cycles to a problem time of 11.16 μ sec. However, because of a computational problem along the vertical axis, the results after 9 μ sec are suspect. The slide line grid at 9.41 μ sec is compared to the original calculation at 9.36 μ sec in Figure 3.49. The soil zones adjacent to the gage in the slide line grid are still distorted but in the opposite direction from the normal grid. It appears the slide line algorithms allowed the soil to slide excessively toward the bottom of the grid. The displacement of the bottom and side of the gage is about the same in both calculations but there is a great difference at the top, particularly near the vertical axis. This condition became worse as the calculation proceeded. By the end of the calculation, some of the aluminum zones at the top of the gage had crossed over the adjacent soil zones.

The gage response for the slide line calculation is compared to our previous result in Figure 3.50. Up to 9 μ sec, the responses are similar indicating that soil slippage is not effective in shielding the gage from the free field. This is probably because the cylindrical shape ensures that the incident shock always impacts normal to the gage surface and thus is transmitted to the gage interior by what is essentially a 1-D interaction. After 9 μ sec, the smaller displacement of the aluminum at the top of the gage causes an expansion of the area occupied by the silastic rubber and thus a lower pressure inside the gage.

A second calculation was made in which we shifted from free sliding to tied sliding along the gage/soil interface. With this option, the points on each side of the slide line are tied together and, in theory, the results should be the same as those given by the calculation without slide lines.



(a) Grid at 9.36 μsec without slide lines.



(b) Grid at 9.41 μsec with slide lines.

Figure 3.49. Effect of slide lines at the soil/gage interface--Al/silastic cylindrical gage.

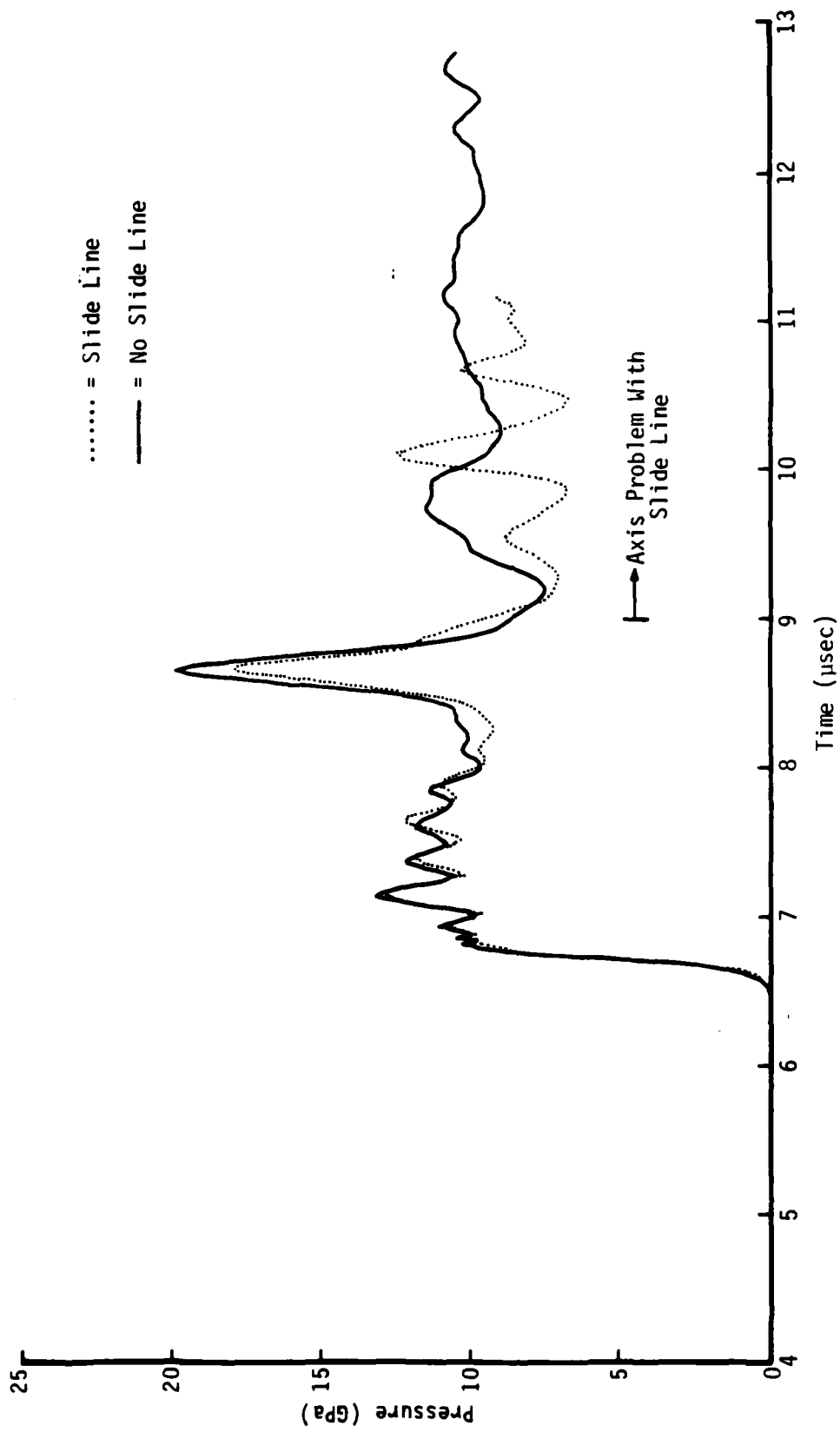


Figure 3.50. Al/Silastic gage response with and without slide lines.

This was not the case as the tied sliding calculation also had the same axis problem at the top of the gage. These calculations appear to have uncovered an error in the slide line algorithms which will be communicated to the people who maintain the STEALTH code for analysis of the problem and suggested corrections.

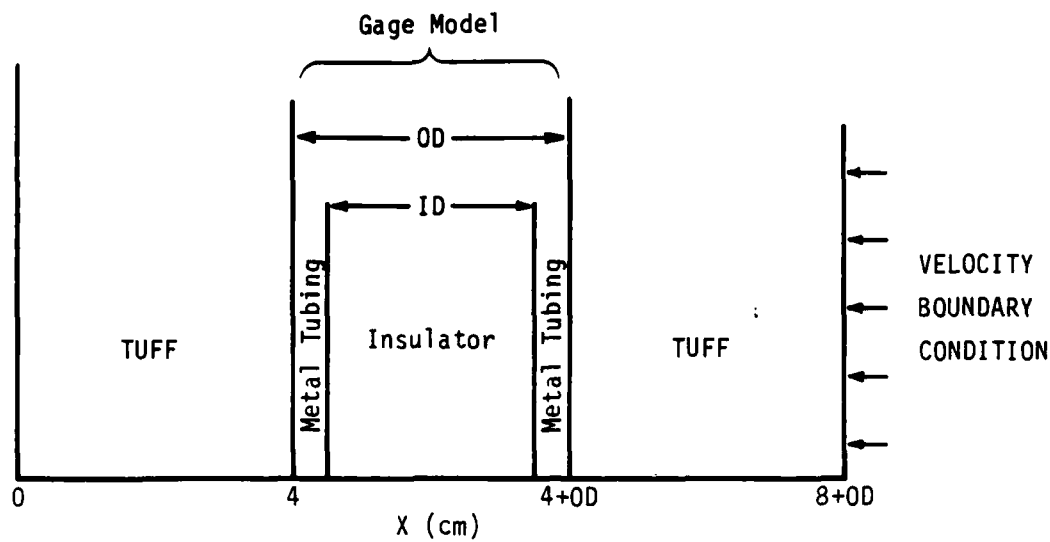
3-5 GAGE MATERIALS STUDY

After the experimental tests of the Al/Teflon and Mg/Teflon cylindrical gages showed Teflon was not a good insulating material, an investigation was made of other material combinations. One aspect of this study was to find the effect of replacing Teflon by other insulating materials. Another was to compare the use of aluminum tubing with magnesium tubing to see if the time and expense of using magnesium was justified in improved gage response.

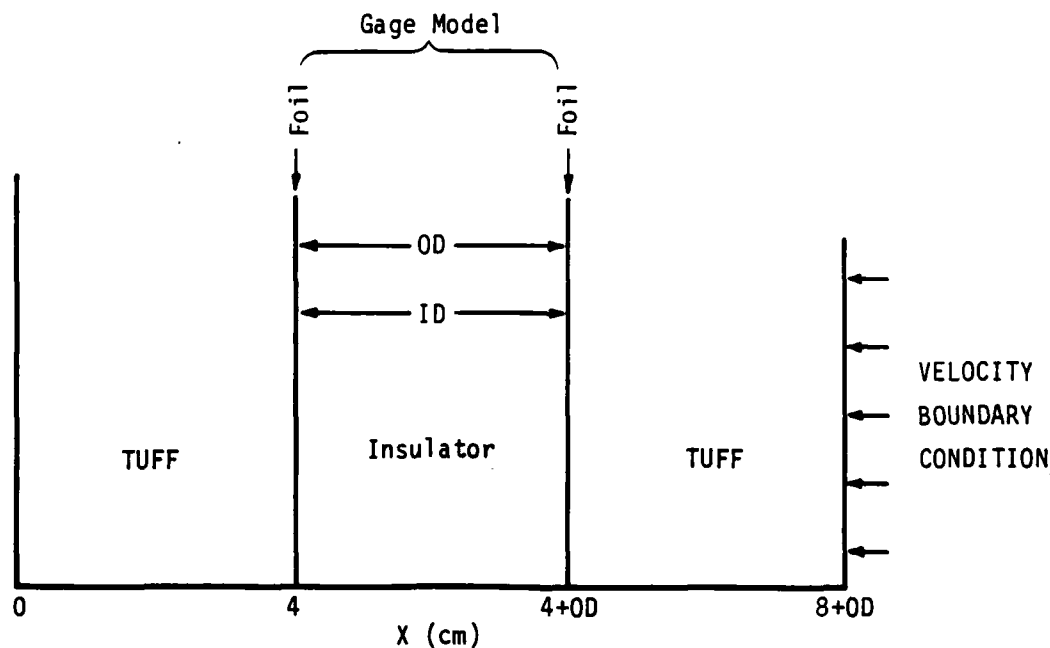
This parameter study was done using a 1-D analog of the SRI cylindrical gage to allow more combinations to be considered in the time available. The insulating materials included were Teflon, silastic rubber, epoxy and polyethylene. These were combined with aluminum tubing, magnesium tubing and aluminum foil. Other metals such as iron and brass were not considered because their densities were relatively high compared to the soil. The equation-of-state data used is given in Table 2.1.

The 1-D model of the cylindrical gage is shown in Figure 3.51a. This model represents a cross section through the center of the gage. Translated from 2-D to 1-D, the metal tubing becomes two metal plates separated by a distance equal to the tubing inner diameter. The space between the plates is filled with the insulating material. The total package (plates and insulator) has a thickness equal to the tubing outer diameter.

Soil regions 4 cm thick were added on each side of the gage model. Zones of equal mass were used in the gage region with the number depending on the gage materials and dimensions. The soil zones were mass matched at the gage/soil boundaries and then increased geometrically by about five percent going towards the grid outer boundaries. About 100 zones were used in



(a) Initial configuration with Al and Mg tubing.



(b) Initial configuration with Al foil.

Figure 3.51. Models for 1-D calculations of the cylindrical stress gage.

each calculation. A velocity boundary condition imposed at one soil outer boundary generated the stress wave that traveled through the soil to impact the gage. This wave was transmitted into the gage and through to the other soil region. The pressure at the center of the gage was edited and assumed to represent what a piezoresistive wire at the same location would measure.

The first calculations made were for Al/Teflon and Al/silastic rubber to test the model. If the center pressures had the same features as those obtained in the 2-D calculations, then this model could be used to study material variations. If the results were greatly different, then it would mean that 2-D effects dominated the gage response and a 1-D model could not be used.

The center pressure obtained from the 1-D Al/Teflon calculation is shown in Figure 1.16a and should be compared with the 2-D results shown in Figure 1.12b. One sees both curves have the same features. The sharp initial rise when the pressure wave reaches the center of the gage is followed by a plateau region that lasts until the pressure spike representing the bottom reflection arrives. After this spike, there is another plateau region at about the incident wave pressure with some smaller oscillations caused by additional reflections. The absolute time of the initial rise is different because of the different soil thicknesses in the two calculations. The time between the initial rise and the bottom reflection spike is not the same because the pressure in the center of the insulating material was edited in the 1-D calculation while in the 2-D calculation the wire could move relative to the insulating material.

The pressure levels are similar in the two calculations. Ignoring the initial oscillations in the 2-D calculation which are mostly numerical noise caused by the wire motion algorithm, the first plateau region is about 11.5 GPa for the 1-D model and 12.5 GPa for the 2-D model. The bottom reflection spike reaches 18 GPa and 20 GPa, respectively. It should be noted that Figure 1.12b shows the results of the calculation made with the original wire motion algorithm. With the revised algorithm, the 2-D peak was also 18 GPa (see Figure 3.37).

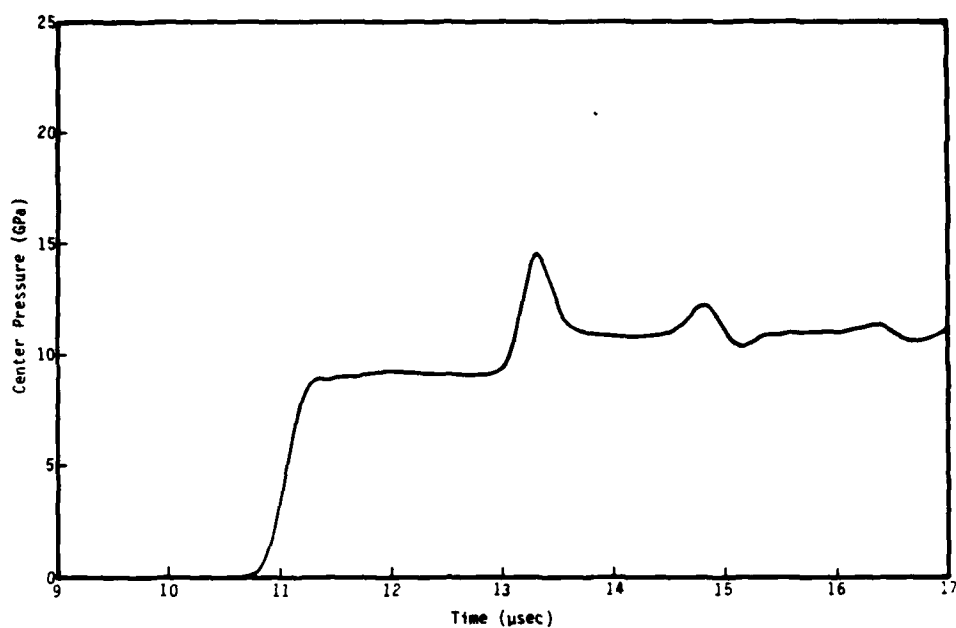
Similar results were obtained using aluminum tubing with silastic rubber. The 1-D and 2-D pressure curves are shown in Figures 1.16b and 1.14, respectively. These curves have the same similarities and differences as described above for the Al/Teflon case. Of interest in Figure 1.16b is the clear indication of the passage of a second and third reflected wave through the center of the gage.

The center pressures from the Al/epoxy and Al/polyethylene calculations are shown in Figure 3.52. We see the expected features in both cases but the magnitudes in the first plateau region and that of the bottom reflection spike are lower. The passage of second and third reflected waves is also seen.

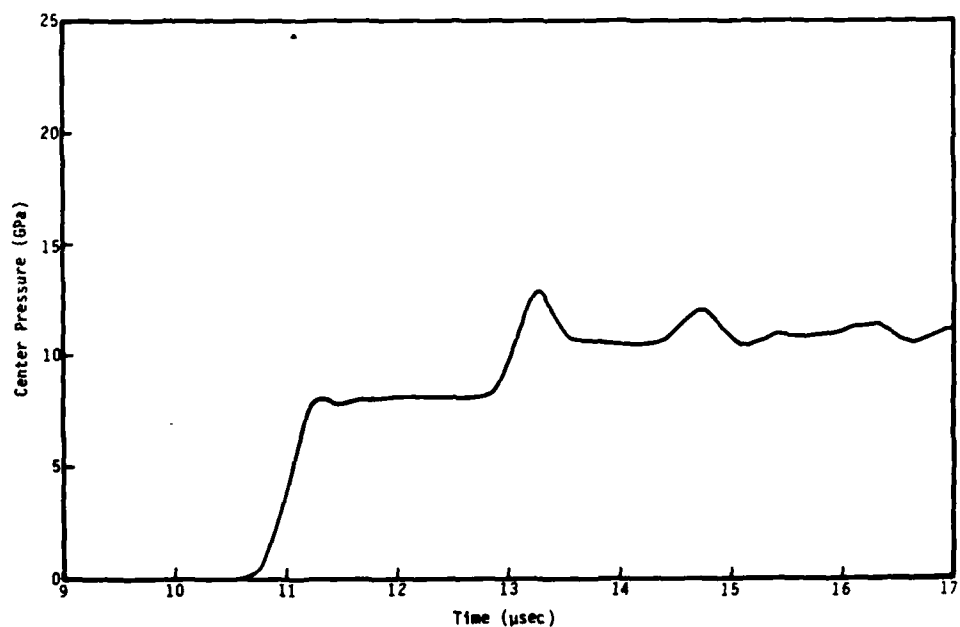
The results of these four calculations are summarized in Figure 3.53. All of these cases correspond to cylindrical gages with the same dimensions as the Al/silastic gage (see Table 3.1). The only difference is the insulator material. For the incident pressure wave of 11 GPa, we see the first plateau pressure is larger if the insulator density is greater than the soil density and smaller when the insulator density is less than the soil density. For the three low-density insulators, this pressure is nearly linear in density. The peak of the reflection spike is also plotted in Figure 3.53 and follows the same trend with density.

The same series of 1-D calculations was repeated with magnesium tubing with the same dimensions as used in the Mg/Teflon gage (see Table 3.1). The 1-D results for the Mg/Teflon combination are shown in Figure 1.17a. This did not agree as closely with the 2-D results shown in Figure 1.12a as was the case with aluminum tubing. In particular, the reflection spike was reduced and broadened compared to the 2-D results. A second calculation was made with the magnesium thickness equal to that used for aluminum. This result is shown in Figure 1.17b. Reducing the magnesium thickness narrowed the reflection spike but did not change its peak value.

The results from the 1-D calculations for the Mg/silastic, Mg/epoxy and Mg/polyethylene combinations were similar to those shown in Figure 1.17a.



(a) Al/epoxy gage



(b) Al/polyethylene gage

Figure 3.52. Center pressure from 1-D calculations of the Al/epoxy and Al/polyethylene cylindrical gages.

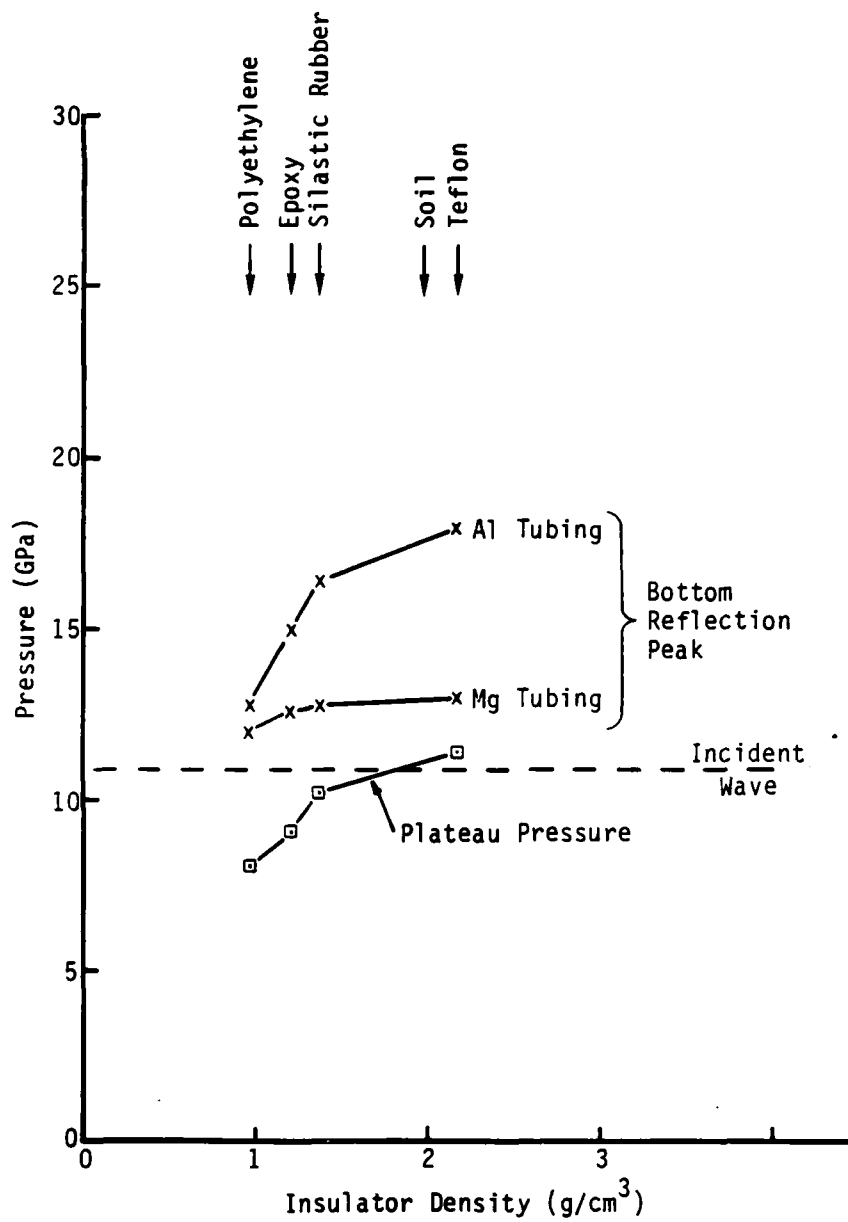


Figure 3.53. Effect of insulator density on response of cylindrical stress gage.

With the thick magnesium tubing, the reflection spikes were broad. Their peak magnitudes varied with insulator density but only in a narrow range going from 13 GPa for Teflon down to 12 GPa for polyethylene. These results are plotted in Figure 3.53. The pressures of initial plateaus were nearly identical to those found in the corresponding aluminum calculations.

The equal plateau pressures obtained with both tubing materials was an interesting result that led us to find out what happened when the tubing thickness was made very small. Such would be the case, for example, if aluminum foil were wrapped around the insulating material as was done in the final design for the TDR gage (see Figure 1.2). While not providing any structural strength, the foil would be an adequate electrical shield for the prevention of EMP currents in the gage conductors.

Calculations were made using aluminum foil and the four insulating materials. The initial STEALTH grid for these calculations is shown in Figure 3.51b. As with the third TDR gage design, the foil was assumed to be very thin and left out of the computational grid. The pressure levels obtained from the foil/Teflon and foil/silastic calculations are shown in Figure 1.18. In both cases, the center pressure initially rises to the value characteristic of the insulating material. This pressure is maintained until the reflected shock from the bottom of the gage reaches the center. Now, however, instead of a reflection spike, the pressure simply shifts to another plateau with a magnitude equal to the incident wave. Calculations made using epoxy and polyethylene as the insulating material also showed the same behavior.

SECTION 4

FLAT PACK STRESS GAGE

Flat pack stress gages of the design shown in Figure 1.19 have been used to make soil stress measurements in many HE and UGT experiments. The operation of this gage is discussed in Section 1.4. Although most of our effort was devoted to the 2-D STEALTH calculations of the TDR particle velocity gage and the cylindrical stress gage, we made a number of 1-D STEALTH calculations using a simple model of the flat pack gage.

The initial configuration for the 1-D STEALTH calculations is shown in Figure 4.1. The flat pack gage was modeled as two metal plates surrounding a thin insulator region. Calculations were made with iron and aluminum plates. Teflon was used to represent the Kapton insulating tape. The manganin piezoresistive element was omitted because of its extreme thinness compared to the insulator and plate thicknesses. Instead, the pressure at the center of the Teflon region was edited to indicate what a piezoresistive element at the same location would measure. In most calculations, the gage model was placed between two soil regions, each 4 cm in width.

The STEALTH grid was zoned in the same manner for all the calculations. Each zone in the gage model had approximately the same mass per unit area with the number varying according to the plate material and its thickness. Mass matching was also done at the two gage/soil interfaces. Going away from the gage, the soil zones were increased geometrically by about 5 percent. With this scheme the number of soil zones is the same in each calculation while the number of zones in the gage region varies as shown in Table 4.1. Some other calculations were made with 1-cm-wide soil regions and finer zoning in the gage region. The results did not differ significantly from those obtained with the coarser grid.

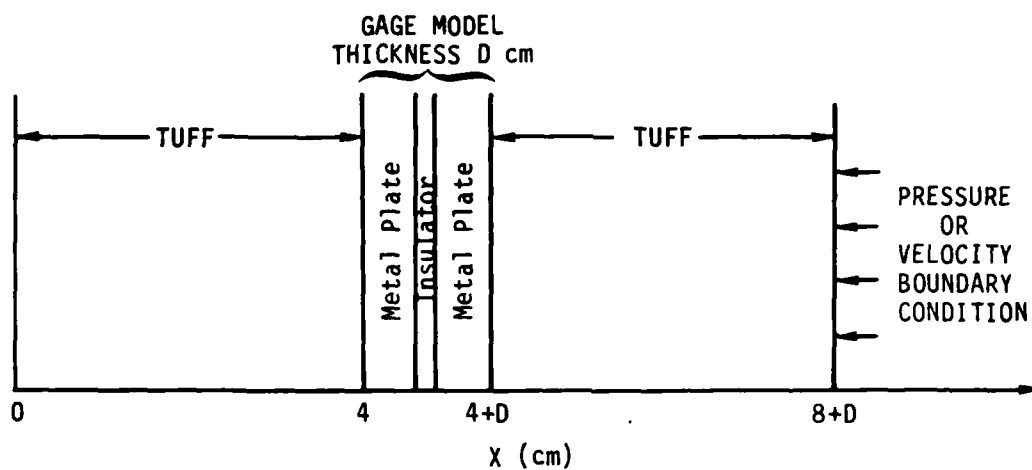


Figure 4.1. Initial configuration for flat pack gage calculations.

Table 4.1. Zoning for the flat pack gage calculations.

| METAL PLATE | | NUMBER OF ZONES | |
|-------------|----------------|-----------------|-------|
| MATERIAL | THICKNESS (cm) | GAGE* | TOTAL |
| Iron | 0.16 | 25 | 85 |
| Iron | 0.32 | 49 | 110 |
| Aluminum | 0.16 | 9 | 69 |
| Aluminum | 0.32 | 17 | 78 |

*Teflon region was one zone 0.0508 cm wide.

One end of the grid shown in Figure 4.1 was fixed and a pressure or velocity boundary condition imposed on the other soil outer boundary. Initially a pressure boundary condition of the form

$$P = P_0 e^{-t/t_0}$$

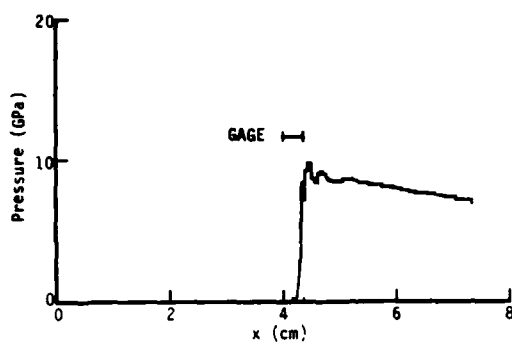
where $P_0 = 10$ GPa and $t_0 = 30$ μ sec was used. It was noticed that the boundary velocity decreased substantially when reflected pressure waves reached the outer boundary. This behavior also occurred in the TDR gage calculations (see Section 2-1) but only along part of the grid boundary. In 1-D geometry, the entire boundary is affected. To mitigate this problem, the pressure boundary condition was replaced by the velocity boundary condition

$$V = 0.124 - 0.00247 t \quad \text{cm}/\mu\text{sec} .$$

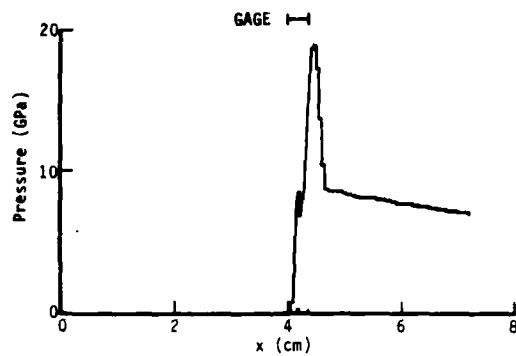
This linear velocity gives approximately the same magnitude stress wave as the pressure boundary condition for t less than 30 μ sec.

The boundary condition generates a stress wave that travels through the soil and impacts the gage. Eventually a transmitted stress wave appears on the other side of the gage in the second soil region. Because this is a 1-D model, there is no way for the incident wave to pass over and envelop the gage. In an actual experiment, this would begin to occur in a few microseconds at the edges of the gage. A 2-D calculation would be needed to determine the magnitude of this effect on the gage response.

The early time interaction of the flat pack gage with 0.16 mm iron plates with an incident stress wave is shown in Figure 4.2. The position of the gage model at each time is indicated on the plots. The free field pressure as a function of time is given in Figure 1.20a while the computed gage center pressure is given in Figure 1.20c.



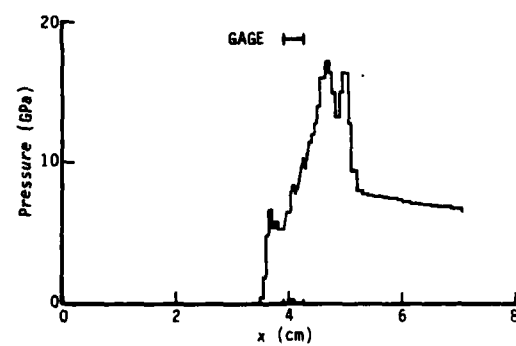
(a) $t = 10 \mu\text{sec}$



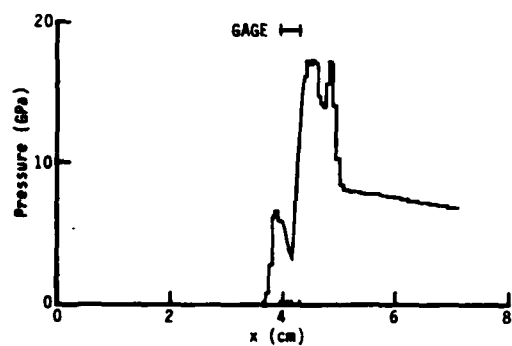
(b) $t = 10.5 \mu\text{sec}$



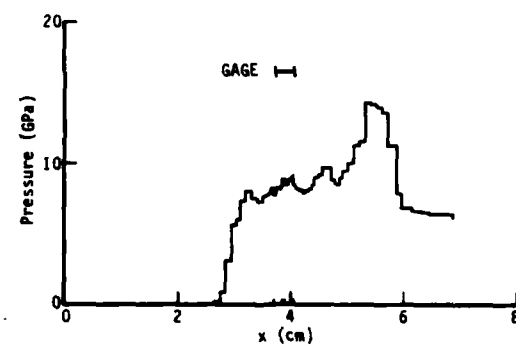
(c) $t = 11 \mu\text{sec}$



(d) $t = 11.5 \mu\text{sec}$



(e) $t = 12 \mu\text{sec}$



(f) $t = 14 \mu\text{sec}$

Figure 4.2. Pressure plots at several times for flat pack stress gage with 0.16 mm iron plates.

At 10 μ sec, the incident wave with a strength of 9 GPa has just reached the gage (see Figure 4.2a). On encountering the iron/tuff interface, the shock strength is approximately doubled to 19 GPa at 10.5 μ sec (Figure 4.2b). This strong pulse is transmitted as a stress wave into the gage and also causes a reflected wave to move into the already shocked soil. These two waves can be seen clearly at 11.0 μ sec in Figure 4.2c. It is also about this time that the gage reaches its maximum compression with the pressure in the Teflon center region nearly 25 GPa (see Figure 1.20c). The high pressures in the gage are relieved by the gage expanding. The pressures are dramatically lower at 11.5 μ sec (see Figures 1.20c and 4.2d). Also note in Figure 4.2d the second shock in the soil caused by the gage expansion.

In the time period from 10 to 11.5 μ sec, the gage has gone from its initial state to a highly compressed state and then expanded. At 12 μ sec, the gage is again being compressed (see Figure 4.2e). This oscillation peaks at about 12.3 μ sec with the center pressure at 13 GPa (Figure 1.20c). The third oscillation peaks at about 13.8 μ sec with a center pressure of 10 GPa. The pressure profile at 14 μ sec is shown in Figure 4.2f. The shock wave has moved about 1 cm into the soil on the opposite side of the gage from the velocity boundary condition. On the other side, the reflected shock and the shock from the first oscillation of the gage have merged together and decayed to about 14 GPa. The smaller shock behind this peak may be from the second gage oscillation. In the gage itself, the pressure is fairly uniform between 8 and 9 GPa.

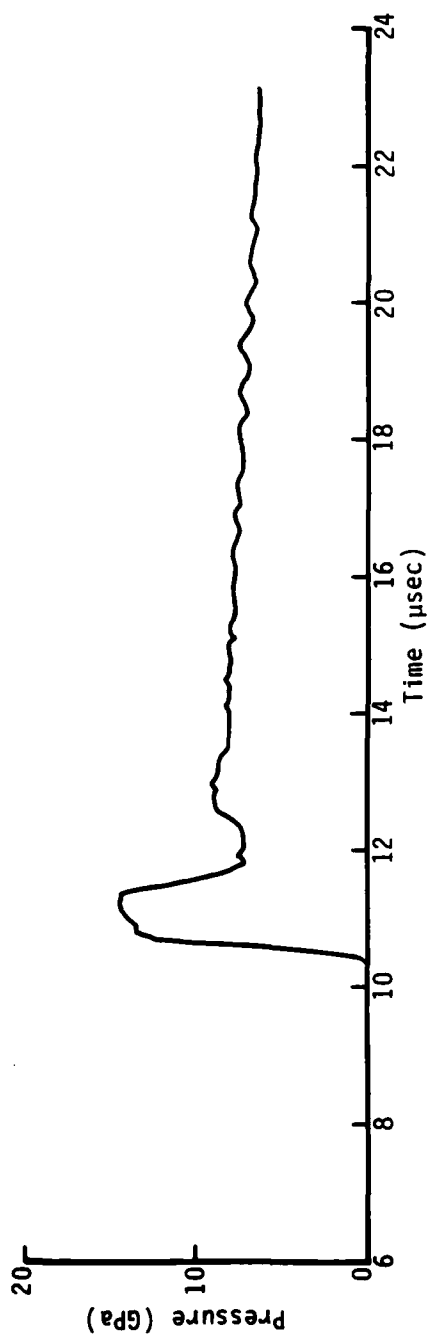
These oscillations are the cause of the "ringing" seen in the flat pack gage response. As the gage expands and contracts, the two iron plates move together and apart. The center insulating material alternately compresses and expands, raising and lowering the pressure seen by the piezoresistive element accordingly. In our calculation, the plates were free to move independently. In the actual gages, they are welded together along the edges which will constrain their motion to some degree.

The plate oscillations are started by the reflection of the incident shock at the gage/soil interface. The magnitude of the reflection is a function of the density change across the interface. With the iron plates, the density ratio is about four and the reflected wave magnitude is about double that of the incident wave. To see the effect of changing the density ratio, a similar 1-D calculation was run with 0.16 cm aluminum plates. In all other aspects, the problems were identical.

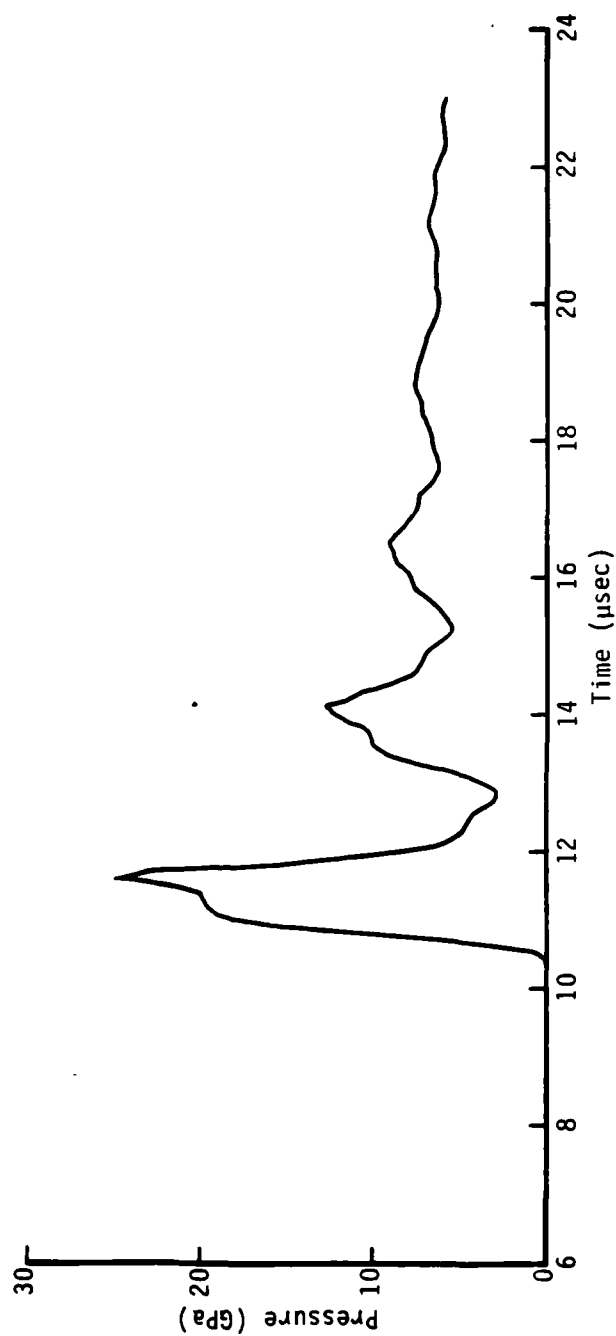
With aluminum, the density ratio is about 1.4 and the reflected pressure was lowered to 14 GPa. This led to smaller gradients as the transmitted wave passed through the gage. The center pressure for this case is shown in Figure 1.20b. Only one large oscillation occurs with a peak at about 14 GPa. After this peak, the center pressure decays to a low of 8 GPa, and then approximates the free field pressure for the remainder of the calculation. In addition to decreasing the magnitude of the gage oscillations, changing from iron to aluminum plates also seems to result in a more damped system.

Additional 1-D calculations were made with thicker plates (see Table 4.1). Similar results were obtained with some timing differences. The center pressure for the case with 0.32-cm-thick iron plates is shown in Figure 4.3b. The initial oscillation peak is again about 25 GPa and the succeeding peaks also have about the same values as seen with the 0.16 cm plates. However, the period of the oscillations has increased from about 1.5 μ sec (peak to peak) with the thin plates to about 2.5 μ sec for the thick plates.

A calculation was also made with 0.32 cm aluminum plates. The computed center pressure for this case is shown in Figure 4.3a. Comparing with Figure 1.20b we see the responses are similar with only one large oscillation when aluminum is used. Again the period of the oscillation is larger with the thicker plates.



(a) Aluminum plates, 0.32 cm thick



(b) Iron plates, 0.32 cm thick

Figure 4.3. Center pressure from 1-D calculations of flat pack gages with 0.32-cm-thick plates.

This set of calculations was rather limited in scope. Other variations could be tried, such as unequal plate thicknesses, varying the width of the insulator region, and so on, to see if further reductions in the oscillations could be made. Even if a theoretically better design is found, fabrication problems or failures in field testing might prevent its use. However, based on our initial results, the construction and testing of an aluminum flat pack gage should be considered.

REFERENCES

1. Hofmann, R., "STEALTH, A Lagrange Explicit Finite Difference Code for Solids, Structural and Thermohydraulic Analysis," Electric Power Research Institute Report EPRI NP-176-1, June 1976, Revised Version (April 1978).
2. Sites, K., "Development of a Particle Velocity Gauge for Use in High Stress Nuclear UGT Experiments," Paper presented at Defense Nuclear Agency Conference on Instrumentation for Nuclear Weapons Effects, March 30 - April 1, 1982.
3. Keough, D., and P. DeCarli, SRI International Corporation. Private communication, July 15, 1981.
4. Keough, D., and P. DeCarli, SRI International Corporation. Private communication, January 7, 1982.
5. Mow, C.C., "On the Effects of Stress-Wave Diffraction on Ground-Shock Measurements: Part I," Rand Corporation Memorandum RM-4341-PR, January 1965.
6. Whitener, J., Research and Development Associates. Private communication, December 16, 1981.
7. Chan, R.K.C., "A Generalized Arbitrary Lagrangian-Eulerian Method for Incompressible Flows with Sharp Interfaces," Journal of Computational Physics 17, 311-331 (1975).

APPENDIX
DETERMINATION OF THE VELOCITY OF THE PIEZORESISTIVE WIRE

The piezoresistive wire at the center of the cylindrical stress gage was modeled as a rigid body in the 2-D STEALTH calculations. This allowed the wire to be included in the calculations as a velocity boundary condition instead of being described by very small zones which would have limited the problem time step. However, it was necessary to provide an algorithm for calculating the acceleration in order to change the wire velocity each cycle.

Initially, the algorithm was based on a scheme used for rigid body motion in a specialized version of the STEALTH code. This algorithm was used for the brass/epoxy, Mg/Teflon and Al/Teflon gage calculations. The first of these was a fine-zoned grid. The latter two had coarse grids and exhibited what appeared to be large numerical oscillations in the average wire pressure and the wire velocity (see Figures 3.25 and 3.35) when compared with similar quantities for the brass/epoxy gage (Figure 3.13).

These oscillations led us to perform calculations for a soil-only grid similar to that used for the cylindrical stress gages and for a rectangular grid. The results for the web grid were noisy while those from the rectangular grid were much smoother. This comparison suggested that the wire motion algorithm was inadequate, at least in a coarse grid. A new algorithm was developed based on the method used to move centroid points in the DRAGNET code, a Lagrangian radiation hydrodynamics code. The new method provided some improvement in test calculations, particularly in the wire velocity. It was used in a recalculation of the Al/Teflon gage and the calculation of the Al/silastic gage.

This appendix describes the original algorithm and the soil-only calculations made to test its effectiveness. This is followed by a description of the centroid wire motion algorithm and the results of test calculations using it in a soil-only grid. Both algorithms were used for calculating the Al/Teflon gage. The average wire pressure and velocity for those two calculations is compared in Figure 3.37.

In both algorithms, it is assumed the wire is a rigid cylinder of constant radius R surrounded by a uniform media in which a stress field is present. For this case, the net force in the y -direction is

$$F_y = \int_0^{2\pi} (\tau_{yy} \cos\theta + \tau_{xy} \sin\theta) R d\theta ,$$

where τ_{yy} and τ_{xy} are the stresses at the surface of the cylinder. If the media is hydrodynamic (zero yield strength) then $\tau_{yy} = -P$ and $\tau_{xy} = 0$ where P is the pressure. In this special case, the net force integral becomes

$$F_y = - \int_0^{2\pi} P R \cos\theta d\theta .$$

If there is symmetry about the y -axis, then the contributions to the force integral from the τ_{xy} term will cancel and the force integral reduces to

$$F_y = \int_0^{\pi} \tau_{yy} R \cos\theta d\theta ,$$

where the integration path goes around a semicircle.

In the cylindrical stress gage calculations, the piezoresistive wire is at the center of a planar web grid such as shown in Figure A.1. Because of symmetry, only half the wire is needed. The wire boundary is

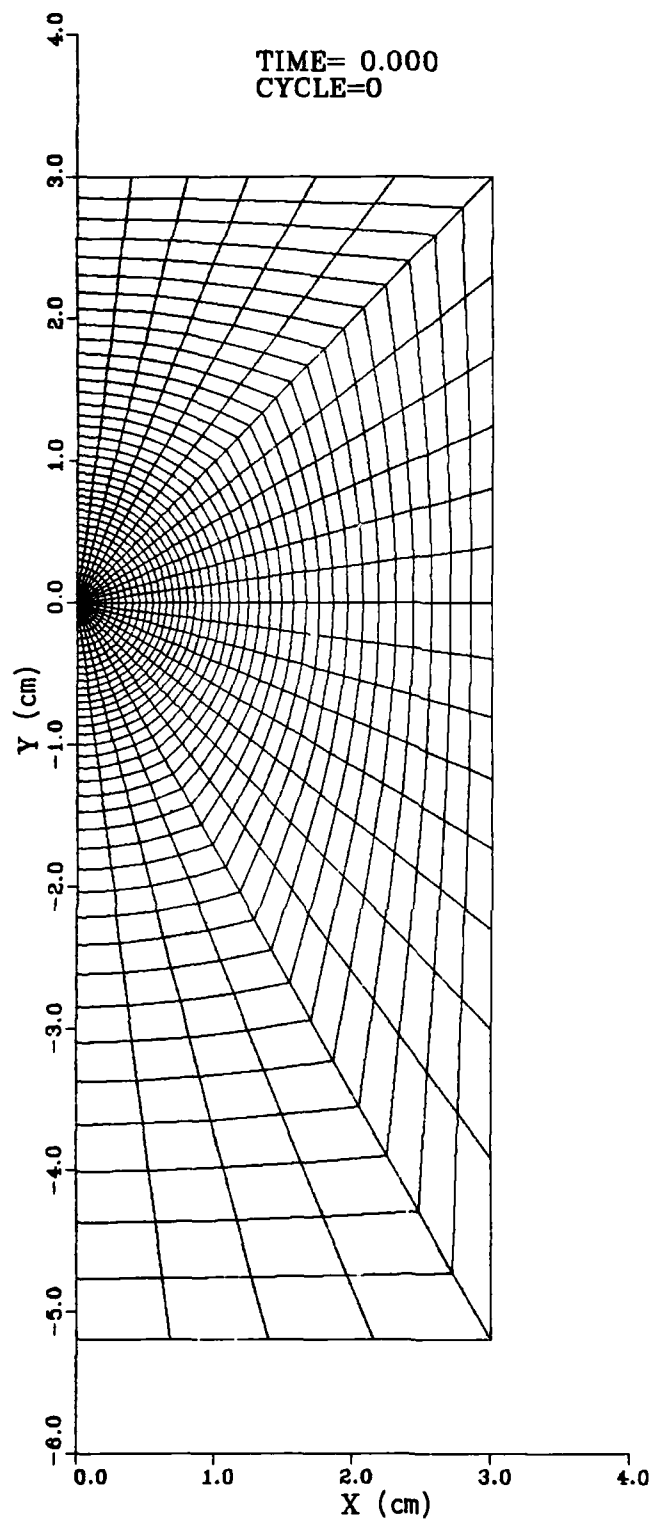
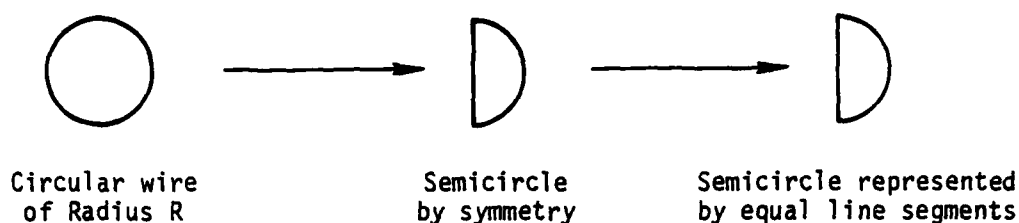


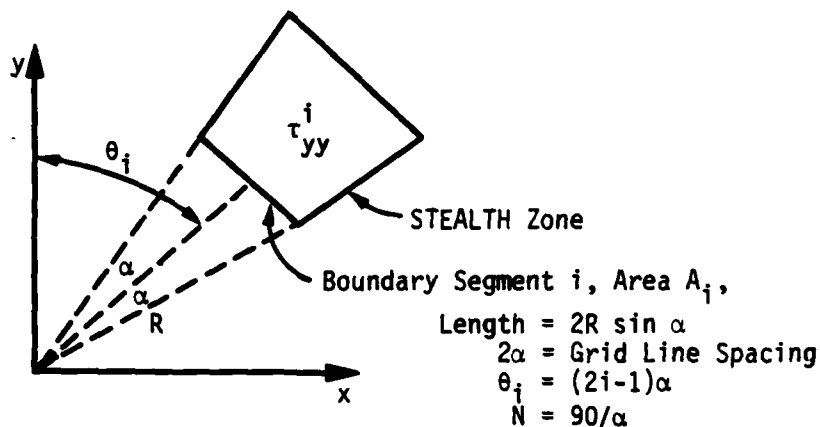
Figure A.1. Web grid for test problem.

defined by a series of grid points connected by line segments. For the wire to act as a rigid body, each of these grid points must be moved the same distance each cycle.



The radial grid lines connected to the wire surface are equally spaced and if extended would meet at the center of the wire with constant angular spacing between adjacent lines. For 5° spacing, the wire boundary is formed with 36 equal line segments; for 7.5° spacing, there are 24 equal line segments.

The STEALTH zone adjacent to each of the line segments forming the wire boundary has a zone centered material stress field (τ_{yy} , τ_{xx} , τ_{xy}) that changes as a function of time. This stress field is used to evaluate the force integral F_y in both wire motion algorithms.



In the original algorithm, the zone-centered stress in Zone i , τ_{yy}^i , was assumed to be the same as the stress τ_{yy} acting on the surface of the wire. The magnitude of the force on each boundary segment is $\tau_{yy}^i A_i$ where A_i is the boundary area. The area is equal to the segment length times 1 cm and replaces $R d\theta$ in the force integral. The term $\cos \theta$ is replaced by $\cos \theta_i$, where θ_i is the angle from the y -axis to the center of the boundary segment. This implies that the direction of the force on the segment is radially inward along the line with angle θ_i from the y -axis.

The force integral is approximated as the sum of the forces in the y -direction on each boundary segment:

$$F_y = \sum_{i=1}^N A_i \tau_{yy}^i \cos \theta_i$$

$$= 2R \sin \alpha \sum_{i=1}^N \tau_{yy} \cos \theta_i .$$

The acceleration in the y -direction is

$$a_y = \frac{F_y}{M}$$

where M = wire mass in the semicircle per unit length
 $= \pi R^2 \rho / 2$
 ρ = wire density.

By symmetry, the acceleration in the x -direction is zero.

The wire acceleration is calculated at the beginning of each cycle and used to find the new wire velocity

$$v_y^{\text{new}} = v_y^{\text{old}} + a_y \Delta t ,$$

where Δt is the appropriately centered time step. This velocity is stored as part of the boundary conditions and eventually used to determine the new wire position at the end of the cycle.

At the same time as the wire velocity is calculated, we also calculated the average pressure around the wire. This quantity was edited each cycle as an indication of the pressure recorded by the gage.

The web grid shown in Figure A.1 was used for the algorithm test calculations. This grid has the same outer dimensions and boundary conditions as the grid used for the Al/Teflon cylindrical gage calculation. However, for the test problems, all the zones contained soil with density 1.97 g/cm^3 and the tuff equation of state. Uniformly spaced circular grid lines were used out to 0.7 cm from the wire. Beyond that distance, the spacing changed geometrically to the grid outer boundary similar to the zoning in the cylindrical gage calculations. For comparison with the rectangular grid, the wire density was set equal to the soil density.

The rectangular grid is shown in Figure A.2. It has the same outer dimensions as the web grid. The zone spacing in the y-direction was chosen to be similar to the web grid zoning along the y-axis. The velocity condition used in the cylindrical gage calculations was imposed on the top of the grid. For comparison with the web grid calculations, the velocity and average pressure at the grid point initially at $x=0$ and $y=0$ was edited each cycle.

With the rectangular zoning, the results were as expected. The downward-moving shock wave traveled approximately $0.42 \text{ cm}/\mu\text{sec}$ and reached the test point at about $7 \mu\text{sec}$. Because of the coarse zoning and the use of artificial viscosity, the pressure and particle velocity took about $0.4 \mu\text{sec}$ to rise to the expected values of 10.9 GPa and $0.133 \text{ cm}/\mu\text{sec}$, respectively. At later times, these values are maintained with small numerical oscillations as shown in Figure A.3 (pressure) and Figure A.4 (velocity).

Several web grid problems were run varying problem parameters such as use of rezoning, magnitude of artificial viscosity terms, etc. All the problems gave very oscillatory results. For example, with rezoning in the

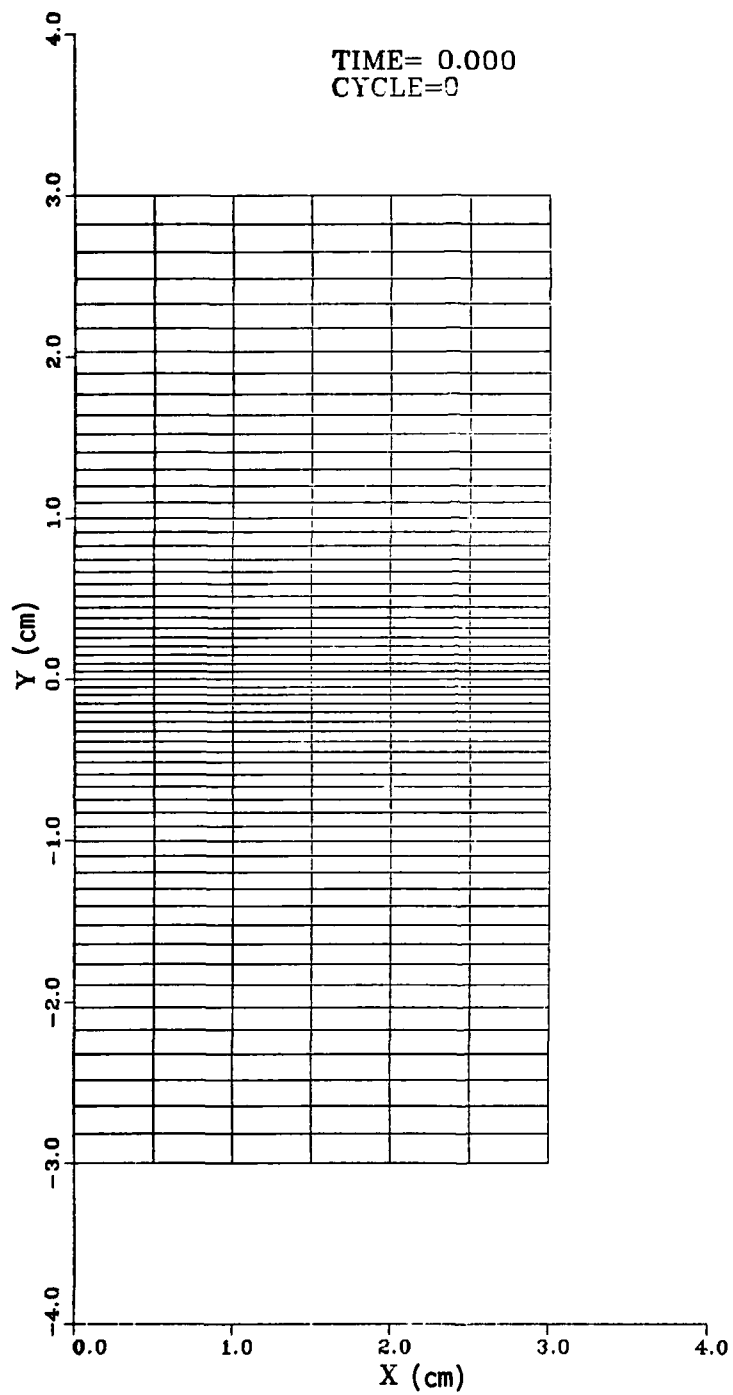
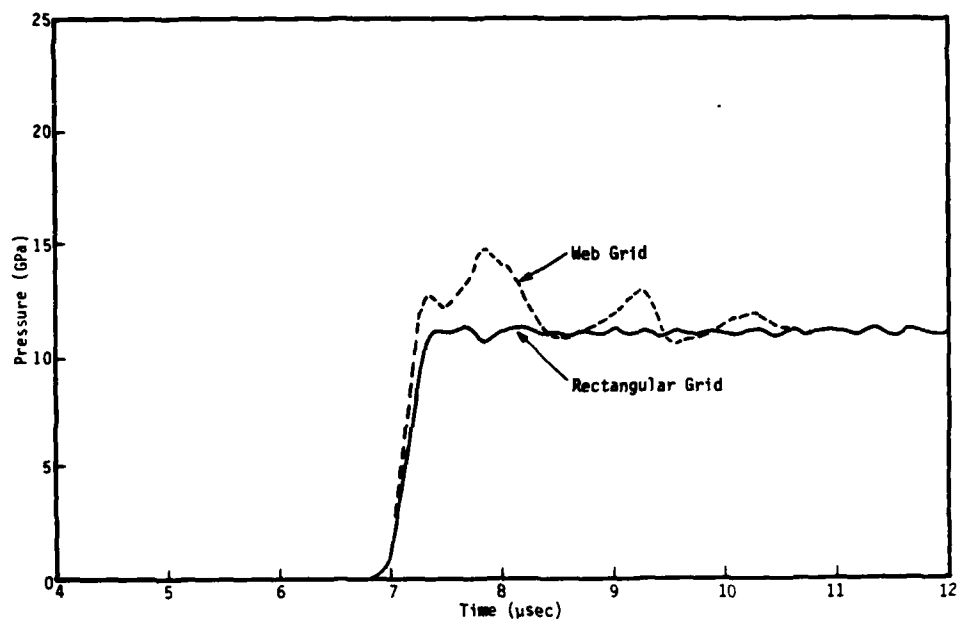
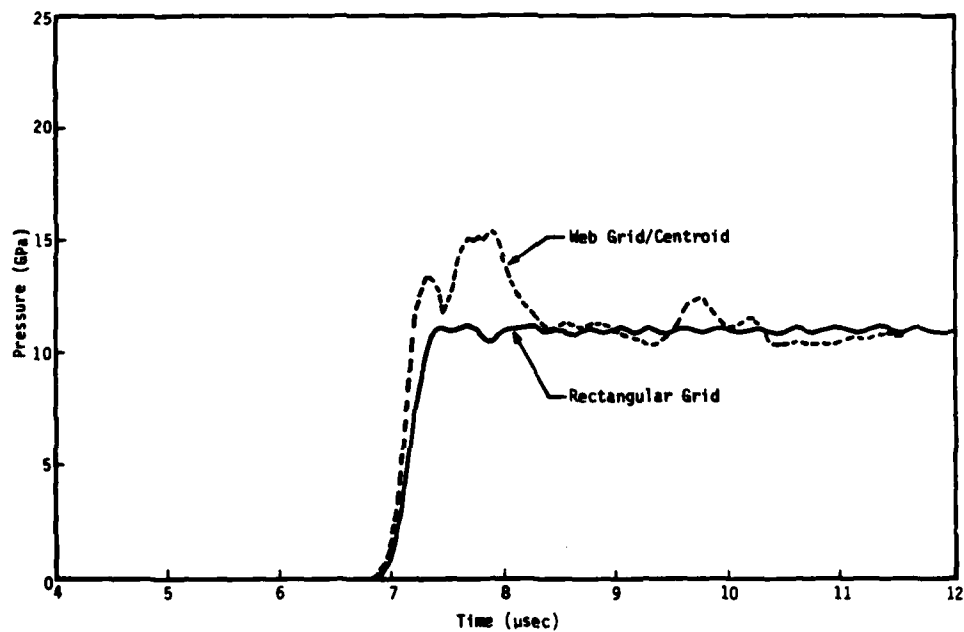


Figure A.2. Rectangular grid for test problem.

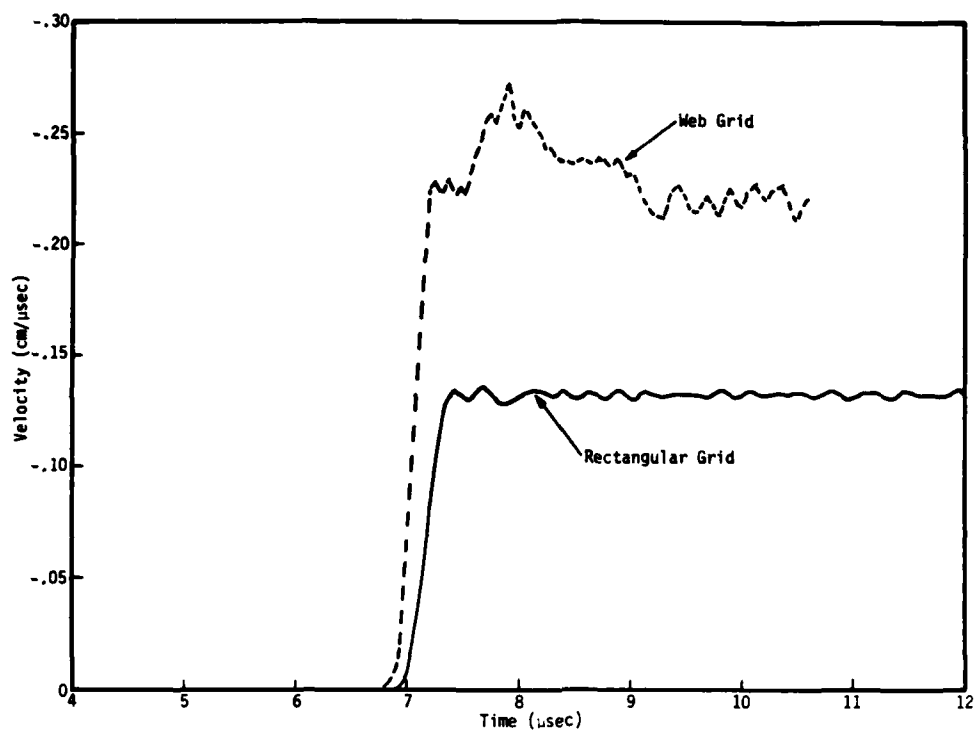


(a) Original algorithm

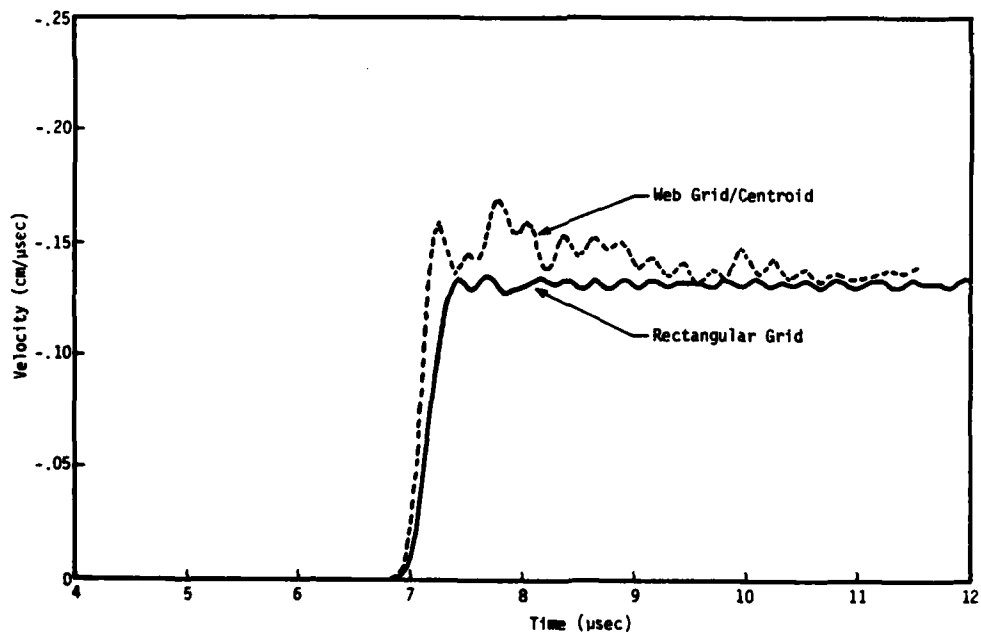


(b) Centroid algorithm

Figure A.3. Comparison of average pressure at gage center for rectangular and centroid grids.



(a) Original algorithm



(b) Centroid algorithm

Figure A.4. Comparison of velocity at gage center for rectangular and centroid grids.

inner 14 grid lines (the gage region) and the standard quadratic artificial viscosity term, the results varied substantially from those obtained in the rectangular grid. The average wire pressure (see Figure A.3a) initially overshoots to about 15 GPa and then undergoes an oscillatory decay with time to the correct value. The wire velocity, shown in Figure A.4a, reaches nearly double the free field particle velocity and maintains that value at late times. These and similar results from other calculations, some with fine zoning, led us to change the wire motion algorithm.

Rethinking the theoretical basis of the original wire motion algorithm, we found two possible problem areas. First, the force integral requires knowledge of the stress field at the wire surface and we have only the zone centered stresses in the zones surrounding the wire. Second, in computing the summation for the force integral we had assumed that the incremental forces were acting perpendicularly to the line segments comprising the wire surface. However, the zones surrounding the wire distort with time, even with rezoning (see Figure 3.34), so that lines drawn from the zone centers to the wire surface are in general not perpendicular to the wire. Even in a perfect gage the zones would tilt towards the x-axis after being compressed by the passage of a shockwave.

The centroid wire motion algorithm attempts to account for the effects discussed above. It is based on the method used in the DRAGNET code to move centroid points which occur at the center of spheres or cylinders when web zoning such as shown in Figure A.1 is used. The gage wire is very nearly a centroid point as its area is only about 2 percent of the area of the adjacent zones. The new algorithm becomes identical to the DRAGNET algorithm if the wire shrinks to a point with zero mass.

The basis of the centroid algorithm is shown in Figure A.5. To better use the zone centered stresses, the force integral is computed along the integration surface denoted by the dashed line. This surface is defined by connecting the midpoints of the radial grid lines that form the boundaries of the zones adjacent to the wire. Along this path, the summation for the force integral becomes

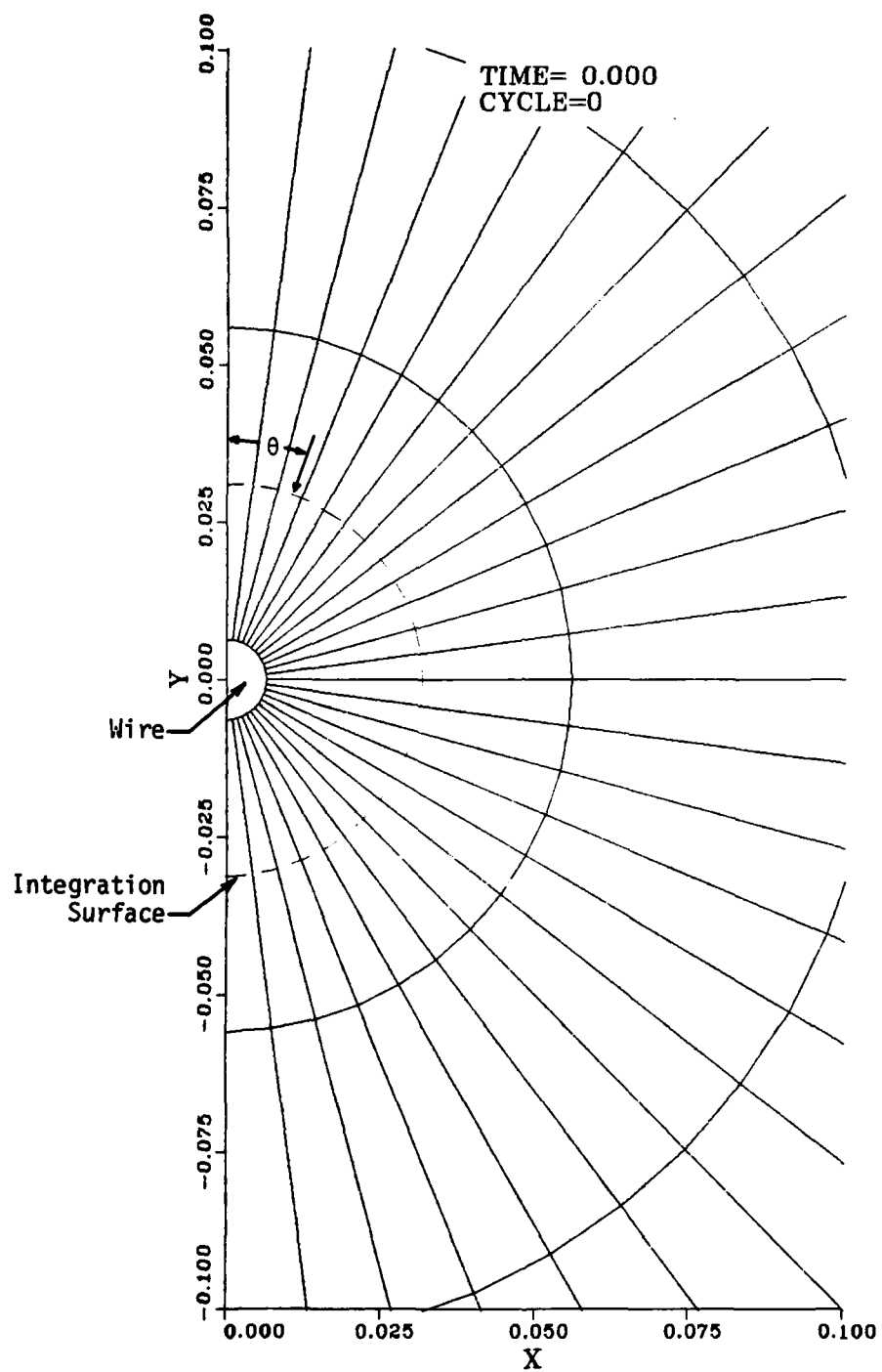


Figure A.5. Zones used in the centroid wire motion algorithm.

$$F_y = \sum_{i=1}^N A_i \tau_{yy}^i \cos \theta_i$$

where A_i = length of line segment in Zone i

$$= \sqrt{(x_i^c - x_{i-1}^c)^2 + (y_i^c - y_{i-1}^c)^2}$$

τ_{yy}^i = y -direction zone centered stress in Zone i

θ_i = angle between the normal to the line segment with length A_i and the y -axis

N = number of zones adjacent to wire.

It is easy to show that

$$\cos \theta_i = \frac{x_i^c - x_{i-1}^c}{A_i}$$

so that the summation for F_y reduces to

$$F_y = \sum_{i=1}^N \tau_{yy}^i (x_i^c - x_{i-1}^c)$$

The volume enclosed by the dotted line segments contains a total mass M per unit length equal to the wire mass M_w plus the partial masses of the adjacent zones. This mass is:

$$M = M_w + \sum_{i=1}^N \rho_i V_i$$

where M_w = wire mass in the semicircle per unit length

ρ_i = density in Zone i

V_i = volume of Zone i between line segment A_i and the wire per unit length.

The acceleration of this mass in the y-direction is:

$$a_y = \frac{F_y}{M} .$$

This is assumed to also be the acceleration of the wire. Note that this formulation limits reasonably as the wire mass goes to zero.

The centroid algorithm was tested on three soil-only calculations with the web grid shown in Figure A.1. These were a purely Lagrange calculation (no rezoning), a calculation with rezoning in the inner 14 grid lines, and a Lagrange calculation with a node coupler to smooth velocity fluctuations. The node coupler was a version of the one proposed by Chan (Reference 7) to reduce "hour-glassing" in Lagrangian grids caused by alternate sign numerical errors.

The wire pressure and velocity from the calculation with the rezone region are compared with the rectangular grid results in Figures A.3b and A.4b, respectively. Both the pressure and velocity initially overshoot the expected values and then exhibit an oscillatory decay to the expected values over a few microseconds. Without rezoning, the results were similar but with larger overshoot and oscillations. With the node coupler, the initial overshoot was about the same but the fluctuations were smaller and nearly completely damped by 9 μ sec.

The differences between the old and new algorithms can also be seen in Figures A.3 and A.4. The average pressure curves behave similarly, suggesting that this quantity is not greatly sensitive to the details of the wire motion. However, there is a great improvement in the wire velocities with the centroid algorithm. While the old algorithm gave a wire velocity that was almost a factor of two greater than the expected value, the values computed with the new method limit to approximately the soil particle velocity.

These results imply that the centroid algorithm gives better late time results but is not effective in reducing the initial overshoot. In fact, there was significant improvement at early times as well. This can be seen in Figure A.6 which plots the wire pressure versus wire velocity from the initial motion up to the first pressure peak. Shown in this figure are curves for the rectangular grid, the web grid with the old algorithm, and the web grid with the new centroid algorithm.

For the rectangular grid, the pressure versus velocity line has an initial sharp rise followed by a nearly linear path to the expected values (10.9 GPa, -0.133 cm/ μ sec). The line for the old algorithm has a very much different behavior. The pressure rises much more slowly with wire velocity until the peak wire velocity is reached after which there is a sharp rise to the peak pressure with little change in the velocity. The new algorithm gives a pressure versus velocity curve that is much like the rectangular case but overshoots the expected values by about 20 percent.

While these results show the centroid algorithm is an improvement over the original wire motion algorithm, there is still what appears to be numerical noise in the computed gage response. Other factors than the wire motion algorithm that may be responsible include the basic differencing scheme used in the STEALTH code, the coarseness of the grid and the rezone scheme but time was not available for further investigation of this problem.

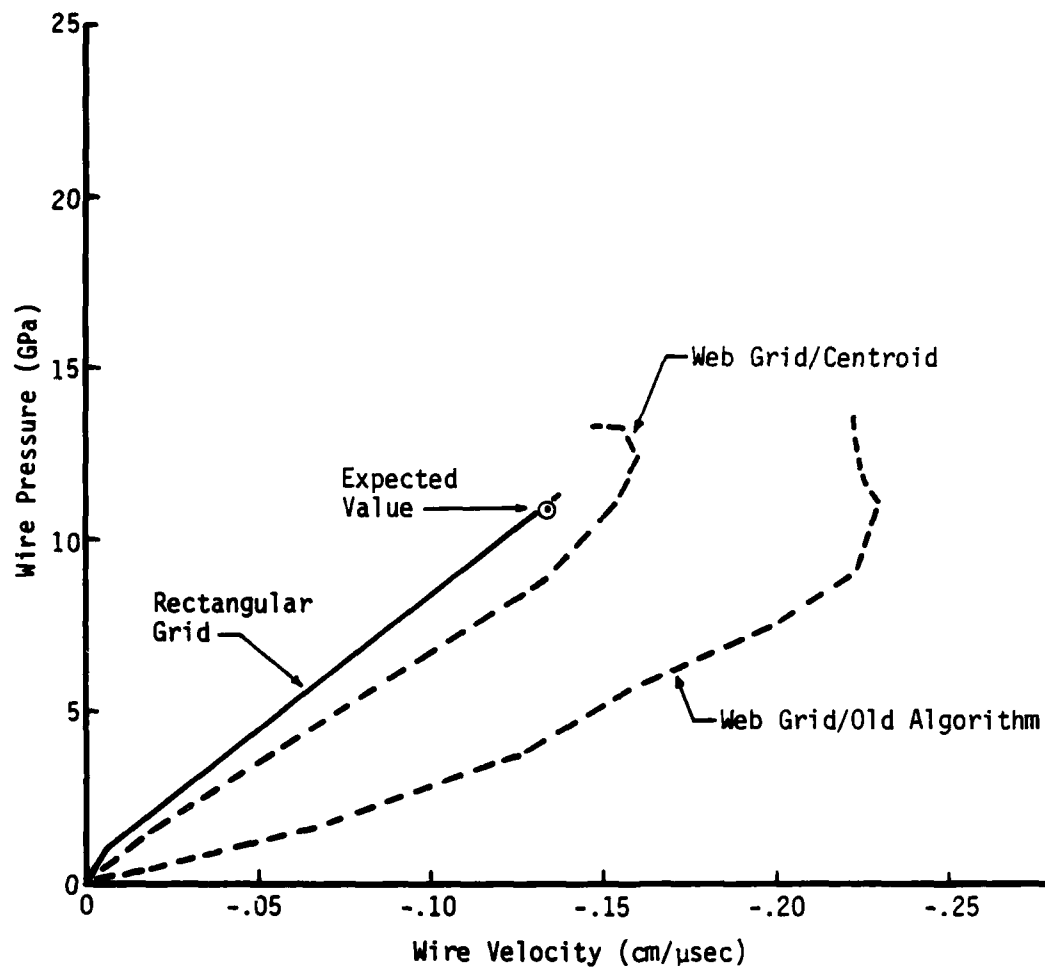


Figure A.6. Wire pressure as a function of wire velocity to the first pressure peak.

DISTRIBUTION LIST

DEPARTMENT OF DEFENSE

Assistant to the Secy of Def
Atomic Energy
ATTN: Executive Asst

Defense Nuclear Agency
ATTN: SPAS
ATTN: SPTD, T. Kennedy
ATTN: SPSS, J. Jones
ATTN: STRA
ATTN: STSP
ATTN: SPTD, D. Miller
4 cy ATTN: STTI/CA

Defense Tech Info Ctr
12 cy ATTN: DD

Field Command
Defense Nuclear Agency
ATTN: FCTT
ATTN: FCTT, W. Summa
ATTN: FCT
ATTN: FCTEI
ATTN: FCTOU

Field Command Test Directorate
ATTN: FCTC, Mr LaComb

Joint Chiefs of Staff
ATTN: J-5 Nuc Div/Strat Div

Under Secy of Def for Rsch & Engrg
ATTN: Strat & Space Sys, OS

DEPARTMENT OF THE ARMY

BMD Systems Cmd
ATTN: BMDSC-HW, R. Dekalb
ATTN: BMDSC-HLE, R. Webb

Harry Diamond Labs
ATTN: DELHD-NW-P, J. Gwaltney
ATTN: DELHD-TA-L

US Army Engr Waterways Exper Station
ATTN: B. Weich

US Army Nuc & Chem Agency
ATTN: Library

DEPARTMENT OF THE NAVY

Naval Rsch Lab
ATTN: Code 2627

Naval Surface Wpns Ctr
ATTN: Code F31

DEPARTMENT OF THE AIR FORCE

Air Force Systems Cmd
ATTN: DLW

Ballistic Missile Ofc/DAA
ATTN: ENSN

DEPARTMENT OF THE AIR FORCE (Continued)

Air Force Wpns Lab
ATTN: SUL
ATTN: NTE, M. Plamondon
ATTN: NTE, Capt Johnson

OTHER GOVERNMENT AGENCY

Central Intelligence Agency
2 cy ATTN: Tech Lib

DEPARTMENT OF ENERGY CONTRACTORS

University of California
Lawrence Livermore National Lab
ATTN: Tech Info Dept Lib
ATTN: L-21, D. Oakley

Los Alamos National Lab
ATTN: Reports Library
ATTN: MS F670, J. Norman

Sandia National Labs
ATTN: J. Plimpton
ATTN: Tech Lib 3141

DEPARTMENT OF DEFENSE CONTRACTORS

Astron Rsch & Engrg
2 cy ATTN: J. Huntington

California Rsch & Tech, Inc
ATTN: K. Kreyenhagen

Cushing Associates
ATTN: V. Cushing

Electro-Mech Sys, Inc
ATTN: R. Shunk

General Rsch Corp
ATTN: E. Steele

H-Tech Labs, Inc
ATTN: B. Hartenbaum

Kaman Sciences Corp
ATTN: Library
ATTN: F. Shelton

Kaman Sciences Corp
ATTN: E. Conrad

Kaman Tempo
ATTN: DASIAc

Kaman Tempo
ATTN: DASIAc

Pacific-Sierra Rsch Corp
ATTN: L. Johnson
ATTN: H. Brode, Chairman SAGE
ATTN: L. Schlessinger

Pacific-Sierra Rsch Corp
ATTN: G. McLellan

DEPARTMENT OF DEFENSE CONTRACTORS (Continued)

R&D Associates

ATTN: Tech Info Ctr
ATTN: P. Haas
ATTN: J. Lewis

S-CUBED

ATTN: K. Pyatt
ATTN: D. Grine
ATTN: Library
ATTN: P. Coleman

Science & Engrg Associates, Inc
ATTN: J. Cramer

Science & Engrg Associates, Inc
ATTN: J. Stockton

DEPARTMENT OF DEFENSE CONTRACTORS (Continued)

Science Applications, Inc

ATTN: H. Wilson
4 cy ATTN: R. Schlaug

Science Applications, Inc
ATTN: K. Sites

SRI International

ATTN: P. De Carli
ATTN: D. Keough

Tech Reps, Inc

ATTN: R. Holmes

Washington State University
ATTN: Prof Y. Gupta

END

FILMED

12-84

DTIC